

***Vibrational spectroscopy for characterisation of a cyclic antimicrobial peptide***

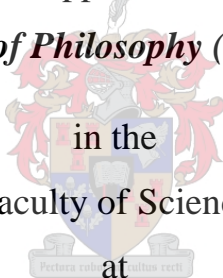
by

**Ngaatendwe Buhle Cathrine Pfukwa**

Dissertation approved for the degree

***Doctor of Philosophy (Physics)***

in the  
Faculty of Science  
at

The crest of Stellenbosch University, featuring a shield with a blue and red design, topped with a crown and surrounded by a red and white border. Below the shield is a banner with the Latin motto "Pacta sunt ossa recti".

Stellenbosch University

Supervisor: Dr. Pieter H. Neethling

Co-supervisor: Prof. Marina Rautenbach

Co-supervisor: Prof. Anthony W. Parker

Co-supervisor: Prof Erich G. Rohwer

Department of Physics

Stellenbosch University

December 2021

## **Declaration**

By submitting this thesis electronically, I Ngaatendwe Buhle Cathrine Pfukwa declare that the entirety of the work contained therein is my own, original work, that I am the sole author thereof (save to the content explicitly stated otherwise), that reproduction and publication thereof by Stellenbosch University will not infringe any third party rights and that I have not previously in its entirety or in part submitted it for obtaining any qualification.

.....

**Ngaatendwe Buhle Cathrine Pfukwa**

.....

December 2021

Copyright © 2021 Stellenbosch University

All rights reserved

## Abstract

In order to understand antimicrobial peptide action towards membrane surfaces it is imperative to first understand the structure and conformational behaviour of the antimicrobial in solution environments representative of the target membrane. Information on conformational behaviour can be extracted in more detail from analysis of the peptide secondary structure using the structural sensitivity afforded by two dimensional infrared (2D-IR) spectroscopy with which subtle details of peptide structure, which may not be well resolved with one dimensional infrared (1D-IR) spectroscopy, can be obtained. With 2D-IR spectroscopy spectral content is spread over two frequency axes and the high time resolution on femtosecond and picosecond timescales for transient processes provides an advantage over conventional techniques such as X-ray diffraction, circular dichroism (CD) or Ultraviolet spectroscopy.

In this study the aims were to evaluate the adaptability of two-dimensional infrared (2D-IR) spectroscopy, together with multivariate data analysis methods such as principal component analysis (PCA), to provide and extract spectral details which can be correlated to changes in structure of a cationic antimicrobial peptide (CAMP) gramicidin S (GS). GS was selected as prototype as it is a well characterised anti-parallel  $\beta$ -sheet peptide, active by disrupting bacterial membranes, consequently causing membrane penetration.

Furthermore, a qualitative working relationship between 1D and 2D IR and Raman spectroscopy in corroboration with quantum mechanical (QM) simulations was established towards correlating GS spectral features to conformational secondary structural changes. The structural changes were used to elucidate the conformational behaviour of GS in selected solvent environments which are representative of GS target membrane lipid bilayers. The solvent environments were an aqueous ubiquitous environment ( $\text{H}_2\text{O}/\text{D}_2\text{O}$ ), a membrane mimetic partially polar environment (1-octanol) and a membrane mimetic strongly H-bonded environment (TFE). Self-association of GS was promoted in  $\text{H}_2\text{O}/\text{D}_2\text{O}$  and 1-octanol forming aggregates which persisted in solution at increasing peptide concentration, as revealed from increase in the  $\beta$ -sheet content and loss in  $\beta$ -turns. While in TFE, a strong H-bonding solvent, the GS aggregates were molecularly solvated. These changes were correlated to occur in the residues which contribute greatly to the amphiphilic nature of GS. Further solvent effects on the structural factors contributing to GS bioactivity are discussed.

The thermostability of GS was investigated for the temperature range 20-80 °C. The dissociation of GS aggregates/small oligomers to monomeric structures in 1-octanol was favoured at elevated

temperatures. Thermodynamic parameters were extracted and the dissociation process was described by a bimodal profile with two identified melting transitions at  $T_{m1} = 45\text{ }^{\circ}\text{C}$  and  $T_{m2} = 57\text{ }^{\circ}\text{C}$ .

Results obtained confirmed that both IR and Raman can provide complementary results as evidenced by their sensitivity towards hydrophilic and hydrophobic structures in GS. Further providing insight towards the type of residue substituents which can be interchanged in future synthesis of GS derivatives, with the aim of increasing the bioactivity of GS whilst lowering its haemolytic effects. The significance of SERS using silver nanoparticles in detection of low peptide concentrations is reported and a GS concentration of  $1 \times 10^{-5}\text{ M}$  was detected.

Information in this thesis demonstrates the novelty and broad use of 1D and 2D IR, RS and SERS techniques in understanding the solvent and temperature induced conformational changes which occur in GS, which provides information on GS structure towards generation of more bioactive GS derivatives for therapeutic purposes.



**Only believe**



## Acknowledgements

I would like to express my thanks and gratitude to the following persons and institutions:

- First Dr. Pieter H. Neethling, my MSc and PhD supervisor for opening the door when I joined the Laser Research Institute (LRI) back in 2014. I thank you for your constant support, motivation, your guidance and regular concern throughout my academic journey. Your commitment to help and your patience is acknowledged, thank you for shaping me as a young researcher, I am eternally grateful.
- My co-supervisor, Prof. Anthony W. Parker, for your invaluable support and availing the opportunity for me to conduct research at the Central Laser Facility (CLF), RAL, UK. I am grateful for your tremendous support, the many pointers and ideas you gave in my MSc and PhD studies. The knowledge you imparted on me is priceless.
- My co-supervisor Prof. Marina Rautenbach, I owe a lot of gratitude towards the ideas and support you gave in my PhD work. You made the journey easier for me in the Biopeptide group, your detailed contributions towards this work shaped my analytical skills and is deeply acknowledged.
- Prof. Neil T. Hunt, thank you for your immeasurable input and support as I carried out my 2D-IR experiments at the CLF and data analysis. Your willingness to introduce me to a learning new experimental technique shaped my career path in different ways.
- I thank the following for funding my studies, without them this research work would not have been possible; The African Laser Centre for funding my MSc and my PhD studies; The Newton Fund for funding my international travel and funding the duration of my stay as I conducted research in UK;
- Prof. Mark Tame, thank you for funding my final year of my PhD through the SARChi bursary, the funding allowed me to successfully complete my final year of study .
- To my colleagues in the Laser Research Institute (LRI) at Stellenbosch University; thank you for making the days worthwhile, for all the social gatherings, the regular chats and for the most valuable discussions during the LRI meetings. Your contributions are appreciated. Olufemi Olaoye, thank you for your contributions towards the computer simulations in this work.
- Colleagues and friends at CLF, UK; Kay Sowoidnich, Abdullah Ahmed, many thanks for your hospitality and for your ideas and input towards my work. Paul Donaldson, Gregory M. Greetham; thank you for your assistance in my experiments at the CLF.
- Lucy Minnes, I am most grateful for your assistance with my 2D-IR experiments at RAL as well as data analysis, this work would have been a lot harder without you.

- Colleagues in Biopeptide group (Biochemistry) at Stellenbosch University, Arnie Vosloo, thank you for your immeasurable input in my experimental work, Vikus Kumar thank you for your assistance in the computer simulations, Wilma Van Rensburg thank you for proof reading some of my work.
- To my immediate family, my dearest mother, brothers, and sister (and their families) thank you for your unwavering support. Thank you for believing in me and for your prayers. This thesis is dedicated you. *Ndinotenda, Thank you, Baie dankie!*

# Table of Contents

## Declaration

## Abstract

## Acknowledgement

## Table of contents

## List of abbreviations

<b>Chapter 1 Introduction.....</b>	<b>1</b>
1.1 Bacterial resistance to conventional drugs .....	1
1.2 Antimicrobial peptides (AMPs).....	1
1.3 Mode of action for AMPs .....	2
1.4 Gramicidin Soviet (GS) .....	4
1.4.1 Conformational studies of GS .....	4
1.4.2 Structure of GS .....	5
1.4.3 GS mode of action .....	7
1.4.4 Structure-activity relationships in GS .....	8
1.5 IR spectroscopy of proteins and peptides .....	11
1.6 Raman Spectroscopy and Surface Enhanced Raman Spectroscopy of proteins and peptides .	16
1.7 References.....	17
<b>Chapter 2 Instrumentation and Methods .....</b>	<b>35</b>
2.1 Linear and non-Linear spectroscopy .....	35
2.2 Vibrational spectroscopy .....	36
2.2.1 IR absorption spectroscopy .....	36
2.2.2 2D-IR absorption spectroscopy .....	40
2.2.3 IR Materials and sample preparation.....	48
2.2.4 IR Data analysis methods .....	49
2.2.5 Raman spectroscopy (RS) .....	53
2.2.6 Surface enhanced Raman Spectroscopy (SERS).....	56
2.2.7 RS and SERS material and sample preparation .....	60

2.3 Density Functional Theory (DFT) and Quantum Mechanical/Molecular Mechanics (QM/MM) Simulations .....	62
2.4 References.....	63
<b>Chapter 3 Solvent effects on the structure of Gramicidin S .....</b>	<b>75</b>
3.1 Introduction.....	75
3.2 Sample preparations and measurements .....	76
3.3 Results.....	76
3.3.1 FTIR Absorption Spectroscopy .....	77
3.3.2 2D-IR Spectroscopy .....	81
3.3.3 Principal Component Analysis (PCA) of FTIR and 2D-IR spectra .....	84
3.4 Discussion.....	88
3.4.1 Structural assignment using FTIR and 2D-IR data .....	89
3.4.2 Structural assignment from FTIR second derivative analysis for Amide I and II .....	92
3.4.3 Structural assignment from computer simulations on a GS trimer model using QM / MM calculations.....	99
3.4 Conclusion .....	102
3.5 References.....	103
<b>Chapter 4 Temperature effects on the structure of Gramicidin S (GS) .....</b>	<b>110</b>
4.1 Introduction.....	110
4.2 Sample preparation and measurements .....	111
4.3 Results.....	111
4.3.1 FTIR Absorption Spectroscopy .....	111
4.3.2 2D-IR Spectroscopy of GS in 1-octanol.....	114
4.3.3 PCA of temperature dependent changes in the FTIR and 2D-IR spectra .....	116
4.3.4 Thermodynamic analysis of GS thermal profile .....	118
4.3.5 Assignment of spectra from FTIR and 2D-IR.....	124
4.4 Discussion.....	129
4.5 Conclusion .....	130
4.6 References.....	131

<b>Chapter 5 Fundamental characterisation of Gramicidin S (GS) with Raman and Surface Enhanced Raman Spectroscopy .....</b>	<b>135</b>
5.1 Introduction.....	135
5.2 Results and Discussion .....	135
5.2.1 Characterisation of Gramicidin S using Raman spectroscopy and spectral modelling....	135
5.2.2 Characterisation of Gramicidin S mixed with metal nanoparticles using RS and SERS.	154
5.3 Discussion.....	164
5.4 Conclusion .....	165
5.5 References.....	166
<b>Chapter 6 Conclusions and Further Work.....</b>	<b>171</b>
6.1 References.....	174
<b>Chapter 7 Appendix.....</b>	<b>176</b>

## List of Abbreviations and Acronyms

$\alpha$ -helix	alpha helix
AMPs	antimicrobial peptides
NH	amide
$\beta$ -sheet	beta sheet
C	carbon
CAMPs	cationic antimicrobial peptides
C=O	carboxyl
cm	centimetres
CD	circular dichroism
$^{\circ}\text{C}$	degrees Celsius
DFT	density functional theory
DNA	deoxyribonucleic acid
EF	enhancement factor
$\Delta\text{H}$	enthalpy
$\Delta\text{S}$	entropy
$K_{\text{eq}}$	equilibrium constant
FWHM	full width half maximum
$\Delta\text{G}$	Gibbs free energy
GD	gramicidin D
GS	gramicidin S
H-bond/s/ing	hydrogen bond/s/ing
HOMO	highest occupied molecular orbital
IR	infrared
kV	kilo volts
Leu	leucine
LSP	localised surface plasmon
LUMO	lowest unoccupied molecular orbital
mg/mL	milligrams per millilitre
MIC	minimum inhibitory concentration
M	molar
MD	molecular dynamics
NIR	near infrared
NMR	nuclear magnetic resonance

NP	nanoparticle
Orn	ornithine
ppb	part per billion
Phe	phenylalanine
Pro	proline
QM/MM	quantum mechanics / molecular mechanics
RS	Raman spectroscopy
RNA	ribonucleic acid
SERS	Surface enhance Raman spectroscopy
SAMP	synthetic antimicrobial peptide
T	temperature
TEM	transmission electron microscopy
TDC	transition dipole coupling
2D-IR	two-dimensional infrared
f	state fraction
UV	ultraviolet
UV-Vis	ultraviolet – visible
Val	valine
T <sub>w</sub>	waiting time

# Chapter 1 Introduction

## 1.1 Bacterial resistance to conventional drugs

Bacterial resistance is a growing global health concern which has threatened the ability to treat common infections. According to the World Health Organisation (WHO), the emergence and rapid spread of microbial strains with new resistance mechanisms has led to infections which are not treatable with antimicrobial medicines [1]. Bacteria are diverse, and they exhibit three defined types of resistance namely: intrinsic, acquired and adaptive resistance [2]. Resistance mechanisms include: existence of persister cells which are multidrug tolerant invulnerable cells which are neither affected nor killed by bactericides [3]–[5]. Other resistance mechanism also include limited penetration of the bactericidal molecules into the bacterial cell, existence of antibiotic degrading enzymes which consume any antibiotic which penetrates, slow growth rate and several others [4]–[6].

The design of antimicrobials that are less susceptible to evolving resistance mechanisms is necessary, however it is challenging, which has led to antimicrobial peptides (AMPs) being considered as an alternative as they represent a diverse group of novel therapeutics.

## 1.2 Antimicrobial peptides (AMPs)

Antimicrobial peptides (AMPs) are natural defence molecules, gene-encoded and ubiquitous [7], [8]. Many of the naturally occurring peptides are produced by non-ribosomal peptide synthetases (NRPs) [9]. The peptide synthetases are multi-domain enzymes which bind amino acids to create polypeptide chains via amino carboxyl group [10], [11]. AMPs have paved the way for development of novel drugs, to combat the resistance of microbes towards conventional drugs and medicine [12]–[14]. They are part of the human antimicrobial defence system thus, they are less likely to cause undesirable side effects as compared to conventional chemical antibiotics [10]. Also, AMPs tend to target metabolic enzymes which most likely cause resistance and that, together with the AMP mechanism of action make the organism less likely to resist treatment [15].

Cationic antimicrobial peptides (CAMPs) is a class of small peptides, less than 50 amino acids residues in length, positively charged due to the presence of excess lysine or arginine residues in addition to hydrophobic residues and amphipathic in nature [16]. CAMPs or in general AMPs are either naturally occurring or synthetic derivatives, there are more than 3000 AMPs reported [17]. CAMPs are active towards a wide range of organisms including Gram-positive and Gram-negative bacteria [11], [17]–[21] viruses [18], [22]–[24], protozoa [18], [22] and fungi [18], [20], [22], [23], [25]. With the most effective CAMPs killing microorganisms *in vitro* at minimum inhibitory

concentrations (MICs) in the range of 0.25 – 4 ug/mL [26] where most of the antimicrobial peptides breakdown the cytoplasmic membrane integrity [27]. Sources of naturally occurring peptides range from soil, water, fungi, plants, bacteria, insects, fish, amphibians, reptiles, birds to even humans [12], [28], [29]. All relevant information on naturally occurring peptide sources is well documented in databases (Wang, 2004, 2018; Wang, Li and Wang, 2009, 2016; Ageitos et al., 2017). They are classified according to their secondary structures: such as  $\alpha$ -helices,  $\beta$ -sheets and extended peptides [16].

Although conventional antibiotics exist, over the years there has been a rise in anti-biotic resistant organisms, causing these drugs to be less effective. Thus, the introduction of CAMPs offers exciting advantages in that they rapidly kill target cells, have a broad spectrum of activity towards the most resistant clinical pathogens and the net positive charge gives CAMPS a selective toxicity against more negatively charged bacterial cell membranes thus discriminating the cell membrane from neutral cells [17], [26], [27], [34].

### **1.3 Mode of action for AMPs**

Bacterial membranes are made up of proteins and acidic phospholipids such as cardiolipin, phosphatidylglycerol (PG) and phosphatidylethanolamine (PE) [9]. Owing to the acidic phospholipids, bacterial membranes are negatively charged and the phospholipid bilayer makes up the basic component of a cell membrane [9]. Cytoplasmic membranes of bacterial and mammalian erythrocytes are distinct in their phospholipid bilayer components [35], [36]. Thus, the initial stage of contact between a peptide and a membrane involves an electrostatic interaction between positively charged amino acids of the CAMP and the negatively charged phospholipid headgroups of the membrane [9], [36].

The mechanism of action for CAMPs includes inhibition of cell wall division [37], macromolecular synthesis inhibition and membrane permeabilization [38]. Reported MICs differ based on the target organism and type of CAMPs [20], [39], [40]. Most importantly, AMPs are generally membrane active; they compromise the membrane integrity and lead to cell death through different mechanisms such as altering the membrane curvature or fluidity, causing thinning of the membrane, inducing pore formation, and modifying the transmembrane electrochemical gradient [41]. With respect to membrane permeabilization and the process of pore formation, models have been proposed based on examining the activity of individual peptides [9]. The models describe the interaction between a peptide and the cell envelope of bacteria. The models are described as the ‘barrel stave’ model which illustrates that the peptide inserts perpendicularly and binds to the bilayer and accumulates, thus forming pores [15], [42]; the ‘toroidal-pore’ model which proposes that the peptide inserts into the

bilayer, causes stress which induces curvature, thus forming a pore which is lined by peptide and phospholipid headgroup [43]; and the ‘carpet’ model whereby the peptide attaches parallel to the bilayer surface, after reaching a sufficient concentration the peptide causes a detergent-like effect causing membrane disruption [44], [45] (*Figure 1.1*). Thus, through these mechanisms the peptide accumulates on the membrane surface and after reaching a critical concentration, pore formation is induced, causing leakage which leads to cell death [9], [46].

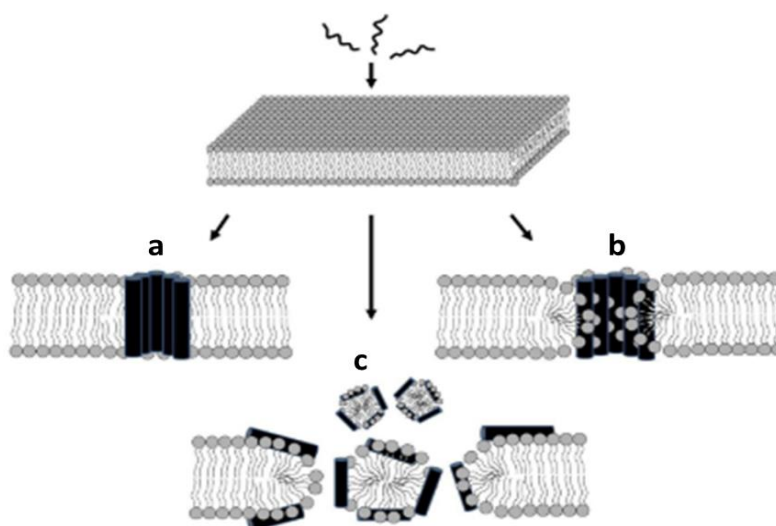


*Figure 1.1 Three types of antimicrobial action against bacterial membrane; a) barrel stave model, b) toroidal pore model c) carpet model. Adapted from [47].*

The diversity of the membrane targeting peptides includes AMPs, synthetic antimicrobial peptides (SAMPs), Gramicidin S (GS) which is an AMP and its synthetic analogues [48]. GS, discovered in the early 1940s saved many lives on the battle fields during World War II, treating infected wounds [49]–[51]. However, it was later discovered to be haemolytic as it compromised the phospholipid bilayer barrier via a wide range of induced defects [48]. Since then there have been a growing interest in understanding gramicidin along with the development of less toxic derivatives together with new antibiotics which offer novel treatment [52]. In a report by Kim *et al.* [53] antibiotics used in clinics target processes such as protein biosynthesis, DNA, RNA, peptidoglycan and folic acid synthesis and these antibiotics are not very effective against infections from quiescent bacteria. More recently, Berditsch *et al.* [54] expanded on the anti-persister, bactericidal and antibiofilm activities of gramicidin S due to its high levels of penetration, stability and its many modes of action towards combating clinical bacterial strains. This makes it necessary to research antibiotics which make use of alternative modes of antimicrobial activity, in particular disruption of the membrane integrity. The membrane is an appealing target because its conservative structure and make-up contributes to the resistance mechanism [48]

## 1.4 Gramicidin Soviet (GS)

This study focuses on a peptide antibiotic produced from soil cultures of genus *Bacillus*. In 1939 Dubos and Cattaneo described a strain of sporulating aerobic bacilli known as *Bacillus brevis* [28]. The strain *Bacillus brevis*, one of a variety of strains found in soil, produced an anti-bacterial which was active against staphylococci and streptococci. From this isolated strain, the antibiotic tyrothricin was obtained which comprised of the cyclic (Tyrocidins 70 – 80 %) and linear (gramicidin D 20 – 25 %) polypeptides, antagonistic towards a range of microorganisms [17], [29]. Thus, tyrothricin became the first AMP to be clinically used in humans and its extended clinical use over a long period of 60 years showed no microbial resistance [55]. This is because AMPs containing D-amino acid residues make the AMPs less susceptible to pathogenic resistance and thus, more effective [17]. Early research illustrates processes on how both polypeptides are extracted, isolated and purified through crystallisation processes and characterised [29], [56], [57]. The section below entails the history and research which has been done on GS and importantly, the types of techniques and spectroscopic methods which have been employed in the understanding and elucidation of GS backbone conformation.

### 1.4.1 Conformational studies of GS

Gramicidin Soviet (GS) is a non-ribosomally synthesised, cationic, decapeptide antibiotic. The peptide is from the same strain as tyrothricin, but it is produced by *Aneurinibacillus migulanus* [49]. It's first isolation was done in 1942 by Gauze and Brazhnikova [14]. Since then, tremendous effort has been put towards elucidation of the structure of GS [58]–[65].

An early study by Hodgkin and Oughton generated molecular models from crystalline derivatives of GS in wet and dry state where details on the molecular weight, size and shape were obtained as preliminary measurements towards X-ray analysis of GS [58]. Using polarised infrared (IR) spectroscopy, Abbott and Ambrose showed that it was possible to distinguish various configurations of polypeptide chains in accordance with the different frequencies of vibration given off from their amide NH-CO- groups. With this information, Abbott and Ambrose applied the same technique to small peptides where crystalline derivatives of GS were utilised and from these derivatives, the IR absorption frequency of carboxyl (C=O) group at position  $1646\text{ cm}^{-1}$  in the amide I region implied the GS molecule to be a folded  $\alpha$ -chain in addition to it having IR dichroism similar to that of folded synthetic polypeptides and  $\alpha$ -keratin [59]. However, X-ray diffraction and chemical data suggested the GS molecule to be a cyclic decapeptide and to have  $\beta$ -chain configuration, [59] evidence which required extensive model building. Further evidence from several GS molecular models confirmed the decapeptide to have a two-fold axis of symmetry [61], [62].

On another X-ray study on a hydrated GS-urea complex, crystalline GS was solved to be a dimer which formed four-stranded intermolecular antiparallel  $\beta$ -sheets [66], a result which was in agreement with subsequent conformational energy minimisation calculations. However, there were slight differences due to intermolecular interaction occurring in the crystal form [63]. Additionally, both the X-ray results and energy calculations confirmed the presence of a hydrogen-bond between the backbone phenylalanine (Phe) carbonyl group and the side chain ornithine (Orn) amino group [67], [68]. These findings highlighted the significance of empirical energy minimisation calculations in determining the low energy structure of GS to provide a link between experimental results and theoretical predictions [63], [64]. Thus, propelling a need to obtain peptide conformation in solution using more rigorous experimental tools such as nuclear magnetic resonance (NMR) spectroscopy [65].

Using NMR spectroscopy, Stern *et al.* [65] investigated solution phase models of GS in deuterated methanol and GS in deuterated dimethyl sulfoxide (DMSO). The results revealed two pentapeptides of [L-Val-L-Orn-L-Leu-D-Phe-L-Pro] arranged anti-parallel next to each other with the four required internal H-bond. The models additionally revealed four slowly and four less slowly exchangeable protons, the valine (Val) amide protons connected to the leucine (Leu) carbonyl oxygens, while the Val carbonyl oxygens connected to the Leu amide protons giving strong internal hydrogen (H)-bond which will have slow exchange rates [65]. From the GS model arrangement by Stern *et al.*, the Phe and proline (Pro) pointed outwards from the ring and thus were not internally bonded such that their amide proton exchange could happen fast, refer to [65] for values of the exchange rates. Naik *et al.* demonstrated that normal mode calculations could provide details on the GS peptide conformation which takes on low-energy structures [69]. Further, molecular dynamics (MD) and density functional theory (DFT) calculations also provided details on the possible GS conformers which are low energy conformations whose secondary structure is governed by non-covalent interactions [64], [70], [71].

### 1.4.2 Structure of GS

From experiments using ultraviolet absorption spectroscopy [72], peptide hydrogen-deuterium exchange [72], optical rotatory dispersion [72], circular dichroism [62], X-ray diffraction [66], MD simulations of GS in DMSO solution [73], NMR [58], magnetisation transfer experiments [73], it was highlighted that any proposed conformation of a GS model had to at least conform to the following restrictions: (1) a centre of symmetry; (2) have internal and external hydrogen bonds; (3) must explain the coupling constants and chemical shifts of carbon (C) atoms, and amide protons; (4)

proposed hydrogen-bonds should involve the amide protons of Val and Leu [58], [61], [65], [72].

Figure 1.2a shows the amino acid residues sequence and positions in GS.

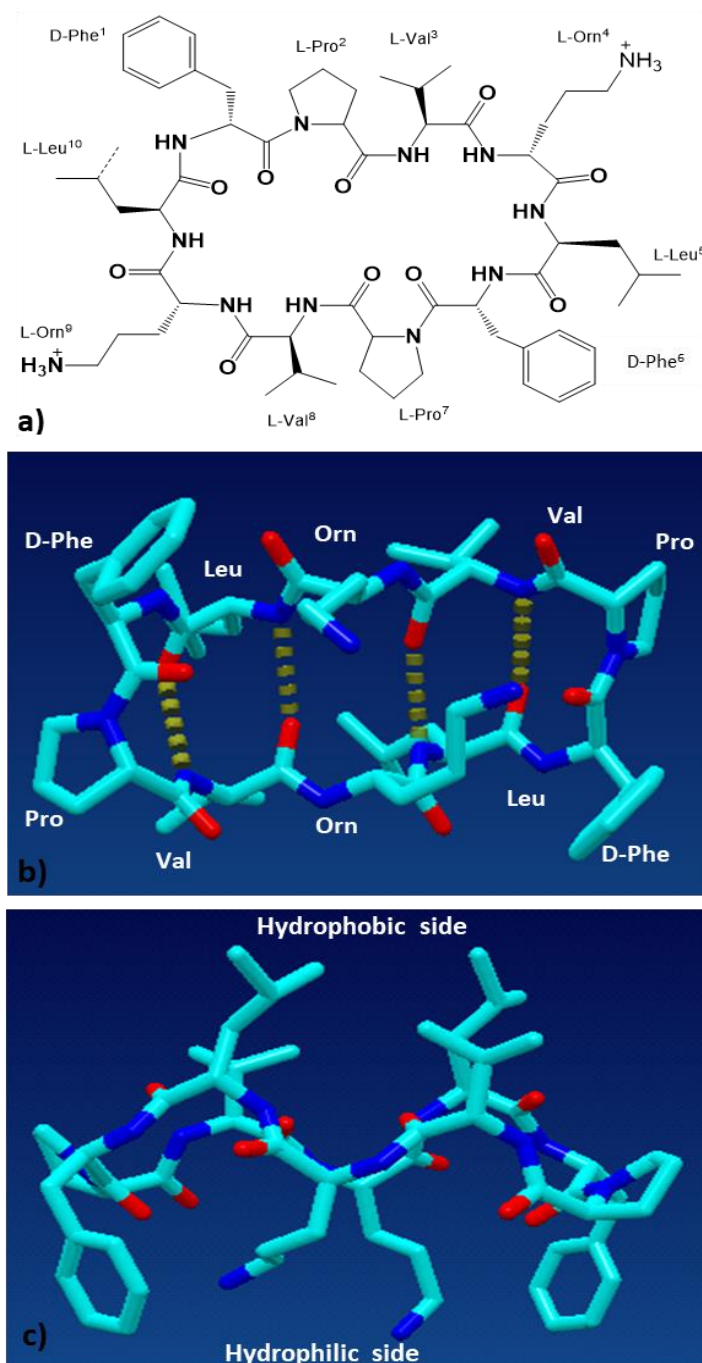


Figure 1.2 Structure of gramicidin S with monoisotopic Mr of 1140.7059. The primary structure of GS is shown in a). Residues are referred to using standard three letter amino acid abbreviations with Orn/O representing ornithine. Residues are numbered according to their order of incorporation during biological synthesis. A modelled low energy 3D structure of GS is shown in b) indicating the optimal arrangement of residues and the intra hydrogen bond. In c) the 3D structure of GS shows the hydrophobic side (top) and hydrophilic side which make up the amphipathic structure of the GS monomer. The low energy GS structure is courtesy of M. Rautenbach and was modelled utilising Yasara 11.3.2 and its crystal structure reported by Saiz et al. [76].

Thus, the modelled three-dimensional structure of GS molecule is shown in *Figure 1.2b* and *c* in its minimum energy conformation. This modelled structure is based on a GS crystal grown in trifluoroacetic and hydrochloric acid reported in [74]. GS forms an anti-parallel  $\beta$ -sheet [58] formed by the tripeptide sequence Val-Orn-Leu [34], closed on both sides by two type II'  $\beta$ -turns [75]–[78] which are formed by D-Phe-Pro sequences [34]. It is a closed ring with  $C_2$  symmetry [61], [65], [68], [71], [79]. Its secondary structure is stabilized by four strong intramolecular hydrogen bonds between NH and CO groups of Val and Leu amino acid residues [34], [69], [76]. GS in its amphiphilic nature has the two positively charged polar Orn residues on one side and four hydrophobic residues (two sequences of Val and Leu) on the other side [34], [65]. In the infrared spectrum GS illustrates  $\beta$ -sheet structures in the range  $1613\text{--}1637\text{ cm}^{-1}$ , and  $1682\text{--}1689\text{ cm}^{-1}$ ,  $\beta$ -turns are from  $1662\text{--}1682\text{ cm}^{-1}$ , with the undefined structures at  $1637\text{--}1645\text{ cm}^{-1}$  [69], [80], [81].

### 1.4.3 GS mode of action

This section explains the significant structural properties of GS which contribute to its antimicrobial activity. GS has antimicrobial activity against both cell membrane and intracellular targets [82]. GS has a broad spectrum of activity against microorganisms and is indiscriminate with respect to the nature of the phospholipid, disrupting bacterial and mammalian cells with equal ability [9], [83]. Additionally, GS targets the membrane as a whole and is non-selective, thus making it highly toxic and can only be applied topically [9], [52], [83]–[85].

The principal targets of GS have been stated as the lipid bilayer of bacterial or erythrocyte membranes [20]. The mechanism of action of GS against bacterial cells, its principal targets, has been described through permeabilization and disruption of the lipid bilayer of the membrane [82]. In the membrane environments GS adopts the active  $\beta$ -sheet structure which in addition to its amphipathic property alters the ion permeability of the lipid membrane [86]. Jelokhani-Niaraki *et al.* [36] illustrate the GS mode of action whereby GS first absorbs into the membrane to form stable  $\beta$ -turn/sheet secondary structure, whereafter GS then interacts with the lipid membrane, changing the shape of the lipid bilayer and consequently facilitates the deterioration of the membrane structure. The GS mode of action has also been reported on bacteria such as Gram-negative *Escherichia coli* (*E. coli*), where it binds to the outer membrane of the bacteria, disrupting its cell permeability barrier and causing efflux of  $K^+$  ion through the outer membrane [87]. Furthermore, it was stated that GS may compete with divalent ions such as  $Ca^{2+}$  and  $Mg^{2+}$  ions which stabilise the lipopolysaccharide moiety of the outer membrane of *E. coli* [87]. According to Staudegger *et al.* [83] in a study on interaction of GS with microbial lipid extracts, a membrane-to-peptide ratio of 25 caused formation of bi-continuous inverted cubic phases, in addition to thinning of the liquid-crystalline bilayer. GS enabled the

formation of inverted cubic phase by increasing the negative curvature stress in the host lipid bilayer; an effect which supported GS mechanism of permeabilization and disruption of the lipid bilayer of the membrane [83]. Several studies have also reported that GS binds to the membrane and causes disorganisation of lipoprotein systems and the permeability barrier of membranes [88], consequentially causing pores or channels in the membrane, resulting in the cell cytoplasmic contents leaking out, killing bacterial cells and lysing erythrocytes [8], [89]–[91].

GS is markedly bactericidal and has antimicrobial activity towards a wide range of Gram-positive bacteria and Gram-negative bacteria as well as pathogenic fungi [16], [28]. GS is highly effective in low amounts, and has been limited to topical applications due to its haemolytic activity even at extremely low concentrations [29]. According to Kondejewski *et al.* [92] minimum inhibitory concentrations (MICs) values for GS ranged from 3 – 12.5 µg/mL for Gram-negative bacteria compared to MICs of 3 µg/mL reported for Gram-positive bacteria. GS was observed to have inhibitory effects on the active transport of [<sup>3</sup>H]alanine and [<sup>3</sup>H]uridine in membrane vesicles isolated from *Bacillus brevis* and *Bacillus subtilis* at concentrations of 2–4 µmol/mg of membrane protein [93]. GS causes the haemolysis on eukaryotic cells such as human red blood cells *in vivo* and *in vitro* at concentration of 50 µg/mol [36], [88], [94]. Rautenbach *et al.* [35] observed that GS is less active and selective compared to the analogous tyrocidines towards the growth of *Plasmodium falciparum* infected erythrocytes with 50 % parasite inhibitory concentration (IC<sub>50</sub>) of about 1.3 µM.

#### 1.4.4 Structure-activity relationships in GS

During the past 40 years substantial efforts have been put towards understanding the structure-activity relationship for GS and its derivatives and several methods of synthesising GS derivatives have been considered in an effort to try and minimise the haemolytic effects of GS whilst enhancing its antimicrobial properties [36], [85]. These methods were targeted towards alterations in the peptide ring size [95], interchanging the types of D-amino acids [36], interchanging the β-strand sequence [46], changes in the β-turn region [85], [96], amphipathicity and cationicity [9], [84], [97] which influence the biological properties of GS.

Firstly, GS adopts the β-hairpin conformation which is the simplest form of an antiparallel β-sheet [96]. A hairpin is defined by a loop made up of two β-strands connected by hydrogen bonds between the CO and NH groups in the backbone [96], [98]. The hairpin further stabilised by the interstrand hydrogen bond interactions [99], the hydrophobic effect [100] and the conformation preference attributed to the β-turn sequence [98] (*Figure 1.3*). In GS the type II' β-turn region has been subject to modifications during the generation of derivatives through the substitution of D-Phe and Pro residues, provided the peptidomimetics have hydrophobic character [101]. The β-turn, as well as the

$\beta$ -sheet, contribute to the hydrophobicity of GS. Overhand *et al.* investigated GS analogues where aromatic sugar amino acids were introduced in the  $\beta$ -turn sequence, finding that  $\beta$ -turn modification can be achieved. However, the presence of aromatic functionality was essential to maintain GS bioactivity [102]. Aromatics provide the cation- $\pi$  interaction which helps to protect the hydrophilic side chains of GS during peptide-membrane interaction [9], [102].

In GS structure hydrophobic residues (Val and Lue) are on one side whilst the hydrophilic residue (Orn) is on the opposite side. Hydrophobicity is an important factor in antimicrobial peptides as it determines the extent to which the peptide penetrates the lipid bilayer [103]. However, there exists a strong correlation between hydrophobicity and haemolytic activity [104], thus, the hydrophobic levels in peptides ought not to be too high as to cause mammalian cell toxicity but moderate enough to maintain the antimicrobial effect and enhance activity [9]. Wieprecht *et al.* examined the relationship between peptide hydrophobicity and membrane permeabilization in a study whereby hydrophobicity of the peptide magainin II amide analogues was varied against the degree of membrane permeabilization, citing that with increasing hydrophobicity there was increase binding and permeabilization towards phosphatidylcholine (PC) rich vesicles [105].

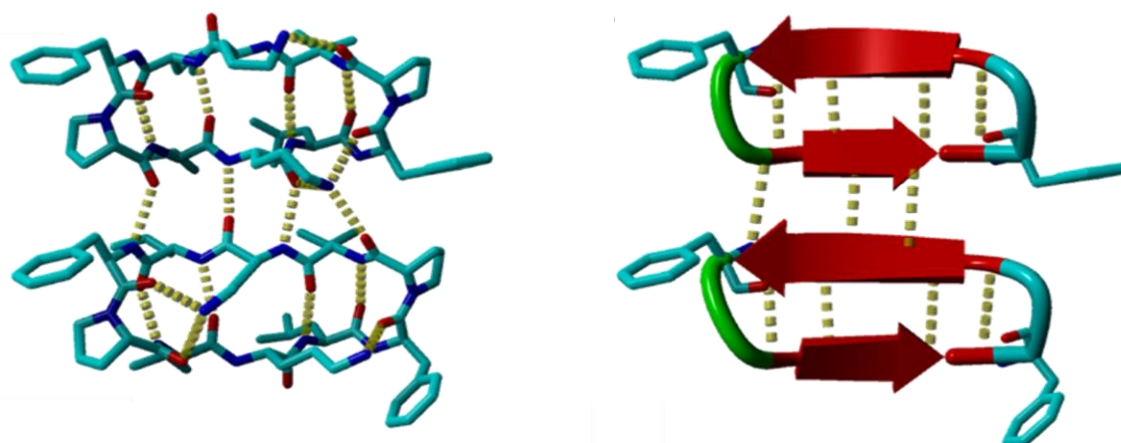


*Figure 1.3 A GS dimer obtained by Docking experiment by using YASARA2 algorithm (left). The dimer has Unidirectional and Opposite directional monomer unit with antiparallel  $\beta$ -sheets. Image on the right represents corresponding ribbon structure, that reveals that unidirectional and opposite directional monomer units with 3 and 4 intermolecular hydrogen bonds between backbones of two peptide molecules. The ribbon structure shows the  $\beta$ -hairpin, which a simplest form of a protein structural motif, made up of adjacent antiparallel  $\beta$ -strands (represented by the red arrows) which are joined by a short loop of two amino acids linking the strands. Generation of this image is explained in Chapter 2.*

The cationicity (net positive charge) of CAMPs is an important factor which aids in their electrostatic interaction with negatively charged phospholipid bacterial membranes [9]. GS has a net positive charge of +2 from the two positively charged basic Orn side chains. The significance of Orn in the antibacterial activity of GS was investigated by Nagamuthi *et al.* [88], reporting that chemical

modifications of the peptide through deamination, carbamylation, formylation, succinylation and maleylation resulted in 90-95 % loss in antimicrobial activity of GS and a further 12-30 % loss of its haemolytic activity. Nagamurthi *et al.* [88] also investigated the importance of the equal contribution from the two amino groups into GS activity and that one amino group cause 50% antimicrobial activity. The Orn residues are on one side while the hydrophobic Leu and Val side chains on the opposite side giving GS an amphiphilic  $\beta$ -structure [46]. The amphiphilic character of GS forms a basis for its antimicrobial activity [9], [102], [106]. In GS, the amphipathicity is also explained by the antiparallel  $\beta$ -strands which arrange to create a polar and non-polar side [9].

The amino acid residue sequence / order of arrangement in GS also has an effect in its activity. Residues can be interchanged to have derivatives which are either very hydrophobic or polar, thus in-turn affecting the hydrophobicity and the amphiphilicity of GS. In the structure-activity relationship studies of GS towards improving its biological profile, several GS derivatives have been described which are as potent as GS, more so better [46], [84]. Though the amphiphilic nature of GS is a significant factor towards its activity, Tamaki *et al.* have described a GS analogue, cyclo[-Val-Leu-Leu-Orn-Leu-D-Phe-Pro]<sub>2</sub>, which is as potent as GS with antiparallel  $\beta$ -sheet conformation but without the amphiphilic property, active towards Gram-positive but not Gram-negative pathogens [84]. Overhand *et al.* described an improved GS derivative, toxic against a number of bacterial strains but with much less toxicity towards human cells, cyclo[<sup>D</sup>Phe-Pro-Orn-AdaGly-Orn]<sub>2</sub>, highly charged with four positively charged Orn residues. This was a GS derivative incorporated with an adamantane moiety which showed the ability to differentiate bacterial and mammalian cells at a particular concentration [46]. Additionally, the importance of ring size on GS antimicrobial activity was reported by Kondejewski *et al.* [36] for GS analogues with ring sizes ranging from 4 to 14 amino acid residues, stating that peptides with less than 10 residues presented lack of antimicrobial activity and no haemolytic activity while peptides with 14 residues showed increased haemolytic activity and no antimicrobial activity. Kondejewski *et al.* [36] further elaborated that the 10 residues peptide analogue exhibited a similar profile to that of GS with activity towards Gram-positive, and Gram-negative bacteria and yeast, however with increased haemolytic activity [36], [94], [95].

In these structure-activity relationship studies the emphasis was on the significance of the amphiphilic structure of GS which contributes to its biological activity. In synthesis of GS derivatives, studies have reported that any amino acid residue substitutions which interfered with the amphiphilic, hydrophobic or cyclic hairpin structure of GS would render the peptide less effective towards disruption of bacterial membrane [9], [46], [102], [107]. The amphiphilicity, hydrophobicity, cationicity are significant properties which render GS biologically active. It has been reported that this conformation of GS is maintained in water, protic, aprotic organic solvents of varying polarity,

in detergent micelles and phospholipid bilayers, and even at high temperatures or agents which alter protein conformation [83], [93], [108], [109].

Attempts to explain various mechanisms by which cyclic peptides compromise the bacterial membrane [9] were in some cases incomplete and details on the peptide structure before and after interacting with the membrane have not been explicitly elucidated [109]. Regarding such details, the issue of peptide structure and aggregation/oligomerisation comes into play [41], [109]. Knowing the peptide aggregation/oligomer state is important because in some cases critical concentrations have to be achieved in-order for the peptide to take an active conformation at the membrane interface which disrupts the target membrane [9]. Petkov *et al.* [41] reported on the solution behaviour of an AMP bombinin H2 stating that only when the peptide self-associated to form aggregates did it take an active helix structure, which was not the case when the peptide was in monomeric form. To aid in this direction initial steps are to understand peptide structure and self-organisation in solution phase, in the absence of a membrane, which shall be reported in this thesis for GS. Though the GS mechanism of action has been discussed through various studies where bacterial and fungal targets were used, as mentioned above, its conformational and aggregation behaviour shall be investigated in this study based on its secondary structure, in particular amide I, using IR and Raman based techniques.

IR and Raman spectroscopy have been widely used in protein and polypeptide analysis. The discussion below considers studies where the IR, Raman as well as other well-known techniques were used in extracting details of the secondary structure of protein and peptides, in particular GS. The IR and Raman techniques are elaborated in Chapter 2.

## 1.5 IR spectroscopy of proteins and peptides

When considering IR for protein analysis, details such as chemical properties of groups in a protein molecule, structural conformations together with H-bonding patterns can be extracted from an IR spectrum [110]–[112]. In *Figure 1.4* below, a typical IR spectrum is presented for a protein showing the regions of interest which display the amide I and II vibrational modes [113]. These vibrational modes provide details on secondary structural information.

To understand the shape or conformation which proteins take, we introduce the four levels of protein structure which are primary, secondary, tertiary and quaternary. The basic building block of proteins is the 20 natural amino acids (*Figure 1.5*). Each amino acid consists of the basic amino group ( $-\text{NH}_2$ ); an acidic carboxyl group ( $-\text{COOH}$ ); a hydrogen atom ( $-\text{H}$ ) and a distinct side chain ( $-\text{R}$ ), in which the carboxyl and amino groups participate to form peptide bonds (amide bonds).

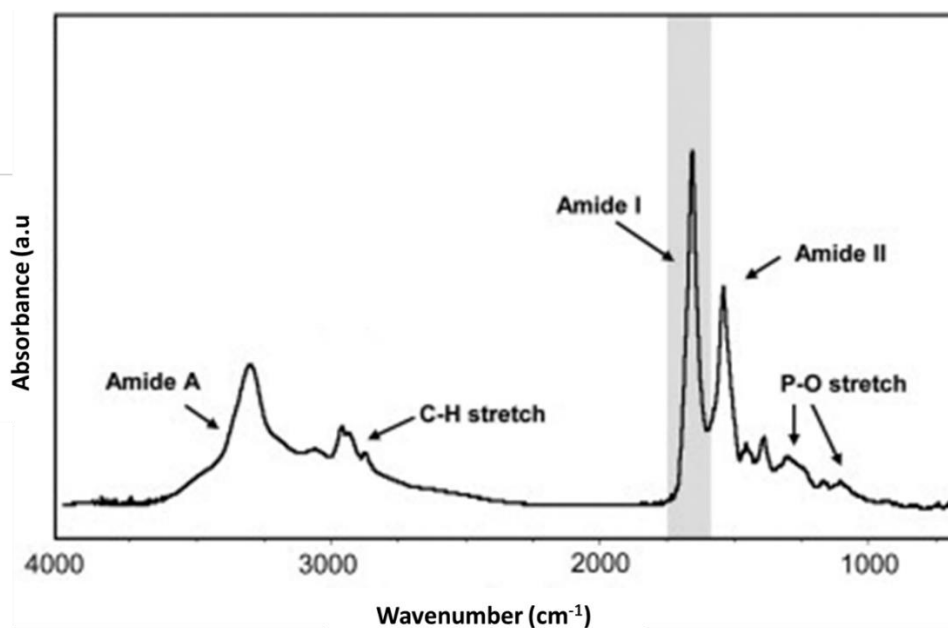


Figure 1.4 An IR spectrum of a typical protein, showing the Amide I band at  $\sim 1650\text{ cm}^{-1}$  and amide II band at  $\sim 1540\text{ cm}^{-1}$ . Adapted from [113].

The primary structure of proteins is simply the amino acid sequence on a protein or polypeptide chain. When the polypeptide chains of the protein backbone interact and fold to form either  $\alpha$ -helix or  $\beta$ -pleated sheets, they form the secondary structure. The overall three-dimensional structure of the subunit of proteins gives the tertiary structure and the quaternary structure is the assembly of subunits [110], [114].

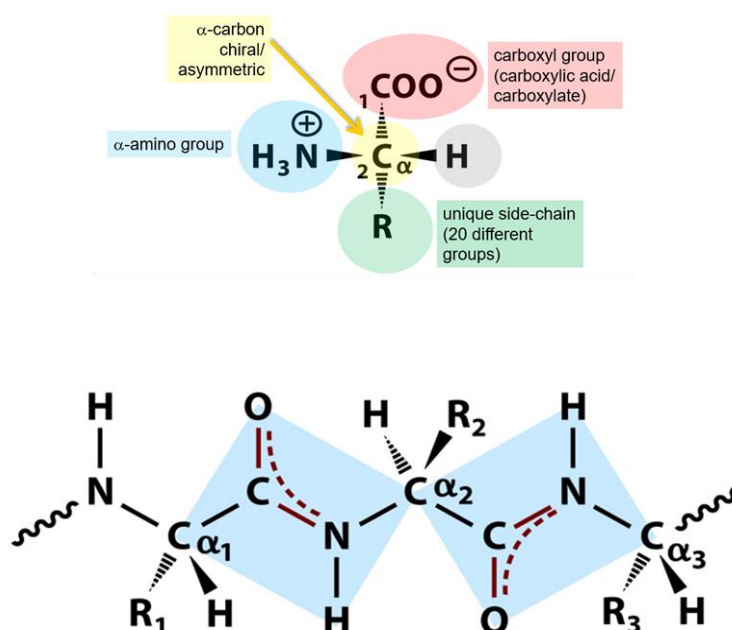
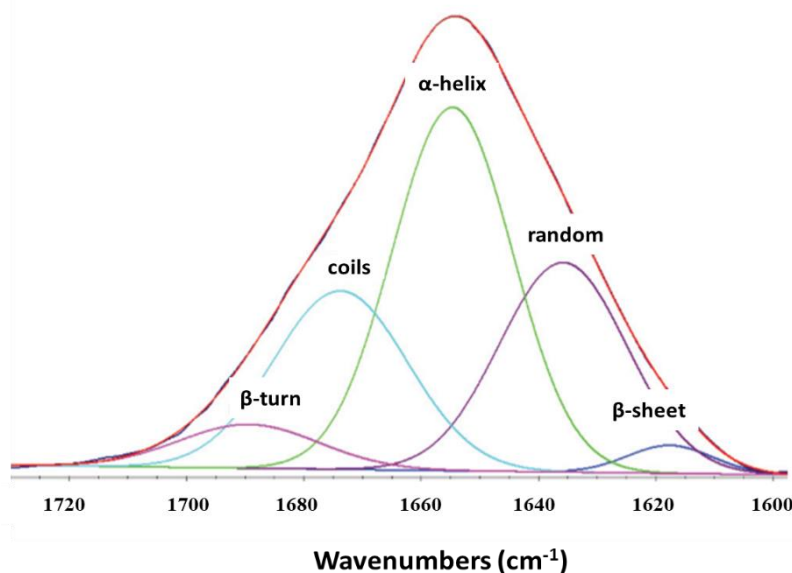


Figure 1.5 A general amino acid (top) structure with four different groups attached at the central  $\alpha$ -carbon and a peptide structure showing the planar peptide bonds. Adapted from [115].

### *IR spectroscopy of the secondary structure of protein and peptides*

The secondary structure of proteins encompasses  $\alpha$ -helices,  $3_{10}$  helix, random structure, coils, and  $\beta$ -sheets (parallel and anti-parallel). As previously described, the GS secondary structure is based on anti-parallel  $\beta$ -sheets as well as type II  $\beta$ -turns (refer to section 1.4.2). In the  $\beta$ -sheets H-bonding occurs in between the peptide strands making the anti-parallel  $\beta$ -sheets more stable. The turns connect secondary structural motifs and they allow conformational flexibility as the polypeptide can turn to change direction [116], [117].

A typical amide I absorption spectrum displayed in *Figure 1.6*. is known to be highly sensitive to the secondary structure of proteins, resulting in considerable amount of research focused on the amide I using 1D IR spectroscopy in determining the secondary structure of proteins and peptides [20], [117]–[125]. The main emphasis being to correlate spectral features to the structure or conformation [110]. With conventional linear IR spectroscopy, several vibrational modes interact giving a congested spectrum. All the underlying information on molecular contributions is buried in the broad spectrum making it a cumbersome process to unscramble the information underneath and mathematical processes such as band deconvolution may misinterpret the underlying overlapping details [116] (*Figure 1.6*).



*Figure 1.6 The deconvolution of the amide I band of BSA. Adapted from [126].*

The need to extract more information from the amide I band gradually led to development of multidimensional spectroscopic techniques. With such techniques there is interaction of radiation with molecules over varying time and frequency scales, giving details on how the present chemical

moieties experiencing different environments are coupling and their orientation [127]. The pre-existing techniques used in extracting information from biological systems include X-ray diffraction, CD spectroscopy, IR spectroscopy and multidimensional NMR (2D-NMR) spectroscopy. Of these methods, NMR has been the most significantly used tool, based on the response of the nuclear spin to an external magnetic field [128]–[131]. However, the emergence of multidimensional IR (2D-IR) in the past decade, presented a novel IR based technique which combined appreciable ultrafast time and structural resolution [132]. It is acknowledged that 2D-IR is analogous to 2D-NMR in that with the former, interaction of vibrational modes gives a direct indication of the corresponding interacting molecular groups, information which is relatable to both techniques in structure determination [132], [133]. Both 2D-NMR and 2D-IR are capable of elucidating participating functional groups in a molecule in solution phase environment and provide details on the structure and dynamics in that system [132]. However, an important difference between the techniques is the time ranges and resolutions which can be accessed in real time. This relates to the time a particular biological reaction takes place. While 2D-NMR and 2D-IR are complementary and can both access different time regimes, ranging from femtoseconds to seconds [132], [134], the major difference is that with NMR the narrow line width gives an intrinsically slow time resolution and the time it takes for the perturbed system to decay to its state before perturbation (dephasing time) for a spectroscopic transition is limited but with 2D-IR fast dephasing times gives higher time resolution, able to access ultrashort time scale transient processes in the femtosecond time domain [132], [133]. The ability of 2D-IR to provide ultrafast dynamics on the femtosecond to picosecond timescale is an additional advantage of the technique over conventional techniques such as CD spectroscopy and X-ray crystallography. Ultrafast timescales allow observation of fast dynamics. Thus, IR and 2D-IR spectroscopy were considered for this study.

In extracting secondary structure information, one important mechanism that results in the amide I band being sensitive is known as the transition dipole coupling (TDC) [111], [135]. The TDC is the resonance oscillation of dipoles in neighbouring amide groups. When oscillators vibrate at the same frequency, there is strong coupling [136]. The TDC analysis is effective in quantification of secondary structure [136], [137] and has been employed in distinguishing different peptide conformers from 2D-IR measurements [138]. Effects of TDC are exciton transfer whereby oscillators transfer energy amongst themselves, and band splitting where shifting of the amide I band occurs depending on orientation of the oscillator [110], [116], [139]. In this thesis, calculations with reference to TDC shall be considered in determining the secondary structural changes happening to the amide I which are probed by different solvent environments and temperature.

As mentioned earlier, GS is a membrane targeting antimicrobial peptide and understanding the detailed mechanism of interaction is of prime importance. In particular, understanding aspects of the peptide structure before and after interaction with a membrane are details which contribute to illustrating the biological function of the peptide [109]. A preliminary step in this direction is to determine peptide structure in aqueous solution and its aggregation behaviour before interaction with a cell surface [140]–[142].

A study on conformational behaviour and peptide aggregation of a peptide  $\alpha$ -synuclein reported that formation of  $\beta$  structures was induced in high concentrations of alcohols; methanol (MeOH), ethanol (EtOH), trifluoroethanol (TFE) whereby the process was driven by self-association of the peptide to form oligomers from monomer units aggregating at high peptide concentration ( $> 3.00$  mg/mL) [140]. The formation of  $\beta$ -sheets in  $\alpha$ -synuclein was followed through using biophysical techniques, far-UV CD and FTIR spectroscopy together with data analysis methods of curve fitting and second derivatives, to demonstrate that depending on solvent environment and temperature, the peptide could either self-associate and form fibrils, amorphous aggregates or soluble oligomers [140]. In solvent studies, alcohols of low polarity, such as TFE, strengthen the intramolecular hydrogen bonds and the stability of the secondary structure of the peptide [90], [140], [143]–[145]. This shall be investigated using 2D-IR in our study. Using IR absorption spectroscopy, Lewis *et al.* [146] related the frequency shifts of the  $\beta$ -sheet region of GS molecule to the polarity and H-bonding potential of different solvent environments [146]. This structure dependency on solvent environment shall be investigated in our study. Smith and Tokmakoff performed FTIR and 2D-IR molecular dynamics (MD) simulations on GS in non-H-bonding solvent DMSO and correlated the simulated and experimental spectral features to GS structure, citing that their simulated model was transferable to other solvents [147]. Due to the cytotoxicity of GS towards red blood cells leading to lysis, denoted haemolytic activity, GS is limited to topical applications therapeutically and efforts are still ongoing in designing GS analogues with high therapeutic index (low cytotoxicity with high selectivity towards pathogens) [148]. This potential of GS as a lead compound in the design in therapeutics was highlighted in 2019 by Luo *et al.* [149] reporting newly discovered therapeutic properties of GS which included antitumor and anti- $A\beta$  amyloid activities. Therefore, derivatives of GS have been generated with the focus on optimising the structure and activity of the peptide to make it more effective for therapy [58], [66], [150], [151]. Present studies on GS are invested in optimising and understanding the peptide structure, function, use and its behaviour in bilayer lipid membranes to fully elucidate the mechanism of membrane disruption according to the peptide's mode of action. Kotmale *et al.* [152], identified that the structure can be mimicked by conformational locking of the peptide backbone, without hindering its biological function and elaborated on how GS conformation would be affected by generation of a truncated

analogue, replacing the two D-Phe-L-Pro dipeptide moieties with either a D-Pro or anthranilic acid for inducing  $\beta$ -turns or introducing a constrained amino acid, respectively [152]. The substitution of L- with D-Pro gave stable  $\beta$ -turns (hairpin turn) and stabilised the intrapeptide  $\beta$ -sheet, which led to a novel group of cyclic analogues of GS [153]. To improve GS crystallisation, Asano *et al.* [154] generated a GS analogue where the Orn was replaced with a hydrophobic Leu in-order to minimise structural disorders from Orn. However, GS analogues in which the Orn residues were replaced or modified were found to be devoid of any antimicrobial activity which highlighted the importance of the Orn-residues and the cationic character of GS [88], [93]. These studies highlighted the type of environmental changes which can be used to probe peptides, in particular GS, and using the responses to elucidate structure-activity relations.

In this study 1D IR spectroscopy shall be used as a standard method to elucidate the secondary structure [67] of GS together with 2D-IR spectroscopy to extract detailed structural information with a high time resolution [133]. The use of 2D-IR coupled with principal component analysis (PCA) shall provide details on the coupling of the units within the amide I vibrational mode of the peptide backbone [155]. Difference spectroscopy and 2<sup>nd</sup> derivative analysis methods shall also be used to obtain hidden and fine spectral details, corroborated by theoretical calculations to confidently elucidate peptide-peptide / peptide-solvent interactions within selected environments. The 2<sup>nd</sup> derivative method has been applied as a data analysis method in environments where the peptide self-associated to form oligomers under varying solvent and temperature environment [140]. The use of detectable high GS concentrations can lead to peptide aggregation/oligomerisation, thus the self-association and dissociation of GS in the selected solvents and temperature environments shall be reported. GS is known to aggregate in the membrane, causing leakage and eventually cell death [57], thus details on the aggregation behaviour of GS in a membrane mimicking / non-membrane solvent environment shall be reported. To provide confidence in interpretation of our experimental results, theoretical results based on simulations of IR and Raman spectra of a GS model(s) shall be correlated with results obtained experimentally. GS spectra have been simulated in DMSO [147] but our simulations will consider a H-bonding solvent (water) and also nearest neighbour effects.

## **1.6 Raman Spectroscopy and Surface Enhanced Raman Spectroscopy of proteins and peptides**

Raman spectroscopy (RS), as a unique label-free and non-destructive technique, has been utilised in studying the secondary structure of proteins and peptides. The major vibrational modes of proteins which contribute to the Raman spectrum include the amide bands in the protein or peptide backbone, and the amino acid side chains [112], [156]–[158]. The protein amide I band (mostly C=O stretch)

commonly used in interpreting secondary structure is located in the range  $1600 - 1690 \text{ cm}^{-1}$ . For  $\beta$ -sheet peptides the amide I band is located in range  $1665 - 1680 \text{ cm}^{-1}$ , the amide II band is near  $1550 / 1480 - 1580 \text{ cm}^{-1}$  and the amide III vibration is at  $1200 - 1340 / 1230 - 1300 \text{ cm}^{-1}$  [116], [117], [157], [159], [160]. Early RS studies have documented the IR and Raman spectra of crystalline GS along with band assignments [69], [69] which shall be used as references for this thesis on RS of GS in solution environment in correlation with spectral simulations.

RS has found broad use in studies which include protein-protein interactions, protein aggregation and fibril formation [157] revealing the secondary structure of proteins and peptides, in biology [161], biochemistry [162] and medicine [5], [163], [164]. In recent years, Surface Enhanced Raman Spectroscopy (SERS) has been used in characterisation and detection of low concentrations CAMPs using colloidal nanoparticles produced via chemical reduction. Citrate reduced nanoparticles have been well reported and can be rapidly and easily prepared at various sizes [165]–[167]. A study by Hernandez *et al.* determined the most favourable, termed ‘optimum’, size of citrate capped gold colloids produced via chemical reduction, which enabled detection of therapeutic cationic peptides (somatostatin-14 and its analogue octreotide) at very low concentrations, in the range of  $10^{-6} - 10^{-7} \text{ M}$  [168]–[170]. Hernandez *et al.* further reported that over time, those large size NPs were subject to degradation as the citrate ions oxidise, where-as small size NPs retained their characteristics [168]. Even though smaller size nanoparticles have been successfully utilised in drug delivery [164], protein detection and analysis required larger nanoparticles sizes [168]. Further studies highlighted an important aspect of the ability of the peptides to cause aggregation of negatively charged gold and silver colloids owing to the cationic nature of the peptides, enabling detection of low concentrations [168]–[170]. This ability to aggregate NPs shall be investigated for GS in this study from which we can deduce the compatibility of GS and either silver or gold NPs. Further knowledge on RS and SERS spectral signatures of GS shall be reported in corroboration with theoretical calculations on a GS model. Significant GS vibrational modes shall be discussed in identifying the amino acid residues which contribute to the physicochemical properties of GS detectable using Raman spectroscopy. Using the complementarity of IR and Raman, spectra of GS in the non-aqueous solvents shall be compared.

## 1.7 References

- [1] “Antimicrobial resistance,” 2020. <https://www.who.int/news-room/fact-sheets/detail/antimicrobial-resistance> (accessed Nov. 07, 2020).
- [2] E. Tacconelli *et al.*, “Discovery, research, and development of new antibiotics: the WHO priority list of antibiotic-resistant bacteria and tuberculosis,” *Lancet Infect. Dis.*, vol. 18, no. 3,

pp. 318–327, 2018, doi: 10.1016/S1473-3099(17)30753-3.

- [3] D. S. Br e, “The durative temporal subordinating conjunctions: Since and until,” *J. Semant.*, vol. 4, no. 1, pp. 1–46, 1985, doi: 10.1093/jos/4.1.1.
- [4] C. de la Fuente-N u ez, F. Reffuveille, L. Fern andez, and R. E. Hancock, “Bacterial biofilm development as a multicellular adaptation: antibiotic resistance and new therapeutic strategies,” *Curr. Opin. Microbiol.*, vol. 16, pp. 580–589, 2013, doi: 10.1016/j.mib.2013.06.013.
- [5] U. R omling and C. Balsalobre, “Biofilm infections, their resilience to therapy and innovative treatment strategies,” *Journal of Internal Medicine*, vol. 272, no. 6, pp. 541–561, 2012, doi: 10.1111/joim.12004.
- [6] J. W. Costerton, P. S. Stewart, and E. P. Greenberg, “Bacterial biofilms: a common cause of persistent,” *Infect. Sci.*, vol. 284, no. 21 May, pp. 1318–1322, 1999, Accessed: Jul. 02, 2019. [Online]. Available: <http://science.sciencemag.org/>.
- [7] J. A. Vosloo, J. L. Snoep, and M. Rautenbach, “Manipulation of the tyrocidine production profile of *Brevibacillus parabrevis* to produce a new subset of peptides , the tryptocidines,” 2016, no. July 2014.
- [8] M. Rautenbach, H. A. Ey gh -Bickong, N. M. Vlok, M. Stander, and A. de Beer, “Direct surfactin-gramicidin S antagonism supports detoxification in mixed producer cultures of *Bacillus subtilis* and *Aneurinibacillus migulanus*,” *Microbiol. (United Kingdom)*, vol. 158, no. 12, pp. 3072–3082, 2012, doi: 10.1099/mic.0.063131-0.
- [9] M. R. Yeaman and N. Y. Yount, “Mechanisms of antimicrobial peptide action and resistance,” *Pharmacol. Rev.*, vol. 55, no. 1, pp. 27–55, 2003, doi: 10.1124/pr.55.1.2.
- [10] C. D. Sumi, B. W. Yang, I. Yeo, and Y. T. Hahm, “Antimicrobial peptides of the genus *Bacillus*: a new era for antibiotics,” *Microbiology*, vol. 61, pp. 93–103, 2014, [Online]. Available: [www.nrcresearchpress.com/cjm](http://www.nrcresearchpress.com/cjm).
- [11] J. A. Vosloo, M. A. Stander, A. N. N. Leussa, B. M. Spathelf, and M. Rautenbach, “Manipulation of the tyrothricin production profile of *Bacillus aneurinolyticus*,” *Microbiol. (United Kingdom)*, vol. 159, no. PART 10, pp. 2200–2211, 2013, doi: 10.1099/mic.0.068734-0.
- [12] A. J. Park, J. P. Okhovat, and J. Kim, “Antimicrobial peptides,” in *Clinical and Basic*

*Immunodermatology: Second Edition*, vol. 26, no. 1, 2017, pp. 81–95.

- [13] B. Mishra, S. Reiling, D. Zarena, and G. Wang, “Host defense antimicrobial peptides as antibiotics: design and application strategies,” *Current Opinion in Chemical Biology*, vol. 38, pp. 87–96, Jun. 2017, doi: 10.1016/j.cbpa.2017.03.014.
- [14] T. Korzybski, Z. Kowszyk-Gindifer, and W. Kurylowicz, *Antibiotics: Origin, Nature and Properties*, I. Elsevier, 2013.
- [15] N. Shagaghi, M. Bhave, E. A. Palombo, and A. H. A. Clayton, “Revealing the sequence of interactions of PuroA peptide with *Candida albicans* cells by live-cell imaging,” *Sci. Rep.*, vol. 7, 2017, doi: 10.1038/srep43542.
- [16] R. E. W. Hancock, “The bacterial outer membrane as a drug barrier,” *Trends Microbiol.*, vol. 5, no. 1, pp. 37–42, 1997, doi: 10.1016/S0966-842X(97)81773-8.
- [17] J. M. Ageitos, A. Sánchez-Pérez, P. Calo-Mata, and T. G. Villa, “Antimicrobial peptides (AMPs): Ancient compounds that represent novel weapons in the fight against bacteria,” *Biochemical Pharmacology*, vol. 133, pp. 117–138, Jun. 2017, doi: 10.1016/j.bcp.2016.09.018.
- [18] H. Zhao, “Mode of Action of Antimicrobial peptides,” University of Helsinki, 2003.
- [19] W. van Rensburg and M. Rautenbach, “Results : Antimicrobial activity Results : Haemolytic activity.” p. 7602.
- [20] E. J. Prenner, R. N. A. Lewis, and R. N. McElhaney, “The interaction of the antimicrobial peptide gramicidin S with lipid bilayer model and biological membranes,” *Biochim. Biophys. Acta - Biomembr.*, vol. 1462, no. 1–2, pp. 201–221, 1999, doi: 10.1016/S0005-2736(99)00207-2.
- [21] P. J. Loll, E. C. Upton, V. Nahoum, N. J. Economou, and S. Cocklin, “The high resolution structure of tyrocidine A reveals an amphipathic dimer,” *Biochim. Biophys. Acta - Biomembr.*, vol. 1838, no. 5, pp. 1199–1207, 2014, doi: 10.1016/j.bbamem.2014.01.033.
- [22] A. Giuliani, G. Pirri, and S. F. Nicoletto, *Antimicrobial peptides: an overview of a promising class of therapeutics*, vol. 2, no. 1. 2007.
- [23] H. K. Kang, C. Kim, C. H. Seo, and Y. Park, “The therapeutic applications of antimicrobial peptides (AMPs): a patent review,” *J. Microbiol.*, vol. 55, no. 1, pp. 1–12, 2017, doi:

10.1007/s12275-017-6452-1.

- [24] W. A. Eimer *et al.*, “Alzheimer’s Disease-Associated  $\beta$ -Amyloid Is Rapidly Seeded by Herpesviridae to Protect against Brain Infection,” *Neuron*, vol. 99, no. 1, pp. 56-63.e3, Jul. 2018, doi: 10.1016/j.neuron.2018.06.030.
- [25] W. Van Rensburg, “Characterization of natural antimicrobial peptides adsorbed to different matrices,” University of Stellenbosch, 2015.
- [26] R. E. W. Hancock and R. Lehrer, “Cationic peptides: A new source of antibiotics,” *Trends in Biotechnology*, vol. 16, no. 2, pp. 82–88, 1998, doi: 10.1016/S0167-7799(97)01156-6.
- [27] J. A. Vosloo, “Optimised bacterial production and characterisation of natural antimicrobial peptides with potential application in agriculture,” University of Stellenbosch, 2016.
- [28] R. J. Dubos and C. Cattaneo, “Studies on a bactericidal agent extracted from a soil bacillus : III. Preparation and activity of a protein-free fraction,” *J. Exp. Med.*, vol. 70, no. 3, pp. 249–56, 1939, [Online]. Available: <http://jem.rupress.org/cgi/pmidlookup?view=long&pmid=19870906>.
- [29] R. D. Hotchkiss and R. J. Dubos, “The isolation of bactericidal substances from cultures of *Bacillus brevis*,” *J. Biol. Chem.*, vol. 141, pp. 155–162, 1941.
- [30] Z. Wang and G. Wang, “APD: The antimicrobial peptide database,” *Nucleic Acids Res.*, vol. 32, no. DATABASE ISS., pp. 590D – 592, 2004, doi: 10.1093/nar/gkh025.
- [31] G. Wang, X. Li, and Z. Wang, “APD2: The updated antimicrobial peptide database and its application in peptide design,” *Nucleic Acids Res.*, vol. 37, no. SUPPL. 1, pp. 933–937, 2009, doi: 10.1093/nar/gkn823.
- [32] G. Wang, X. Li, and Z. Wang, “APD3: The antimicrobial peptide database as a tool for research and education,” *Nucleic Acids Res.*, vol. 44, no. D1, pp. D1087–D1093, 2016, doi: 10.1093/nar/gkv1278.
- [33] G. Wang, “The Antimicrobial Peptide Database,” *International Journal of Peptide Research and Therapeutics*, Jun. 20, 2018. <http://link.springer.com/10.1007/s10989-018-9741-6> (accessed Jun. 20, 2019).
- [34] R. N. A. H. Lewis *et al.*, “Fourier transform infrared spectroscopic studies of the interaction of the antimicrobial peptide gramicidin S with lipid micelles and with lipid monolayer and bilayer

- membranes,” *Biochemistry*, vol. 38, no. 46, pp. 15193–15203, 1999, doi: 10.1021/bi9912342.
- [35] M. Rautenbach, N. M. Vlok, M. Stander, and H. C. Hoppe, “Inhibition of malaria parasite blood stages by tyrocidines, membrane-active cyclic peptide antibiotics from *Bacillus brevis*,” *Biochim. Biophys. Acta - Biomembr.*, vol. 1768, no. 6, pp. 1488–1497, 2007, doi: 10.1016/j.bbamem.2007.01.015.
- [36] M. Jelokhani-Niaraki, L. H. Kondejewski, S. W. Farmer, R. E. W. Hancock, C. M. Kay, and R. S. Hodges, “Diastereoisomeric analogues of gramicidin S: Structure, biological activity and interaction with lipid bilayers,” *Biochem. J.*, vol. 349, no. 3, pp. 747–755, 2000, doi: 10.1042/bj3490747.
- [37] A. Penesyanyan, S. S. Nagy, S. Kjelleberg, M. R. Gillings, and I. T. Paulsen, “Rapid microevolution of biofilm cells in response to antibiotics,” *npj Biofilms Microbiomes*, vol. 5, no. 1, 2019, doi: 10.1038/s41522-019-0108-3.
- [38] J. P. S. Powers and R. E. W. Hancock, “The relationship between peptide structure and antibacterial activity,” *Peptides*, vol. 24, no. 11, pp. 1681–1691, 2003, doi: 10.1016/j.peptides.2003.08.023.
- [39] R. E. Hancock, “Cationic peptides: Effectors in innate immunity and novel antimicrobials,” *Lancet Infect. Dis.*, vol. 1, no. 3, pp. 156–164, 2001, doi: 10.1016/S1473-3099(01)00092-5.
- [40] L. Zhang, Z. hui Fang, Q. li Li, and C. Y. Cao, “A tooth-binding antimicrobial peptide to prevent the formation of dental biofilm,” *J. Mater. Sci. Mater. Med.*, vol. 30, no. 4, 2019, doi: 10.1007/s10856-019-6246-6.
- [41] P. Petkov, E. Lilkova, N. Ilieva, and L. Litov, “Self-association of antimicrobial peptides: A molecular dynamics simulation study on bombinin,” *Int. J. Mol. Sci.*, vol. 20, no. 21, pp. 15–23, 2019, doi: 10.3390/ijms20215450.
- [42] G. Ehrenstein and H. Lecar, “Electrically gated ionic channels in lipid bilayers,” *Q. Rev. Biophys.*, vol. 10, no. 1, pp. 1–34, Feb. 1977, doi: 10.1017/S0033583500000123.
- [43] K. Matsuzaki, K.-I. Sugishita, M. Harada, N. Fujii, and K. Miyajima, “Interactions of an antimicrobial peptide, magainin 2, with outer and inner membranes of Gram-negative bacteria,” 1997. Accessed: May 30, 2019. [Online]. Available: <https://core.ac.uk/download/pdf/82768106.pdf>.
- [44] E. Gazit, I. R. Miller, P. C. Biggin, M. S. Sansom, and Y. Shai, “Structure and orientation of

the mammalian antibacterial peptide cecropin P1 within phospholipid membranes.,” *J. Mol. Biol.*, vol. 258, no. 5, pp. 860–70, 1996, doi: 10.1006/jmbi.1996.0293.

- [45] Y. Pouny, D. Rapaport, A. Mor, P. Nicolas, and Y. Shai, “Interaction of Antimicrobial Dermaseptin and Its Fluorescently Labeled Analogues with Phospholipid Membranes1,” vol. 31, pp. 12416–12423, 1241, doi: 10.1021/bi00164a017.
- [46] V. V. Kapoerchan *et al.*, “An adamantyl amino acid containing gramicidin S analogue with broad spectrum antibacterial activity and reduced hemolytic activity,” *Chem. - A Eur. J.*, vol. 16, no. 40, pp. 12174–12181, 2010, doi: 10.1002/chem.201001686.
- [47] S. C. Park, Y. Park, and K. S. Hahm, “The role of antimicrobial peptides in preventing multidrug-resistant bacterial infections and biofilm formation,” *Int. J. Mol. Sci.*, vol. 12, no. 9, pp. 5971–5992, 2011, doi: 10.3390/ijms12095971.
- [48] C. Dias and A. P. Rauter, “Membrane-targeting antibiotics: Recent developments outside the peptide space,” *Future Med. Chem.*, vol. 11, no. 3, pp. 211–228, 2019, doi: 10.4155/fmc-2018-0254.
- [49] M. Wenzel *et al.*, “The multifaceted antibacterial mechanisms of the pioneering peptide antibiotics tyrocidine and gramicidin S,” *MBio*, vol. 9, no. 5, p. 20, 2018, doi: 10.1128/mBio.00802-18.
- [50] H. L. Van Epps, “René Dubos: unearthing antibiotics,” *J. Exp. Med.*, vol. 203, no. 2, p. 259, 2006, doi: 10.1084/jem.2032fta.
- [51] Y. M. Gall and M. B. Konashev, “The discovery of Gramicidin S: the intellectual transformation of G.F. Gause from biologist to researcher of antibiotics and on its meaning for the fate of Russian genetics.,” *Hist. Philos. Life Sci.*, vol. 23, no. 1, pp. 137–150, 2001.
- [52] D. Ciumac, H. Gong, X. Hu, and J. R. Lu, “Membrane targeting cationic antimicrobial peptides,” *J. Colloid Interface Sci.*, vol. 537, pp. 163–185, 2019, doi: 10.1016/j.jcis.2018.10.103.
- [53] W. Kim *et al.*, “A selective membrane-targeting repurposed antibiotic with activity against persistent methicillin-resistant *Staphylococcus aureus*,” *Proc. Natl. Acad. Sci. U. S. A.*, vol. 116, no. 33, pp. 16529–16534, 2019, doi: 10.1073/pnas.1904700116.
- [54] M. Berditsch *et al.*, “Supreme activity of gramicidin S against resistant, persistent and biofilm cells of staphylococci and enterococci,” *Sci. Rep.*, vol. 9, no. 1, pp. 1–15, 2019, doi:

10.1038/s41598-019-54212-z.

- [55] M. Stauss-Grabo, S. Atiye, T. Le, and M. Kretschmar, “Decade-long use of the antimicrobial peptide combination tyrothricin does not pose a major risk of acquired resistance with gram-positive bacteria and candida spp,” *Pharmazie*, vol. 69, no. 11, pp. 838–841, 2014, doi: 10.1691/ph.2014.4686.
- [56] Sigma-aldrich, “Gramicidin from *Bacillus brevis*,” pp. 2–3, 1884.
- [57] G. F. Gause and M. G. Brazhnikova, “Gramicidin S and its use in the treatment of infected wounds [3],” *Nature*, vol. 154, no. 3918. Nature Publishing Group, p. 703, 1944, doi: 10.1038/154703a0.
- [58] G. M. Schmidt, D. C. Hodgkin, and B. M. Oughton, “A crystallographic study of some derivatives of gramicidin S.,” *Biochem. J.*, vol. 65, no. 4, pp. 744–750, 1957, doi: 10.1042/bj0650744.
- [59] N. B. Abbott and E. J. Ambrose, “The configuration of the polypeptide chain in small peptides such as gramicidin S,” *Proc. R. Soc. London. Ser. A. Math. Phys. Sci.*, vol. 219, no. 1136, pp. 17–32, 1953, doi: 10.1098/rspa.1953.0128.
- [60] G. Ehrlich and G. B. B. M. Sutherland, “Contribution of Side-Chains to the Infra-Red Spectra of Proteins: the 6.5- $\mu$  Band,” *Nature*, vol. 172, no. 4380, pp. 671–672, 1953, doi: 10.1038/172671b0.
- [61] D. C. Hodgkin and B. M. Oughton, “Possible molecular models for gramicidin S and their relationship to present ideas of protein structure.,” *Biochem. J.*, vol. 65, no. 4, pp. 752–756, 1957, doi: 10.1042/bj0650752.
- [62] L. C. Craig, E. J. Harfenist, and A. C. Paladini, “Dialysis Studies. VII. The Behavior of Angiotensin, Oxytocin, Vasopressin, and Some of Their Analogs,” *Biochemistry*, vol. 3, no. 6, pp. 764–769, Jun. 1964, doi: 10.1021/bi00894a005.
- [63] G. Némethy and H. A. Scheraga, “Hydrogen bonding involving the ornithine side chain of gramicidin S,” *Biochem. Biophys. Res. Commun.*, vol. 118, no. 2, pp. 643–647, Jan. 1984, doi: 10.1016/0006-291X(84)91351-2.
- [64] F. A. Momany, G. Vanderkooi, R. W. Tuttle, and H. A. Scheraga, “Minimization of Polypeptide Energy. Iv. Further Studies of Gramicidin S,” *Biochemistry*, vol. 8, no. 2, pp. 744–746, Feb. 1969, doi: 10.1021/bi00830a041.

- [65] A. Stern, W. A. Gibbons, and L. C. Craig, "A conformational analysis of gramicidin S-A by nuclear magnetic resonance.," *Proc. Natl. Acad. Sci. U. S. A.*, vol. 61, no. 2, pp. 734–741, 1968, doi: 10.1073/pnas.61.2.734.
- [66] S. E. Hull, P. Karlsson, P. Main, M. M. Woolfson, and E. J. Dodson, "The crystal structure of a hydrated gramicidin S-urea complex [10]," *Nature*, vol. 275, no. 5677, pp. 206–207, 1978, doi: 10.1038/275206a0.
- [67] V. A. Lorenz-Fonfria, "Infrared Difference Spectroscopy of Proteins: From Bands to Bonds," *Chem. Rev.*, vol. 120, no. 7, pp. 3466–3576, 2020, doi: 10.1021/acs.chemrev.9b00449.
- [68] S. Rackovsky and H. A. Scheraga, "Intermolecular anti-parallel  $\beta$  sheet: Comparison of predicted and observed conformations of gramicidin S," *Proc. Natl. Acad. Sci. U. S. A.*, vol. 77, no. 12 I, pp. 6965–6967, 1980, doi: 10.1073/pnas.77.12.6965.
- [69] V. M. Naik, S. Krimm, J. B. Denton, G. Nemethy, and H. A. Scheraga, "Vibrational analysis of peptides, polypeptides and proteins: XXVII. Structure of gramicidin S from normal mode analyses of low-energy conformations.," *Int. J. Pept. Protein Res.*, vol. 24, no. 6, pp. 613–626, 1984, doi: 10.1111/j.1399-3011.1984.tb03168.x.
- [70] K. Joshi, D. Semrouni, G. Ohanessian, and C. Clavaguéra, "Structures and IR spectra of the gramicidin s peptide: Pushing the quest for low-energy conformations," *J. Phys. Chem. B*, vol. 116, no. 1, pp. 483–490, 2012, doi: 10.1021/jp207102v.
- [71] M. Dygert, G. Nobuhiro, and H. A. Scheraga, "Use of a Symmetry Condition to Compute the Conformation of Gramicidin S," *Macromolecules*, vol. 8, no. 6, pp. 750–761, Nov. 1975, doi: 10.1021/ma60048a016.
- [72] D. Balasubramanian, "The Conformation of Gramicidin S in Solution," *J. Am. Chem. Soc.*, vol. 89, no. 21, pp. 5445–5449, Oct. 1967, doi: 10.1021/ja00997a027.
- [73] D. Mihailescu and J. C. Smith, "Molecular dynamics simulation of the cyclic decapeptide antibiotic, gramicidin S, in dimethyl sulfoxide solution," *J. Phys. Chem. B*, vol. 103, no. 9, pp. 1586–1594, Mar. 1999, doi: 10.1021/jp983674t.
- [74] A. L. Llamas-Saiz, G. M. Grotenbreg, M. Overhand, and M. J. Van Raaij, "Double-stranded helical twisted  $\beta$ -sheet channels in crystals of gramicidin S grown in the presence of trifluoroacetic and hydrochloric acids," *Acta Crystallogr. Sect. D Biol. Crystallogr.*, vol. 63, no. 3, pp. 401–407, Feb. 2007, doi: 10.1107/S0907444906056435.

- [75] M. Kuczer, D. Konopińska, and G. Rosiński, “Insect gonadotropic peptide hormones : some recent,” *J. Pept. Sci.*, no. October 2006, pp. 16–26, 2007, doi: 10.1002/psc.
- [76] A. L. Llamas-Saiz, G. M. Grotenbreg, M. Overhand, and M. J. Van Raaij, “Double-stranded helical twisted  $\beta$ -sheet channels in crystals of gramicidin S grown in the presence of trifluoroacetic and hydrochloric acids,” *Acta Crystallogr. Sect. D Biol. Crystallogr.*, vol. 63, no. 3, pp. 401–407, 2007, doi: 10.1107/S0907444906056435.
- [77] D. Mihailescu and J. C. Smith, “Atomic detail peptide-membrane interactions: Molecular dynamics simulation of gramicidin S in a DMPC bilayer,” *Biophys. J.*, vol. 79, no. 4, pp. 1718–1730, 2000, doi: 10.1016/S0006-3495(00)76424-1.
- [78] Y. A. Ovchinnikov *et al.*, “The conformation of gramicidin S and its N,N'-diacetyl derivative in solutions,” *Biochem. Biophys. Res. Commun.*, vol. 39, no. 2, pp. 217–225, 1970, doi: 10.1016/0006-291X(70)90781-3.
- [79] D. H. Huang, R. Walter, J. D. Glickson, and N. R. Krishna, “Solution conformation of gramicidin S: An intramolecular nuclear Overhauser effect study,” *Proc. Natl. Acad. Sci. U. S. A.*, vol. 78, no. 2 I, pp. 672–675, 1981, doi: 10.1073/pnas.78.2.672.
- [80] P. I. Haris and D. Chapman, “Does Fourier-transform infrared spectroscopy provide useful information on protein structures ?,” no. 17. Elsevier Science Publishers, pp. 328–333, 1992.
- [81] C. R. Baiz, M. Reppert, and A. Tokmakoff, “Introduction to Protein 2D IR Spectroscopy,” *Ultrafast Infrared Vib. Spectrosc.*, no. 22, pp. 361–404, 2012, doi: 10.1201/b13972.
- [82] R. E. W. Hancock and D. S. Chapple, “Peptide antibiotics,” *Antimicrob. Agents Chemother.*, vol. 43, no. 6, pp. 1317–1323, 1999, doi: 10.1128/aac.43.6.1317.
- [83] E. Staudegger *et al.*, “X-ray studies on the interaction of the antimicrobial peptide gramicidin S with microbial lipid extracts: Evidence for cubic phase formation,” *Biochim. Biophys. Acta - Biomembr.*, vol. 1468, no. 1–2, pp. 213–230, 2000, doi: 10.1016/S0005-2736(00)00260-1.
- [84] M. Tamaki, K. Sawa, S. Kikuchi, M. Shindo, and Y. Uchida, “A novel, antimicrobially active analog of gramicidin S without amphiphilic conformation,” *J. Antibiot. (Tokyo)*, vol. 59, no. 6, pp. 370–372, 2006, doi: 10.1038/ja.2006.54.
- [85] C. Priem, A. Andréwuttke, M. Berditsch, A. S. Ulrich, and A. Geyer, “Scaling the Amphiphilic Character and Antimicrobial Activity of Gramicidin S by Dihydroxylation or Ketal Formation,” 2017, doi: 10.1021/acs.joc.7b02177.

- [86] C. Solanas *et al.*, “Sequence inversion and phenylalanine surrogates at the  $\beta$ -Turn enhance the antibiotic activity of gramicidin S,” *J. Med. Chem.*, vol. 53, no. 10, pp. 4119–4129, May 2010, doi: 10.1021/jm100143f.
- [87] T. Katsu, H. Kobayashi, and Y. Fujita, “Mode of action of gramicidin S on Escherichia coli membrane,” *BBA - Biomembr.*, vol. 860, no. 3, pp. 608–619, 1986, doi: 10.1016/0005-2736(86)90560-2.
- [88] G. Nagamurthi and S. Rambhav, “Gramicidin-S : Structure – activity relationship \*,” *J. Biosci.*, vol. 7, no. 3 & 4, pp. 323–329, 1985.
- [89] T. J. Franklin and G. A. Snow, *Biochemistry and Molecular Biology of Antimicrobial Drug Action*. New York (USA): Chapman and Hall, 1988.
- [90] E. J. Prenner, R. N. A. H. Lewis, M. Jelokhani-Niaraki, R. S. Hodges, and R. N. McElhaney, “Cholesterol attenuates the interaction of the antimicrobial peptide gramicidin S with phospholipid bilayer membranes,” *Biochim. Biophys. Acta - Biomembr.*, vol. 1510, no. 1–2, pp. 83–92, Feb. 2001, doi: 10.1016/S0005-2736(00)00337-0.
- [91] L. Béven and H. Wróblewski, “Effect of natural amphiphatic peptides on viability, membrane potential, cell shape and motility of mollicutes,” *Res. Microbiol.*, vol. 148, no. 2, pp. 163–175, 1997, doi: 10.1016/S0923-2508(97)87647-4.
- [92] L. H. Kondejewski, S. W. Farmer, D. S. Wishart, R. E. W. Hancock, and R. S. Hodges, “Gramicidin S is active against both gram-positive and gram-negative bacteria,” *Int. J. Pept. Protein Res.*, vol. 47, no. 6, pp. 460–466, 1996, doi: 10.1111/j.1399-3011.1996.tb01096.x.
- [93] W. Danders *et al.*, “Antibacterial action of gramicidin S and tyrocidines in relation to active transport, in vitro transcription, and spore outgrowth,” *Antimicrob. Agents Chemother.*, vol. 22, no. 5, pp. 785–790, 1982, doi: 10.1128/AAC.22.5.785.
- [94] L. H. Kondejewski, S. W. Farmer, D. S. Wishart, C. M. Kay, R. E. W. Hancock, and R. S. Hodges, “Modulation of structure and antibacterial and hemolytic activity by ring size in cyclic gramicidin S analogs,” *J. Biol. Chem.*, vol. 271, no. 41, pp. 25261–25268, 1996, doi: 10.1074/jbc.271.41.25261.
- [95] L. H. Kondejewski *et al.*, “Dissociation of antimicrobial and hemolytic activities in cyclic peptide diastereomers by systematic alterations in amphipathicity,” *J. Biol. Chem.*, vol. 274, no. 19, pp. 13181–13192, 1999, doi: 10.1074/jbc.274.19.13181.

- [96] B. Legrand *et al.*, “Thiazole-based  $\gamma$ -building blocks as reverse-turn mimetic to design a gramicidin S analogue: Conformational and biological evaluation,” *Chem. - A Eur. J.*, vol. 20, no. 22, pp. 6713–6720, 2014, doi: 10.1002/chem.201402190.
- [97] S. R. Griffiths-Jones, A. J. Maynard, and M. S. Searle, “Dissecting the stability of a  $\beta$ -hairpin peptide that folds in water: NMR and molecular dynamics analysis of the  $\beta$ -turn and  $\beta$ -strand contributions to folding,” *J. Mol. Biol.*, vol. 292, no. 5, pp. 1051–1069, 1999, doi: 10.1006/jmbi.1999.3119.
- [98] E. De Alba, M. A. Jiménez, and M. Rico, “Turn Residue Sequence Determines-Hairpin Conformation in Designed Peptides,” 1997. Accessed: Dec. 14, 2020. [Online]. Available: <https://pubs.acs.org/sharingguidelines>.
- [99] K. L. Constantine *et al.*, “Structural and Dynamic Properties of a  $\beta$ -Hairpin-Forming Linear Peptide. 1. Modeling Using Ensemble-Averaged Constraints,” *J. Am. Chem. Soc.*, vol. 117, no. 44, pp. 10841–10854, 1995, doi: 10.1021/ja00149a007.
- [100] M. Ramírez-Alvarado, F. J. Blanco, and L. Serrano, “De novo design and structural analysis of a model  $\beta$ -hairpin peptide system,” *Nat. Struct. Mol. Biol.*, vol. 3, pp. 604–612, 1996.
- [101] C. Solanas *et al.*, “Therapeutic Index of Gramicidin S is Strongly Modulated by D-Phenylalanine Analogues at the-Turn,” doi: 10.1021/jm800886n.
- [102] G. M. Grotenbreg *et al.*, “ $\beta$ -turn modified gramicidin S analogues containing arylated sugar amino acids display antimicrobial and hemolytic activity comparable to the natural product,” *J. Am. Chem. Soc.*, vol. 128, no. 23, pp. 7559–7565, 2006, doi: 10.1021/ja0588510.
- [103] D. Eisenberg, E. Schwarz, M. Komaromy, and R. Wall, “Analysis of membrane and surface protein sequences with the hydrophobic moment plot,” *J. Mol. Biol.*, vol. 179, no. 1, pp. 125–142, 1984, doi: 10.1016/0022-2836(84)90309-7.
- [104] Y. Wan, A. Stanovych, D. Gori, S. Zirah, C. Kouklovsky, and V. Alezra, “ $\beta,\gamma$ -diamino acids as building blocks for new analogues of Gramicidin S: Synthesis and biological activity,” *Eur. J. Med. Chem.*, vol. 149, pp. 122–128, Apr. 2018, doi: 10.1016/j.ejmech.2018.02.053.
- [105] T. Wieprecht *et al.*, “Peptide hydrophobicity controls the activity and selectivity of magainin 2 amide in interaction with membranes,” *Biochemistry*, vol. 36, no. 20, pp. 6124–6132, 1997, doi: 10.1021/bi9619987.
- [106] C. Appelt, A. Wessolowski, M. Dathe, and P. Schmieder, “Structures of cyclic, antimicrobial

peptides in a membrane-mimicking environment define requirements for activity,” *J. Pept. Sci.*, vol. 14, no. 4, pp. 524–527, Apr. 2008, doi: 10.1002/psc.924.

- [107] J. Swierstra, V. Kapoerchan, A. Knijnenburg, A. van Belkum, and M. Overhand, “Structure, toxicity and antibiotic activity of gramicidin S and derivatives,” *Eur. J. Clin. Microbiol. Infect. Dis.*, vol. 35, no. 5, pp. 763–769, 2016, doi: 10.1007/s10096-016-2595-y.
- [108] R. N. A. H. Lewis *et al.*, “Fourier transform infrared spectroscopic studies of the interaction of the antimicrobial peptide gramicidin S with lipid micelles and with lipid monolayer and bilayer membranes,” *Biochemistry*, vol. 38, no. 46, pp. 15193–15203, 1999, doi: 10.1021/bi9912342.
- [109] M. Jelokhani-Niaraki, E. J. Prenner, C. M. Kay, R. N. McElhaney, R. S. Hodges, and L. H. Kondejewski, “Conformation and other biophysical properties of cyclic antimicrobial peptides in aqueous solutions,” *J. Pept. Res.*, vol. 58, no. 4, pp. 293–306, 2001, doi: 10.1034/j.1399-3011.2001.00893.x.
- [110] A. Barth, “Infrared spectroscopy of proteins,” *Biochim. Biophys. Acta - Bioenerg.*, vol. 1767, no. 9, pp. 1073–1101, 2007, doi: 10.1016/j.bbabbio.2007.06.004.
- [111] M. Z. Peter Hamm, *Concepts and Methods of 2D-IR spectroscopy*. New York: Cambridge University Press, 2012.
- [112] A. Barth and C. Zscherp, “What vibrations tell about proteins,” *Q. Rev. Biophys.*, vol. 35, no. 4, pp. 369–430, 2002, doi: 10.1017/S0033583502003815.
- [113] L. M. Miller, M. W. Bourassa, and R. J. Smith, “FTIR spectroscopic imaging of protein aggregation in living cells,” *Biochimica et Biophysica Acta - Biomembranes*, vol. 1828, no. 10, pp. 2339–2346, 2013, doi: 10.1016/j.bbammem.2013.01.014.
- [114] N. Taniguchi, “Amino Acids and Proteins,” in *Medical Biochemistry*, 3rd ed., M. A. D. J. W. Baynes, Ed. China: Elsevier, 2010, pp. 5–21.
- [115] H. R. Horton, L. A. Moran, R. S. Ochs, D. J. Rawn, K. G. Scrimgeour, and H. R. Horton, *Principles of Biochemistry (3rd Edition)*. Prentice Hall, 1995.
- [116] A. Barth and C. Zscherp, “What vibrations tell us about proteins.,” *Q. Rev. Biophys.*, vol. 35, no. 4, pp. 369–430, 2002, doi: 10.1017/S0033583502003815.
- [117] A. Barth, “The infrared absorption of amino acid side chains,” *Progress in Biophysics and Molecular Biology*, vol. 74, no. 3–5, pp. 141–173, 2000, doi: 10.1016/S0079-6107(00)00021-

3.

- [118] M. Wolpert and P. Hellwig, "Infrared spectra and molar absorption coefficients of the 20 alpha amino acids in aqueous solutions in the spectral range from 1800 to 500 cm<sup>-1</sup>," *Spectrochim. Acta - Part A Mol. Biomol. Spectrosc.*, vol. 64, no. 4, pp. 987–1001, 2006, doi: 10.1016/j.saa.2005.08.025.
- [119] D. J. Hirsh, J. Hammer, W. L. Maloy, J. Blazyk, and J. Schaefer, "Secondary structure and location of a magainin analogue in synthetic phospholipid bilayers," *Biochemistry*, vol. 35, no. 39, pp. 12733–12741, 1996, doi: 10.1021/bi961468a.
- [120] C. Carrillo, J. A. Teruel, F. J. Aranda, and A. Ortiz, "Molecular mechanism of membrane permeabilization by the peptide antibiotic surfactin," *Biochim. Biophys. Acta - Biomembr.*, vol. 1611, no. 1–2, pp. 91–97, 2003, doi: 10.1016/S0005-2736(03)00029-4.
- [121] J. Kong and S. Yu, "Fourier transform infrared spectroscopic analysis of protein secondary structures," *Acta Biochim. Biophys. Sin. (Shanghai)*, vol. 39, no. 8, pp. 549–559, 2007, doi: 10.1111/j.1745-7270.2007.00320.x.
- [122] W. Gallagher, "FTIR Analysis of Protein Structure," no. 1958, pp. 662–666, 1997, [Online]. Available: [https://www.chem.uwec.edu/chem455\\_s05/pages/Manuals/FTIR\\_of\\_proteins.pdf](https://www.chem.uwec.edu/chem455_s05/pages/Manuals/FTIR_of_proteins.pdf).
- [123] M. Kačuráková and M. Mathlouthi, "FTIR and laser-Raman spectra of oligosaccharides in water: Characterization of the glycosidic bond," *Carbohydr. Res.*, vol. 284, no. 2, pp. 145–157, 1996, doi: 10.1016/0008-6215(95)00412-2.
- [124] M. Jackson and H. H. Mantsch, "The Use and Misuse of FTIR Spectroscopy in the Determination of Protein Structure," *Crit. Rev. Biochem. Mol. Biol.*, vol. 30, no. 2, pp. 95–120, 1995, doi: 10.3109/10409239509085140.
- [125] D. M. Byler and H. Susi, "Examination of the secondary structure of proteins by deconvolved FTIR spectra," *Biopolymers*, vol. 25, no. 3, pp. 469–487, 1986, doi: 10.1002/bip.360250307.
- [126] S. Sukumaran, "Protein secondary structure elucidation using FTIR spectroscopy," 2018.
- [127] P. Hamm and M. T. Zanni, *Concepts and Methods of 2D Infrared Spectroscopy*. Cambridge University Press, 2011.
- [128] L. E. Townsley, W. A. Tucker, S. Sham, and J. F. Hinton, "Structures of gramicidins A, B, and C incorporated into sodium dodecyl sulfate micelles," *Biochemistry*, vol. 40, no. 39, pp.

11676–11686, 2001, doi: 10.1021/bi010942w.

- [129] G. R. Grimsley, B. M. P. Huyghues-Despointes, C. N. Pace, and J. M. Scholtz, “Measuring the Conformational Stability of a Protein by NMR,” *Cold Spring Harb. Protoc.*, vol. 2006, no. 1, p. pdb.prot4244, 2006, doi: 10.1101/pdb.prot4244.
- [130] E. K. Tiburu, J. Zhuang, H. N. A. Fleischer, P. K. Arthur, and G. A. Awandare, “Expression, purification, and monitoring of conformational changes of hCB2 TMH67H8 in different membrane-mimetic lipid mixtures using circular dichroism and NMR techniques,” *Membranes (Basel)*, vol. 7, no. 10, p. 13, 2017, doi: 10.3390/membranes7010010.
- [131] F. Li *et al.*, “Conformation and dynamics of a cyclic disulfide-bridged peptide: Effects of temperature and solvent,” *J. Phys. Chem. B*, vol. 117, no. 13, pp. 3560–3570, 2013, doi: 10.1021/jp4007334.
- [132] P. Hamm, J. Helbing, and J. Bredenbeck, “Two-dimensional infrared spectroscopy of photoswitchable peptides,” *Phys. Chem.*, vol. 59, pp. 291–317, 2008.
- [133] N. T. Hunt, “2D-IR spectroscopy: Ultrafast insights into biomolecule structure and function,” *Chem. Soc. Rev.*, vol. 38, no. 7, pp. 1837–1848, 2009, doi: 10.1039/b819181f.
- [134] N. A. Lakomek, T. Carlomagno, S. Becker, C. Griesinger, and J. Meiler, “A thorough dynamic interpretation of residual dipolar couplings in ubiquitin,” *J. Biomol. NMR*, vol. 34, no. 2, pp. 101–115, 2006, doi: 10.1007/s10858-005-5686-0.
- [135] P. Hamm, M. Lim, and R. M. Hochstrasser, “Structure of the amide I band of peptides measured by femtosecond nonlinear-infrared spectroscopy,” *J. Phys. Chem. B*, vol. 102, no. 31, pp. 6123–6138, 1998, doi: 10.1021/jp9813286.
- [136] J. Kubelka, J. Kim, P. Bour, and T. A. Keiderling, “Contribution of transition dipole coupling to amide coupling in IR spectra of peptide secondary structures,” *Vib. Spectrosc.*, vol. 42, no. 1, pp. 63–73, 2006, doi: 10.1016/j.vibspec.2006.04.003.
- [137] J. W. Brauner, C. R. Flach, and R. Mendelsohn, “A quantitative reconstruction of the amide I contour in the IR spectra of globular proteins: From structure to spectrum,” *J. Am. Chem. Soc.*, vol. 127, no. 1, pp. 100–109, 2005, doi: 10.1021/ja0400685.
- [138] P. Stevenson and A. Tokmakoff, “Distinguishing gramicidin D conformers through two-dimensional infrared spectroscopy of vibrational excitons,” *J. Chem. Phys.*, vol. 142, no. 21, 2015, doi: 10.1063/1.4917321.

- [139] J. Bandekar and S. Krimm, "Vibrational Spectroscopy of L-Valyl-Glycyl-Glycine, a Parallel-Chain  $\beta$ -Structure\*," vol. 27, no. 38, pp. 885–908, 1988.
- [140] L. A. Munishkina, C. Phelan, V. N. Uversky, and A. L. Fink, "Conformational behavior and aggregation of  $\alpha$ -synuclein in organic solvents: Modeling the effects of membranes," *Biochemistry*, vol. 42, no. 9, pp. 2720–2730, 2003, doi: 10.1021/bi027166s.
- [141] G. Lindblom and P. O. Quist, "Protein and peptide interactions with lipids: structure, membrane function and new methods," *Curr. Opin. Colloid Interface Sci.*, vol. 3, no. 5, pp. 499–508, 1998, doi: 10.1016/S1359-0294(98)80024-1.
- [142] M. Jelokhani-Niaraki, R. S. Hodges, J. E. Meissner, U. E. Hassenstein, and L. Wheaton, "Interaction of gramicidin S and its aromatic amino-acid analog with phospholipid membranes," *Biophys. J.*, vol. 95, no. 7, pp. 3306–3321, 2008, doi: 10.1529/biophysj.108.137471.
- [143] F. D. Sonnichsen, J. E. Van Eyk, R. S. Hodges, and B. D. Sykes, "Effect of Trifluoroethanol on Protein Secondary Structure: An NMR and CD Study Using a Synthetic Actin Peptide," *Biochemistry*, vol. 31, no. 37, pp. 8790–8798, 1992, doi: 10.1021/bi00152a015.
- [144] M. J. Bodkin and J. M. Goodfellow, "Hydrophobic solvation in aqueous trifluoroethanol solution," *Biopolymers*, vol. 39, no. 1, pp. 43–50, 1996, doi: 10.1002/(sici)1097-0282(199607)39:1<43::aid-bip5>3.3.co;2-5.
- [145] M. Buck, "Trifluoroethanol and colleagues: Cosolvents come of age. Recent studies with peptides and proteins," *Quarterly Reviews of Biophysics*, vol. 31, no. 3, pp. 297–355, 1998, doi: 10.1017/S003358359800345X.
- [146] R. N. A. H. Lewis *et al.*, "Fourier transform infrared spectroscopic studies of the interaction of the antimicrobial peptide gramicidin S with lipid micelles and with lipid monolayer and bilayer membranes," *Biochemistry*, vol. 38, no. 46, pp. 15193–15203, 1999, doi: 10.1021/bi9912342.
- [147] A. W. Smith and A. Tokmakoff, "Amide I two-dimensional infrared spectroscopy of  $\beta$ -hairpin peptides," *J. Chem. Phys.*, vol. 126, no. 4, 2007, doi: 10.1063/1.2428300.
- [148] C. Solanas *et al.*, "Therapeutic index of gramicidin S is strongly modulated by D-phenylalanine analogues at the  $\beta$ -turn," *J. Med. Chem.*, vol. 52, no. 3, pp. 664–674, 2009, doi: 10.1021/jm800886n.
- [149] J. Luo *et al.*, "Inhibiting and reversing amyloid- $\beta$  peptide (1-40) fibril formation with

Gramicidin S and engineered analogues,” *Chem. - A Eur. J.*, vol. 19, no. 51, pp. 17338–17348, 2013, doi: 10.1002/chem.201301535.

- [150] S. Laiken, M. Printz, and L. C. Craig, “Circular Dichroism of the Tyrocidines and Gramicidin S-A.,” *J. Biol. Chem.*, vol. 244, no. 16, pp. 4454–4457, 1969.
- [151] K. Yamada *et al.*, “Stereochemistry of protected ornithine side chains of gramicidin S derivatives: X-ray crystal structure of the bis-boc-tetra-N-methyl derivative of gramicidin S,” *J. Am. Chem. Soc.*, vol. 124, no. 43, pp. 12684–12688, 2002, doi: 10.1021/ja020307t.
- [152] A. S. Kotmale *et al.*, “Conformational studies of Ant-Pro motif-incorporated cyclic peptides: Gramicidin S and avellanin,” *New J. Chem.*, vol. 42, no. 2, pp. 1197–1201, 2018, doi: 10.1039/c7nj03701e.
- [153] R. V Nair *et al.*, “Organic & Biomolecular Chemistry Formation of a pseudo- $\beta$ -hairpin motif utilizing the Ant-Pro reverse turn: consequences of stereochemical reordering †,” *Org. Biomol. Chem.*, vol. 12, p. 774, 2014, doi: 10.1039/c3ob42016g.
- [154] A. Asano, S. Matsuoka, C. Minami, T. Kato, and M. Doi, “[Leu2]Gramicidin S preserves the structural properties of its parent peptide and forms helically aligned  $\beta$ -sheets,” *Acta Crystallogr. Sect. C Struct. Chem.*, vol. 75, pp. 1336–1343, 2019, doi: 10.1107/S2053229619011872.
- [155] L. Minnes *et al.*, “Quantifying Secondary Structure Changes in Calmodulin Using 2D-IR Spectroscopy,” *Anal. Chem.*, vol. 89, no. 20, pp. 10898–10906, 2017, doi: 10.1021/acs.analchem.7b02610.
- [156] A. Culka, J. Jehlička, and H. G. M. Edwards, “Acquisition of Raman spectra of amino acids using portable instruments: Outdoor measurements and comparison,” *Spectrochim. Acta - Part A Mol. Biomol. Spectrosc.*, vol. 77, no. 5, pp. 978–983, 2010, doi: 10.1016/j.saa.2010.08.034.
- [157] D. Kurouski, R. P. Van Duyne, and I. K. Lednev, “Exploring the structure and formation mechanism of amyloid fibrils by Raman spectroscopy: A review,” *Analyst*, vol. 140, no. 15, pp. 4967–4980, 2015, doi: 10.1039/c5an00342c.
- [158] E. C. Le Ru and P. G. Etchegoin, *Principles of Surface Enhanced Raman Spectroscopy and related plasmonic effects*, no. 1. 2009.
- [159] A. M. Dwivedi and S. Krimm, “Vibrational analysis of peptides, polypeptides, and proteins. XV. Crystalline polyglycine II,” *Biopolymers*, vol. 21, no. 12, pp. 2377–2397, 1982, doi:

10.1002/bip.360211205.

- [160] A. Rygula, K. Majzner, K. M. Marzec, A. Kaczor, M. Pilarczyk, and M. Baranska, "Raman spectroscopy of proteins: A review," *J. Raman Spectrosc.*, vol. 44, no. 8, pp. 1061–1076, 2013, doi: 10.1002/jrs.4335.
- [161] J. De Gelder, K. De Gussen, P. Vandenabeele, and L. Moens, "Reference database of Raman spectra of biological molecules.," *Raman Spectrosc.*, vol. 38, pp. 1133–1147, 2007, [Online]. Available: <http://onlinelibrary.wiley.com/doi/10.1002/jrs.1734/epdf>.
- [162] A. Downes and A. Elfick, "Raman spectroscopy and related techniques in biomedicine," *Sensors*, vol. 10, no. 3, pp. 1871–1889, 2010, doi: 10.3390/s100301871.
- [163] N. P. Ivleva, M. Wagner, A. Szkola, H. Horn, R. Niessner, and C. Haisch, "Label-free in situ SERS imaging of biofilms," *J. Phys. Chem. B*, vol. 114, no. 31, pp. 10184–10194, 2010, doi: 10.1021/jp102466c.
- [164] P. M. Tiwari, K. Vig, V. a. Dennis, and S. R. Singh, "Functionalized Gold Nanoparticles and Their Biomedical Applications," *Nanomaterials*, vol. 1, no. 1, pp. 31–63, 2011, doi: 10.3390/nano1010031.
- [165] N. Leopold and B. Lendl, "A New Method for Fast Preparation of Highly Surface-Enhanced Raman Scattering (SERS) Active Silver Colloids at Room Temperature by Reduction of Silver Nitrate with Hydroxylamine Hydrochloride," *J. Phys. Chem. B*, vol. 107, no. 24, pp. 5723–5727, 2003, doi: 10.1021/jp027460u.
- [166] A. Shkilnyy, M. Soucé, P. Dubois, F. Warmont, M.-L. Saboungi, and I. Chourpa, "Poly(ethylene glycol)-stabilized silver nanoparticles for bioanalytical applications of SERS spectroscopy.," *Analyst*, vol. 134, no. 9, pp. 1868–1872, 2009, doi: 10.1039/b905694g.
- [167] M. V. Cañameres, J. V. Garcia-Ramos, J. D. Gómez-Varga, C. Domingo, and S. Sanchez-Cortes, "Comparative study of the morphology, aggregation, adherence to glass, and surface-enhanced Raman scattering activity of silver nanoparticles prepared by chemical reduction of Ag<sup>+</sup> using citrate and hydroxylamine," *Langmuir*, vol. 21, no. 18, pp. 8546–8553, 2005, doi: 10.1021/la050030l.
- [168] E. López-Tobar *et al.*, "Large size citrate-reduced gold colloids appear as optimal SERS substrates for cationic peptides," *J. Raman Spectrosc.*, vol. 48, no. 1, pp. 30–37, 2017, doi: 10.1002/jrs.4976.

- [169] B. Hernández *et al.*, “From bulk to plasmonic nanoparticle surface: behavior of two potent therapeutic peptides, octreotide and pasireotide,” *Phys. Chem. Chem. Phys.*, no. 1, pp. 24437–24450, 2016, doi: 10.1039/C6CP04421B.
- [170] E. López-Tobar *et al.*, “Anchoring sites of fibrillogenic peptide hormone somatostatin-14 on plasmonic nanoparticles,” *J. Phys. Chem. C*, vol. 119, no. 15, pp. 8273–8279, 2015, doi: 10.1021/acs.jpcc.5b00485.

## Chapter 2 Instrumentation and Methods

### 2.1 Linear and non-Linear spectroscopy

The spectroscopic methods employed in this study shall be outlined first as linear and non-linear methods. Linear or 1D spectroscopy refers to interaction of light with matter where by one weak incident radiation ( $I_{in}$ ) is considered. After interacting with the chemical sample, the outgoing ( $I_{out}$ ) radiation response signal is what is then detected. In IR spectroscopy, the absolute frequency at which the sample absorbs radiation (single or multiple incoming radiation fields) is measured [1], whilst in Raman spectroscopy the relative frequencies at which the sample scatters are measured [1]–[3]. Linear spectroscopy however gives rise to ambiguities in cases where there is need to interpret observations such as peak broadening and decomposing of the peaks to obtain details in the sample. Relaxation and dynamics cannot be deduced from a linear process. Non-linear spectroscopy involves two or more incident radiations used to obtain a response from matter in cases where a linear response is inadequate. Two or more incident fields act on the dipoles of a sample where macroscopic oscillating polarization is generated [3]–[7]. This is illustrated in *Figure 2.1*. Our study employed both linear (1D IR and Raman) and non-linear (2D-IR) spectroscopic methods, and these shall be introduced and illustrated below. To understand IR absorption spectroscopy, it is important to explain molecular vibrations which is done below in section 2.2.

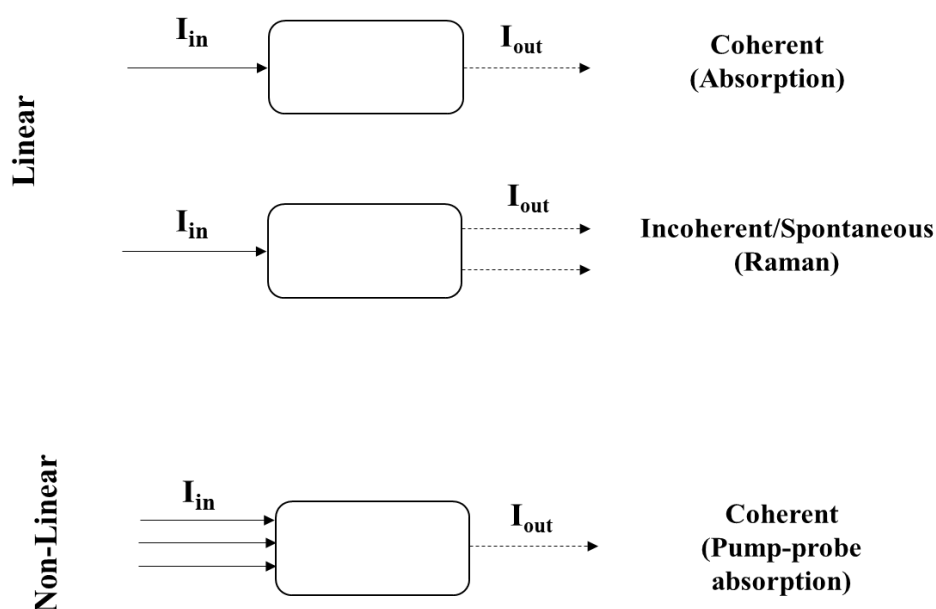


*Figure 2.1* Difference in mechanism for Linear and non-linear spectroscopy. The linear spectroscopy representing both IR absorption and Raman which give coherent and spontaneous outgoing radiation respectively. The non-linear spectroscopy represents pump-probe IR absorption. Adapted from [1], [3].

## 2.2 Vibrational spectroscopy

Vibrational transitions can either be observed with IR or Raman spectroscopy whereby molecular vibrational modes are probed. IR or Raman transitions appear in the region  $10^2 - 10^4 \text{ cm}^{-1}$  of the electromagnetic spectrum [1]. In spectroscopy chemical species are probed by radiation with particular energy from the electromagnetic spectrum (*Figure 2.2*), whereby the radiation is either absorbed or scattered as a function of frequency [1]. To understand vibrational spectroscopy, IR or Raman, it is important to first understand molecular vibrations. 1D and 2D-IR spectroscopy is explained first in section 2.2.1 and section 2.2.2, respectively and Raman spectroscopy is explained in section 2.2.5.

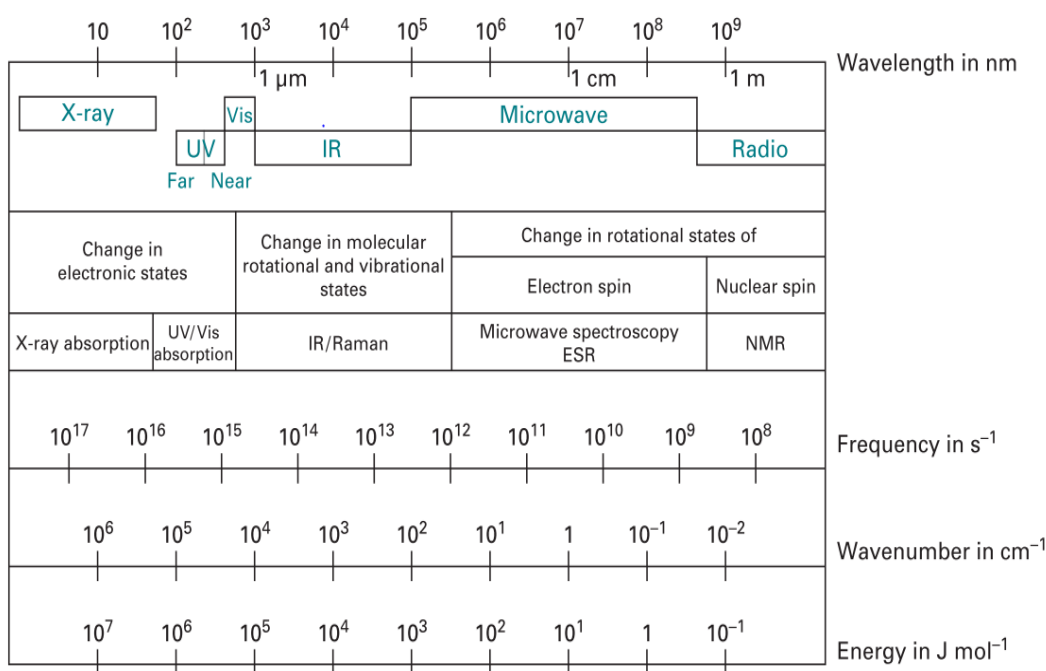


Figure 2.2 The electromagnetic spectrum. Image adapted from [84].

### 2.2.1 IR absorption spectroscopy

In linear IR spectroscopy, infrared radiation excites vibrational transitions of molecules [8]. As a convenient way to understand molecular vibrations, consider a diatomic molecule with its two atoms of mass  $m_1$  and  $m_2$ , connected by a chemical bond. Molecular vibrations are governed by quantum mechanics. The chemical bonds inside the molecules oscillate like springs, and by so doing they display simple harmonic motion. The energies of the molecular vibrations are quantized according to *Equation 2.1*;

$$E_v = \hbar\omega \left( v + \frac{1}{2} \right) \quad 2.1$$

Where  $\nu$  represents vibrational quantum numbers from 0, 1, 2, ...,

From *Equation 2.1*,  $\omega$  is the angular frequency of the oscillator, given by  $\omega = \sqrt{\frac{k}{m_{eff}}}$ , with  $k$  being effective spring constant of the potential and  $m_{eff}$  the effective mass given by  $m_{eff} = \frac{m_1 m_2}{m_1 + m_2}$ . The energies described by *Equation 2.1* are the energies allowed in a potential energy curve of a diatomic molecule, whose potential well is described by *Equation 2.2*;

$$V = \frac{1}{2} kx^2 \quad 2.2$$

Where  $k$  is the force constant on the bond and  $x$  is the length stretched spring from equilibrium position.

In quantum mechanics the point of lowest energy, where  $\nu = 0$ , is known as the zero-point energy, with an energy of  $\frac{1}{2} \hbar\omega$ . At the zero-point molecules never stops vibrating. The energy only changes in units of  $\hbar\omega$ . Considering a harmonic oscillator, the separation of energy levels is the same, given by  $\hbar\omega$ , and it does not allow any bond dissociation. However, in the case of a real molecule this is not the case as molecules are anharmonic oscillators and the potential for a diatomic molecule is described by the Morse potential function (*Figure 2.3*). In time resolved IR spectroscopy anharmonicity is significant and shall be discussed later.

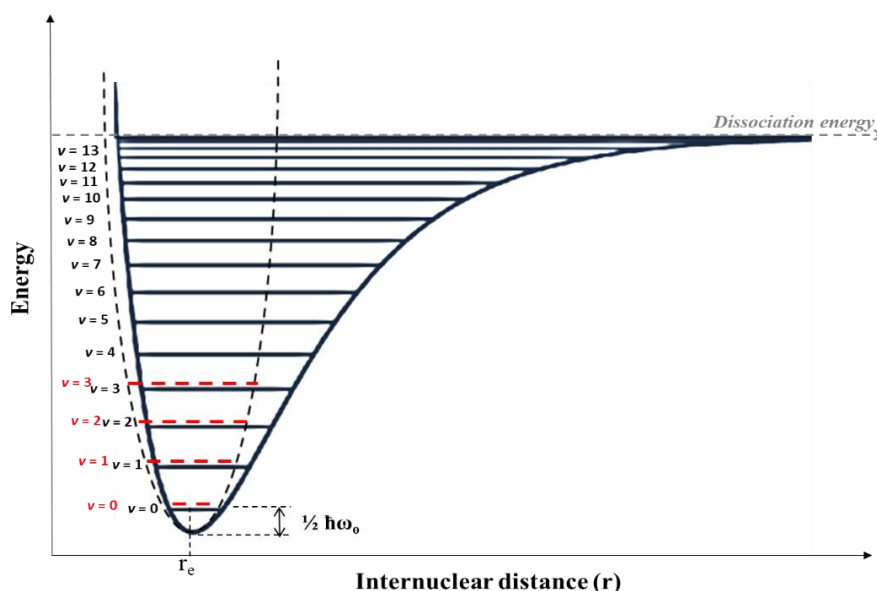


*Figure 2.3* A representation of the potential energy curve for the diatomic molecule, the Morse potential well (bold black line) and the harmonic potential (dashed black line). The energy levels of the harmonic oscillator are evenly spaced. In the Morse potential curve the energy levels becomes closer spaced at high excitations. Image adapted from [1], [9].

According to the quantum mechanics selection rules, only transitions involving  $\Delta v = \pm 1$  are allowed for a harmonic oscillator, with  $\Delta v = +1$  (absorption) and  $\Delta v = -1$  (emission). In the case of anharmonic transition weaker  $\Delta v = \pm 2, \pm 3, \dots$  transitions can be allowed. The gross selection rule for a change in vibrational state, states that there must be a change in the electric dipole moment of the molecule when atoms are displaced. The  $\Delta v = 1$  of  $v = 0 \rightarrow 1$ , are the fundamental transitions and are the strongest in IR and Raman [1], [2], [10].

Vibrational modes can either be IR or Raman active or both [1]. For a vibration to be IR active and be observed in the IR spectrum, there must be a change in the permanent dipole during motion, while for a vibration to be Raman active there must be a change in polarizability of a molecule [1]. For polyatomic molecules, the vibrations can be resolved into normal modes of vibration which are mainly stretching or bending vibrations (*Figure 2.4*). The motion of a particle is described by degrees of freedom namely rotational, translational and vibrational. A molecule with N atoms will have a total of  $3N$  degrees of freedom. Linear molecules have  $3N-5$  while non-linear molecules have  $3N-6$  degrees of freedom / normal modes of vibration [1], [2], [11], [12].

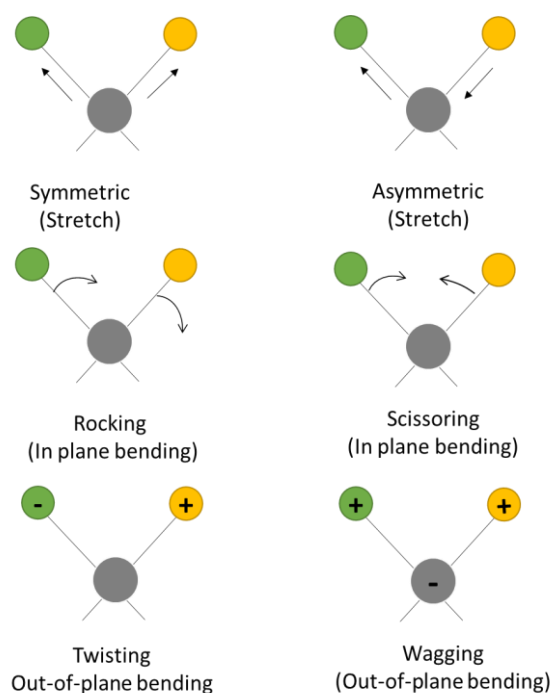


*Figure 2.4 The different types of molecular vibrations mainly stretching and bending. Adapted from [1].*

### 2.2.1.1 FTIR absorption spectrometer

FTIR measurements in this study were carried out using a Bruker Vertex 70v spectrometer with a resolution of  $1.0 \text{ cm}^{-1}$ . The FTIR instrument was based on a Michelson interferometer consisting of a movable mirror, a stationary mirror, a beam splitter, a Helium:Neon (He:Ne) light source which is

used to measure the movement of the mirror and hence calibrates the spectrum, and an IR light source which interacts with the sample (Figure 2.5) [7], [8].

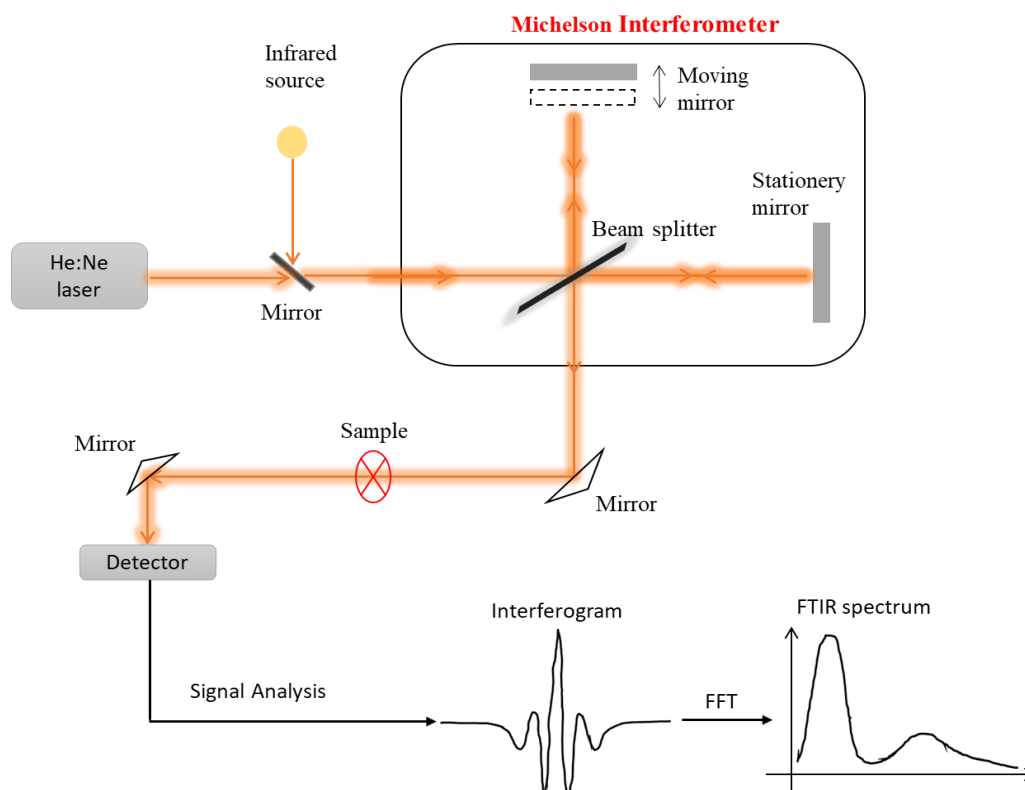


Figure 2.5 Schematic of an FTIR spectrometer based on a Michelson interferometer. Adapted from [8].

Radiation from an IR light source with intensity,  $I_o$ , passes to the beam splitter. The beam splitter splits the radiating beam into two beams. One light beam is reflected to the movable mirror, whilst the other beam is transmitted to the stationary mirror. The movable mirror creates an optical path difference between the two beams which results in the detection of an interferogram. Both the movable and the stationary mirrors reflect back the beams towards the beam splitter, where again 50 % of that radiation is transmitted through the beam splitter to the sample and to the detector (refer to Figure 2.5). At the sample, IR light with incident intensity,  $I_o$ , passes through a sample of concentration,  $c$ , contained in a cuvette of optical path length,  $l$ , and if the sample is homogenous, it will absorb light according to the Beer Lambert law (Equation 2.3), and light is then transmitted with intensity,  $I$ . Thus,

$$A = \log_{10} \frac{I_o}{I} = \epsilon cl \quad 2.3$$

Where  $A$  is the absorbance;  $I_o$  is the incident intensity;  $I$  is the transmitted intensity,  $\epsilon$  is the molar absorption coefficient in ( $\text{M}^{-1} \text{cm}^{-1}$ ),  $c$  is the molar (M) concentration and  $l$  is the optical length in

(cm). The Beer Lambert law relates the light attenuated after passing through a material with the material properties. From the sample, light passes through to the detector where light signal is measured relative to the movable mirror to create an interferogram [8]. The computer performs a Fourier transform on the data to generate a spectrum whose peaks can be assigned according to the vibrations of a sample [1], [8], [13].

### 2.2.2 2D-IR absorption spectroscopy

The need to fully understand fast processes and dynamics of matter motivated the advancement and development of non-linear time-resolved experiments. Non-linear spectroscopy is used to investigate, processes that occur on fast time scales as short as picoseconds ( $10^{-12}$  s) to femtoseconds ( $10^{-15}$  s) [7]. To overcome the limitations of detectors such as fast photodiodes which only have temporal resolutions on the order of  $10^{-10}$  s, a fundamental approach towards time-resolved measurements was conceived through a technique called pump-probe spectroscopy [14], [15]. Our study employed a 2D-IR spectroscopic method, and the simpler pump-probe spectroscopy is first illustrated below.

#### *Pump-probe spectroscopy*

IR pump-probe spectroscopy is a third order non-linear spectroscopic method as well as an absorption difference technique [7]. It involves a pump (excitation) pulse which undergoes two interactions with the sample material followed by a probe (detection) pulse [16]. A sub-picosecond pump pulse interacts with the sample whereby a population state is created. Molecules are excited from the ground vibrational state ( $v = 0$ ) /  $|0\rangle \times |0\rangle$  to the first vibrational excited state ( $v = 1$ ) /  $|1\rangle \times |1\rangle$ . After a short waiting time,  $T_w$ , the probe then interacts with the sample. The probe interacts with either the ground  $|0\rangle \times |0\rangle$  or the  $|1\rangle \times |1\rangle$  population states following the time delay,  $T_w$ , between the pump and probe pulses. With increasing  $T_w$ , the probability of molecules relaxing back to ground state increases. A schematic of a typical pulse sequence is as shown below in (Figure 2.6) [7].

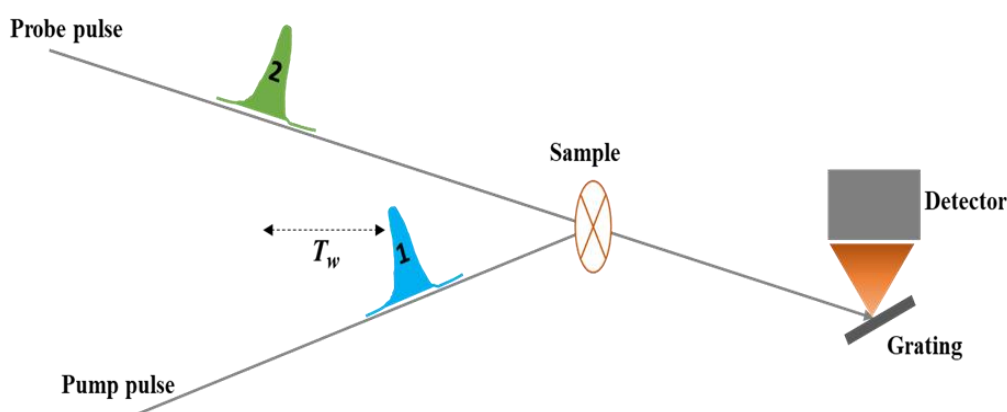


Figure 2.6 A schematic of the pump-probe spectroscopy setup showing the pulse sequence. Adapted from [4].

During experiments,  $T_w$ , can be altered and controlled to allow for measurement of vibrational lifetimes. If  $T_w = 0$ , the molecules which would have been excited by the pump pulse from the ground to the first excited state will remain in the first excited state as relaxation would not have occurred. However, if  $T_w$  is longer, then the vibrational relaxation from first excited state to ground state will be increased and the absorption difference will become smaller as  $T_w$  increases. Thus, the coherent state created by the probe pulse will depend on the relaxation which would have occurred during  $T_w$ , such that vibrational lifetimes of the vibrational transitions can be directly measured [17], [18].

Pump probe spectroscopy is an absorption difference technique. The probe pulse is measured with the pump pulse on and off by use of a chopper which chops the pump pulse at half the repetition rate of the probe pulse. As a result, the pump-probe spectrum will be the difference spectrum of the probe spectrum when the pump was on minus when the pump was off resulting in the change of absorption due to the pump. Consider vibrational energy levels in a molecule (*Figure 2.7a*). The pump pulse is incident on molecules in the ground vibrational state ( $\nu = 0$ ). When the molecules absorb the incident photons they are excited to the first vibrational excited state ( $\nu = 1$ ). As the probe pulse comes in after a short waiting time,  $T_w$ , there is reduced absorption for the  $\nu = 0 - 1$  transition as the ground would have been depopulated by the pump. The probe pulse can also excite the first excited state to cause population of the second vibrational excited state,  $\nu = 1 - 2$ . The pump-probe spectrum will show a positive peak at lower frequency resulting from the excited state absorption (ESA) from the first excited state to the second due to the probe pulse. The second peak at a slightly higher frequency will be from stimulated emission from the first excited state to the ground state. The separation of the two peaks being due to anharmonicity of the potential [7]. The pump pulse's energy, intensity, wavelength, bandwidth or polarisation can be manipulated depending on how the sample is to be excited. The changes in the optical state of the sample, such as the transmission, is measured relative to the delay time between the arrival of the pump and the probe pulses [19]. Information of the relaxation of vibrational states of the probed system is then provided [1], [2], [7], [20]–[22]. The spectrum generated from exciting and detecting a particular vibrational mode is shown in *Figure 2.7b*, where the change in absorbance is plotted against the wavenumbers/probe frequency, as is the norm in 2D-IR spectroscopy from literature.

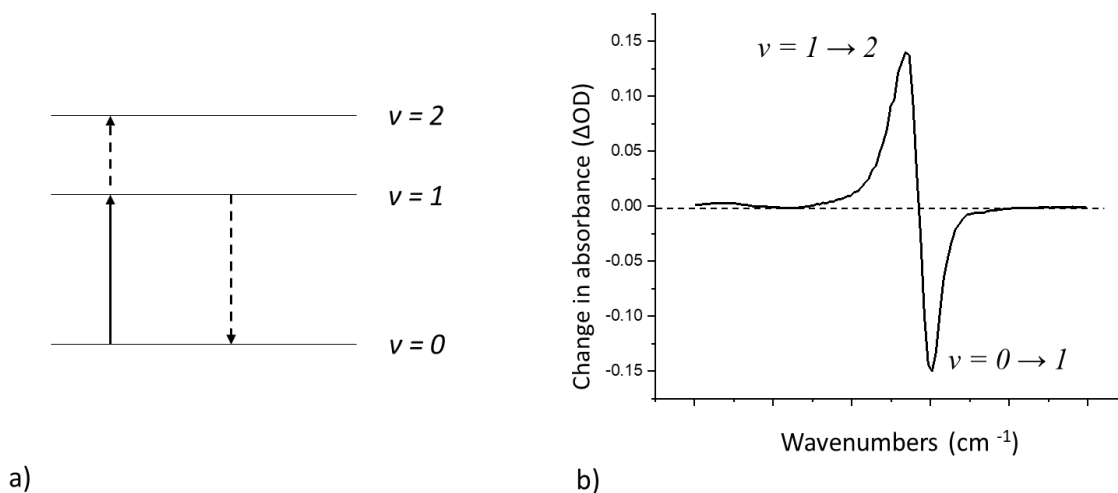


Figure 2.7 A schematic of the vibrational states in (a) considered when a particular vibrational mode is excited and detected and the resulting spectrum generated (b). In a) the bold arrow indicates transition from ground vibrational state to the first vibrational excited state. The dashed arrows indicate responses from first to second excited state absorption and the stimulated emission process from first excited state to ground vibrational excited state. Adapted from [23].

## 2D-IR spectroscopy

When atoms in a molecule change their specified positions, a chemical rearrangement takes place, which also causes a change in the vibrational structure. Such events can be probed and followed in real time. Nuclear motion takes place at timescales in the order of  $10^{-13} - 10^{-12}$  seconds and thus, studying the molecular dynamics of, for instance, biological molecules requires instrumental resolutions on the order of picoseconds or better [24], [25]. With a multidimensional non-linear spectroscopic technique there is enough sensitivity to probe structural changes and to monitor the time evolution of these changes [6].

2D-IR spectroscopy builds on pump-probe spectroscopy and utilizes three interaction pulses. With 2D-IR different contributions on vibrational couplings and relaxation dynamics can be obtained by spreading information over a second frequency axis. The pump frequency axis can be created by using either frequency domain or time domain methods. Of the two, the simpler approach is the frequency-domain approach whereby the center frequency of a narrow broadband pulse is scanned to generate the second axis. With the use of narrow broadband pulses there is increased pulse duration which then reduces the temporal resolution. To obtain more information from short-lived biological processes which occur at timescales of  $\sim 1$ ps, the methodology must have short durations and thus, the time-domain approach becomes more appropriate. This study utilized the time domain approach, which measures the third order response function of the ensemble. It is based on three laser pulses; the first two being the pump pulses which are separated by time,  $\tau$ , and the third pulse which is the

probe pulse follows after a time,  $T_w$ . The time between the probe pulse and the emitted signal after interaction is,  $t$ . The pulse sequence shall be explained based on *Figure 2.8*.

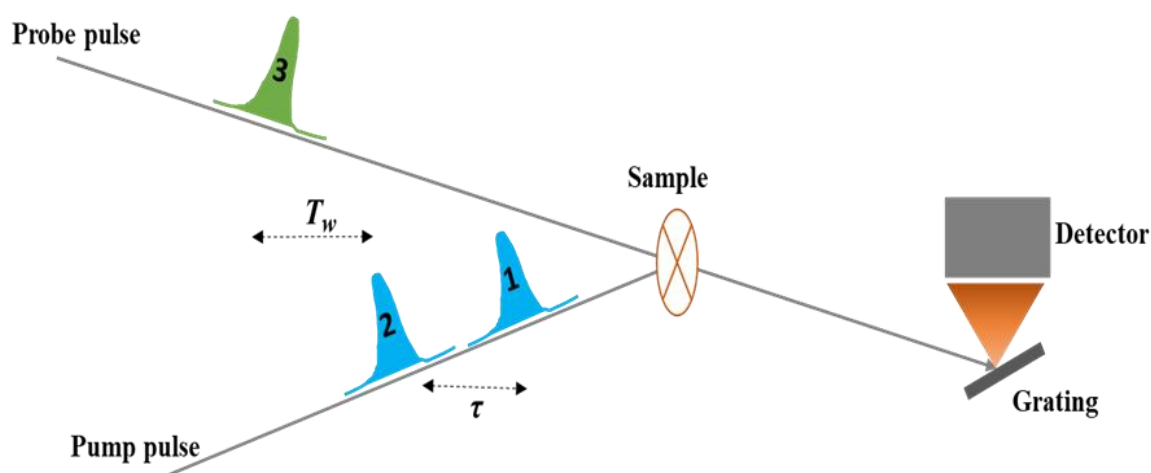


*Figure 2.8* A schematic of a 2D-IR pump-probe-probe based setup. The pump pulse first interacts with the sample and after a waiting time,  $T_w$ , two probe pulses separated by time,  $\tau$ , come in and interact with the sample. A pulse is then passed to the detector

2D-IR enables direct interrogation of chemical bonds of a sample material and how they interact with each other and with the environment, thus showing resolution high enough to provide details on the interactions of the vibrational modes [4]–[6], [26]–[28]. Initially the ensemble is in ground vibrational state. When the first pump pulse interacts with the ensemble, a coherent superposition is created between the ground and the first excited states. After this first interaction, the phase coherence is lost and the macroscopic polarization initially created with the first pump pulse will decay as a result of dephasing between the molecules. This occurs in-between the time delay,  $\tau$ , between the first and second pump pulses. The timings between the two pulses can be controlled and varied by use of a pulse shaper, which shall be explained for the 2D-IR instrument employed in this thesis.

The second pump pulse converts the coherent superposition into a population state, either of the ground or first excited state. During the time between the second pump pulse and the third probe pulse,  $T_w$ , the population state evolves due to processes such as spectral diffusion, vibrational relaxation and energy transfer between coupled modes. After  $T_w$ , the third pulse (probe) interacts with sample to induce a second superposition, restoring the macroscopic polarization of the system. This results in emission of a signal, known as the photon echo, after a time,  $t$ . This emitted signal is collinear and indistinguishable from the probe pulse, therefore it is self-heterodyned, that is, it is correctly phased across the detection axis. When the signal is dispersed on the detector array it forms

the probe axis of the 2D-IR spectrum. The excitation or pump frequency axis is as a result of Fourier transforming the signal as a function of the time delay between the two pump pulses [7], [28], [29].

### ***2D-IR spectral features***

Firstly, a 2D-IR spectrum is a correlation map with two axes for the pump (excitation) frequency and for the probe (detection) frequency. Observables from a typical 2D-IR spectrum include the pump and probe frequencies, cross-peaks, diagonal peaks, the main diagonal and 2D line-shapes. Peaks on the main diagonal are as a result of the infrared pulses interacting with the same vibrational modes, thus interrogating a single location in the structure. The main diagonal is a reflection of excitation and detection of the same frequencies. While the cross peaks which appear on opposite sides of the diagonal, are generated when IR pulses interact with vibrational modes in different locations. They appear upon excitation of a particular mode then detecting a different one due to transfer of energy or coupling of different vibration modes. These features are indicative of vibrational coupling and further details on relative orientations of the molecule can be deduced and used to elucidate the structure [4], [14], [25], [27], [30], [31]. Formation of the major peaks and other 2D-IR spectral features are conveyed in (*Figure 2.10*) which shows two coupled vibrational modes, the 2D image which they generate as well as the energy transitions which take place in the process. But first, before explaining the occurrence of cross peaks a simpler system of a single vibrational mode from an anharmonic oscillator is considered below and the key aspects of the energy transitions and the resulting spectra are shown (*Figure 2.9*).

*Figure 2.9* shows a two pulse pump-probe sequence and the energy level diagram is with reference to that of a single vibrational mode from an anharmonic oscillator [4], [6]. Upon interaction with an incident pump photon with energy enough for the ( $0 \rightarrow 1$ ) transition, the photon excites the oscillator from the ground state to the first vibrational energy level. The ground state is depopulated such that any incident probe photon of the same energy will not be absorbed, in the event that the oscillator has not decayed back to the ground state. When the probe photon is incident, the absence of an oscillator in the ground state results in a negative absorption, also known as bleaching. In addition, the excited oscillator can experience stimulated emission back to the ground state which has the same energy as bleaching for the ( $1 \rightarrow 0$ ) transition, further reducing the change in absorption of the probe pulse. Furthermore, the excited oscillator can absorb the probe photon, to be promoted to the second vibrational excited state in the ( $1 \rightarrow 2$ ) transition generating a positive peak (positive change in absorption) (*Figure 2.9*).

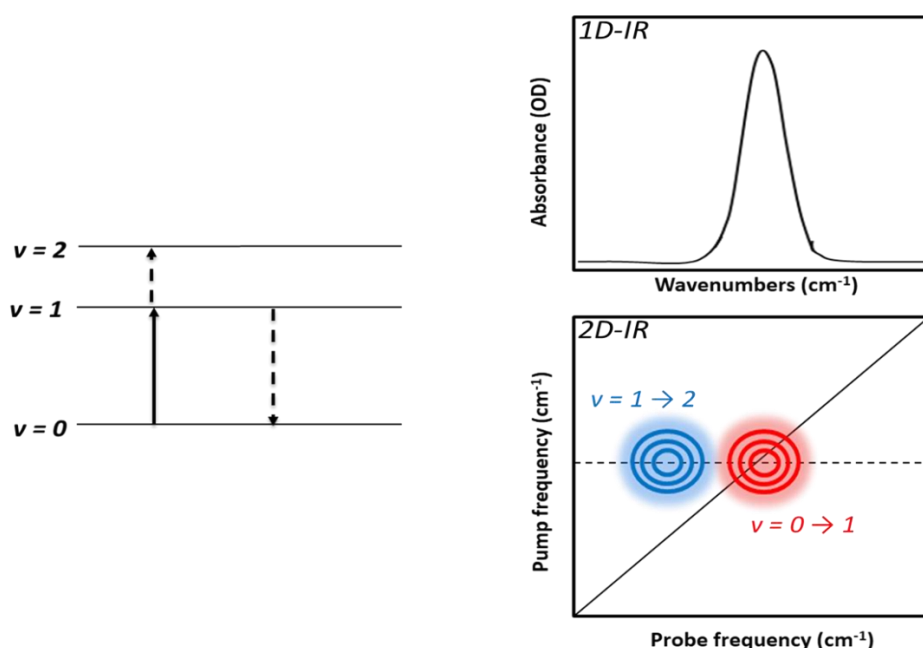


Figure 2.9 A representation for a single vibrational mode of an anharmonic oscillator. a) is the energy level diagram showing the bold arrow for excitation from ground to first vibrational energy level from the pump process. The probe process then gives responses from the dashed arrows; either cause excitation to the second vibrational excited state  $1 \rightarrow 2$  transition or bleaching  $1 \rightarrow 0$ . b) is the resulting 2D-IR spectrum showing peaks from the  $0 \rightarrow 1$  and  $1 \rightarrow 2$  transition, and corresponding FTIR spectrum. Adapted from [81].

Henceforth, consider a system of two coupled oscillators. A molecule that is vibrationally excited experiences a change in the charge distribution and this is measured using a quantity called the *transition dipole*. Consider two vibrational modes of a molecule, sufficiently close in the presence of the other's potential such that they are considered *coupled*. When coupling happens there is shifting of electronic orbitals, hence vibrational frequencies also shift. Coupling strength depends on the orientation and the separation of the oscillators [4]. In Figure 2.10 assignment of peaks is done with reference to the energy level diagram where the ground state is denoted as  $|00\rangle$ , the first excited state is denoted as  $|10\rangle$  and  $|01\rangle$  for the two modes, the second excited state is denoted as  $|20\rangle$  and  $|02\rangle$  and the combination band is between the two modes as  $|11\rangle$ .

The on-diagonal and the off-diagonal regions shall be considered in the 2D spectrum in Figure 2.10. Both the two coupled modes share a common ground state  $|00\rangle$ . The red peak on the diagonal, (1) + (2) ( $v=0 \rightarrow 1$ ), is for the ground state to the first excited state transitions while the blue peak is from the first to the second excited state transition (3) ( $v=1 \rightarrow 2$ ). The off-diagonal peaks come from exciting from the first excited state to the combination band denoted ( $|11\rangle$ ). If the same photon energy was required for the ( $0 \rightarrow 1$ ) and ( $1 \rightarrow 2$ ) transitions, then the oscillator would be said to be *harmonic*. However, this is not the case and the oscillator is *anharmonic* as more energy is required for the ( $0 \rightarrow 1$ ) transition as compared to the ( $1 \rightarrow 2$ ) transition [4], [5], [14], [18], [25], [29] (Figure 2.10).

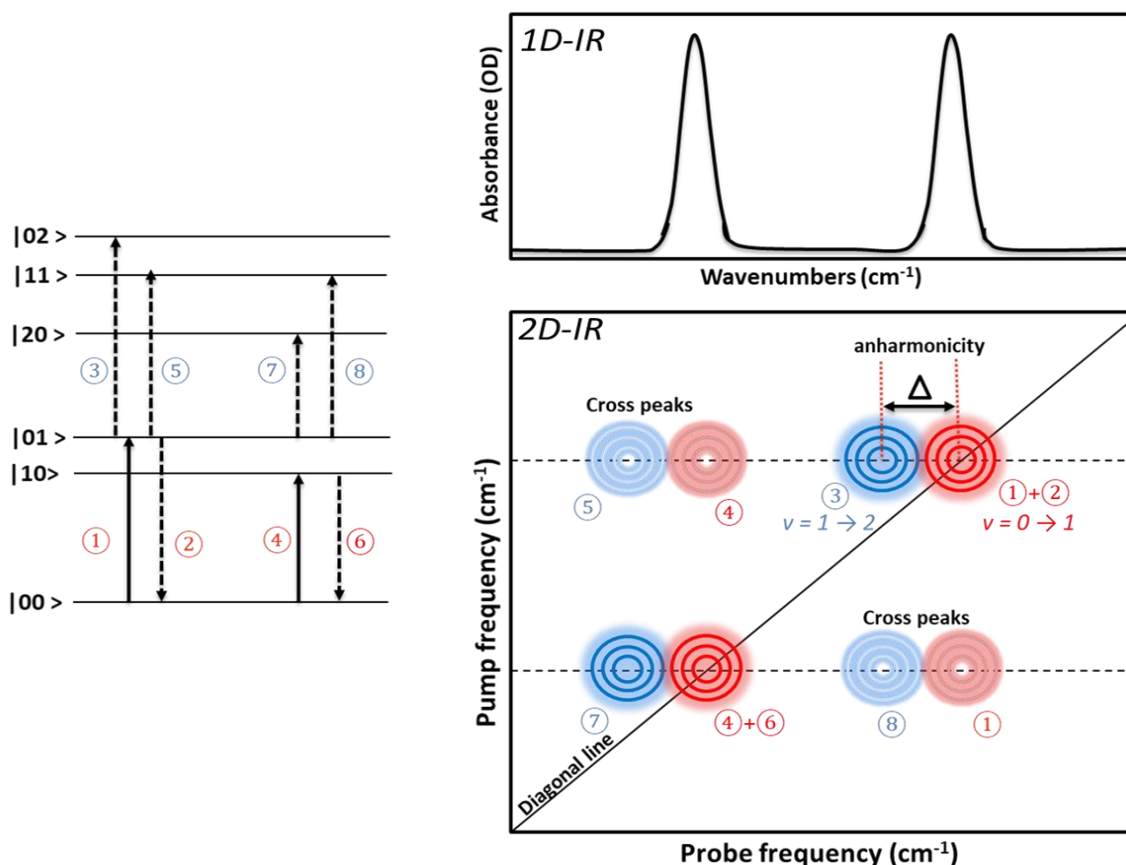


Figure 2.10. A schematic for a system of two vibrational modes showing the energy level diagram for the coupled modes and the corresponding 2D-IR spectra. Anharmonic shift (the 2 split peaks) is represented by  $\Delta$ . Cross peaks are present on either side of the main diagonal. Image adapted from [4].

In addition to the 2D features explained, 2D line-shapes also give details on the nature of the interaction between coupled vibrational modes and the solvent environment. From (Figure 2.11) the degree of ellipticity discerns information on homogenous and in-homogenous broadening. Circular vibrational line profiles are indicative on *homogenous* solute-solvent interactions but when there is *in-homogenous* broadening, the vibrational line-shapes become elongated along the diagonal, a situation which happens when the rapid fluctuations in the system causes changes in absorption transitions which are slower than the time delays. Inhomogenous broadening occurs in transitions involving hydrogen-bonded functional groups and amide I bands of proteins [4], [6], [25], [32], [33].

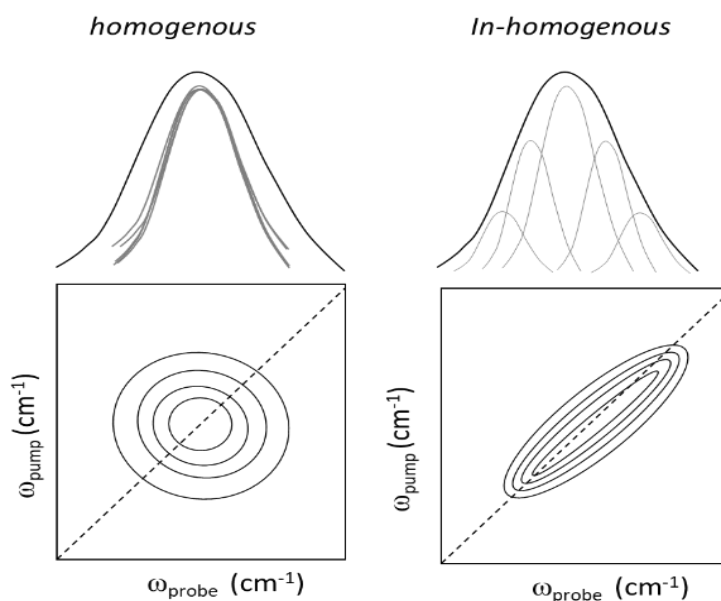


Figure 2.11 Homogenously and inhomogenously broadened vibrational line-shapes in 1D and 2D. image adapted from [4].

### 2.2.2.1 2D-IR absorption spectrometer

The lifetime instrument is housed at the Rutherford Appleton Laboratory (RAL) in Oxford, UK. The instrument is based on a pump pulse pair and a probe pulse which shall be illustrated below [34].

One oscillator feeds 2 Yb:KGW regenerative amplifiers. The amplifiers in turn seed the 2 OPAs; 1 for the pump and another for the probe beam. The instrument has a 3<sup>rd</sup> OPA which can generate a 2<sup>nd</sup> probe beam, however in this work this 2<sup>nd</sup> probe beam was not utilized [35], [36]. The probe amplifier generates pulses at a repetition rate of 100 kHz and pulse duration of 180 fs centered at 1032 nm with a total output power of 6 W. Whilst the pump pulse also generates pulses at a repetition rate of 100 kHz with a pulse duration of 260 fs and pulses centered at 1032 nm with a total output power of 15 W [35]. The pump amplifier which drives OPA1 produces pump pulsed which are tunable within the range 2100 – 13000 nm and the probe amplifier driving OPA2, and the additional OPA3, provides one or two separate probes tunable from 4000 - 13000. With two separate probe OPAs two different spectral regions can be simultaneously probed. The setup makes use of a MIR pulse shaper which results in programmable pump beam frequency such that the phase relation of the 2 pump pulse is always known [37], [38]. A single pump pulse from the OPA enters the pulse shaper, as it enters it is collimated by a mirror and proceeds to be dispersed by a grating. The light then proceeds to pass through a germanium acousto-optic modulator (AOM). The modulator is coupled to a waveform generator which is programmed such that an acoustic wave passes along the germanium crystal reshaping the incoming pump pulse to the desired output. Using the pulse shaper

enable modulation of the pump pulse which produces a pulse pair with known intensity and phase and the AOM is varied to change the timing between the pulse pair. This results in outgoing pump pulses at different time delays, ( $\tau$ ) between the 2 pump pulses. The pump pulse pair proceeds to a computer-controlled delay stage where the time separation between the pump and probe is set. The pump and probe pulses are then focused by a gold parabolic mirror onto the sample. After interacting with the sample, the pump pulse is directed and dumped on a non-reflective surface and the emitted signal proceeds to a gold parabolic mirror where it is re-collimated. The signal is then spectrally dispersed by the grating and goes to the MCT pixel detector, yielding the probe frequency axis of the 2D-IR spectra. The detector is cooled with liquid nitrogen [7], [37], [39].

This setup achieves a probe frequency spectral resolution of  $1.5 \text{ cm}^{-1}$ . The signal frequencies detected at each pixel are collected as a function of ( $\tau$ ) and Fourier transformed with respect to ( $\tau$ ) giving the pump frequency of the 2D-IR spectra. A central frequency at  $1650 \text{ cm}^{-1}$ , at 200 fs pulse duration and  $100 \text{ cm}^{-1}$  band width are used in the setup [36]. The  $\tau$  range used in the 2D-IR measurements was -0.3 – 4 ps. More details on this instrument, with regards to system setup, pulse shaping and its ability to generate high-quality data are illustrated and published by Donaldson and co-workers [26], [34], [35].

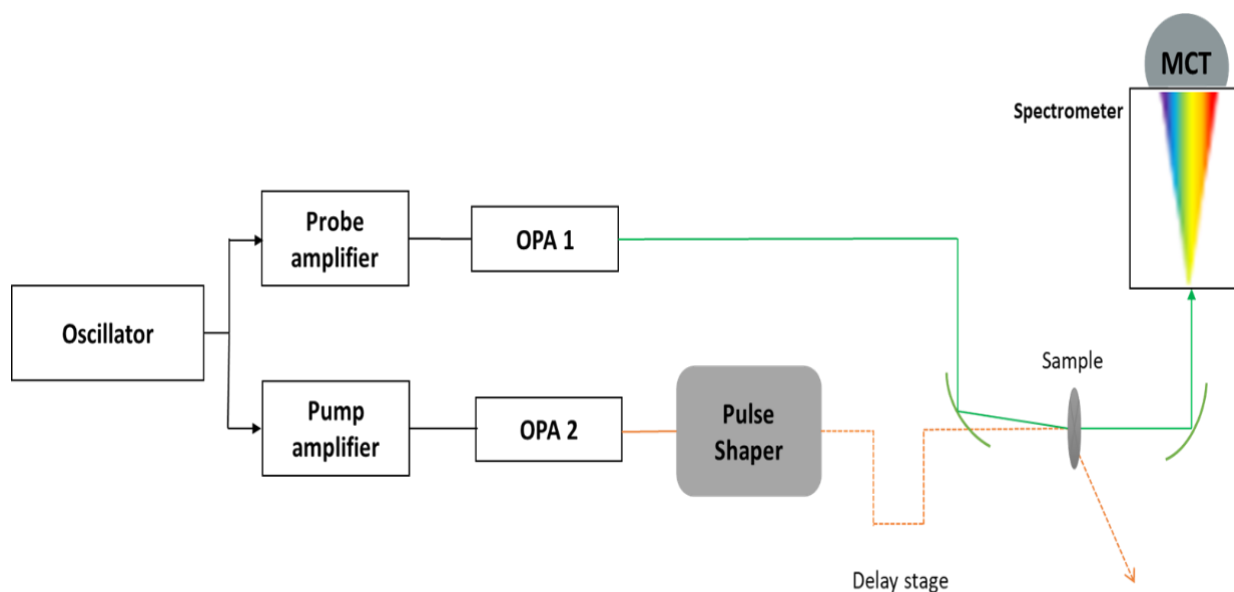


Figure 2.12 schematic of the 100 kHz Dual-amplifier laser system for time-resolved multiple-probe (IR) spectroscopy based on Ytterbium potassium gadolinium tungstate ( $\text{Yb:KGW}$ ) laser medium, and the 2D-IR spectrometer. Adapted from [35].

### 2.2.3 IR Materials and sample preparation

#### Materials

Materials used in this study were Gramicidin S (>99% purity as determined with mass spectrometry) purchased from Sigma Aldrich (St. Louis, MO, USA). Deuterium oxide ( $\geq 99\%$ ,  $\text{D}_2\text{O}$ ), 1-octanol ( $\geq$

99%, 1-octanol) and trifluoroethanol ( $\geq 99\%$ , TFE) were purchased from Sigma Aldrich (Gillingham, UK) and used without further purification.

### *Sample preparation*

In our experiments, for all 1D and 2D IR measurements a transmission cell (sample holder) was employed and assembled as shown below in *Figure 2.13*. A volume of 30  $\mu\text{l}$  of liquid sample was housed in between 2 mm thick calcium fluoride ( $\text{CaF}_2$ ) windows with a 50  $\mu\text{m}$  polytetrafluoroethylene (PTFE) / Teflon spacer and housed in a transmission cell (Harrick). The spacer provided the path length. The same sample holder was used to collect both 1D IR absorption and 2D-IR measurements which were either static or temperature controlled. For temperature-controlled measurements, an external water bath was connected to the sample holder and the water circulated around the sample compartment.

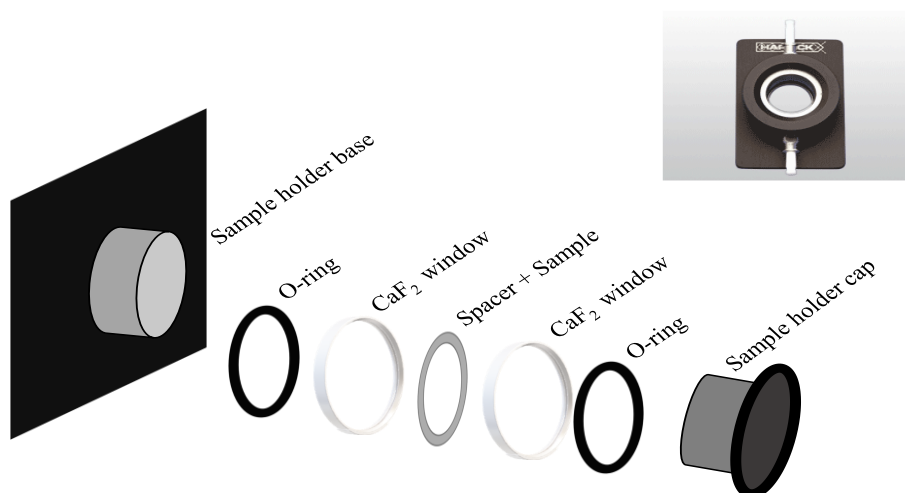


*Figure 2.13 Schematic of the components of a transmission cell used as a sample holder. The labelled parts are displayed according to how the sample holder is set up. The insert is for how the sample holder looks when assembled (Adapted from Harrick Scientific Products Inc documents) [40].*

### **2.2.4 IR Data analysis methods**

The data analysis methods which shall be implemented in this thesis and the information which they provide are discussed below.

#### *Implementation of transition dipole coupling (TDC) in determining secondary structure*

As previously discussed, that TDC is a measure of the conformational sensitivity of the amides vibrational spectrums when studying proteins and peptides [41]. The TDC contribution was considered in 2D-IR data analysis in this thesis.

The amide I of proteins has been utilised immensely in studies of protein secondary structure. Structures present which include  $\alpha$ -helices, random coils,  $\beta$ -sheets, amide groups have their characteristic absorption frequencies which differ depending on the protein or polypeptide. Some of these structures may tend to overlap or be congested, making it difficult to resolve them and make conclusive assignments. The amide I vibrational modes have strong IR transition dipole moments which are modulated by couplings. Thus, the transition dipole strength can be and has been employed as a significant quantity for assigning secondary structures [5], [42], [43]. It is strongly highlighted that in studies where assignment using vibrational frequencies were rather inconclusive the transition dipole strength can be employed [42]–[45].

Linear spectroscopies are insensitive to couplings and hence to transition dipole strength when compared to non-linear spectroscopies. Experimentally, the transition dipole cannot be extracted from either FTIR or 2D-IR alone, as, for instance, the precise protein sample concentrations are required in-order to do so [43]. In most experiments, the protein sample concentration is unknown and in some cases it fluctuates for systems with secondary structures in equilibrium [44]. Also, for 2D-IR information on beam overlaps and pump intensities would be required for accurate determination of the transition dipole [44]. Furthermore, the transition dipole cannot be determined because under the redistribution of the oscillator strength, the area under the FTIR spectra does not change for whatsoever structure is present and thus the whole spectrum cannot be deconvolved to its various contributions [42], [43]. Thus, for absorption spectroscopy, the area under the absorption spectrum is independent of the vibrational coupling because it scales as the transition dipole squared ( $|u|^2$ ) for FTIR and thus the area is conserved [42]. While for 2D-IR the transition dipole scales as ( $|u|^4$ ) and the area under the diagonal peak is not conserved. As a result, this makes non-linear spectroscopy more sensitive to the vibrational coupling changes [23], [42], [43].

As mentioned before, neither FTIR nor 2D-IR techniques are adequate on their own in determining the transition dipole strength. However, without knowledge of these details, the transition dipole can be determined by use of the amplitude ratios from 1D and 2D spectroscopy [42], [43]. Both spectroscopies scale linearly with concentration but not with transition dipole [42]. This study employs a modified approach of determining the transition dipole, implemented by Minnes *et al.* in accordance to Grechko and Zanni to ascertain the secondary structures present in a GS in different solvent environments as well as at elevated temperatures [42]–[44].

### ***Principal component analysis (PCA) and difference spectra***

Difference spectroscopy for both FTIR and 2D-IR was performed relative to the 1.00 mg/mL sample in-order to establish changes in the spectrum caused by elevated concentrations (results shown in

Chapter 3). FTIR data processing included solvent subtraction, baselining and normalising followed by obtaining the difference spectra. Similar data processing, except for smoothing, was done for 2D-IR data.

In Chapter 4, which discusses the temperature studies of GS, IR absorption spectra were analysed using difference spectroscopy and PCA after solvent subtraction, baselining and normalising the data. For 2D-IR the data was solvent subtracted and normalised. Difference spectra for both FTIR and 2D-IR were obtained by subtracting the spectrum at 20 °C (native state) from the spectrum at elevated temperatures, for all temperatures considered. This was done to obtain data of the peptide changes from its native state.

A multivariate data analysis method known as Principal Component Analysis (PCA) package from Origin 2018b was used. We applied PCA in our data analysis to extract the main spectral changes due to the conditions imposed on GS. PCA was performed on all FTIR and 2D-IR measurements, after solvent subtraction, smoothing as previously described and normalisation to the maximum intensity to eliminate minor fluctuations due to electronic noise and sample variation and in signal intensity. PCA is a dimensionality reduction method applied on large data sets for identification of corrections and patterns amongst different variables and to create low dimension data with which shows the main variations, without losing any significant information. After reduction the outcome is then represented into the main components (*Figure 2.14*).

PCA is used on spectroscopic data for qualitative analysis and reduces the data into three sets of variables; PCs, scores, loadings and residuals from random noise. For the PCs, each PC captures as much of the variation within the data as possible and this variation is removed and a new PC is determined. PC1 captures the majority of the variation in the data set, while the following PCs (PC2, PC3, ...) each consecutively capture the remaining variation of the data set which is unrelated to the previous PC. Scores are arranged as columns which show the variation represented by the principal components. Loadings illustrate the weight or importance of each variable within the original data and it is possible to see the most significant variables from loadings. Mathematically, after PCA the data is represented using *Equation 2.4*;

$$\text{Original data} = \text{Scores} \cdot \text{Loadings}^T + \text{Residuals} \quad 2.4$$

$$\text{Original data} = (\text{scores} \times \text{PC1 loading}) + \text{scores} \times \text{PC2 loading} + \dots \quad 2.5$$

Additionally, the original data can be reconstructed from the scores and loadings, using *Equation 2.5*, however, some dimensions which would have been discarded may be lost [46]–[50].

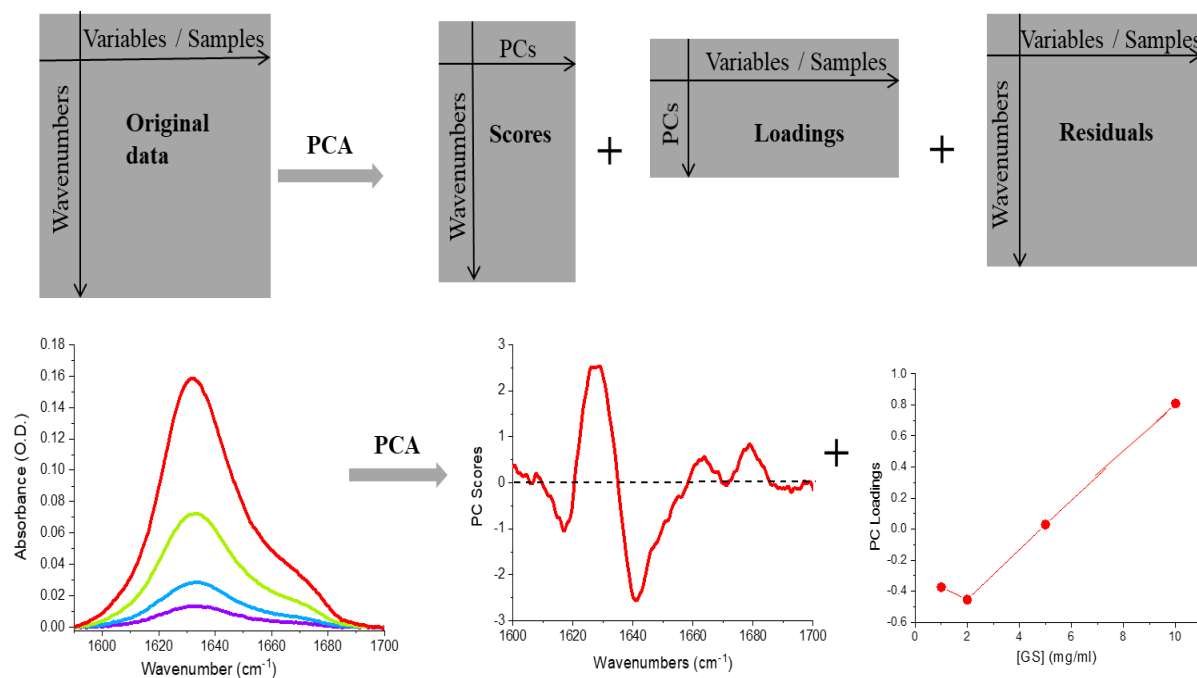


Figure 2.14 Top row images are for the PCA model transforming the original data set represented as a matrix, to the output of scores, loadings and residuals. The bottom row shows the data, scores and loadings which are represented spectroscopically, residuals are not plotted.

### FTIR data analysis from second derivative spectra

Second (2<sup>nd</sup>) derivative spectral analysis has been extensively used as a data analysis method in protein and peptide studies [8], [51]. Peaks resolved/identifiable in a second derivative spectra of FT-IR absorbance spectra can be assigned to the secondary structures in the region of amide I, II and III following reference data [52]–[55]. Significant information can be obtained on the stability and structural details of proteins and peptides in various environments by use of FTIR absorption spectra and its 2<sup>nd</sup> derivative [54].

In this study, for each IR absorption spectrum acquired for GS in a selected solvent, the spectrum of the solvent blank was subtracted so as to only consider the peptide response. The original raw FTIR spectral data is presented as is for the first FTIR results in Chapter 3. In spectra presented for global analysis the data is not smoothed but only solvent subtracted. In spectra presented for first derivative of FTIR data, data processing was done using GraphPad Prism 8 Project software. In the second derivative spectra analysis, data was also processed using GraphPad Prism 8 Project and the S/N of 2<sup>nd</sup> derivative spectra was calculated using the formula as shown below. The S/N was calculated using *Equation 2.6* below:

$$\frac{S}{N} = \frac{\frac{d^2A}{dv^2}}{SD \text{ of ave } \frac{d^2A}{dv^2} \text{ of Amide I or II range}}$$

Where  $\left(\frac{d^2A}{dv^2}\right)$  is the 2<sup>nd</sup> derivative of the normalised FTIR signal and SD the standard deviation of the average (ave) 2<sup>nd</sup> derivative signal of the Amide I range. An example of the spectra is shown in *Figure 2.15*, from the S/N spectra of the 2<sup>nd</sup> derivative *Figure 2.15a*, a noise cut off of  $\pm 2$  was considered and peaks with signal intensity above  $\pm 2$  were identified. Furthermore, from the several peaks identified, not all these peaks represented structures present in GS, but peak positions were assigned in regions where structure is expected. Important to note is that though 2D-IR analysis provides greater detail in terms of coupling, results from the FTIR 2<sup>nd</sup> derivative analysis also revealed more structural details because FTIR measurements were performed at an instrumental frequency resolution of  $0.1 \text{ cm}^{-1}$  while 2D-IR measurements were performed at a probe frequency resolution of  $1.5 \text{ cm}^{-1}$ . Results from the 2<sup>nd</sup> derivative analysis further correlated with our spectra simulations on the GS model.

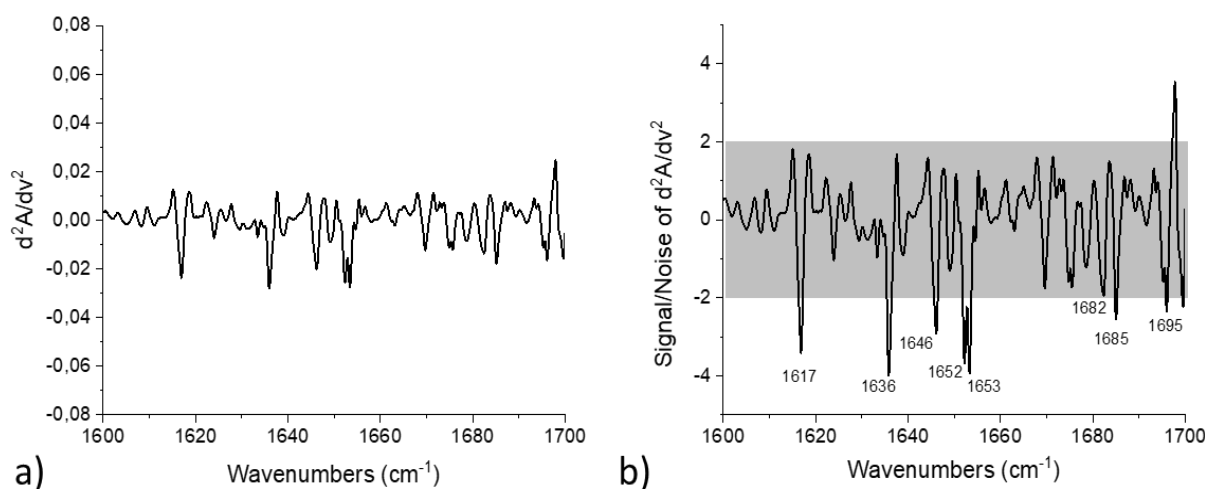


*Figure 2.15* A representation of the 2<sup>nd</sup> derivative spectra (a) and the S/N spectra (b) of GS in solvent TFE at high concentration of 10 mg/ml. In spectrum b) identified and labeled are peaks not within the cut-off signal range of  $\pm 2$  representing the structures present in GS.

## 2.2.5 Raman spectroscopy (RS)

### *Principles of the Raman scattering effect*

Several processes occur during the interaction of light with matter, and these include absorption, emission, scattering, and linear and non-linear processes, used in molecular spectroscopy [2]. For a

scattering interaction between a photon and a molecule, the oscillating electromagnetic field of the incident photon induces a polarisation on the molecule electron cloud putting the molecule in a higher energy state, thus creating a short-lived state, known as the *virtual* state, between the photon and the molecule [1] (*Figure 2.16*). Due to the instability of the virtual state the photon is almost immediately emitted. For most scattering events, the dominant process is when there is no energy transfer between the incident photon and the molecule, such that the molecule is left at the same energy level as before the interaction and the photon is scattered with the same energy as before [1]. This is referred to as elastic or *Rayleigh* scattering. When there is exchange of energy between the incident photon and the molecule, the photon is scattered at a different energy and from the incident photon. The energy difference will correspond to the transition states taken by the molecule between the vibrational energy levels and this is an inelastic scattering referred to as *Raman scattering* [1], [9], [56]–[59].

In reality only a small fraction of photons are Raman scattered, typically of the order of 1 out of  $10^6 - 10^{10}$  photons [60]. A photon with incident energy,  $E_i$ , when scattered with less energy,  $E_s$ , will have the molecule promoted from the vibrational ground state,  $\nu=0$ , to the first excited state,  $\nu=1$  of the vibrational mode with vibrational energy  $\hbar\omega_\nu = E_i - E_s$ . This is known as the *Stokes* process. In the case of a photon scattered with more energy, the molecule will transfer its energy to the photon and the molecule will be relaxed from vibrational excited state  $\nu=1$  to the ground state  $\nu=0$ , a transition of energy  $\hbar\omega_\nu = E_s - E_i$ . This is known as the anti-Stokes process. In-order for the anti-Stokes process to happen the molecule will have to already be in an excited state, which is not always the case unless through thermal excitation. Both the Stokes and anti-Stokes processes are equally likely to happen but in most cases at room temperature molecules are usually in the ground vibrational state, according to Boltzmann distribution, which implies that the Stokes process has a higher chance of occurring [1], [2], [61], [62]. Thus, Stokes signal is more intense than the anti-Stokes and that is why Stokes Raman scattering is considered [2] (*Figure 2.16*).

### ***Vibrational modes***

The energy levels in *Figure 2.16* are for a single vibrational mode present in a molecule. Thus, polyatomic molecules will have several vibrational modes and the number of vibrational modes is given by  $3N - 6$ , where  $3N$  is the total number of the degrees of freedom and we have to exclude the 3 translational and 3 rotational modes. Linear molecules have 1 less rotational degree of freedom and hence have  $3N - 5$  total vibrational modes.

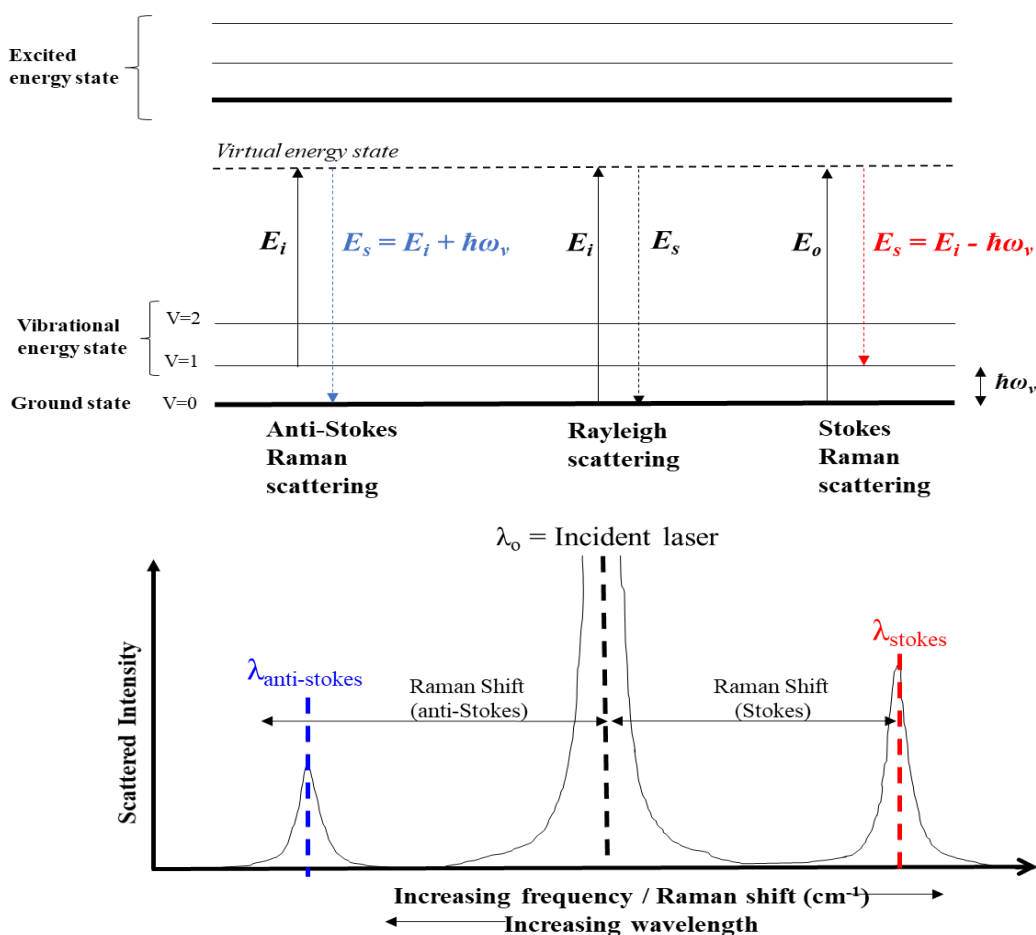


Figure 2.16 A simplified Jablonski diagram for Rayleigh, Stokes and anti-Stokes Raman scattering processes. Image adapted from [1].

### Raman selection rules

The primary selection rule states that in-order for a vibrational mode to be Raman active, there has to be a change in the molecular polarizability during the vibration [1]. Polarizability is the movement of electrons in response to an external field. In the presence of an external electric field, the positive charges of the molecule are attracted to the negative pole of the field while the negative electrons are attracted to the positive pole. This separation of charge produces an induced dipole,  $\mu$ , expressed as;  $\mu = \alpha E$ , where  $\alpha$  is the polarizability and  $E$  the electric field strength. The rule of mutual exclusion states that for molecules with centre of symmetry, no vibration is both infrared and Raman active. Symmetric vibrations with respect to the centre of symmetry are Raman active but not infrared active while anti-symmetric vibrations with respect to the centre of symmetry are infrared active but not Raman active [1], [9], [57], [63]. Of the vibrational modes illustrated in Figure 2.4, stretching vibrations are strong in Raman spectroscopy and these are shown below in Figure 2.17 for the CO<sub>2</sub> molecule. By considering the normal modes of vibration for the linear CO<sub>2</sub> molecule, the vibration that is symmetric with respect to the centre of symmetry is Raman active but not infrared active

Figure 2.17 a) [1], whereas the antisymmetric vibrations with respect to the centre of symmetry are IR active but not Raman active Figure 2.17 b) and c) [1].

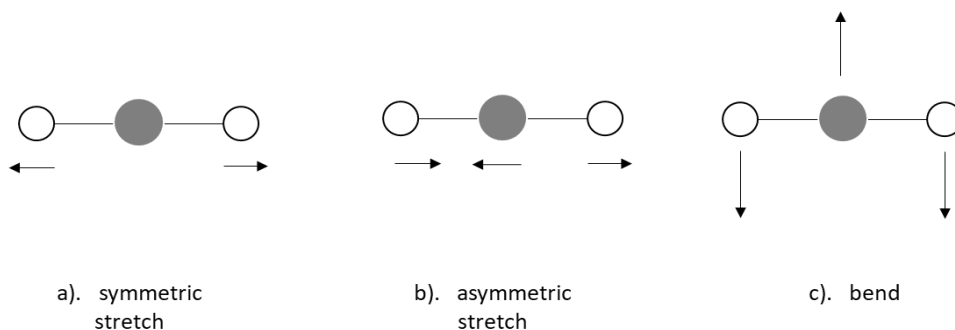


Figure 2.17 Atomic motions in normal modes of vibration in  $\text{CO}_2$  molecule. Image adapted from [1].

## 2.2.6 Surface enhanced Raman Spectroscopy (SERS)

The early reports on intense Raman scattering was through use of electrochemical systems. Fleischmann and co-workers reported on the significant enhancement of Raman signals of pyridine adsorbed at monolayer coverage on silver electrodes in comparison to pyridine liquid aqueous environment [64], [65]. Further studies by independent groups of Jeanmaire and Van Dyne [66] and Albrecht and Creighton [67] highlighted the influence of a roughened surface when they observed that the Raman scattering signal for pyridine on a silver electrode can be enhanced a million-times when the scatterer is adsorbed on or near colloidal silver and gold sols, eventually reporting it as SERS. Enhancement mechanisms were established; with Jeanmaire and Van Dyne proposing the electromagnetic (EM) effect and Albrecht and Creighton the charge transfer effect. Over the years, SERS has been used worldwide, with new applications increasing steadily year-by-year. Most recently, Wang and co-workers [68] reported for the first time on novel silver nanoparticle (AgNP) sponge-based three-dimensional (3D) platform with ultra-sensitive SERS activity towards detection of antibiotics. In this report an enormous SERS enhancement factor of  $5.30 \times 10^{10}$  was obtained for methylene blue, which was detected at a low concentration of  $10^{-14}$  M. Furthermore, application towards detection of low concentrations of antibiotic solutions of ciprofloxacin and enrofloxacin yielded limits of detections of 0.351 and 0.359 ppb respectively, and a linear relation between the signal strength and the concentration ( $R^2 = 0.9827$ ) indicated the capability of the substrate to be used for SERS quantification [68]. In another 2020 report, Gao *et al.* demonstrated that silver nanoparticles and antimicrobial peptides can be combined to create novel composite material with enhanced antibacterial, lower toxicity and increased stability. In their study, by incorporating a 13 amino acid peptide with AgNPs, minimum inhibitory concentrations of up to  $7.8 \mu\text{g/mL}$  against *E. coli* were obtained in preliminary antibacterial tests [69]. Such reports demonstrated on the

importance of incorporation of metallic substates towards detection of antimicrobials active against common bacterial strains.

### ***SERS active substrates***

The optical properties of colloids and suspensions are shape and size dependant. Nanostructures possess remarkable chemical and physical properties which are distinctly different from bulk material and this has resulted in different types of nanostructures being made, from nanoparticles, 1D, 2D and 3D nanostructures [65], [70]–[72]. It was proved that the nanoparticle sizes from 5 – 70 nm gave an appreciable SERS effect and that nanoparticles of sizes smaller than 5 nm deviated from the plasmon behaviour exhibited by larger sizes [73]. Difference in shape and size of nanoparticles brings about differences in surface polarisation. With an increase in sharp edges there will be increased charge separation which causes red-shifting of the extinction spectra [74]. Increase in symmetry of the nanoparticles also increases the localised surface plasmon resonance (LSPR) intensity [74], [75]. There are also instances where the enhancement is increased when a molecule is "trapped" in-between two or more nanoparticle junctions. Such regions are known as 'hot-spots' where there is intense electromagnetic field and the Raman signal is dramatically enhanced [76], [77]. The strong dependence of the LSPR on the shape and size of the nanoparticles has seen the use of higher order structures, in sensitive detection of bio-materials. A current issue to resolve, however, in implementation of SERS technology is reproducibility from sample-to-sample and substrate-to-substrate and this remains a limitation [74].

Metals such as silver (Ag), gold (Au), aluminium (Al) and copper (Cu) have been known to have distinct optical properties from standard dielectrics due to the presence of free conduction electrons in them [2], [78] The plasmon resonance frequencies of such metals falls in the same range as that of the visible and NIR light used for excitation. For SERS it is important for the substrate to not only be chemically inert, but biocompatible and easily accessible. The nanoparticles can either be immobilized on solid substrates or suspended in solution from synthesis via chemical reduction. The unique physical (plasmon resonance, morphology) and chemical (pH, aggregation, surface adsorption of molecules, adherence to surfaces) [79]–[82] properties of plasmonic nanoparticles employed in Surface Enhanced Raman spectroscopy (SERS) have led to their extensive applications.

There are several methods used for preparation of nanoparticles. These include laser ablation, photo-induced reduction and chemical reduction [57], [58]. The easiest and most widely used method being chemical reduction which produces different sized colloids suspended in a liquid. It is easily achieved and there are production of counter-ions during the reaction which promote stability [58]. Ideally a

metal salt is reduced by a reducing and a capping agent such as sodium borohydride [83], hydroxylamine hydrochloride [84], [85] or sodium citrate [86], [87]. By controlling factors such as the reducing agent, pH of reactants, reaction temperature and reaction time, nanoparticles of varying shapes and sizes can be synthesized [58], [74].

### ***Surface plasmon resonance***

Metallic nanoparticles can be thought of as composed of positive ions surrounded by a ‘sea of free negative electrons’ located in the conduction band. Upon interaction of the free electrons with incident photons, the electrons oscillate to generate strong electromagnetic fields to form plasmons [88]. These surface plasmons oscillate at their own resonance frequency and by so doing, it increases the electromagnetic field surrounding the nanoparticle. This collective oscillation of plasma near the surface of the metal is known as surface plasmon resonance (SPR) and when a molecule is adsorbed or in close proximity to the metallic surface, the Raman signal benefits from the increased electromagnetic field [88], [89].

### ***Enhancement mechanism***

Two enhancement mechanisms have been accepted to be responsible for the enhancement of Raman signal; a long range electromagnetic (EM) effect and a short range chemical (CM) effect, with the former being major contributor [2], [90].

During EM mechanism the electromagnetic field is amplified when the radiation field couples with the localised surface plasmons (LSP) of the metallic nanoparticles. A time-varying electric field,  $E_o$ , when incident on a metallic nanoparticle displaces the free electrons to create an oscillating dipole [59], [63]. The dipole oscillates at its own characteristic frequency. The molecule in close proximity experiences both the incident field ( $E_o$ ) and the field generated by the surface plasmon ( $E_p$ ), to have  $E_i = E_o + E_p$ . The field  $E_p$  depends on parameters which are the sphere’s radius,  $r$ ; the distance from the metal surface to the molecule,  $d$ ; the metal dielectric constant; and the incident field,  $E_o$  [59]. After interaction with the molecule, in the event of Stokes Raman scattering, the emitted Raman field,  $E_s$ , will be red-shifted with respect to the incident electric field. This field  $E_s$  can also polarise the metal nanoparticle to further be enhanced through the same mechanism giving a final field  $E_f = E_s + E_{en}$ , where  $E_n$  is the additional component of enhancement due to the elastic scattering producing further induced dipole in the molecule [59]. The enhancement of the electric field,  $E$ , is approximately proportional to  $|E^4|$  and in the order of  $10^6$ - $10^8$  [2], [90] (*Figure 2.18*).

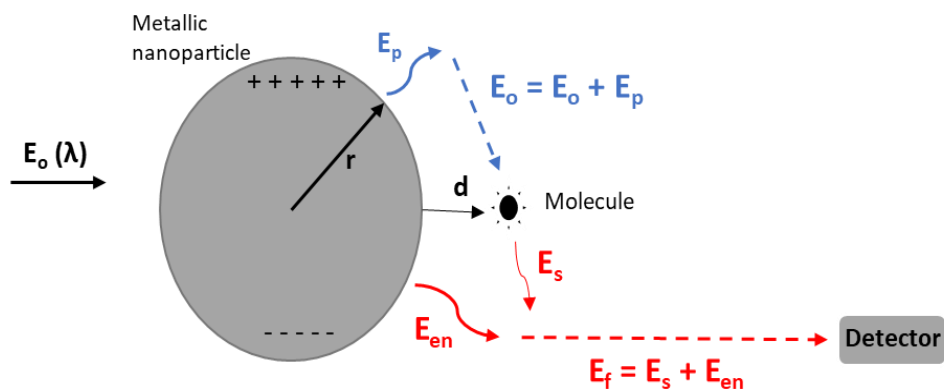


Figure 2.18 A schematic representation of the electromagnetic (EM) enhancement mechanism for SERS. In the first step a time-varying electric field  $E_o$  is incident on a metallic nanoparticle displaces the free electrons to create an oscillating dipole. The molecule experiences both the incident field and the field generated by the surface plasmon,  $E_i = E_o + E_p$ . For the second step, in the event of Stokes Raman scattering the emitted Raman field,  $E_s$ , can also polarise the metal nanoparticle to further be enhanced through the same mechanism giving a final field  $E_f = E_s + E_{en}$ . Image adapted from [59].

The chemical effect (CM) arises when there is direct contact between the molecule and the metallic surface. Chemical interaction, mainly charge transfer, occurs between the adsorbates and the metallic surface [59]. The charge transfer occurs between the electrons in the Fermi level of the metal and the unoccupied molecular orbital (LUMO) of the adsorbate and vice versa, this broadens and shifts the electronic levels in the molecule thus giving the resonance Raman effect which leads to SERS [2], [89] (Figure 2.19). Enhancement factor can be in the order of  $10^2$ - $10^3$ . Hence, CM happens on a molecular scale while EM has long range effects, while they both work to generate the SERS effect.

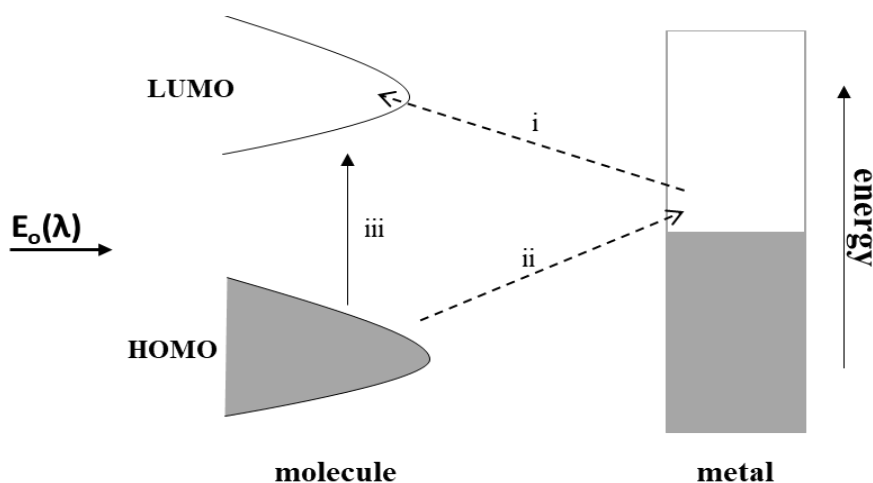


Figure 2.19 A schematic representation of the chemical (CM) enhancement mechanism for SERS. Upon adsorption, charge transfer occurs through process (i) and (ii) between the molecule and the metal. Process (iii) between the HOMO and LUMO shows the resonant Raman process. Image adapted from [59].

### ***Raman versus Infrared spectroscopy***

Raman and IR techniques provide complementary information on vibrational frequencies, however each technique has its own advantages and disadvantages. Raman selection rules require changing polarizability while IR rules require changing dipole moment. Some molecular vibrations are only Raman active while some are solely infrared active, for instance molecules with a centre of symmetry where the rule of mutual exclusion applies. In resonance Raman the excitation wavelength can be fine-tuned to match particular vibrations of particular chromophores in a molecule to give resonance enhancement. Aqueous solutions of samples in water can be measured with Raman without any major interfering bands from water, while infrared is greatly affected by the strong absorption of water. Usually, no sample preparation is required for Raman, but with infrared sample preparation can be challenging and thus, other infrared based techniques such as attenuated total reflectance Fourier transform infrared (ATR-FTIR) allow for little sample preparation [1].

Raman spectroscopy is an analytical technique used to measure the scattered light from vibrational modes of a sample to provide both chemical and structural information in addition to identifying the substance using their Raman fingerprint [76], [91]. Raman spectroscopy (RS) has been employed in wide range of applications, ranging from tissue diagnosis in biomedicine [92], characterisation and identification of materials – such as historical artefacts, paintings [93], food e.g. meat [94], [95] and milk products, bones and proteinaceous materials including amino acids, proteins and peptides [96]–[99]. When analysing protein structure in aqueous states such as dilute solutions of varying concentrations, Raman spectroscopy can have limited sensitivity. The weak Raman signal can also be explained by the low scattering cross section [10]. Hence, to improve sensitivity on molecular identification, the Raman signal can be significantly enhanced via SERS explained above [74], [100]–[102].

#### **2.2.7 RS and SERS material and sample preparation**

Gramicidin S (>99% purity as determined with mass spectrometry) was purchased from Sigma Aldrich (St. Louis, MO, USA). Silver and gold nanoparticles (100 nm diameter) at concentrations of 0.02 mg/mL and 0.03 mg/mL, respectively, with sodium citrate as stabiliser, purchased from Sigma Aldrich, UK, were used for the SERS measurements. MilliQ water was used for preparation of GS solutions. A stock solution of GS was prepared at 1 M from which lower concentrations were prepared by dilution, to have several samples. A 1 cm path length quartz cuvette was used as sample holder. For measurement of the absorption spectra of the peptide in solution with colloids, the solution was thoroughly mixed before each scan to ensure a uniform solution, as the nanoparticles will tend to settle on the bottom as aggregation progresses.

### ***Instrumentation: inVia Renishaw Raman microscope***

A Renishaw inVia Raman microscope equipped with an electrically cooled charge coupled device detector was used for normal RS and SERS measurements (Figure 2.20) [103]. The instrument consists of a monochromatic near infrared diode laser light source, operating at 830 nm (1); waveplates which control the direction of polarisation (2), a beam expander (3); a microscope with objectives (4) which can be interchanged, a 50x long working distance objective was used, and laser light of  $\sim 53$  mW is directed onto the sample (5) placed on a X-Y translation stage. Scattered light is collected via 180° backscattering geometry, via the microscope (4) to the Rayleigh and rejection filters for reduction of Rayleigh intensity and elimination of stray light (6). Light then passes through an adjustable slit to a spectrometer (7) equipped with a grating of 1200 lines/mm and an air cooled CCD detector (8). The captured spectra are processed using a personal computer.

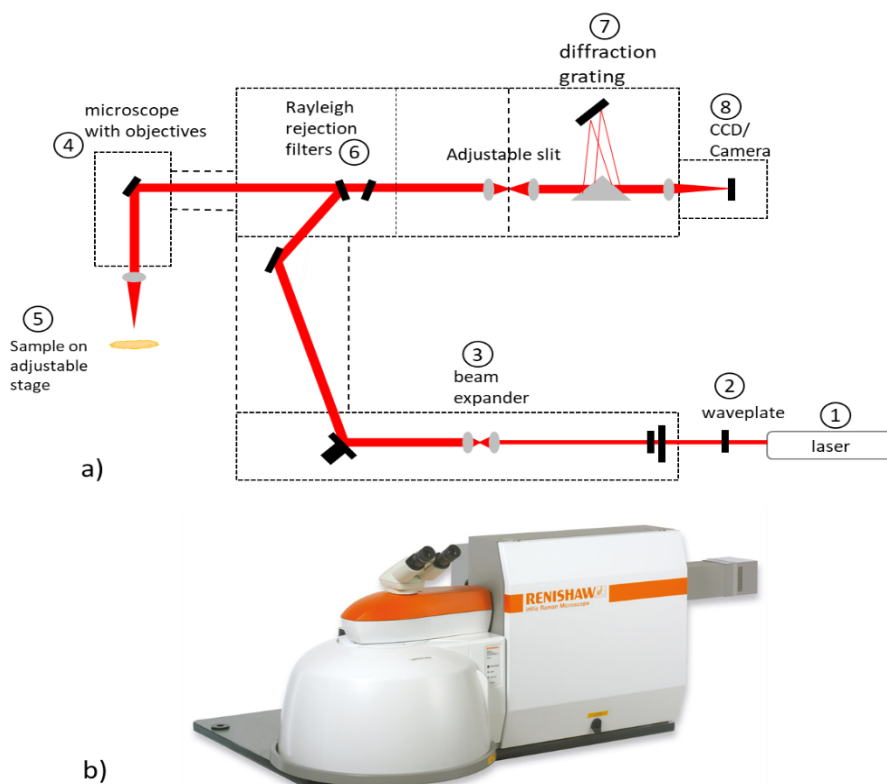


Figure 2.20 a) is a schematic of the inVia Raman microscope and b) is an image of the commercial instrument adapted from Renishaw documents and website [103].

### ***RS and SERS measurements and Data analysis***

Spectra were collected with an accumulation time of 50 s. Short scans were considered, so as not to overexpose the large size NPs, to avoid degradation by radiation exposure. Origin 2018b software was used for processing of the RS and SERS solution spectra. Baseline corrections were performed and in some cases, smoothing was applied using the Savitzky-Golay filter from Origin software to

minimise high frequency noise. Spectra presented were recorded in the range 400 – 1800  $\text{cm}^{-1}$  which consisted of significant bands of interest. Absorption spectra are presented after background correction.

## **2.3 Density Functional Theory (DFT) and Quantum Mechanical/Molecular Mechanics (QM/MM) Simulations**

Simulations were considered in this thesis in order to support and validate experimental results obtained on GS. By correlating spectral features between the simulated and measured spectra, conformational changes in GS could be confidently interpreted. Simulations enable theoretical evaluation of the peptide and structural changes occurring in the peptide under chosen condition. In this thesis two different atom selections on the GS monomer model were considered for simulating IR and RS spectra using both density functional theory (DFT) and quantum mechanical/molecular mechanics (QM/MM) (these atom selections are described in Chapter 5). On the monomer model simulations were performed to model the participation of the amino acid side chain functional groups and peptide backbones in molecular packing. Only one trimer model was considered for QM/MM simulations of IR and RS spectra. Simulations on GS have previously been done for crystalline GS [104], [104] and GS in DMSO [105]. Results from these studies shall be referred to in spectral interpretation and assignments on our IR and Raman simulations for GS in solution with water as the solvent. The models are presented and explained in greater detail in the relevant chapters. Band assignments on the simulated spectra were done based on mode observations viewed in GaussView 5. In this work;

- i). Monomer models were created from X-ray structures obtained by Prof Marina Rautenbach (SU), with reference to crystal structure reported by *Saiz et al.* [106].
- ii). From the monomer models, the dimer model was created, and from the dimer, the trimer model was created by Dr Vikus Kumar (SU).
- iii). Spectral simulations using Gaussian 09 package on the generated GS monomer and trimer models were performed by Dr Olufemi Olaoye (SU).
- iv). Band assignments of vibrational modes in the monomer and trimer model spectra was done by visually observing the structural groups and modes of vibration using GaussView 5 software and assigning to the spectral feature which the vibrating mode contributes to. Viewing the vibrating modes in GaussView 5 software enabled the assignment of the calculated peak with the contributing amino acid. This was done by Marina Rautenbach (SU), Olufemi Olaoye (SU) and Cathrine Pfukwa (SU).

### ***Docking and simulation in monomer and trimer modelling***

The monomer model was generated first and from it the dimer and trimer were generated. A computational model for the gramicidin S (GS) monomer was obtained from its crystal structure as reported by *Saiz et al.* [106], [107]. The model was optimized by molecular dynamics (MD) simulations by setting up a time step of 500 fs and steepest energy optimization using YASARA V11.2.18 software [108]. Preliminary global docking was performed to obtain a “blind” docking results of the two minimized monomers of GS to form dimers. For peptide docking, the search space was subsequently narrowed all around the atoms, and the search set to 50 docking experiments. The same monomer molecules were used either as receptor or ligand that were pre-processed by only assigning bond orders. Docking was performed *in vacuo* at 298 K to predict the possible structure of the dimer. The obtained dimers were further subjected to steepest energy optimization with YASARA2 algorithm to remove conformational stress. In the simulation process, the two GS monomer conformers were manually orientated, but then allowed to randomly interact in an *in-vacuo* simulation cell to allow for the maximum number of low energy conformers and dimer interactions [107]. To obtain trimers, different dimers with either parallel or antiparallel arrangement of monomer units were used as receptors and monomer unit as donor that were placed in a search space that was narrowed all around the atoms [107].

### ***Spectral simulation on GS models using Gaussian 09 package***

Gaussian 09 DFT package made available through the Centre for High Performance Computing in Cape Town was used for all the calculations. Density functional calculations were carried out using B3LYP energy exchange-correlation functional and a 6-31g (d, p) basis set. To account for neighbour-neighbour interactions as well as the influence of H-bonding on the eigen modes obtainable from the peptides, quantum mechanical/molecular mechanics (QM / MM) level of theory were implemented through the ONIOM framework available in Gaussian 09. Relative to the experimental spectra, the best ONIOM framework for the exchange-correlation energy/basis set was found to be B3LYP/6-31g(d,p):UFF. The structures were subjected to simultaneous optimisation of the atomic redundant coordinates and frequency calculations including both Raman and infra-red spectra. Water as a solvent was modelled through the framework of polarizable continuum model (PCM) with a dielectric constant of 78.35.

## **2.4 References**

- [1] J. R. Ferraro, K. Nakamoto, and C. W. Brown, *Introductory Raman Spectroscopy*, Second. Elsevier Science (USA), 2003.

- [2] E. C. Le Ru and P. G. Etchegoin, *Principles of Surface Enhanced Raman Spectroscopy and related plasmonic effects*, no. 1. 2009.
- [3] A. Tokmakoff, “Nonlinear Spectroscopy,” *MIT Department of Chemistry*, 2009. [http://home.uchicago.edu/~tokmakoff/NLS/Notes/11.1.-4.\\_Nonlinear\\_Spectroscopy\\_4-09.pdf](http://home.uchicago.edu/~tokmakoff/NLS/Notes/11.1.-4._Nonlinear_Spectroscopy_4-09.pdf) (accessed Nov. 09, 2020).
- [4] P. Hamm and M. T. Zanni, *Concepts and Methods of 2D Infrared Spectroscopy*. Cambridge University Press, 2011.
- [5] C. R. Baiz, M. Reppert, and A. Tokmakoff, “Introduction to Protein 2D IR Spectroscopy,” *Ultrafast Infrared Vib. Spectrosc.*, no. 22, pp. 361–404, 2012, doi: 10.1201/b13972.
- [6] N. T. Hunt, “2D-IR spectroscopy: Ultrafast insights into biomolecule structure and function,” *Chem. Soc. Rev.*, vol. 38, no. 7, pp. 1837–1848, 2009, doi: 10.1039/b819181f.
- [7] M. Z. Peter Hamm, *Concepts and Methods of 2D-IR spectroscopy*. New York: Cambridge University Press, 2012.
- [8] A. Barth, “Infrared spectroscopy of proteins,” *Biochim. Biophys. Acta - Bioenerg.*, vol. 1767, no. 9, pp. 1073–1101, 2007, doi: 10.1016/j.bbabi.2007.06.004.
- [9] E. C. Le Ru and P. G. Etchegoin, *Principles of Surface Enhanced Raman Spectroscopy*. Elsevier, 2009.
- [10] E. C. Le Ru, M. Meyer, and P. G. Etchegoin, “Surface Enhanced Raman Scattering Enhancement Factors: A Comprehensive Study,” *J. Phys. Chem. C*, vol. 111, no. 37, pp. 13794–13803, 2007, doi: 10.1021/jp0687908.
- [11] D. Kowolik, K. (University of California, “Normal modes.” [http://chemwiki.ucdavis.edu/Physical\\_Chemistry/Spectroscopy/Vibrational\\_Spectroscopy/Vibrational\\_Modes/Normal\\_Modes](http://chemwiki.ucdavis.edu/Physical_Chemistry/Spectroscopy/Vibrational_Spectroscopy/Vibrational_Modes/Normal_Modes) (accessed Jun. 30, 2014).
- [12] H. Yu *et al.*, “Impact of ultraviolet radiation on the aging properties of SBS-modified asphalt binders,” *Polymers (Basel)*, vol. 11, no. 7, 2019, doi: 10.3390/polym11071111.
- [13] A. Jabs, “Determination of Secondary Structure in Proteins by Fourier Transform Infrared Spectroscopy (FTIR).” [http://jenalib.leibniz-fli.de/ImgLibDoc/ftir/IMAGE\\_FTIR.html](http://jenalib.leibniz-fli.de/ImgLibDoc/ftir/IMAGE_FTIR.html) (accessed Dec. 07, 2016).
- [14] N. T. Hunt, “Transient 2D-IR spectroscopy of inorganic excited states,” *Dalt. Trans.*, vol. 43,

no. 47, pp. 17578–17589, 2014, doi: 10.1039/c4dt01410c.

- [15] S. Woutersen, Y. Mu, G. Stock, and P. Hamm, “Hydrogen-Bond Lifetime Measured by Time-Resolved 2D-IR Spectroscopy: N-Methylacetamide in Methanol,” Accessed: Jul. 10, 2017. [Online]. Available: [https://www.researchgate.net/profile/Sander\\_Woutersen/publication/222660066\\_Hydrogen-bond\\_lifetime\\_measured\\_by\\_time-resolved\\_2D-IR\\_spectroscopy\\_N-methylacetamide\\_in\\_methanol/links/02e7e51f67fbca8ead000000/Hydrogen-bond-lifetime-measured-by-time-resolved-2D-IR-spectroscopy-N-methylacetamide-in-methanol.pdf](https://www.researchgate.net/profile/Sander_Woutersen/publication/222660066_Hydrogen-bond_lifetime_measured_by_time-resolved_2D-IR_spectroscopy_N-methylacetamide_in_methanol/links/02e7e51f67fbca8ead000000/Hydrogen-bond-lifetime-measured-by-time-resolved-2D-IR-spectroscopy-N-methylacetamide-in-methanol.pdf).
- [16] A. Ghosh, J. S. Ostrander, and M. T. Zanni, “Watching Proteins Wiggle: Mapping Structures with Two-Dimensional Infrared Spectroscopy,” *Chem. Rev.*, vol. 117, no. 16, pp. 10726–10759, 2017, doi: 10.1021/acs.chemrev.6b00582.
- [17] P. Hamm, “Principles of Nonlinear Optical Spectroscopy : A Practical Approach or : Mukamel for Dummies,” *Univ. Zurich*, vol. 41, no. 5, p. 77, 2005, Accessed: Jun. 07, 2021. [Online]. Available: <http://www.mitr.p.lodz.pl/evu/lectures/Hamm.pdf>.
- [18] M. Khalil, N. Demirdöven, and A. Tokmakoff, “Vibrational coherence transfer characterized with Fourier-transform 2D IR spectroscopy,” *J. Chem. Phys.*, vol. 121, no. 1, pp. 362–373, 2004, doi: 10.1063/1.1756870.
- [19] V. A. Lorenz-Fonfria, “Infrared Difference Spectroscopy of Proteins: From Bands to Bonds,” *Chem. Rev.*, vol. 120, no. 7, pp. 3466–3576, 2020, doi: 10.1021/acs.chemrev.9b00449.
- [20] C. Dorow, “An Introduction to the Technique and Applications of Pump-Probe Spectroscopy,” *Physics (College. Park. Md).*, pp. 1–7.
- [21] A. Barth and C. Zscherp, “What vibrations tell us about proteins.,” *Q. Rev. Biophys.*, vol. 35, no. 4, pp. 369–430, 2002, doi: 10.1017/S0033583502003815.
- [22] A. Hofmann, “12 Spectroscopic techniques : I Spectrophotometric techniques,” in *Principles and techniques of biochemistry and molecular biology*, 2010, pp. 477–521.
- [23] P. Hamm and M. Zanni, *Concepts and Methods of 2D Infrared Spectroscopy*. Cambridge University Press, 2011, 2011.
- [24] F. Remeacle and R. D. Levine, “An electronic time scale in chemistry,” *Proc. Natl. Acad. Sci. U. S. A.*, vol. 103, no. 18, pp. 6793–6798, May 2006, doi: 10.1073/pnas.0601855103.

- [25] M. Khalil, “A Tale of Coupled Vibrations in Solution Told by Coherent Two-Dimensional Infrared Spectroscopy,” *Thesis*, pp. 1–147, 2003, [Online]. Available: [papers://70e99c22-152e-47e4-8805-4dbdb6c09369/Paper/p5666](https://papers://70e99c22-152e-47e4-8805-4dbdb6c09369/Paper/p5666).
- [26] G. M. Greetham, D. Sole, I. P. Clark, A. W. Parker, M. R. Pollard, and M. Towrie, “Time-resolved multiple probe spectroscopy,” *Rev. Sci. Instrum.*, vol. 83, no. 10, 2012, doi: 10.1063/1.4758999.
- [27] Z. Ganim, S. C. Hoi, A. W. Smith, L. P. Deflores, K. C. Jones, and A. Tokmakoff, “Amide I Two-Dimensional Infrared Spectroscopy of Proteins,” *Acc. Chem. Res.*, vol. 41, no. 3, pp. 432–441, 2008, doi: 10.1021/ar700188n.
- [28] P. Hamm, M. Lim, and R. M. Hochstrasser, “Structure of the amide I band of peptides measured by femtosecond nonlinear-infrared spectroscopy,” *J. Phys. Chem. B*, vol. 102, no. 31, pp. 6123–6138, 1998, doi: 10.1021/jp9813286.
- [29] P. Hamm, J. Helbing, and J. Bredenbeck, “Two-dimensional infrared spectroscopy of photoswitchable peptides,” *Phys. Chem.*, vol. 59, pp. 291–317, 2008.
- [30] G. Duxbury, “Concepts and Methods of 2D Infrared Spectroscopy, by Peter Hamm and Martin Zanni,” *Contemp. Phys.*, vol. 52, no. 6, pp. 636–636, 2011, doi: 10.1080/00107514.2011.610521.
- [31] M. T. Zanni, N.-H. Ge, Y. S. Kim, and R. M. Hochstrasser, “Two-dimensional IR spectroscopy can be designed to eliminate the diagonal peaks and expose only the crosspeaks needed for structure determination,” *Proc. Natl. Acad. Sci.*, vol. 98, no. 20, pp. 11265–11270, 2001, doi: 10.1073/pnas.201412998.
- [32] E. E. Fenn and M. D. Fayer, “Extracting 2D IR frequency-frequency correlation functions from two component systems,” *J. Chem. Phys.*, vol. 135, no. 7, p. 74502, 2011, doi: 10.1063/1.3625278.
- [33] A. Huerta-Viga, “Coupled Vibrations in Peptides and Proteins: Structural information using 2D-IR spectroscopy,” University of Amsterdam, 2014.
- [34] G. M. Greetham *et al.*, “A 100 kHz time-resolved multiple-probe femtosecond to second infrared absorption spectrometer,” *Appl. Spectrosc.*, vol. 70, no. 4, pp. 645–653, 2016, doi: 10.1177/0003702816631302.
- [35] P. M. Donaldson, G. M. Greetham, D. J. Shaw, A. W. Parker, and M. Towrie, “A 100 kHz

- Pulse Shaping 2D-IR Spectrometer Based on Dual Yb:KGW Amplifiers,” *J. Phys. Chem. A*, vol. 122, no. 3, pp. 780–787, 2018, doi: 10.1021/acs.jpca.7b10259.
- [36] G. Hithell *et al.*, “Long-range vibrational dynamics are directed by Watson-Crick base pairing in duplex DNA,” *J. Phys. Chem. B*, vol. 120, no. 17, pp. 4009–4018, May 2016, doi: 10.1021/acs.jpcc.6b02112.
- [37] S. H. Shim, D. B. Strasfeld, Y. L. Ling, and M. T. Zanni, “Automated 2D IR spectroscopy using mid-IR pulse shaping and applications to membrane peptides,” *Opt. InfoBase Conf. Pap.*, vol. 104, no. 36, pp. 14197–14202, 2007, doi: 10.1364/ls.2007.lwg2.
- [38] S.-H. Shim, D. B. Strasfeld, E. C. Fulmer, and M. T. Zanni, “Femtosecond pulse shaping directly in the mid-IR using acousto-optic modulation,” *Opt. Lett.*, vol. 31, no. 6, p. 838, Mar. 2006, doi: 10.1364/ol.31.000838.
- [39] S. H. Shim and M. T. Zanni, “How to turn your pump-probe instrument into a multidimensional spectrometer: 2D IR and Vis spectroscopies via pulse shaping,” *Phys. Chem. Chem. Phys.*, vol. 11, no. 5, pp. 748–761, 2009, doi: 10.1039/b813817f.
- [40] “Demountable Liquid Cells | Harrick Scientific Products Inc.” <https://www.harricksci.com/ftir/accessories/group/Demountable-Liquid-Cells> (accessed Sep. 08, 2020).
- [41] J. Kubelka, J. Kim, P. Bour, and T. A. Keiderling, “Contribution of transition dipole coupling to amide coupling in IR spectra of peptide secondary structures,” *Vib. Spectrosc.*, vol. 42, no. 1, pp. 63–73, 2006, doi: 10.1016/j.vibspec.2006.04.003.
- [42] M. Grechko and M. T. Zanni, “Quantification of transition dipole strengths using 1D and 2D spectroscopy for the identification of molecular structures via exciton delocalization: Application to  $\alpha$ -helices,” *J. Chem. Phys.*, vol. 137, no. 18, p. 184202, 2012, doi: 10.1063/1.4764861.
- [43] E. B. Dunkelberger, M. Grechko, and M. T. Zanni, “Transition Dipoles from 1D and 2D Infrared Spectroscopy Help Reveal the Secondary Structures of Proteins: Application to Amyloids,” *J. Phys. Chem. B*, vol. 119, no. 44, pp. 14065–14075, 2015, doi: 10.1021/acs.jpcc.5b07706.
- [44] L. Minnes *et al.*, “Quantifying Secondary Structure Changes in Calmodulin Using 2D-IR Spectroscopy,” *Anal. Chem.*, vol. 89, no. 20, pp. 10898–10906, 2017, doi:

10.1021/acs.analchem.7b02610.

- [45] S. Krimm and J. Bandekdar, "Vibrational analysis of peptides, polypeptides and proteins," *Int. J. Pept. Protein Res.*, vol. 19, pp. 1–29, 1980, doi: 10.1002/bip.1980.360190102.
- [46] D. Brodnjak Voncina, "Chemometrics in analytical chemistry," *TrAC Trends Anal. Chem.*, vol. 15, no. 10, pp. 211–216, 1996, doi: 10.1016/s0165-9936(96)90027-8.
- [47] G. B. Jung, S. W. Nam, S. Choi, G. Lee, and H. Park, "Evaluation of antibiotic effects on *Pseudomonas aeruginosa* biofilm using Raman spectroscopy and multivariate analysis.," *Biomed. Opt. Express*, vol. 5, no. 9, pp. 3238–51, 2014, doi: 10.1364/BOE.5.003238.
- [48] T. Liu, "Statistical Learning for Sample-Limited High-dimensional Problems with Application to Biomedical Data," 2013.
- [49] R. Bro and A. K. Smilde, "Principal component analysis," doi: 10.1039/c3ay41907j.
- [50] K. Varmuza, "Chemometrics in Practical Applications," in *Chemometrics in Practical Applications*, vol. 9, InTech, 2012, pp. 3-.
- [51] J. Li, X. Cheng, and J. C. Lee, "Structure and dynamics of the modular halves of *Escherichia coli* cyclic AMP receptor protein," *Biochemistry*, vol. 41, no. 50, pp. 14771–14778, 2002, doi: 10.1021/bi026383q.
- [52] F. Piccirilli, G. Schirò, V. Vetri, S. Lupi, A. Perucchi, and V. Militello, "Decoding vibrational states of Concanavalin A amyloid fibrils," *Biophys. Chem.*, vol. 199, pp. 17–24, 2015, doi: 10.1016/j.bpc.2015.02.007.
- [53] J. Kong and S. Yu, "Fourier transform infrared spectroscopic analysis of protein secondary structures," *Acta Biochim. Biophys. Sin. (Shanghai)*, vol. 39, no. 8, pp. 549–559, 2007, doi: 10.1111/j.1745-7270.2007.00320.x.
- [54] A. Adochitei and G. Drochioiu, "Rapid characterization of peptide secondary structure by FT-IR spectroscopy," *Rev. Roum. Chim.*, vol. 56, no. 8, pp. 783–791, 2011.
- [55] M. Miyazawa and M. Sonoyama, "Second derivative near infrared studies on the structural characterisation of proteins," *J. Near Infrared Spectrosc.*, vol. 6, no. 1–4, pp. 253–257, 1998, doi: 10.1255/jnirs.204.
- [56] BWTEKInc, "Theory of Raman Scattering," *Raman Spectroscopy*, 2015. <http://bwtek.com/raman-theory-of-raman-scattering/>.

- [57] S. Schlücker, “Surface-enhanced raman spectroscopy: Concepts and chemical applications,” *Angew. Chemie - Int. Ed.*, vol. 53, no. 19, pp. 4756–4795, 2014, doi: 10.1002/anie.201205748.
- [58] S. Schlucker, *Surface Enhanced Raman Spectroscopy Application: Biophysical and life Science Application*. WILEY-VCH Verlag GmbH, 2011.
- [59] S. Siddhanta and C. Narayana, “Surface Enhanced Raman Spectroscopy of Proteins: Implications for Drug Designing,” *Nanomater. Nanotechnol.*, vol. 2, no. 1, pp. 1–13, 2012.
- [60] K. C. Bantz *et al.*, “Recent Progress in SERS Biosensing,” *Phys. Chem. Chem. Phys.*, vol. 13, no. 24, pp. 11551–11567, 2011, doi: 10.1016/j.micinf.2011.07.011.Innate.
- [61] P. N. Bourassa, “Book Reviews: Course Notes on the Interpretation of Infrared and Raman Spectra,” *Appl. Spectrosc.*, vol. 58, no. 11, pp. 323A-323A, 2004, doi: 10.1366/0003702042475583.
- [62] J. Siu, W. Mak, and H. P. C. Fiber, “Raman Characterization of Colloidal Nanoparticles using Hollow-Core Photonic Crystal Fibers by Raman Characterization of Colloidal Nanoparticles using,” 2011.
- [63] E. Smith and G. Dent, *Modern Raman Spectroscopy: A Practical Approach*. John Wiley & Sons, Ltd, 2005.
- [64] M. Fleischmann, P. J. Hendra, and a J. McQuillan, “Raman spectra of pyridine adsorbed at a silver electrode,” *Chem. Phys. Lett.*, vol. 26, no. 2, pp. 163–166, 1974, doi: 10.1016/0009-2614(74)85388-1.
- [65] X. Chen, C. Jiang, and S. Yu, “Nanostructured materials for applications in surface-enhanced Raman scattering,” *CrystEngComm*, vol. 16, pp. 9959–9973, 2014, doi: 10.1039/C4CE01383B.
- [66] D. L. Jeanmaire and R. P. Van Duyne, “Surface raman spectroelectrochemistry,” *Journal of Electroanalytical Chemistry and Interfacial Electrochemistry*, vol. 84, no. 1, pp. 1–20, 1977, doi: 10.1016/S0022-0728(77)80224-6.
- [67] J. A. Creighton, C. G. Blatchford, and M. G. Albrecht, “Plasma Resonance Enhancement of Raman Scattering by Pyridine Adsorbed on Silver or Gold Sol Particles of Size Comparable to the Excitation Wavelength,” *Mol. Chem. Phys.*, vol. 75, no. 0, pp. 790–798, 1979.
- [68] K. Wang, Y. Meng, X. Jiao, W. Huang, D. Fan, and T. C. yi Liu, “Facile Synthesis of an

Economic 3D Surface-Enhanced Raman Scattering Platform for Ultrasensitive Detection of Antibiotics,” *Food Anal. Methods*, 2020, doi: 10.1007/s12161-020-01815-2.

- [69] J. Gao *et al.*, “One step synthesis of antimicrobial peptide protected silver nanoparticles: The core-shell mutual enhancement of antibacterial activity,” *Colloids Surfaces B Biointerfaces*, vol. 186, no. 110704, 2020, doi: 10.1016/j.colsurfb.2019.110704.
- [70] T. a. El-Brolossy *et al.*, “Shape and size dependence of the surface plasmon resonance of gold nanoparticles studied by Photoacoustic technique,” *Eur. Phys. J. Spec. Top.*, vol. 153, no. 1, pp. 361–364, 2008, doi: 10.1140/epjst/e2008-00462-0.
- [71] R. Gref *et al.*, “‘Stealth’ corona-core nanoparticles surface modified by polyethylene glycol (PEG): Influences of the corona (PEG chain length and surface density) and of the core composition on phagocytic uptake and plasma protein adsorption,” *Colloids Surfaces B Biointerfaces*, vol. 18, no. 3–4, pp. 301–313, 2000, doi: 10.1016/S0927-7765(99)00156-3.
- [72] K. Lee and M. a El-sayed, “Gold and Silver Nanoparticles in Sensing and Imaging : Sensitivity of Plasmon Response to Size , Shape , and Metal Composition Gold and Silver Nanoparticles in Sensing and Imaging : Sensitivity of Plasmon Response to Size , Shape , and Metal Composition,” *J. Phys. Chem. B*, pp. 19220–19225, 2006, doi: 10.1021/jp062536y.
- [73] J. Zhang, X. Li, X. Sun, and Y. Li, “Surface enhanced Raman scattering effects of silver colloids with different shapes,” *J. Phys. Chem. B*, vol. 109, no. 25, pp. 12544–12548, 2005, doi: 10.1021/jp050471d.
- [74] E. Petryayeva and U. J. Krull, “Localized surface plasmon resonance : Nanostructures , bioassays and biosensing — A review,” *Anal. Chem.*, vol. 706, no. 1, pp. 8–24, 2011, doi: 10.1016/j.aca.2011.08.020.
- [75] K. Ismail, “Fabrication and characterisation of SERS substrates through photo-deposition of Gold Nanoparticles,” 2015.
- [76] R. Pilot, R. Signorini, C. Durante, L. Orian, M. Bhamidipati, and L. Fabris, “A review on surface-enhanced Raman scattering,” *Biosensors*, vol. 9, no. 2, 2019, doi: 10.3390/bios9020057.
- [77] P. Alonso-González *et al.*, “Resolving the electromagnetic mechanism of surface-enhanced light scattering at single hot spots,” *Nat. Commun.*, vol. 3, no. 684, 2012.
- [78] X. F. Zhang, Z. G. Liu, W. Shen, and S. Gurunathan, “Silver nanoparticles: Synthesis,

- characterization, properties, applications, and therapeutic approaches,” *Int. J. Mol. Sci.*, vol. 17, no. 9, 2016, doi: 10.3390/ijms17091534.
- [79] A. Albanese, P. S. Tang, and W. C. W. Chan, “The effect of nanoparticle size, shape, and surface chemistry on biological systems,” *Annual Review of Biomedical Engineering*, vol. 14, no. 1, pp. 1–16, 2012, doi: 10.1146/annurev-bioeng-071811-150124.
- [80] M. V. Cañamares, J. V. Garcia-Ramos, J. D. Gómez-Varga, C. Domingo, and S. Sanchez-Cortes, “Comparative study of the morphology, aggregation, adherence to glass, and surface-enhanced Raman scattering activity of silver nanoparticles prepared by chemical reduction of Ag<sup>+</sup> using citrate and hydroxylamine,” *Langmuir*, vol. 21, no. 18, pp. 8546–8553, 2005, doi: 10.1021/la050030l.
- [81] R. A. Sperling and W. J. Parak, “Surface modification, functionalization and bioconjugation of colloidal inorganic nanoparticles,” *Philos. Trans. A. Math. Phys. Eng. Sci.*, vol. 368, no. 1915, pp. 1333–1383, 2010, doi: 10.1098/rsta.2009.0273.
- [82] K. B. Mogensen and K. Kneipp, “Size-dependent shifts of plasmon resonance in silver nanoparticle films using controlled dissolution: Monitoring the onset of surface screening effects,” *J. Phys. Chem. C*, vol. 118, no. 48, pp. 28075–28083, 2014, doi: 10.1021/jp505632n.
- [83] B. D. Howes, S. Scatragli, M. P. Marzocchi, and G. Smulevich, “Surface-enhanced resonance Raman spectroscopy of rifamycins on silver nanoparticles: Insight into their adsorption mechanisms,” *J. Raman Spectrosc.*, vol. 37, no. 9, pp. 900–909, 2006, doi: 10.1002/jrs.1519.
- [84] M. V. Cañamares, J. V. Garcia-Ramos, S. Sanchez-Cortes, M. Castillejo, and M. Oujja, “Comparative SERS effectiveness of silver nanoparticles prepared by different methods: A study of the enhancement factor and the interfacial properties,” *J. Colloid Interface Sci.*, vol. 326, no. 1, pp. 103–109, 2008, doi: 10.1016/j.jcis.2008.06.052.
- [85] N. Leopold and B. Lendl, “A New Method for Fast Preparation of Highly Surface-Enhanced Raman Scattering (SERS) Active Silver Colloids at Room Temperature by Reduction of Silver Nitrate with Hydroxylamine Hydrochloride,” *J. Phys. Chem. B*, vol. 107, no. 24, pp. 5723–5727, 2003, doi: 10.1021/jp027460u.
- [86] X. Li, J. J. Lenhart, and H. W. Walker, “Aggregation kinetics and dissolution of coated silver nanoparticles,” *Langmuir*, vol. 28, no. 2, pp. 1095–1104, 2012, doi: 10.1021/la202328n.
- [87] P. C. Lee and D. Meisel, “Adsorption and surface-enhanced Raman of dyes on silver and gold

- sols,” *J. Phys. Chem.*, vol. 86, no. 17, pp. 3391–3395, 1982, doi: 10.1021/j100214a025.
- [88] J. L. Hammond, N. Bhalla, S. D. Rafiee, and P. Estrela, “Localized Surface Plasmon Resonance as a Biosensing Platform for Developing Countries,” *Biosensors*, vol. 4, pp. 172–188, 2014, doi: 10.3390/bios4020172.
- [89] M. K. Hossain and Y. Ozaki, “Surface-enhanced Raman scattering: Facts and inline trends,” *Raman Spectrosc.*, vol. 97, no. 2, pp. 192–201, 2009.
- [90] D. A. Long, *The Raman effect: a unified treatment of the theory of Raman scattering by molecules*. 2002, vol. 8. 2002.
- [91] A. C. S. Talari, Z. Movasaghi, S. Rehman, and I. U. Rehman, “Raman spectroscopy of biological tissues,” *Appl. Spectrosc. Rev.*, vol. 50, no. 1, pp. 46–111, 2015, doi: 10.1080/05704928.2014.923902.
- [92] P. Naglic, “Raman spectroscopy for medical diagnostics,” University of Ljubljana, 2012.
- [93] A. Nevin, I. Osticioli, D. Anglos, A. Burnstock, S. Cather, and E. Castellucci, “Raman Spectra of Proteinaceous Materials Used in Paintings : A Multivariate Analytical Approach for Classification and Identification,” *Anal. Chem.*, vol. 79, no. 16, pp. 6143–6151, 2007.
- [94] K. Sowoidnich and H. D. Kronfeldt, “Shifted excitation Raman difference spectroscopy at multiple wavelengths for in-situ meat species differentiation,” *Appl. Phys. B Lasers Opt.*, vol. 108, no. 4, pp. 975–982, 2012, doi: 10.1007/s00340-012-5160-0.
- [95] K. Sowoidnich, H. Schmidt, H. D. Kronfeldt, and F. Schwägele, “A portable 671 nm Raman sensor system for rapid meat spoilage identification,” *Vib. Spectrosc.*, vol. 62, pp. 70–76, 2012, doi: 10.1016/j.vibspec.2012.04.002.
- [96] A. Rygula, K. Majzner, K. M. Marzec, A. Kaczor, M. Pilarczyk, and M. Baranska, “Raman spectroscopy of proteins: A review,” *J. Raman Spectrosc.*, vol. 44, no. 8, pp. 1061–1076, 2013, doi: 10.1002/jrs.4335.
- [97] E. López-Tobar *et al.*, “Anchoring sites of fibrillogenic peptide hormone somatostatin-14 on plasmonic nanoparticles,” *J. Phys. Chem. C*, vol. 119, no. 15, pp. 8273–8279, 2015, doi: 10.1021/acs.jpcc.5b00485.
- [98] B. Hernández *et al.*, “From bulk to plasmonic nanoparticle surface: behavior of two potent therapeutic peptides, octreotide and pasireotide,” *Phys. Chem. Chem. Phys.*, no. 1, pp. 24437–

24450, 2016, doi: 10.1039/C6CP04421B.

- [99] E. López-Tobar *et al.*, “Large size citrate-reduced gold colloids appear as optimal SERS substrates for cationic peptides,” *J. Raman Spectrosc.*, vol. 48, no. 1, pp. 30–37, 2017, doi: 10.1002/jrs.4976.
- [100] A. Sileikaite, I. Prosycevas, J. Puiso, A. Juraitis, and A. Guobiene, “Analysis of Silver Nanoparticles Produced by Chemical Reduction of Silver Salt Solution,” *Mater. Sci.*, vol. 12, no. 4, pp. 287–291, 2006, doi: 10.1002/jid.
- [101] S. L. Kleinman *et al.*, “Structure enhancement factor relationships in single gold nanoantennas by surface-enhanced raman excitation spectroscopy,” *J. Am. Chem. Soc.*, vol. 135, no. 1, pp. 301–308, 2013, doi: 10.1021/ja309300d.
- [102] C. L. Haynes, A. D. Mcfarland, and R. P. Van Duyne, “Surface-enhanced Raman spectroscopy,” *Anal. Chem.*, vol. 77, no. 17, pp. 338-A-346-A, 2005.
- [103] Renishaw, “inVia confocal Raman microscope Renishaw.” <https://resources.renishaw.com/download.aspx?lang=en&data=110298&btn=1> (accessed Aug. 24, 2020).
- [104] V. M. Naik, S. Krimm, J. B. Denton, G. Nemethy, and H. A. Scheraga, “Vibrational analysis of peptides, polypeptides and proteins: XXVII. Structure of gramicidin S from normal mode analyses of low-energy conformations,” *Int. J. Pept. Protein Res.*, vol. 24, no. 6, pp. 613–626, 1984, doi: 10.1111/j.1399-3011.1984.tb03168.x.
- [105] A. W. Smith and A. Tokmakoff, “Amide I two-dimensional infrared spectroscopy of  $\beta$ -hairpin peptides,” *J. Chem. Phys.*, vol. 126, no. 4, 2007, doi: 10.1063/1.2428300.
- [106] A. L. Llamas-Saiz, G. M. Grotenbreg, M. Overhand, and M. J. Van Raaij, “Double-stranded helical twisted  $\beta$ -sheet channels in crystals of gramicidin S grown in the presence of trifluoroacetic and hydrochloric acids,” *Acta Crystallogr. Sect. D Biol. Crystallogr.*, vol. 63, no. 3, pp. 401–407, 2007, doi: 10.1107/S0907444906056435.
- [107] M. Rautenbach, V. Kumar, J. A. Vosloo, Y. Masoudi, R. J. van Wyk, and M. A. Stander, “Oligomerisation of tryptocidine C, a Trp-rich cyclodecapeptide from the antimicrobial tyrothricin complex,” *Biochimie*, vol. 181, pp. 123–133, 2021, doi: 10.1016/j.biochi.2020.12.006.
- [108] E. Krieger, G. Koraimann, and G. Vriend, “Increasing the precision of comparative models

with YASARA NOVA - A self-parameterizing force field,” *Proteins Struct. Funct. Genet.*,  
vol. 47, no. 3, pp. 393–402, May 2002, doi: 10.1002/prot.10104.

## Chapter 3 Solvent effects on the structure of Gramicidin S

### 3.1 Introduction

The design and development of antimicrobial peptides (AMPs) that are less susceptible to resistance compared to conventional drugs is an ongoing concern, with the main focus being on structure and function [1], [2]. Antimicrobial activity has mostly been explained through membrane disruption leading to cell death [3], [4] via unique modes of action [1], [5], [6]. In understanding the structure-function relationships of AMPs, there are properties of individual peptides that have been found to be influential on the peptide activity and include charge, hydrophobicity, amphipathicity as well as intermolecular interactions between the AMPs [4]. Intermolecular interaction between peptides can also influence their activity. While some peptides are effective in monomeric structure [7], [8], for other peptides oligomerization or aggregation is suspected to be important in the membrane disruption process of target cells [3], [9]–[11]. For many of the AMPs, the activity against a target cell membrane depends on the concentration of the AMP because the AMPs interact and self-associate at optimum concentration to form pores on the target cell membrane [12]. The interaction of AMPs with phospholipid membranes has been studied using various biophysical techniques [6], [9], [13]–[24], however, the study of peptide self-association in solution environments which are representative of membrane environment is not well represented [25] and is significant as it paves the initial stages in understanding peptide behaviour and intermolecular interactions which modulate AMP activity. This chapter shall investigate the self-association behaviour of gramicidin S (GS) in selected solution environments representative of membrane environments.

GS was chosen for this study utilising advanced IR techniques since it is a known prototype cyclic peptide used in studying molecular complexity and behaviour of amphipathic peptides in different solvents with a variety of biophysical methods. [17]. The goal of the work presented is to demonstrate how 2D-IR can be utilised to identify solvent and environmental changes in GS structure. More detailed information regarding the flexibility of GS in solution and how it changes conformation and/or oligomerisation state can be monitored by use of different solvents and/or by temperature probing, in particular by focusing on the amide I region ( $1600\text{--}1700\text{ cm}^{-1}$ ) and part of the amide II region ( $1500\text{--}1600\text{ cm}^{-1}$ ). In the pursuit of furthering the understanding of GS behaviour using this powerful and novel technique, we selected to study GS in solution phase using both water and solvents that emulate lipid membranes (a target of GS) and stabilise hydrogen bonded networks. This study shall consider behaviour of GS in solution and its conformational changes in selected solvents utilising FTIR and 2D-IR measurements. Results will demonstrate how 2D-IR can be utilised to identify solvent and environmental changes in GS structure by utilising the sensitivity of the amide I

band on the anti-parallel  $\beta$ -sheet(s) to solvent perturbation effects. In the following study (reported in Chapter 4) temperature dependent studies will demonstrate how the 2D-IR spectral signature, with a focus on Amide I mode are perturbed at elevated temperatures.

With 2D-IR being a powerful technique, results obtained seek to provide insight on structural stability, peptide-peptide and peptide-solvent interaction, and H-bond present in the system using GS as a model compound.

### 3.2 Sample preparations and measurements

GS solutions at concentrations of 1.00, 2.00, 5.00 and 10.0 mg/mL ( $8.76 \times 10^{-4}$ ,  $1.75 \times 10^{-3}$ ,  $4.38 \times 10^{-3}$ ,  $8.76 \times 10^{-3}$  mol/L, respectively) were analytically prepared in each solvent (TFE, D<sub>2</sub>O and 1-octanol) in a transmission cell. 2D-IR spectra were collected in steps of 0.1 ps between 0.4 – 3 ps. An FTIR spectrum of each sample was acquired before and after a 2D-IR measurement to ensure / check that no physical changes occurred on the prepared sample. Each spectrum that is presented is the average of 10 scans. All measurements were done at ambient temperature.

### 3.3 Results

For the FTIR and 2D-IR studies of GS the solvent systems and concentration ranges have been carefully selected to either lead to aggregates or micellar structures, ordered hydrogen bonded networks or mimic membrane associated monomeric or dimeric structures. A well-studied fluoro-alcohol, trifluoroethanol, TFE, known as membrane mimicking solvent and hydrogen bond stabiliser, was chosen to assess the hydrogen bonded networks. TFE has been widely used as it is known to enhance the secondary structure formation in small peptides [26] and in some cases TFE stabilises the structure [27]. As aqueous solvent, deuterated water (D<sub>2</sub>O) is used as a solvent instead of H<sub>2</sub>O because the latter absorbs in the region  $1600 - 1700 \text{ cm}^{-1}$  used for amide I secondary structure studies. Aqueous solvents will lead to hydrophobic clustering and aggregation at high concentrations of amphipathic molecules such as GS. Lastly, 1-octanol was selected as an amphipathic alcohol to complement the amphipathic structure of GS, as well as to emulate a membrane environment. Most solution studies of GS in TFE, D<sub>2</sub>O and 1-octanol have been based on CD spectroscopy [28]–[32]. One study of GS with D<sub>2</sub>O was done using FTIR, with the GS prepared either from acidic aqueous solutions or organic solvents such as methanol [33].

### 3.3.1 FTIR Absorption Spectroscopy

In our global analysis we considered the amide I absorption ( $1600 - 1700 \text{ cm}^{-1}$ ) of peptide bonds and amino groups. In this range we expect C=O stretching in  $\beta$ -sheets and  $\beta$ -turns, and C-C stretching of the aromatic ring of Phe [34]–[36].

For better detectivity and to obtain significant counts in 2D-IR, a concentration range from 1.00 – 10.0 mg/mL was considered. Therefore, FTIR spectra were measured at four GS concentrations, 1.00, 2.00, 5.00 and 10.0 mg/mL, at ambient temperature in  $\text{D}_2\text{O}$ , 1-octanol and TFE. When the total amide I IR absorption over the concentration range is considered good linear trends were found for all three solvent systems (*Figure 3.1*). A linear dependence of absorption on peptide concentration implies the presence of single species in the aqueous environment [30]. This confirmed that the GS remained in solution and that the IR detector was not saturated. There was however a slight deviation from linearity for GS in  $\text{D}_2\text{O}$  ( $R^2 = 0.98$ ) which could indicate a solubility issue or signal changes due to aggregation. 1-octanol and  $\text{D}_2\text{O}$  showed almost an identical increase in signal over the concentration range and similar response factors (linear slopes). TFE had a considerably higher total absorption and higher response factor. This indicates that GS have more structural elements in TFE with amide I absorption and that these elements could be increasing more with increase in concentration than the elements in water and 1-octanol.

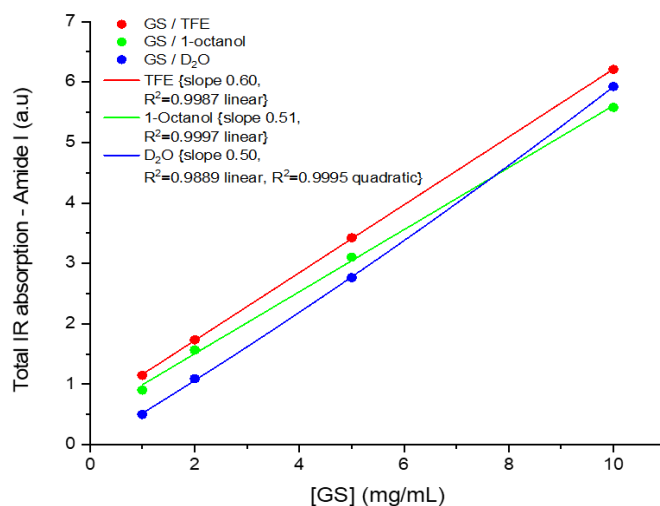


*Figure 3.1 Total Amide I IR absorption trends for concentrations 1.00, 2.00, 5.00 and 10.0 mg/mL for GS in  $\text{D}_2\text{O}$ , 1-octanol and TFE.*

The GS structures in TFE has a higher absorption and a higher response factor (linear slope) of 0.60 versus that of GS in  $\text{D}_2\text{O}$  at 0.50 and GS 1-octanol at a slightly higher 0.51. This strongly indicates that more ordered GS structures are present in TFE, even at the low concentrations as TFE supports

ordered structure [27]. As concentration increases the probability of aggregation of GS is likely to increase, but at what concentration this happens is unknown. When increasing peptide concentration in the solvent environment, there will be fewer solvent molecules available per peptide molecule. There is therefore less competition for interactions, such as hydrogen bonds (H-bond) which could promote interactions in and between peptide molecules. The solvent concentration is lower when there is a higher peptide concentration leading to more chances of peptide molecules to have collisions which have positive interactions at higher concentration.

More detailed analysis of the global IR spectra revealed interesting aspects of the prominent structures of GS in the different solvents. For each of the GS solutions the position of the global peak absorption maximum was deduced utilising first derivative spectra (*Figure 3.2, Table 3.1*). There is a clear difference in IR amide I absorption peak shape, maximum and total amide I absorption for GS in the three solvents. D<sub>2</sub>O peak maximum remains at  $1633\pm 0.5\text{ cm}^{-1}$  for all the concentrations while octanol peak maximum is blue shifted to  $1647\text{-}1649\text{ cm}^{-1}$  with decreasing GS concentration. The IR amide I absorption of GS in TFE encompasses both that in D<sub>2</sub>O and 1-octanol giving it a broad peak with two maxima of which one is more pronounced at  $1640\text{-}1643\text{ cm}^{-1}$  with increasing GS concentration. TFE supports hydrogen-bonded (H-bonded) structures of both the peptide backbone and the side chains [26], [37], [38]. Ordered H-bonded GS structures in TFE possibly encompasses both structure subsets found in D<sub>2</sub>O and 1-octanol and could explain the broad GS peak maxima in TFE (*Figure 3.2*).

With increase in concentration, there is shift to lower frequency of peaks from  $1649\text{ cm}^{-1}$  (1.00 mg/mL) to  $1647\text{ cm}^{-1}$  (10.0 mg/mL) for GS in 1-octanol, but a shift to higher frequency for TFE  $1640\text{ cm}^{-1}$  (1.00 mg/mL) to  $1643\text{ cm}^{-1}$  (10.0 mg/mL) (refer to *Table 3.1*). No change was observed for D<sub>2</sub>O ( $1633\text{ cm}^{-1}$  in both 1.00 mg/mL and 10.0 mg/mL). However, a blue-shifted shoulder developed in all three solvents with increase in concentration. This could indicate the formation of higher order structures. The shoulder is more pronounced in TFE which could indicate higher order hydrogen bonded structures, as TFE is known to stabilise such structures in proteins [37], [38].

*Table 3.1 Global analysis of the peak maxima of the amide I FTIR spectra of GS at different concentrations in three solvents of different polarity.*

Solvent	Dielectric constant	Peak Maximum ( $\text{cm}^{-1}$ )			
		1 mg/mL	2 mg/mL	5 mg/mL	10 mg/mL
D <sub>2</sub> O	78.28	1633	1633	1633	1633
1-Octanol	10.30	1649	1645	1647	1647
TFE	8.55	1640	1640	1642	1643

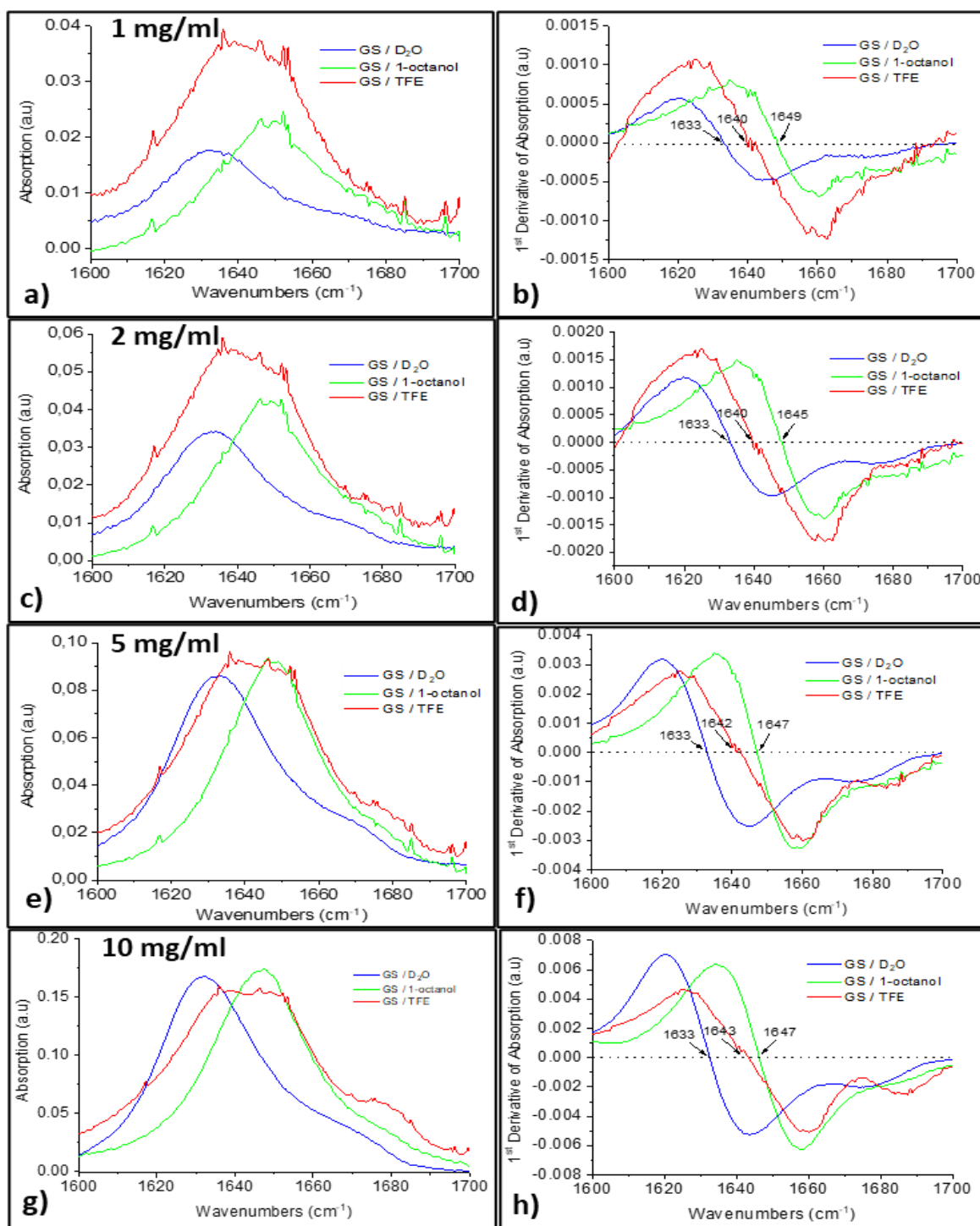


Figure 3.2 FTIR spectra for concentrations 1.00, 2.00, 5.00 and 10.0 mg/mL for GS in D<sub>2</sub>O, 1-octanol and TFE. The graphs (a, c, e, g) depicts the original FTIR spectra (solvent subtracted) for comparison between solvents. The graphs (b, d, f, h) is the 1<sup>st</sup> derivative spectra to determine the peak maximum for each GS concentration and solvent system.

At low GS concentration, the absorption by GS in D<sub>2</sub>O is much lower than that on both 1-octanol and TFE (Figure 3.2a). This implies less freedom for the vibrations of the amide groups / structures present in D<sub>2</sub>O, either due to quenching because of interaction with D<sub>2</sub>O such that the vibrations may be constrained/limited due to aggregation or a much lower concentration of certain structures exists.

With increasing concentration, the GS in D<sub>2</sub>O peak maxima at 5.00 and 10.0 mg/mL increases suggesting presence of ordered structures and a possible rearrangement of groups (*Figure 3.2e* and *g*). This subset of GS structures in D<sub>2</sub>O approaches the absorption of possibly similar structures in TFE. As there is a higher density of peptide molecules and less competition from water molecules, there could be more ordered interactions. At 1.00 mg/mL the peak maxima of GS in 1-octanol is higher than the peak maxima of GS in D<sub>2</sub>O and at 10.0 mg/mL the intensity of the peak maxima for GS in 1-octanol also increases to higher than that of GS in D<sub>2</sub>O and in TFE. At around 5.00 mg/mL for GS in 1-octanol, the subset of absorbing GS structures increases in absorption compared to that observed in TFE (*Figure 3.2e*).

Overall, it can be deduced that a certain subset of the GS structures dominate in an aqueous (D<sub>2</sub>O) environment, while another subset of structures dominate in an 1-octanol environment. It is possible that both these subsets exist in TFE and that the vibrational character of these GS structures are the two extremes observed in TFE, which both increase with increasing concentration.

For further analyses of the solvents and GS concentration only the maxima were considered in order to ascertain any peak shifts (correlating with structural changes) and intensity changes at different concentrations and in different solvents. The comparative absorption spectra in *Figure 3.3* show increase in peptide concentration correlates with increase in absorption intensity over the whole spectrum, which was shown in *Figure 3.2* above. This is observed for all three solvents however, the increase is not equal at all wavenumbers. This indicates that structures related to oligomers are forming at higher GS concentrations.

From *Figure 3.3*, the normalised and the difference spectra of GS in D<sub>2</sub>O show loss of structure from 1600 – 1625 cm<sup>-1</sup>, as well as a loss from 1635 – 1700 cm<sup>-1</sup>. There is gain in structure from 1625 – 1635 cm<sup>-1</sup> related to in  $\beta$ -sheet structures. No peak shift is identified from the normalised spectra, but there is narrowing of peaks with increasing concentration. Normalised spectra for GS in 1-octanol showed a clear peak shift to lower wavenumbers with an increase in concentration, as previously noted (refer to *Table 3.1*), as well as narrowing of peaks with increasing concentration. The peak shift suggests formation of more dominant structures in the solvent environment as peptide concentration increases and thus the new emerging structure will vibrate at a different frequency [30]. There is a loss in structure at 1645 – 1700 cm<sup>-1</sup>. There is increase in intensity at 1635 – 1645 cm<sup>-1</sup> which indicates a gain in  $\beta$ -sheet content.

The normalised spectra for GS in TFE resembled contributions which we observed in both D<sub>2</sub>O and 1-octanol. Increase in structure is present at higher wavenumbers 1645 – 1660 cm<sup>-1</sup> and a major

increase close to  $1680\text{ cm}^{-1}$ , regions where vibrations related to  $\beta$ -sheet and  $\beta$ -turns are expected. These structures are already present even at 1.00 and 2.00 mg/mL, supporting the hypothesis that H-bonded structures are already present in TFE, even at low concentrations, as TFE supports H-bond [38].

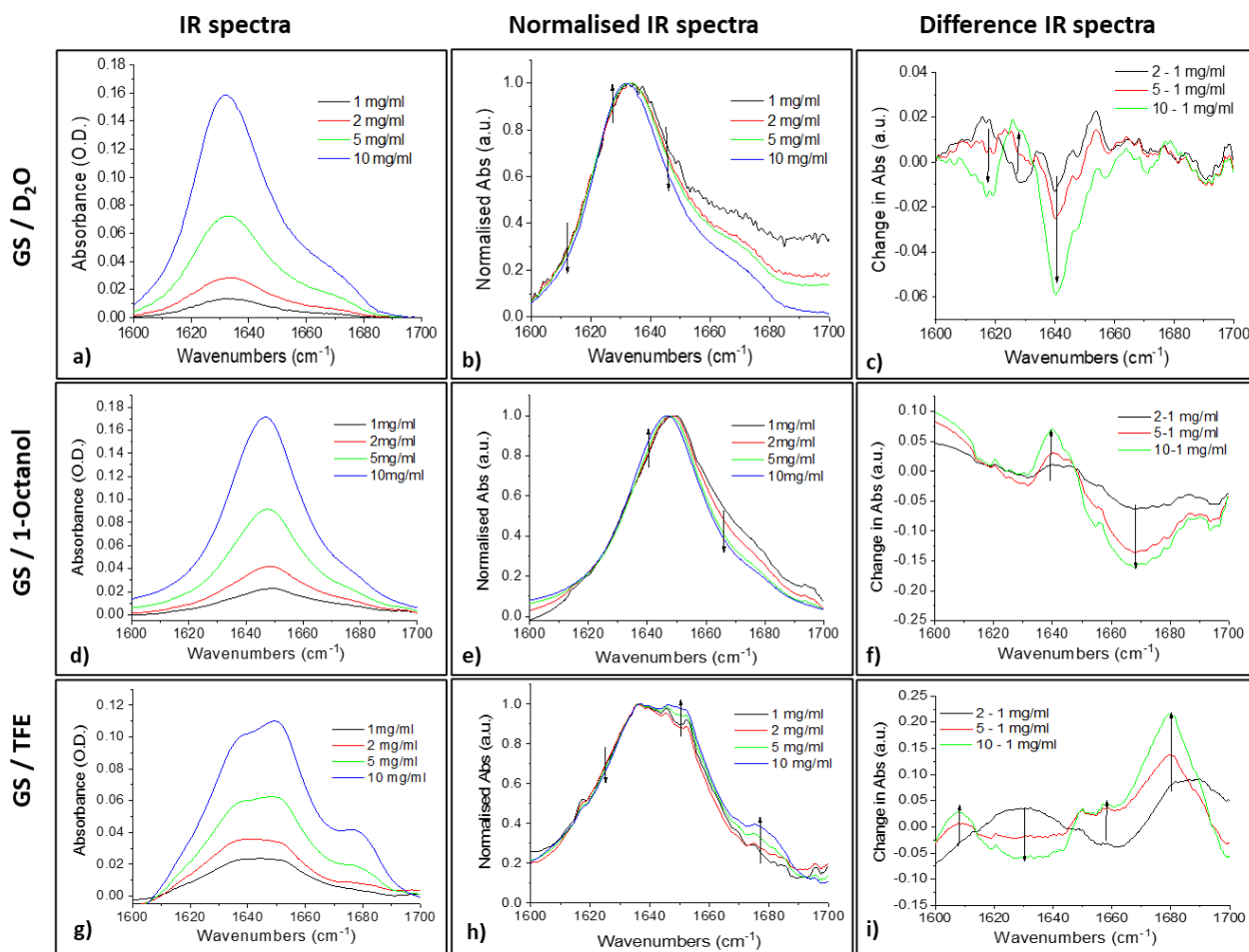


Figure 3.3 Comparative FTIR spectra for concentrations 1.00, 2.00, 5.00 and 10.0 mg/mL for GS in  $D_2O$ , 1-octanol and TFE with graphs showing normal spectra at the four different concentrations (a, d, g), normalised spectra (b, e, h) and difference spectra (c, f, i). Arrows indicate an increase or decrease in absorption.

To summarise the FTIR results, we observe differences in the IR spectra in the different solvent environments. The differences include amide I band shifts and spectral features which are related to structural changes, additionally, concentration also changes the IR spectrum.

### 3.3.2 2D-IR Spectroscopy

Following up on the changes observed in the global analysis of the FTIR data, the same GS preparations were analysed with 2D-IR. As observed from the FTIR analysis, in 2D-IR we expect to see minimal/no peak shifting for GS in  $D_2O$ , but shifts to low and high frequency for GS in 1-octanol

and TFE respectively, due to the different polarity of the solvents. Peak positions given are the probe positions.

2D-IR spectra for 1.00, 2.00, 5.00 and 10.0 mg/mL concentrations for GS in solvents D<sub>2</sub>O, 1-octanol and TFE are presented in *Figure 3.4*. With increasing dielectric constant and difference in H-bonding potential of the solvents, the peak positions shift to higher frequency. There is significant peak shifting of the maxima with increasing concentration for GS in 1-octanol and TFE. Between 1.00 and 10.0 mg/mL, the peak maximum ( $\nu = 0 - 1$  transition) in D<sub>2</sub>O has limited shift, as expected; from 1636  $\rightarrow$  1635  $\text{cm}^{-1}$ . In 1-octanol there is shifting to lower frequency from 1651  $\rightarrow$  1648  $\text{cm}^{-1}$  and in TFE there is shifting to higher frequency 1655  $\rightarrow$  1656  $\text{cm}^{-1}$ , correlating with the FTIR results in these solvents. A well pronounced minor peak is also present along the diagonal, near 1680  $\text{cm}^{-1}$  and this minor peak is lost at high concentration in both D<sub>2</sub>O and 1-octanol. This is different from the FTIR results of GS in TFE where the contributions from D<sub>2</sub>O and octanol are observed, with a greater increase in structure close to 1680  $\text{cm}^{-1}$ . Evident in TFE is that at high concentration of GS the peak near 1680  $\text{cm}^{-1}$  persists, which is not the case in the other two solvents.

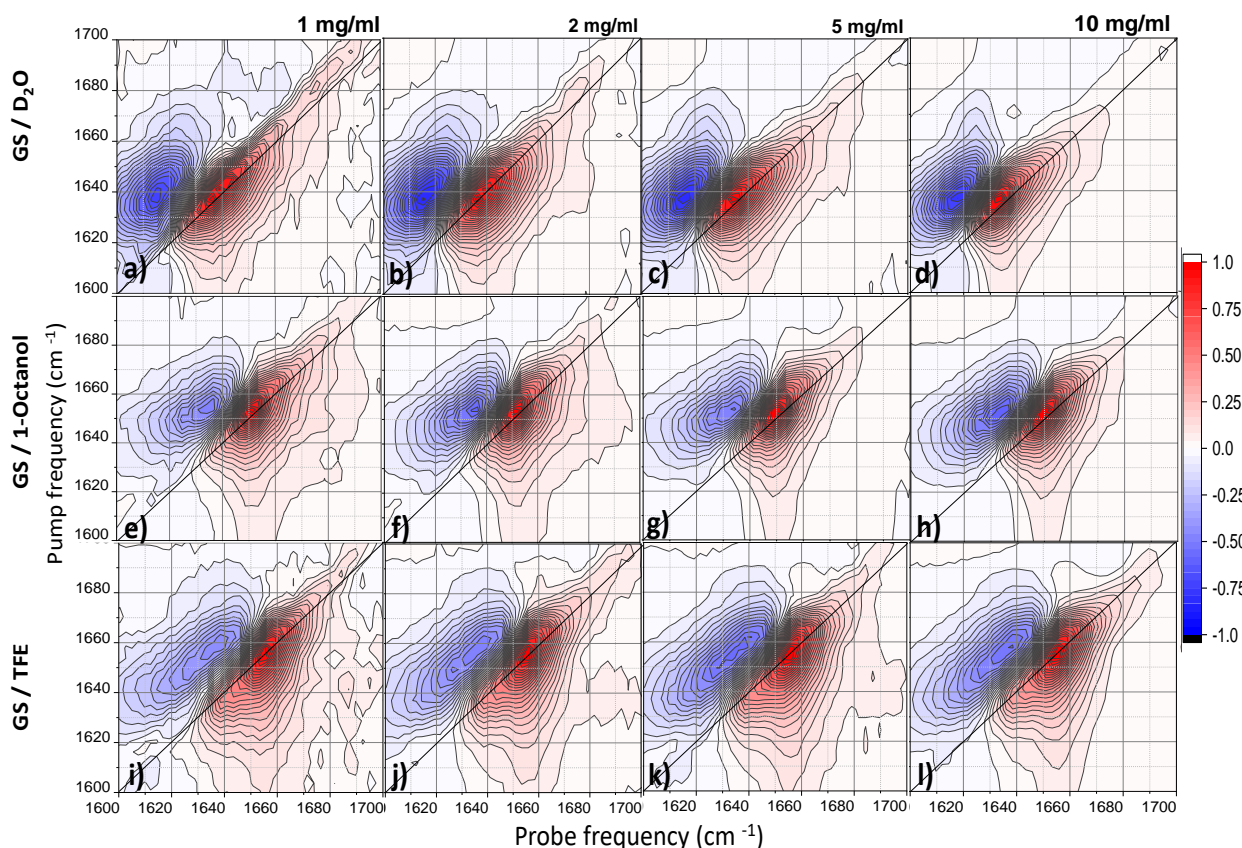


*Figure 3.4* Comparative 2D-IR spectra for GS in D<sub>2</sub>O (a, b, c, d), GS in 1- octanol (e, f, g, h), GS / TFE (i, j, k, l) at 1.00, 2.00, 5.00 and 10.0 mg/mL.

The positive  $\nu = 0 - 1$  transition peak on the main diagonal is accompanied by the off-diagonal negative peak for  $\nu = 1 - 2$  transition. The separation of these two peaks along the probe frequency axis is due to the anharmonicity of the amide I potential which is not constant across the mode (*Figure 3.5*). The anharmonicity changed across the line-shapes in each sample and across samples. Fitting two Gaussian functions to two different slices at pump values  $1640$  and  $1650$   $\text{cm}^{-1}$  returned different anharmonicities. In  $\text{D}_2\text{O}$  for pump frequencies at  $1640$  and  $1650$   $\text{cm}^{-1}$  the anharmonicity respectively was  $11$  and  $7$   $\text{cm}^{-1}$  for  $1.00$   $\text{mg/mL}$  and  $9$  and  $14$   $\text{cm}^{-1}$  for  $10.0$   $\text{mg/mL}$ . In solvent 1-octanol it was  $10$  and  $12$   $\text{cm}^{-1}$  for  $1.00$   $\text{mg/mL}$  and  $9$  and  $13$   $\text{cm}^{-1}$  for  $10.0$   $\text{mg/mL}$  and in TFE it was  $15$  and  $17$   $\text{cm}^{-1}$  for  $1.00$   $\text{mg/mL}$  and  $7$  and  $17$   $\text{cm}^{-1}$  for  $10.0$   $\text{mg/mL}$ . This is a strong indication of the effect the solvent has on the vibrational potential of the Amide I mode in GS.

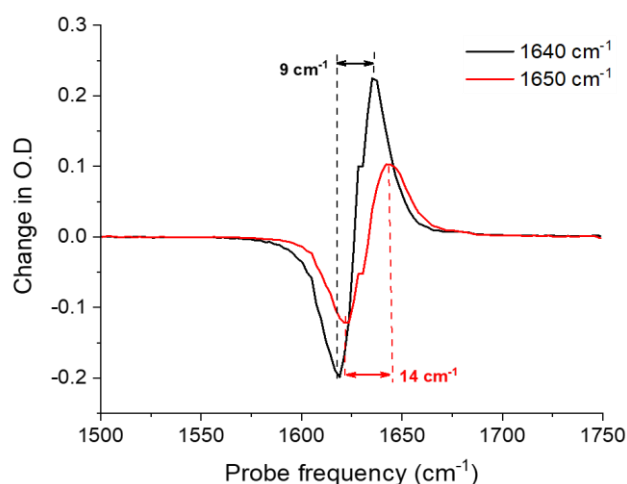


*Figure 3.5* An example of spectra indicating how the anharmonicity was determined. Spectra of pump slices for GS in  $\text{D}_2\text{O}$  taken at  $1640$  and  $1650$   $\text{cm}^{-1}$ , used to show the anharmonic shift of the diagonal peak.

## 2D-IR Difference Spectra Analysis

To highlight spectral changes caused by increasing concentration which indicate conformational changes and/or oligomerisation in the peptide preparation, difference spectra shall be considered (*Figure 3.6*). Difference spectra, after normalization, between the highest and lowest concentrations,  $10.0$  and  $1.00$   $\text{mg/mL}$  for GS in  $\text{D}_2\text{O}$  showed a negative feature on the diagonal at ( $1643$   $\text{cm}^{-1}$ , blue arrow), together with a positive feature above the diagonal ( $1628$   $\text{cm}^{-1}$ , red arrow), indicating a loss and a gain respectively of the  $\nu = 0 - 1$  intensity (*Figure 3.6c*). The positions of these changes correspond to those observed in the IR absorption difference spectra (*Figure 3.3c*). An accompanying negative (black arrow) and positive peak (orange arrow) were also observed in the position of the  $\nu = 1 - 2$  transition. In 1-octanol, for the difference spectrum for concentrations  $10.0$  and  $1.00$   $\text{mg/mL}$ , there is a negative feature on the diagonal ( $1665$   $\text{cm}^{-1}$ , blue arrow), alongside a positive feature slightly

above the diagonal ( $1641\text{ cm}^{-1}$ , red arrow), again respectively indicating a loss and a gain of the  $\nu = 0 - 1$  intensity (Figure 3.6f). This also corresponds to the changes observed in the IR absorption difference spectra (Figure 3.3f). A negative feature ( $1624\text{ cm}^{-1}$ , black arrow) indicates a loss is observed in the position of the  $\nu = 1 - 2$  transition with no accompanying positive peak.

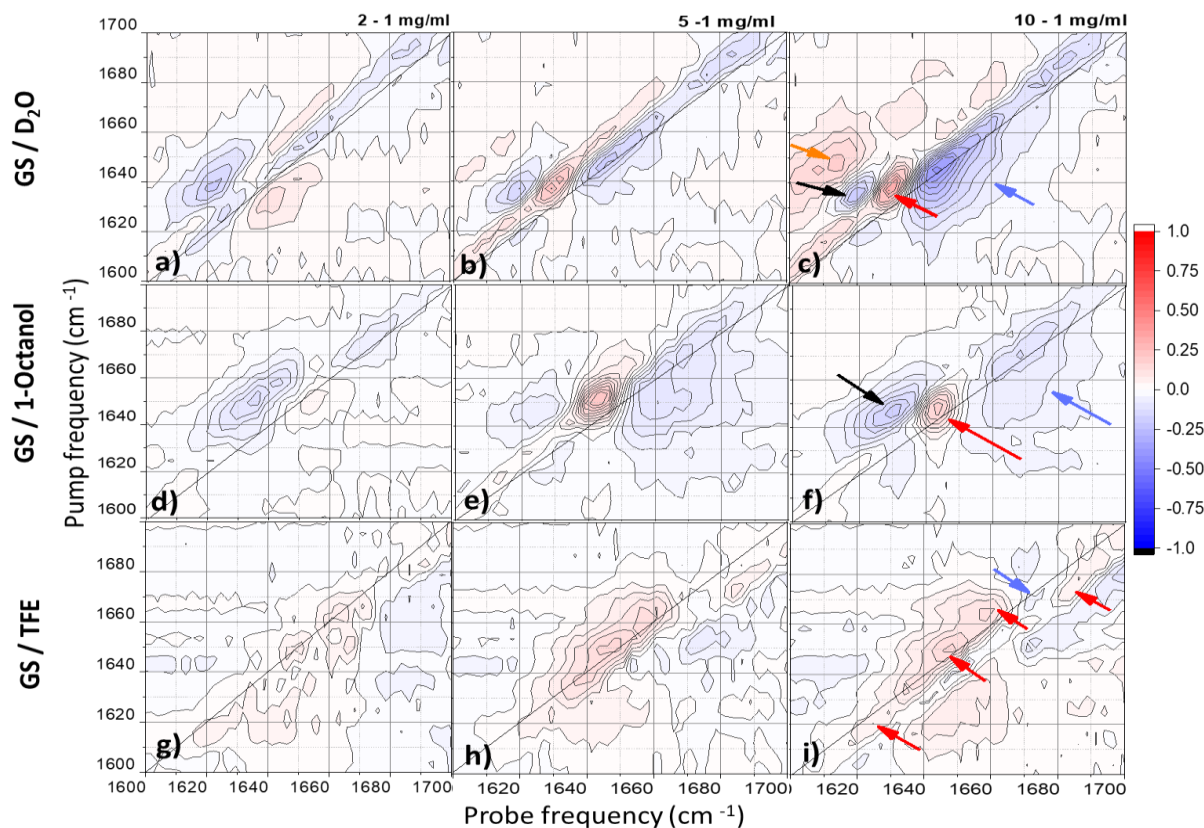


Figure 3.6 2D-IR difference spectra at 2.00 – 1.00, 5.00 – 1.00 and 10.0 – 1.00 mg/mL for GS in  $D_2O$  (a, b, c), GS in 1 – octanol (d, e, f), GS in TFE (g, h, i). Red and blue arrow show a gain and loss, respectively, in intensity for the  $\nu=0-1$  transition, while black and orange indicate a gain and loss, respectively, for the  $\nu=1-2$  transition.

In TFE, the difference spectrum for concentrations 10.0 and 1.00 mg/mL showed several positive features along the diagonal ( $1620, 1650, 1660$  and  $1685\text{cm}^{-1}$ , red arrows) together with a minor negative feature below the diagonal ( $1670\text{ cm}^{-1}$ , blue arrow). These were in the position of the  $\nu = 0 - 1$  transition, indication a gain and loss in the band's intensity (Figure 3.6i). These features are similar with the changes observed in IR absorption difference spectra (Figure 3.3i).

### 3.3.3 Principal Component Analysis (PCA) of FTIR and 2D-IR spectra

Principal component analysis (PCA) was applied to the FTIR and 2D-IR spectra in-order to extract significant features from the spectral results and to better identify variations between the different concentrations in each solvent.

PCA on the FTIR and the 2D-IR data was performed on the four different concentrations for each solvent. In both cases, the data was well represented with two principal components; PC 1 and PC 2. Other principal components such as PC 3 was not considered as it did not show significant information and represented scatter. PC 1 for 2D data (in *Figure 3.7*) was concentration independent and represented the average spectra (*Figure 3.8*) across the four concentrations measured per solvent. PC 2 showed the concentration dependant variations because the spectra encompassed features observed in the difference spectra. The positive peak positions for the PC 1 spectral component of FTIR and 2D-IR are in *Table 3.2*.

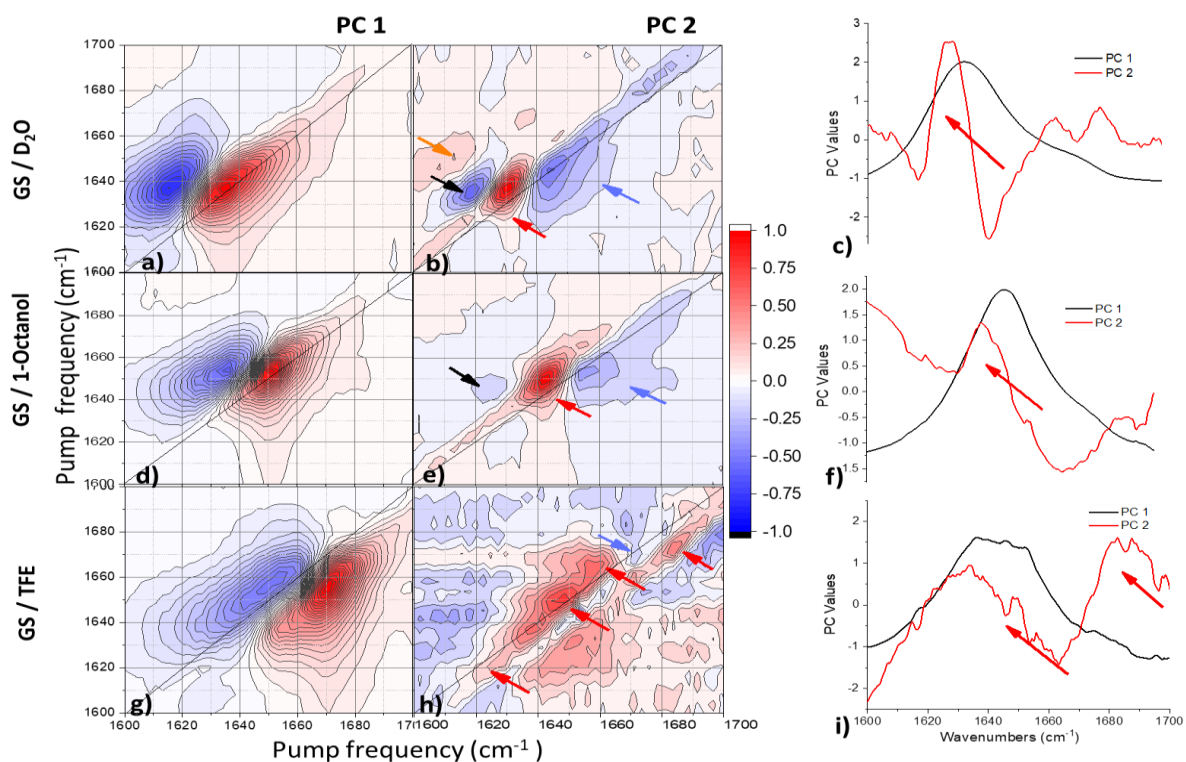


*Figure 3.7* PC1 and PC2 spectra for GS in D<sub>2</sub>O; PC 1 (a), PC 2 (b) from 2D-IR and PC 1 and PC 2 (c) for FTIR data. GS in 1 - octanol; PC 1 (d), PC 2 (e) from 2D-IR and PC 1 and PC 2 (f) for FTIR data. GS in TFE; PC 1 (g), PC 2 (h) from 2D-IR and PC 1 and PC 2 (i) for FTIR data.

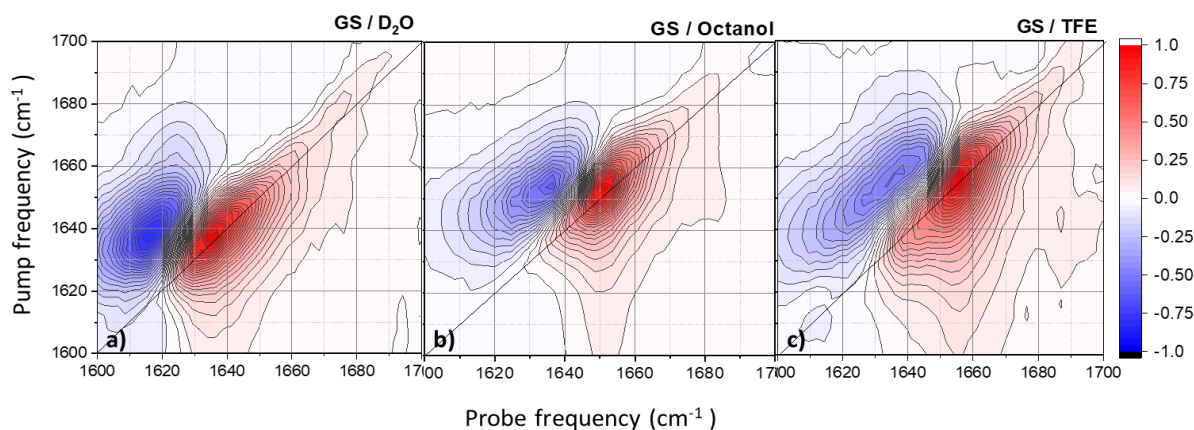


*Figure 3.8* Average spectra for GS in D<sub>2</sub>O (a), GS in 1 - octanol (b), GS in TFE (c).

*Table 3.2 Table of values for the negative and positive peak positions from 2D-IR PC1 component and the positive peak positions of FTIR PC1 component. Data is extracted from the PC1 component which represents the average spectra. The 2D-IR peak positions are from Gaussian fits to slices taken on the 2D-IR spectra parallel to the probe frequency axis at a pump frequency of 1635, 1650 and 1655  $\text{cm}^{-1}$  for GS in  $\text{D}_2\text{O}$ , 1-octanol and TFE, respectively.*

GS in Solvent	Dielectric constant	PC 1		FTIR
		(-) ve peak	(+) ve peak	
$\text{D}_2\text{O}$	78.28	1617	1634	1632
1-Octanol	10.30	1637	1651	1646
TFE	8.55	1651	1670	1650

The FTIR spectra reconstructed from PC 1 showed positive broad bands centred at frequencies given in *Table 3.2* for the different solvents while reconstructed 2D-IR PC1 distribution spectra showed positive ( $\nu = 0 - 1$ ) and negative ( $\nu = 1 - 2$ ) peaks. The 2D-IR and FTIR PC 2 contribution for  $\text{D}_2\text{O}$  and 1-octanol showed disappearance of a cross peak/shoulder at 1640 and 1655  $\text{cm}^{-1}$ , respectively (*Figure 3.7*). These changes were also observed in the difference spectra, with increasing concentration. Wavenumber position of the peaks were obtained from a Gaussian curve fitting function, fitting spectral slices taken at the wavenumber of the maximum intensity.

The negative and positive peak pairs identified from PCA represented those observed from the original 1D and 2D data. The positions for the negative and positive peak pairs per concentration and solvent for PC2 component are given in *Table 3.3*. Negative peaks were caused by loss in intensity, while positive peaks signified a gain in a particular feature. The PC loadings for FTIR and 2D-IR are as shown in *Figure 3.9*. From the loadings, PC1 is concentration independent, while PC2 is concentration dependent. The variation in PC2 can be from the diagonal peak, which grows and shifts with increasing concentration, probably representing the  $\beta$ -sheet structures persisting in the peptide preparations and in all three solvents, while at the same time the off-diagonal peak is lost. This aspect is discussed further in the spectral assignment section 3.4.1.

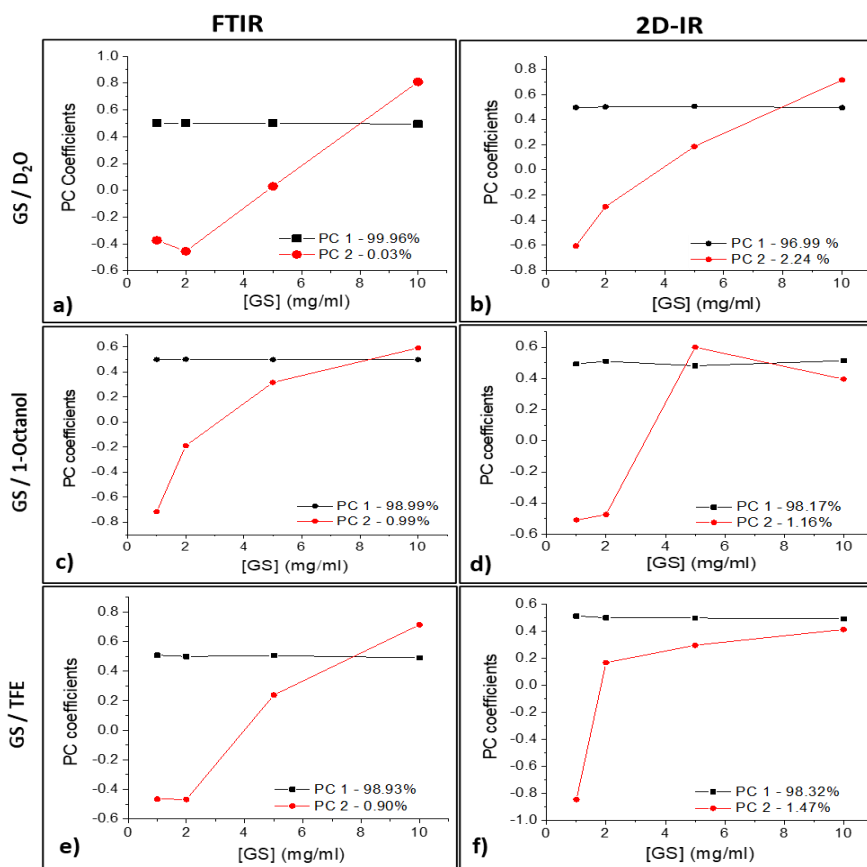


Figure 3.9 PC coefficients for GS / D<sub>2</sub>O for FTIR (a) and 2D-IR (b), GS / 1 - octanol for FTIR (c) and 2D-IR (d), GS / TFE for FTIR (e) and 2D-IR (f).

Table 3.3 Table of values for PCA done on 2D-IR and FTIR data. Data is extracted from the PC2 component which represents the difference spectra. Peak positions are from Gaussian fits to pump slices taken parallel to the probe frequency axis at locations where there is a positive or negative peak.

GS in Solvent	Dielectric constant	PC 2	
		2D-IR	FTIR
D <sub>2</sub> O	78.28	(-) ve peak	1621
		(+) ve peak	1629
		(-) ve peak	1638
1 - Octanol	10.30	(-) ve peak	1620
		(+) ve peak	1643
		(-) ve peak	1654
TFE	8.55	(+) ve peak	1620
		(+) ve peak	1650
		(+) ve peak	1660
		(-) ve peak	1670
		(+) ve peak	1685

### 3.4 Discussion

The results highlighted the behaviour of GS in the selected solvent environments. In the selected solvents D<sub>2</sub>O, 1-octanol and TFE, the effect of band shifting observed on the major band in both FTIR and 2D-IR data is explained by the nature of solvent environments of different polarity and H-bonding potential. Solvent polarity decreases with decrease in dielectric constant when moving from D<sub>2</sub>O to 1-octanol to TFE (*Table 3.1*). Thus, as the polarity decreases there is a peak shift to higher frequency, which is indicative of the different H-bonding potential of the solvents as expected [20], [33]. It has been reported in IR studies on GS that in polar protic solvents the main amide I band is located near 1629 cm<sup>-1</sup> and this band position shifts with decrease in the protic nature [39].

Water has the ability to form strong H-bonds with the carbonyl and the amide groups in proteins [20]. Structural studies on GS have reported its limited tendency to self-associate [31], [40], [41] due to the electrostatic forces of the two positively charged Orn residues which cause repulsion [42]. In a study on the conformation of cyclic antimicrobial peptides based on GS, it was reported that for concentrations in the range 50.0 – 60.0 μM (or > 50.0 μM) new species were present in peptide aqueous solutions which suggested peptide aggregation [30]. This study indicated that GS10, a peptide derived from GS, had similar biological activity and structure to GS itself. Thus, in relation to our study on GS, the concentrations used in this study, ranging from 0.877 mM (1.00 mg/mL) – 8.77 mM (10.0 mg/mL) are high and aggregated/higher order structures can be expected to be present in solution, although in this study we are referring to 1.00 mg/mL as a low and 10.0 mg/mL as a high concentration. For GS in D<sub>2</sub>O and in 1-octanol at 1.00 mg/mL there is evidence of the presence of antiparallel β-sheets (major peak) and type II β-turns (minor peak) but with increasing concentration (> 1.00 mg/mL) in D<sub>2</sub>O and 1-octanol, the loss of the minor peak could be from reorientation of the existing higher order structures present in the solvent, as we are deducing from the identified loss in the cross peak upon increase in concentration. With increasing concentration there will be more GS molecules per given volume, promoting peptide-peptide interaction/self-assembly which increases aggregation. The minor band in the IR spectra is located at higher frequency ranges from 1660 to 1690 cm<sup>-1</sup>. With increasing GS concentration, the appearance of the minor higher frequency band becomes less pronounced in both D<sub>2</sub>O and 1-octanol, however, in TFE this feature is significant. In GS there are β-turn structures located at higher frequency and results suggests that with decrease of solvent polarity and at high concentrations, the rigid β-turn structures prevail, as in TFE.

TFE (CF<sub>3</sub>CH<sub>2</sub>OH) is an amphipathic solvent and the presence of the -CF<sub>3</sub> group enhances hydrophobicity, which is an important aspect of TFE [43]. The notable characteristics of TFE include its ability to induce β-sheets, β-turns and β-hairpin structures in proteins, to disrupt tertiary structures

while preserving the secondary structure [44]. Furthermore, the physical and chemical properties of TFE resemble those of a bio-membrane, hence the use of TFE as a membrane-mimetic solvent [45]. The working mechanism by which TFE stabilises the protein backbone is unclear [46], but one explanation has described that TFE favourably surrounds the protein and drives water out, thus ‘drying out’ the peptide backbone and promotes backbone hydrogen-bond formation, ultimately stabilising the protein [47]. TFE simulates a hydrophobic environment from which the conformation of peptides which reside in or are bound to membranes can be established [45]. As such in the presence of a structure inducing solvent like TFE the spectral signatures of GS were enhanced with identifiable  $\beta$ -sheets and  $\beta$ -turns in the amide I region, suggesting stability of the secondary structure [46], [48]. The  $\beta$ -turn structures in GS contribute to the hydrophobicity aspect which stabilises the  $\beta$ -hairpin structure of GS, thus from our results, the significant enhancement in  $\beta$ -turn structures for GS in TFE is explained by the hydrophobic-hydrophobic peptide-alcohol interactions which are stabilising the TFE induced structures [49], [50]. GS adopts a  $\beta$ -hairpin structure and the type II  $\beta$ -turns present in GS favourably increase the stability of the hairpin [51].

### 3.4.1 Structural assignment using FTIR and 2D-IR data

We seek further to ascertain the changes observed in both 1D and 2D IR spectroscopies as this will provide coupling information from the system to further assign structure. As discussed in Chapter 2, vibrational spectroscopies are sensitive to polypeptide secondary structure due to the coupling which occurs between amide vibrational modes which are in turn sensitive to the polypeptide backbone conformation and H-bonding [52]. The key mechanism for vibrational coupling is referred to as transition dipole coupling which is the basis of conformational sensitivity of amide vibrations in proteins and polypeptides [52], [53].

A method has been described which utilises transition dipole strength ( $\mu$ ) to identify secondary structure making use of both 1D and 2D spectroscopies. The assignment of the secondary structural changes in the peptide amide I was confirmed using the method by Minnes *et al.* [54] in accordance to Grechko and Zanni [53], [55]. The method is based on the knowledge that the transition dipole strength is sensitive to the secondary structure of a molecule and neither 1D and 2D spectroscopy is sufficient on its own to measure the transition dipole strength due to details which may be difficult to accurately extract such as exact concentration for systems which are kinetically evolving [55], [56]. The 2D-IR diagonals and the IR spectra for calculating the transition dipole spectra are as shown in *Figure 3.10*.

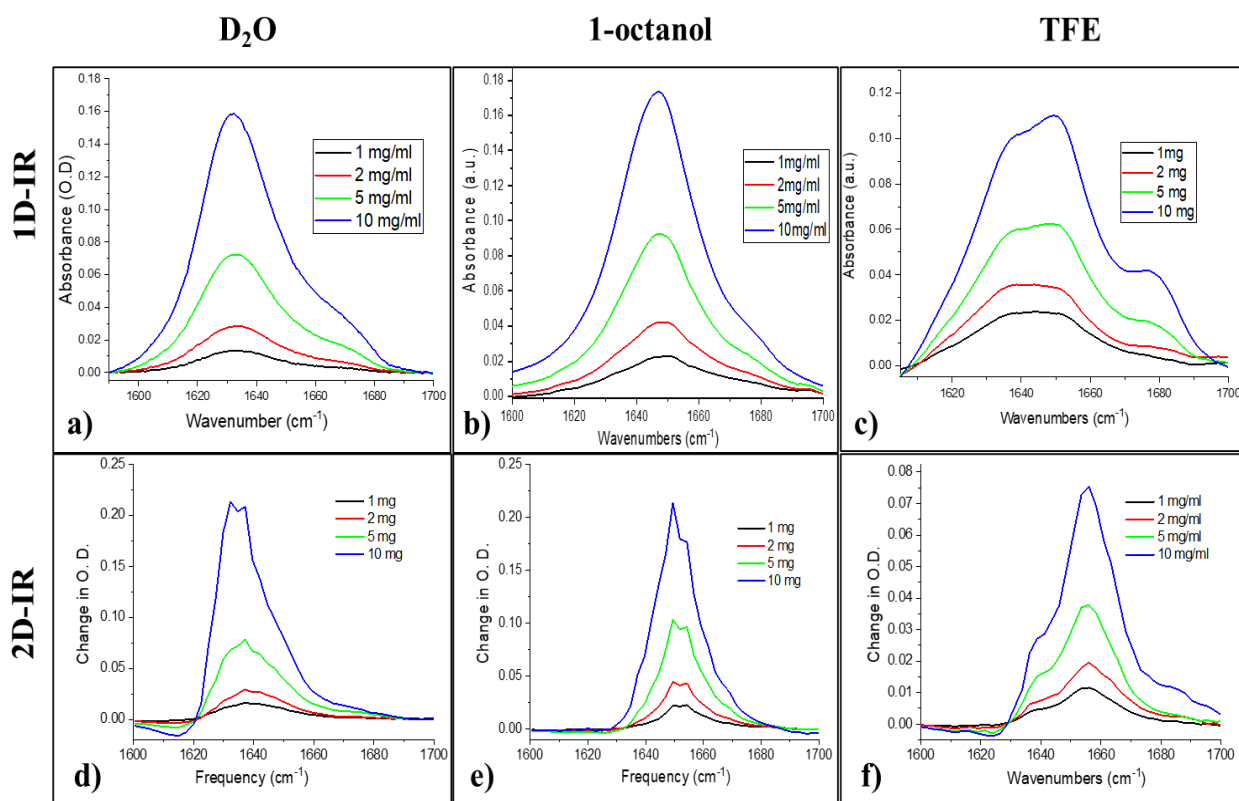


Figure 3.10 1D absorption spectra (a, b, c) and 2D-IR diagonal spectra (d, e, f) at concentrations 1.00, 2.00, 5.00 and 10.0 mg/mL used for calculating transition dipole spectra. The absolute values for spectra were considered to calculate the relative transition dipole spectra.

The signal intensity of both 1D and 2D spectra scales linearly with concentration,  $c$ , (Figure 3.11) but non-linearly with transition dipole strength ( $\mu$ ), that is, in 1D the spectra scales as  $c|\mu|^2$  while in 2D it scales as  $c|\mu|^4$  [54]–[56] which leads to changes in the relative magnitudes of the 1D and 2D signals in the event that the vibrational couplings in the system changes [53], [54]. This is expanded in section 2.2.4. Grecko and Zanni [55] illustrate a methodology whereby the actual / absolute transition dipole is obtained given that all details of the experiments are known. However, we employ the approach described by Minnes *et al.* [54] that relates the amplitude ratios between the 2D-IR diagonals with the IR spectral signals, knowing that the amplitude of the 2D-IR signal increases with increase in vibrational coupling. Thus, the relative changes in transition dipole, with reference to the lowest concentration at 1.00 mg/mL were obtained using the relation in Equation 3.1;

$$d(\omega)^{rel} = \frac{2DIR_c(\omega) OD_{1mg/ml}}{FTIR_c(\omega) \Delta OD_{1mg/ml}} \quad 3.1$$

Whereby,  $d(\omega)^{rel}$  represents the ‘spectrum’ of the relative transition dipole strength [54] and is a function of frequency,  $\omega$ .  $2D-IR_c(\bullet)$  and  $FTIR_c(\bullet)$  are the absolute intensity values for the 2D diagonal and the 1D spectral signals, respectively, and  $OD_{1mg/mL}$  and  $\Delta OD_{1mg/mL}$  are the maxima of

the 1D spectrum and the 2D-IR diagonal signal respectively [54]. The calculated integral area for the absorption spectra does change together with that of 2D-IR where the area increases with increasing concentration as shown in (Figure 3.11). With changes in coupling, the integrated area under the 1D spectrum is conserved while that of 2D is not conserved [55]. With this data changes in coupling with aggregation/oligomerisation was calculated.

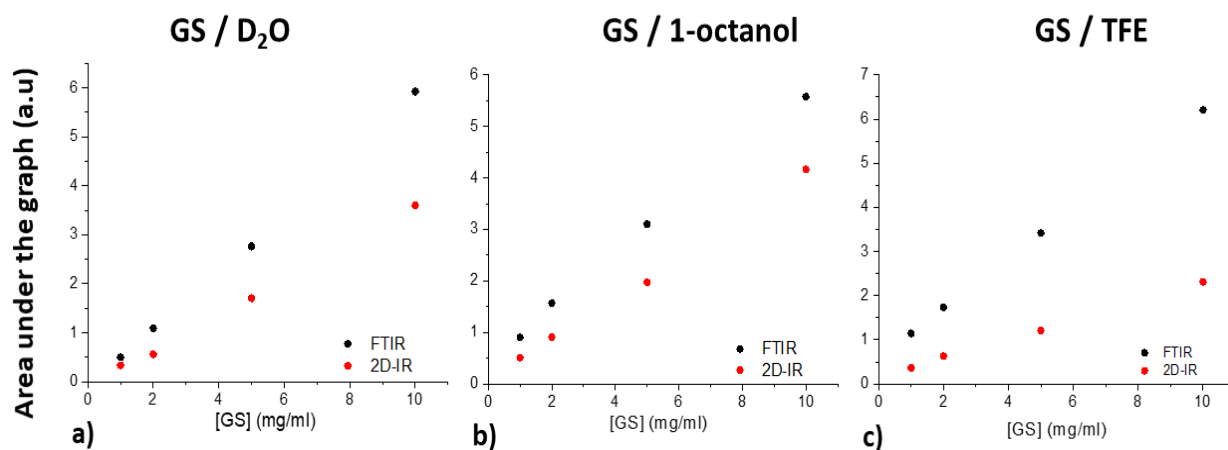


Figure 3.11 Area under the graphs for a) GS in D<sub>2</sub>O, b). GS / 1 - octanol, c). GS / TFE at 1.00, 2.00, 5.00 and 10.0 mg/mL.

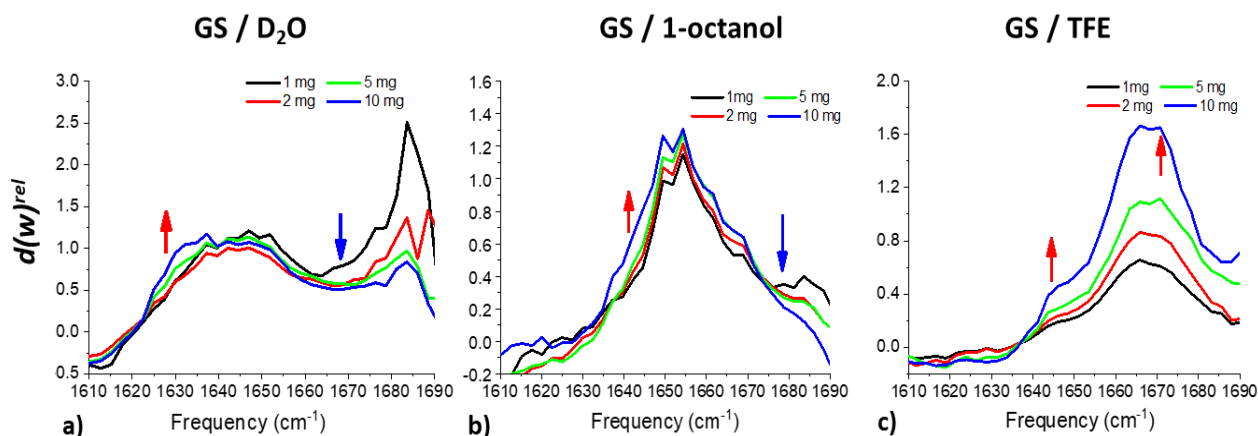


Figure 3.12 Comparative calculated  $d(\omega)^{rel}$  spectra for GS in D<sub>2</sub>O (a), 1 – octanol (b) and TFE(c). The arrows indicate regions where structure content is either increasing (red arrow pointing up) or decreasing (blue arrow pointing down).

The calculated transition dipole strength spectra show the changes in the system. In Figure 3.12, there is increase in transition dipole intensity (red arrows) near 1640 cm<sup>-1</sup>, a similar frequency position as was observed in our PCA analysis of both FTIR and 2D-IR, and the intensity increases with increasing concentration. The decrease in transition dipole intensity at higher frequency (blue arrow) for D<sub>2</sub>O and 1-octanol hints at the loss of the off-diagonal peak, and the loss of  $\beta$ -turns, which was previously mentioned to be happening upon increase in concentration. This loss in the diagonal peak is attributed

to loss in the  $\beta$ -sheet content located at higher frequency as observed from the decreasing transition moment near  $1680\text{ cm}^{-1}$  (*Figure 3.12a* and *b*). This is in line with the FTIR and 2D-IR results. As previously described structures such as  $\beta$ -sheet and turns are promoted in TFE as seen from the increasing transition dipole intensity.

### 3.4.2 Structural assignment from FTIR second derivative analysis for Amide I and II

In order to support the features reported in the transition dipole spectra and simulations and to further delineate the finer details of the structures contributing to the amide I and II absorption spectra, 2<sup>nd</sup> derivative spectra of the normalised FTIR spectra were calculated. Such 2<sup>nd</sup> derivative spectra are frequently used in FTIR spectra analysis to find the absorption peaks mapped to fine structures [57], [58] as discussed in Chapter 2. As some of the spectra exhibited a high level of noise, a signal/noise (S/N) cut-off of  $\pm 2$  was used to determine the most prevalent absorption peaks. For S/N spectra for GS in 1-octanol the 10 mg/ml spectra is excluded because it had a high noise level *Figure 3.13d*.

*Table 3.5* summarises the proposed structures of GS solvent environments related to the different observed vibrations (*Figure 3.13* and *Figure 3.14*), in comparison to those reported in literature. A Gauss 09 derived model of the IR spectrum of a GS trimer was also constructed in collaboration with Dr. O. O. Olaoye and Dr. V. Kumar and compared to the experimental observations (*Figure 3.17*). Results on structural assignment from FTIR amide I and II second derivative spectra shall be presented first, followed by results for spectral simulations on a trimer model. However, in the second derivative analysis reference shall be to the simulated trimer model and band assignments from both results are in *Table 3.5*.

#### *Amide I*

For GS in D<sub>2</sub>O the 2<sup>nd</sup> derivative spectra for the amide I region was noisy and only yielded limited fine structure details (*Figure 3.13a*). In D<sub>2</sub>O (*Figure 3.13b*), the low concentrations at 1.00, 2.00 mg/mL exhibited C=O stretching absorption at  $1702\text{ cm}^{-1}$  and  $1699\text{ cm}^{-1}$  related to  $\beta$ -sheets and the high concentrations (5.00, 10.0 mg/mL) showing absorption between  $1625\text{-}1639\text{ cm}^{-1}$  that may be related to various C=O stretching vibrations. This correlates to the peak positions obtained from PCA results denoted in (*Table 3.2*) and the increasing feature in the  $d(w)^{rel}$  spectra near  $1630\text{ cm}^{-1}$  (*Figure 3.12a*). This further agrees to the band at  $1643\text{ cm}^{-1}$  identified in the trimer model attributed to  $\beta$ -sheet carbonyls (coupled to Orn bending vibrations). A peak at  $1618\text{ cm}^{-1}$  is also observed and could be a C-C stretching of Phe aromatic ring, which also relates to the band at  $1624\text{ cm}^{-1}$  in the trimer model attributed to C-C stretch of Phe. The Orn side chain between  $1650\text{-}1670\text{ cm}^{-1}$  cannot be seen/ clearly identified, possibly because of shielding due to hydration and deuterium exchange. The observed low

resolution is possibly due to aggregation of micellar structures surrounded by the charged amino group of the Orn side chain. We observed, however, Orn side chain vibrations for several bands between 1530–1640  $\text{cm}^{-1}$  in trimer model (Figure 3.18, refer to Table 3.5 for more details on the trimer model and assignments).

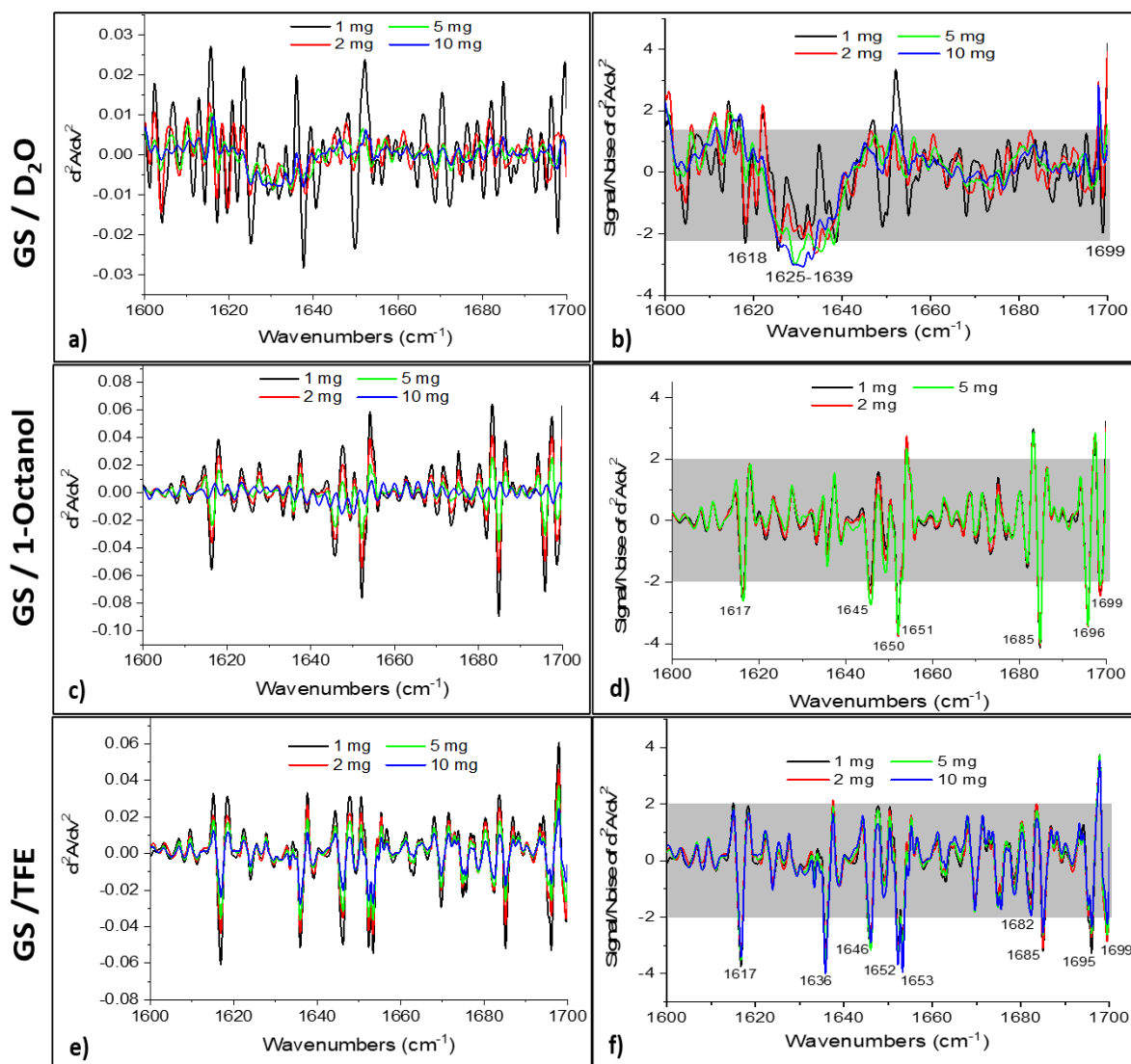


Figure 3.13 Second derivative spectra of the normalised FTIR spectra of GS in D<sub>2</sub>O (1<sup>st</sup> row), GS in 1-octanol (middle, 2<sup>nd</sup> row) and GS in TFE (3<sup>rd</sup> row) at different concentrations for amide I. The derived S/N spectra (b), (d) and (f) show wavenumbers ( $\text{cm}^{-1}$ ) of the peaks from prominent structures, the grey boxes are for guidance showing more clearly the spectral features with  $S/N < 2$ .

For GS in 1-octanol the C-C stretch of the Phe is present at 1617  $\text{cm}^{-1}$  (Figure 3.13d) and this feature is neither present in our PCA (Figure 3.7e and f) nor the  $d(w)^{rel}$  results (Figure 3.12b). However, in the trimer model the Phe contributions are at 1624  $\text{cm}^{-1}$  instead (Figure 3.18, Table 3.5). The structures identified from 1645–1651  $\text{cm}^{-1}$  are for the Orn side chain at 1645–1647  $\text{cm}^{-1}$ , the C=O stretching vibration of  $\beta$ -turns at 1650  $\text{cm}^{-1}$  and C=O stretching vibrations from  $\beta$ -sheets near 1642  $\text{cm}^{-1}$ . These structures are represented by the positive feature at 1643  $\text{cm}^{-1}$  indicated from the PCA

result and also indicated in the transition dipole spectra (*Figure 3.12b*). These modes correlate well with contributions from Orn side chain at 1630-1656  $\text{cm}^{-1}$  and those from  $\beta$ -sheet contributions at 1640  $\text{cm}^{-1}$  in the trimer model (*Figure 3.18*). The 1.00 mg S/N spectra displays high noise levels which indicates that these mentioned structures are supported at high concentration and relates to formation of inverse micellular aggregates.

Fine structure was supported in TFE at all concentrations indicating that the structures were present even at low concentrations (*Figure 3.13f*). This is shown from the difference spectra for 2.00-1.00 mg/mL (*Figure 3.7g*). The C-C stretching from Phe is present at 1617  $\text{cm}^{-1}$ , Orn side chain at 1646  $\text{cm}^{-1}$ . The C=O stretching from  $\beta$ -sheets are present at 1636 and 1695-1699  $\text{cm}^{-1}$  and  $\beta$ -turns at 1652-1685  $\text{cm}^{-1}$ . Similarly, in our trimer model; at 1624  $\text{cm}^{-1}$  is Phe C-C ring stretch; Orn is at 1637, 1641 and 1643  $\text{cm}^{-1}$ ; the C=O stretch from  $\beta$ -sheets is at 1631-3 and 1700  $\text{cm}^{-1}$  and the  $\beta$ -turns are also at 1652-1685  $\text{cm}^{-1}$ . The experimental modes in the amide I agree with those in the trimer model, indicating that oligomeric structures possibly exist in TFE. Our  $d(w)^{rel}$  spectra (*Figure 3.12c*) also supports the existence of fine structure from low concentration as seen by its increase in intensity with increasing concentration.

### ***Amide II***

For analysis of Amide II, correlations in spectral features will be made with reference to the trimer model. Identified bands have been tabulated in *Table 3.5*.

For GS in  $\text{D}_2\text{O}$  the 2<sup>nd</sup> derivative spectra for amide II were noisy and yielded limited fine structure details (*Figure 3.14b*), as was the case for the amide I. Strong bands include the band at 1577  $\text{cm}^{-1}$  from both  $\beta$ -sheets and turns, correlating with the trimer model band at 1575  $\text{cm}^{-1}$ . The Phe stretch at 1542-6  $\text{cm}^{-1}$  in  $\text{D}_2\text{O}$  is also observed in the trimer model at 1546  $\text{cm}^{-1}$ . The vibronic coupling between Phe and amides in the  $\beta$ -turns in trimer model is located at 1545  $\text{cm}^{-1}$ , while in  $\text{D}_2\text{O}$  this band is at 1546  $\text{cm}^{-1}$ . At 1517  $\text{cm}^{-1}$  we observed the C-C Phe ring vibration and bending of the C-H mode, corresponding to trimer model where vibrations were at 1517  $\text{cm}^{-1}$ . The 1509  $\text{cm}^{-1}$  band in  $\text{D}_2\text{O}$  is similar to that in the trimer model at 1507  $\text{cm}^{-1}$  from C-C ring stretch of Phe. The band at 1539  $\text{cm}^{-1}$  could be related to that at 1533  $\text{cm}^{-1}$  in the trimer model, from bending of the Orn amino group (refer to *Table 3.5*).

GS in 1-octanol (*Figure 3.14d*) and TFE gave clear signals (*Figure 3.14f*) and several of the located bands correlate well. In both 1-octanol and TFE GS gave a band at 1505  $\text{cm}^{-1}$  correlating with the trimer model at 1507  $\text{cm}^{-1}$  that attributed it to the Phe C-C ring stretch. The bands at 1521 and 1539  $\text{cm}^{-1}$  in the trimer model from N-H bending vibrations of the  $\beta$ -sheet were observed in 1-octanol and

TFE at 1523 and 1533  $\text{cm}^{-1}$ , respectively. The bands at 1542-4  $\text{cm}^{-1}$  in both solvents are located at 1546  $\text{cm}^{-1}$  in the trimer model which attributed it to N-H bending of the  $\beta$ -turns. At 1560-2  $\text{cm}^{-1}$  in both 1-octanol and TFE we have N-H bending of  $\beta$ -turns which are located at 1557  $\text{cm}^{-1}$  in trimer model. At 1575-7  $\text{cm}^{-1}$  in both the solvents we have again N-H bending of  $\beta$ -turns, which are located at 1577  $\text{cm}^{-1}$  in trimer model. The amide II structures in 1-octanol and TFE seem to be ordered at every concentration, with N-H bending in  $\beta$ -turns being the dominant vibration. The experimental results correspond well with the simulated trimer model as can be seen in *Table 3.5*.

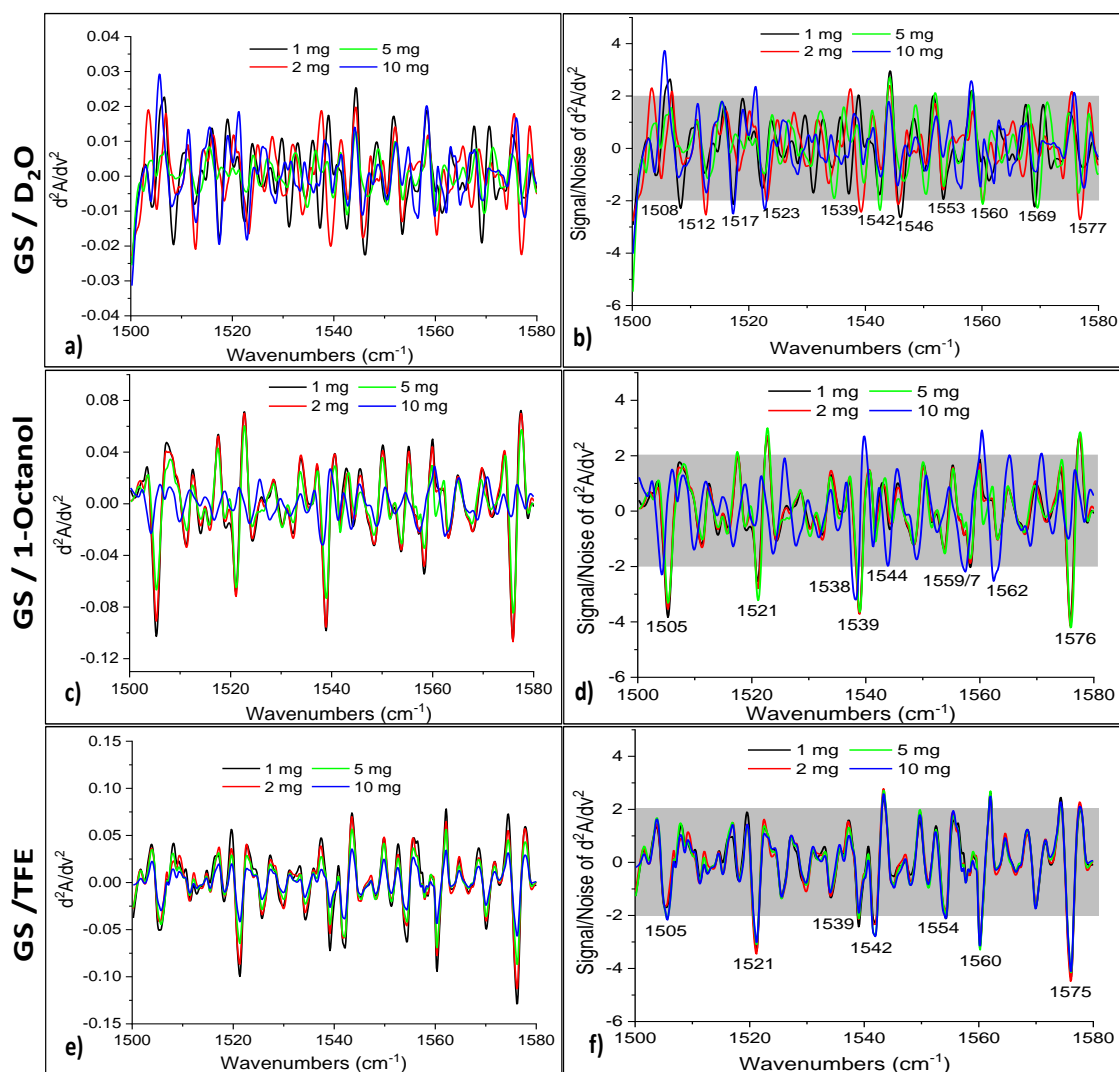


*Figure 3.14* Second derivative spectra of the normalised FTIR spectra of GS in  $\text{D}_2\text{O}$  (1<sup>st</sup> row), GS in 1-octanol (2<sup>nd</sup> row) and GS in TFE (3<sup>rd</sup> row), at different concentrations for amide II. The derived S/N spectra (b), (d) and (f) show wavenumbers ( $\text{cm}^{-1}$ ) of the peaks from prominent structures, the grey boxes are for guidance showing more clearly the spectral features with  $S/N < 2$ .

### ***Trends in fine structure from second derivative spectra for Amide I and II***

In order to clearly observe how the identified spectral fine structures behave in the three solvents with increasing concentration, we considered the trends depicted by signal changes from the second

derivative spectra (refer to *Table 3.4*). In (*Figure 3.13a* and *Figure 3.14a*) it can be seen that D<sub>2</sub>O had more noise because of the presence of many different structures, such that there isn't one chromophore present to give a dominant signal. Thus, there could be many different conformations, including oligomers of GS in solution. For higher concentrations where there is a good signal, it indicates that at high concentration of GS, a specific conformation is present. Thus, with the D<sub>2</sub>O signal, very few defined structures or conformations were observed.

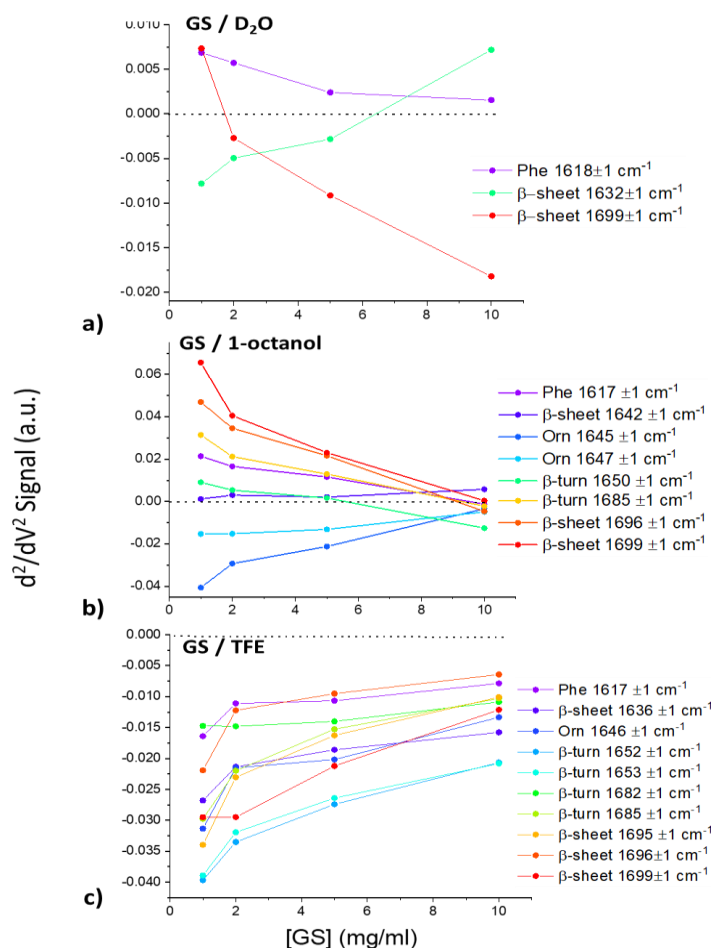


*Figure 3.15 Trends of peaks identified from FTIR second derivative spectral analysis in the Amide I from (Figure 3.13) showing signal changes with increase in peptide concentration for GS in a) D<sub>2</sub>O, b) 1-octanol, and c) TFE.*

The 10 mg spectra in octanol (*Figure 3.13d*) also gives a noisy signal, similar to that given by D<sub>2</sub>O at high concentration, indicating multiple conformations are present resulting in low resolution spectra. Therefore in 10.0 mg/mL for D<sub>2</sub>O and octanol, either the structures are coming out of solution or there is formation of big aggregates with a multitude of conformations. That is possibly why D<sub>2</sub>O (amide I and II) and octanol (amide I) show high noise levels. Also, for amide I in D<sub>2</sub>O the sheet structure at 1632 cm<sup>-1</sup> increases with concentration, while the signal for Phe and sheet content at 1699-1702 cm<sup>-1</sup> decreases (*Figure 3.15a*). This could indicate a conformational change that restricts Phe vibrations, while a different type of sheet or H-bonded structures formed in either aggregates or

micellular structures. In amide II the Phe and  $\beta$ -sheet vibrations decrease with concentration, while the N-H bending vibrations increase (*Figure 3.16a*).

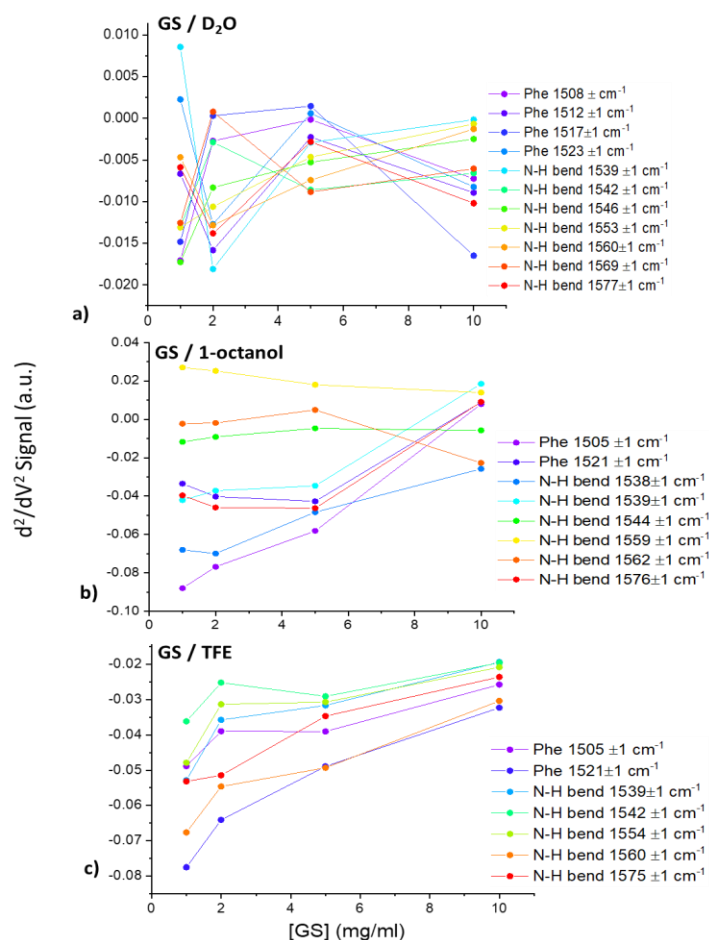


*Figure 3.16 Trends of peaks identified from FTIR second derivative spectral analysis in the Amide II (Figure 3.14) showing signal changes with increase in peptide concentration for GS in a) D<sub>2</sub>O, b) 1-octanol, and c) TFE.*

From the amide I concentration dependent trends in octanol (*Figure 3.15b*), there is an indication of an increase in  $\beta$ -sheet content with carbonyl stretching at  $1642\text{ cm}^{-1}$  and for Orn amino group bending at  $1645$  and  $1647\text{ cm}^{-1}$ . Some signals decrease such as those of the Phe side chain,  $\beta$ -turn and  $\beta$ -sheet at higher wavenumbers. In amide II,  $\beta$ -sheets at  $1521\text{ cm}^{-1}$  increase together with the Phe side chain and  $\beta$ -turns at  $1538$ - $1565/8\text{ cm}^{-1}$ , while the  $\beta$ -turns  $1559$ - $1576\text{ cm}^{-1}$  are lost. This indicated that certain structures are lost in favour of the formation of others, such as inverted micelles, with increasing concentration. TFE spectra is well resolved at all concentrations in both amide I and II (*Figure 3.15c* and *Figure 3.16c*) and all of the structures are present and increase with increasing concentration. This is a good indication of ordered structures present from low to high concentration, as expected in TFE as it is known to support hydrogen bonded structures [37], [38].

Table 3.4 The fine spectral structure components present in GS in D<sub>2</sub>O, 1-octanol and TFE solutions, identified in Figure 3.15 and Figure 3.16 and shown above. The identified amide I and II structures are labelled according to the contributing groups and their response (increase or decrease) to increasing concentration.

Amide I	Wavenumber ±1 cm <sup>-1</sup>	Group	Signal Response		
			D <sub>2</sub> O	1-octanol	TFE
	1617	Phe ring	Increase	Decrease	Increase
	1632-6	β-sheet C=O	Increase		Increase
	1642	β-sheet C=O		Increase	Increase
	1645-7	Orn NH <sub>3</sub> <sup>+</sup>		Increase	Increase
	1650-3	β-sheet C=O		Decrease	Increase
	1682-5	β-turn C=O		Decrease	Increase
	1695-6	β-sheet C=O		Decrease	Increase
	1699	β-sheet C=O	Decrease	Decrease	Increase

Amide II					
	1505-8	Phe C-C stretch	Decrease	Increase	Increase
	1512-7	Phe C-C stretch	Decrease		
	1521-3	Phe C-C stretch	Decrease	Increase	Increase
	1538-9	N-H bending	Increase	Increase	Increase
	1542-6	N-H bending	Increase	Increase	Increase
	1553-9	N-H bending	Increase	Decrease	Increase
	1560-2	N-H bending	Increase	Decrease	Increase
	1569	N-H bending	Decrease		
	1575-7	N-H bending	Decrease	Increase	Increase
	1585-6	Phe C-C stretch			

The results show that ordered structures such as the β-sheets at low frequency are behaving in the same manner, that is, they are emerging in solution and increasing with increasing peptide concentration, regardless of the solvent environment in both amide I and II. This could be attributed to the antiparallel interpeptide β-sheet content present in the peptide GS formed by the tripeptide unit Val-Orn-Leu, with Val and Leu forming the four intramolecular hydrogen bonds involving the amide protons and the carbonyl groups, stabilising the rigid GS structure [33], [59]. As these β-sheet

hydrogen bonds are buried inside the robust cyclic peptide structure, their solution behaviour suggests limited solvent exposure and the results indicate that there is a limited effect on these carbonyl stretching and N-H bending when the solvent system changes.

In amide I, the  $\beta$ -sheet content related to the carbonyl stretching located at higher frequency together with the  $\beta$ -turns are affected by change in solvent system. Octanol ( $\text{CH}_3(\text{CH}_2)_7\text{OH}$ ) was chosen because of its amphipathicity – exhibiting both hydrophobic and hydrophilic character and its carbon/oxygen ratio is akin to that of lipids [60]. Octanol has been said to mimic the properties of a protein interior as it is a partially polar solvent [61], [62]. Our results suggest that octanol is interacting with the hydrophobic side chains (Phe, Pro, Leu and Val), as would be expected due to the hydrophobic forces in this system. Furthermore, octanol it could be limiting or interfering with the aromatic stacking and hydrophobic clustering. The interaction with the amino acids Phe and Pro in the  $\beta$ -turns could put strain on the backbone and led to the loss of some of the  $\beta$ -turns in octanol. This corresponds with loss of the off-diagonal shoulder in the 2D-IR reported above from our PCA results (*Figure 3.7*). TFE supports most electrostatic interactions, particularly H-bonding, as the solvent is the least polar of the selected three [37], [38]. Therefore, GS in TFE will present more interpeptide and intrapeptide hydrogen bonded structures, such as the ordered secondary structures,  $\beta$ -sheets and  $\beta$ -turns, in both amide I and II which were observed with our concentration study together with the Orn side chain. These results strongly indicate the participation of amino acid residues which contribute to the hydrophobicity (aromatics in  $\beta$ -turns) and hydrophilicity/cationicity (positively charged Orn) of GS, responsible for the amphipathic nature of GS which contributes to GS activity [45], [63].

### **3.4.3 Structural assignment from computer simulations on a GS trimer model using QM / MM calculations**

To confirm and validate the experimental results, results from simulated spectra of a GS trimer model were considered (*Figure 3.17*). IR spectral features from the trimer model shall be elaborated (*Figure 3.18*). Generation of the trimer model below has been explained in Chapter 2. Reference shall be made to results on FTIR 2<sup>nd</sup> derivative spectral analysis. As mentioned in section 2.3, band assignments of vibrational modes in the trimer model below was done by visually observing the structural groups and modes of vibration using GaussView 5 software and assigning to the spectral feature which the vibrating mode contributes to.

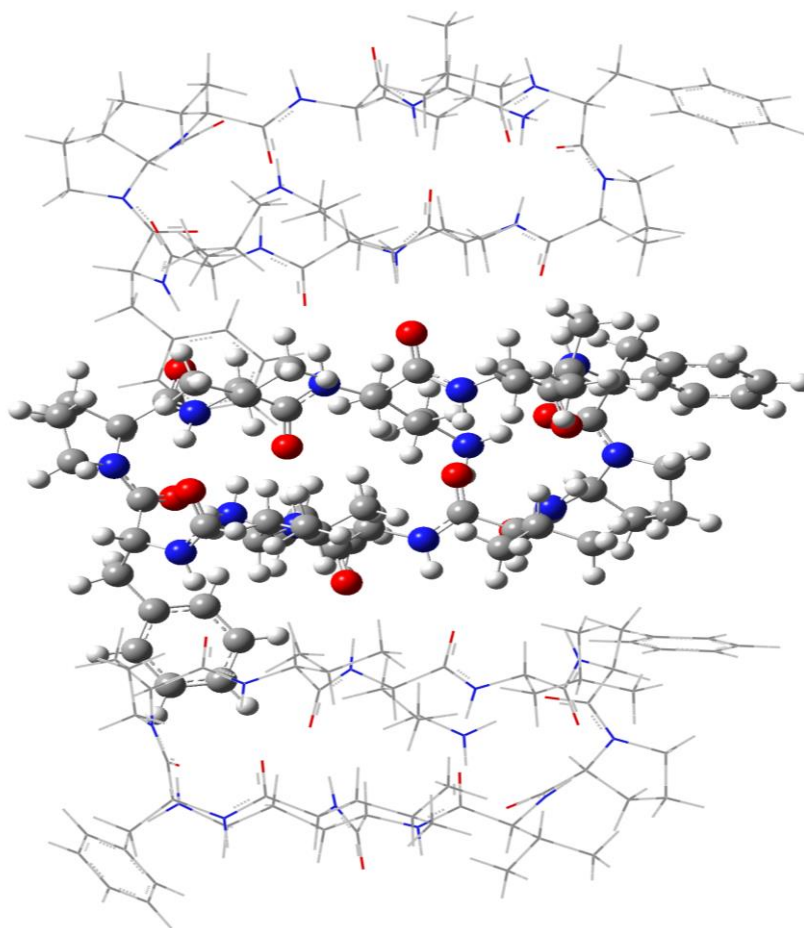


*Figure 3.17 GS trimer model used in the QM / MM simulation to generate FTIR and Raman spectra showing three monomer units. On this structure, QM/MM level of theory was implemented through the ONIOM framework available in Gaussian 09. The structure was subjected to simultaneous optimisation of the atomic redundant coordinates and frequency calculations including infra-red spectra.*

In the amide I region, there are very little observed vibrations from 1670-1700  $\text{cm}^{-1}$  in the trimer model (*Figure 3.18*). The band at 1666  $\text{cm}^{-1}$  is contributed to by carbonyl stretch of the  $\beta$ -turns, which is vibrationally linked to the Orn side chain. The band at 1643  $\text{cm}^{-1}$  is from Orn bending and there is the coupling between the Orn side chain and the  $\beta$ -sheet carbonyls. Orn bands are also at 1641 and 1637  $\text{cm}^{-1}$ . There is also  $\beta$ -sheet and NH bending modes at 1601 and 1608  $\text{cm}^{-1}$ , respectively. The band at 1624 is unrelated to that at 1601  $\text{cm}^{-1}$  and linked to C-C stretch of Phe. For amide II, at 1577  $\text{cm}^{-1}$  there is the  $\beta$ -sheet vibration and at 1568  $\text{cm}^{-1}$  there are the amide bending modes. The strong band at 1545  $\text{cm}^{-1}$  is from coupling of the Phe and the amide in the  $\beta$ -turns. A Phe mode is at 1570  $\text{cm}^{-1}$ .

An appreciable subset of the vibrations from our trimer model correlate well with those from experiments in all solvents ( $\text{D}_2\text{O}$ , 1-octanol and TFE). With reference to the trimer model, these are at; 1505, 1523, 1533, 1546, 1557 and 1577  $\text{cm}^{-1}$ . Refer to *Table 3.5* for detail on the structures which contribute to these bands and the correlating bands from the three solvents. From these results, as summarised in *Table 3.5*, we conclude that the theoretical and experimental assignments are in

agreement with GS literature [64] and those which have been made from DFT calculations on dipeptides [65] and other compounds such as methylacetamide and polycyclic aromatic hydrocarbons [66], [67].

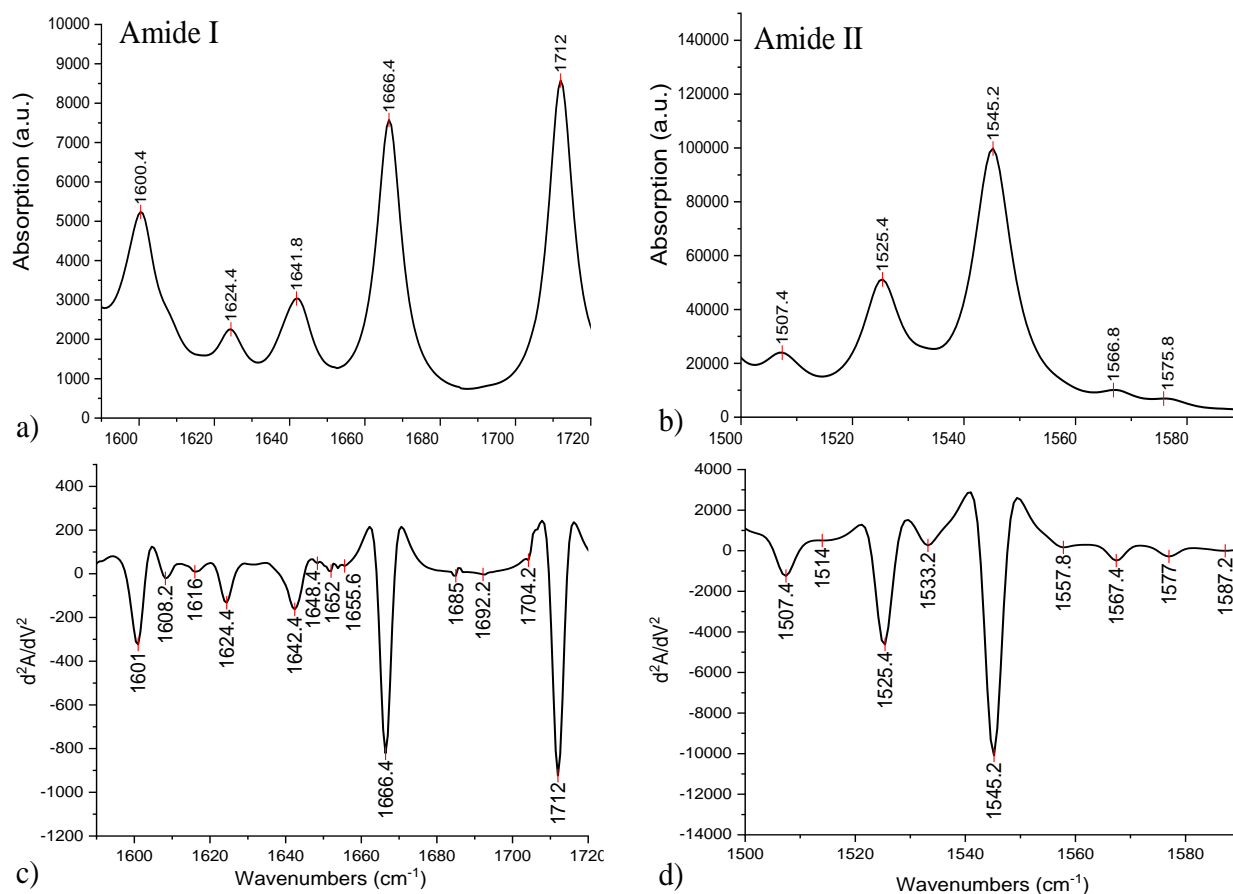


Figure 3.18 IR and  $2^{nd}$  derivative spectra for GS trimer model simulated using QM/MM calculations with assigned bands contributing to Amide I and II modes.

Table 3.5 Summary of FTIR analysis of GS secondary structures and selected amino acid vibrations in different solvent systems. Wavenumbers are shown in  $cm^{-1}$ , numbers in italics indicate vibrational coupling of overlapping IR peaks, numbers in brackets have prominent peaks in  $2^{nd}$  derivative spectra at all concentrations but  $-2 > S/N < 2$ .

Structure or amino acid	Absorbing Group	Literature Models <sup>a-e</sup>	GS <sup>f</sup>	GS Trimer model <sup>g</sup>	D <sub>2</sub> O	TFE	Octanol	
$\beta$ -sheet	Stretching C=O (amide I)	1700	1700	1705	1702	1699	1699 (1701)	
		1695-7		1693		1696, 1695	1696	
		1691-3						
		1641-3	1643	1643				1642
		1630-9		1630-1633, 1640	1630-1633, 1639	1636	(1636)	
	1624-9				1629			
Bending N-H (amide II)	1534	1532	1533	1539	1539 (1534)	1538, 1539		
	1523		1523	1521	1521	1521		

**Table 3.5 continued**

$\beta$ -turn	Stretching C=O (amide I)	1683-91		1685		1685	1685	
		1678-82		1682		(1682)		
		1670-75				(1676/5)		
		1666-74		1667		(1670)	(1673)	
		1659-65						
		1654-8	1655	1652/3		1652/3	1650/1	
	Bending N-H (amide II)	-	1563	1568	1569		1562	
		1559		1557	1553, 1560	1554, 1560	1557, 1559	
		1546-7	1546	1546	1546	1542	1544	
		1575		1577	1577	1575 (1570)	1576	
Orn	Bending NH <sub>3</sub> <sup>+</sup> (Amide I)	-						
		1672-3						
		1667		1667				
		1660						
		1659		1656				
	1647		1648		1646	1645, 1647		
Phe	Stretching C-C (ring) (Amide I and II)	1602	1601	1624	1618	1617	1616	
		1585	1586	1601, 1608			(1586)	
			1525			1517		
			1507	1507		1508, 1512	1505	1505

<sup>a</sup> Krimm *et al.* (1983); <sup>b</sup>Venjaminov & Kalin (1990); <sup>c</sup> Barth (2007), <sup>d</sup>Barth (2000), <sup>e</sup>Kong *et al.* (2007) <sup>f</sup>Naik *et al.* (1984), <sup>g</sup>.

### 3.4 Conclusion

The results from 1D and 2D IR spectroscopies, coupled with data analysis methods PCA and difference spectroscopy to investigate secondary structural changes in GS upon solvent perturbation are in agreement. The shifting of the major band when comparing D<sub>2</sub>O, 1-octanol and TFE confirmed the differences in polarity for the solvent and their different H-bonding potential. Further data analysis of the GS secondary structure by calculation of the transition dipole spectra,  $d(w)^{rel}$  and the 2<sup>nd</sup> derivatives inferred that in the amide I region, the  $\beta$ -sheets located at lower frequency are not affected by changes in solvent environment as they are protected inside the robust GS structure. However, the  $\beta$ -sheets and turns located at higher frequencies are affected when they are solvent exposed, more so in TFE as TFE has strong H-bonding capabilities. Important to note is that  $\beta$ -turns in both amide I and II were sensitive to the amphipathic TFE environment which forms micelle-like structures. Theoretical results from simulations on a trimer model correlated with experimental results in confirming structures present in aggregated GS.

Factors effective in the activity of GS include the amphiphilic, hydrophobic and cyclic hairpin structure. The solvent induced structural changes could be differentiated between a ubiquitous (H<sub>2</sub>O/D<sub>2</sub>O) and a strongly H-bonded (TFE) and partially polar membrane mimicking solvent (1-octanol). The ability to differentiate structural changes being afforded by the sensitivity of 2D-IR spectroscopy. Between a strongly H-bonded and a partially polar solvent, the former supports the formation and existence of all secondary structures in GS which contribute to its amphipathic (hydrophobic and hydrophilic) property which renders GS active. The understanding of GS aggregation/oligomerisation behaviour is key in the generation of GS derivatives aimed at altering residues which contribute to the cationic, hydrophilic, and hydrophobic nature of GS, in enhancing the antimicrobial activity of GS. Solvent studies can provide preliminary results and information which helps elucidate the conformational behaviour of selected bio-active peptide before the peptides are tested on actual targets such as bacterial membranes. Theoretical results based on the trimer model corroborated with experimental results, indicating that depending on whether a peptide is active as a monomer or oligomer (in aggregated form), results can be postulated from simulations prior to conducting experiments.

These results are encouraging with regards to demonstrating the capability of 2D-IR supported by FTIR measurements to investigate small cyclic peptides such as GS. The ability to obtain high quality protein spectra in non-aqueous solvents, with accurate solvent subtraction is a novel result showing how the 2D-IR spectroscopic technique is able to probe peptide and protein structures in environments representative of the membrane environment. Increasing the temperature of GS solutions can be expected to melt the higher order structures which are present at high concentrations, such as those identified in octanol. This shall be reported in detail in Chapter 4.

### 3.5 References

- [1] M. Dostert, C. R. Belanger, and R. E. W. Hancock, "Design and Assessment of Anti-Biofilm Peptides: Steps Toward Clinical Application," *J. Innate Immun.*, vol. 11, no. 3, pp. 193–204, 2019, doi: 10.1159/000491497.
- [2] H. K. Kang, C. Kim, C. H. Seo, and Y. Park, "The therapeutic applications of antimicrobial peptides (AMPs): a patent review," *J. Microbiol.*, vol. 55, no. 1, pp. 1–12, 2017, doi: 10.1007/s12275-017-6452-1.
- [3] J. J. Buffy, A. J. Waring, R. I. Lehrer, and M. Hong, "Immobilization and Aggregation of the Antimicrobial Peptide Protegrin-1 in Lipid Bilayers Investigated by Solid-State NMR," *Biochemistry*, vol. 42, no. 46, pp. 13725–13734, 2003, doi: 10.1021/bi035187w.
- [4] R. Zou, X. Zhu, Y. Tu, J. Wu, and M. P. Landry, "Activity of Antimicrobial Peptide

- Aggregates Decreases with Increased Cell Membrane Embedding Free Energy Cost,” *Biochemistry*, vol. 57, no. 18, pp. 2606–2610, 2018, doi: 10.1021/acs.biochem.8b00052.
- [5] N. Shagaghi, M. Bhave, E. A. Palombo, and A. H. A. Clayton, “Revealing the sequence of interactions of PuroA peptide with *Candida albicans* cells by live-cell imaging,” *Sci. Rep.*, vol. 7, 2017, doi: 10.1038/srep43542.
- [6] E. Gazit, I. R. Miller, P. C. Biggin, M. S. Sansom, and Y. Shai, “Structure and orientation of the mammalian antibacterial peptide cecropin P1 within phospholipid membranes.,” *J. Mol. Biol.*, vol. 258, no. 5, pp. 860–70, 1996, doi: 10.1006/jmbi.1996.0293.
- [7] D. K. V. Kumar *et al.*, “Amyloid- $\beta$  peptide protects against microbial infection in mouse and worm models of Alzheimer’s disease,” *Sci. Transl. Med.*, vol. 8, no. 340, p. 340ra72, May 2016, doi: 10.1126/scitranslmed.aaf1059.
- [8] W. A. Eimer *et al.*, “Alzheimer’s Disease-Associated  $\beta$ -Amyloid Is Rapidly Seeded by Herpesviridae to Protect against Brain Infection,” *Neuron*, vol. 99, no. 1, pp. 56-63.e3, Jul. 2018, doi: 10.1016/j.neuron.2018.06.030.
- [9] Y. Pouny, D. Rapaport, Y. Shai, A. Mor, and P. Nicolas, “Interaction of Antimicrobial Dermaseptin and its Fluorescently Labeled Analogs with Phospholipid Membranes,” *Biochemistry*, vol. 31, no. 49, pp. 12416–12423, 1992, doi: 10.1021/bi00164a017.
- [10] H. Duclohier and H. Wróblewski, “Voltage-dependent pore formation and antimicrobial activity by alamethicin and analogues,” *Journal of Membrane Biology*, vol. 184, no. 1. Springer, pp. 1–12, Nov. 01, 2001, doi: 10.1007/s00232-001-0077-2.
- [11] K. He, S. J. Ludtke, D. L. Worcester, and H. W. Huang, “Neutron scattering in the plane of membranes: Structure of alamethicin pores,” *Biophys. J.*, vol. 70, no. 6, pp. 2659–2666, Jun. 1996, doi: 10.1016/S0006-3495(96)79835-1.
- [12] A. Pino-Angeles and T. Lazaridis, “Effects of Peptide Charge, Orientation, and Concentration on Melittin Transmembrane Pores,” *Biophys. J.*, vol. 114, no. 12, pp. 2865–2874, 2018, doi: 10.1016/j.bpj.2018.05.006.
- [13] D. J. Hirsh, J. Hammer, W. L. Maloy, J. Blazyk, and J. Schaefer, “Secondary structure and location of a magainin analogue in synthetic phospholipid bilayers,” *Biochemistry*, vol. 35, no. 39, pp. 12733–12741, 1996, doi: 10.1021/bi961468a.
- [14] L. A. Munishkina, C. Phelan, V. N. Uversky, and A. L. Fink, “Conformational behavior and aggregation of  $\alpha$ -synuclein in organic solvents: Modeling the effects of membranes,” *Biochemistry*, vol. 42, no. 9, pp. 2720–2730, 2003, doi: 10.1021/bi027166s.
- [15] T. Abraham *et al.*, “Structure-activity relationships of the antimicrobial peptide gramicidin S and its analogs: Aqueous solubility, self-association, conformation, antimicrobial activity and interaction with model lipid membranes,” *Biochim. Biophys. Acta - Biomembr.*, vol. 1838, no.

5, pp. 1420–1429, 2014, doi: 10.1016/j.bbamem.2013.12.019.

- [16] L. Zhang, A. Rozek, and R. E. W. Hancock, “Interaction of Cationic Antimicrobial Peptides with Model Membranes\*,” 2001, doi: 10.1074/jbc.M104925200.
- [17] M. Jelokhani-Niaraki, R. S. Hodges, J. E. Meissner, U. E. Hassenstein, and L. Wheaton, “Interaction of gramicidin S and its aromatic amino-acid analog with phospholipid membranes,” *Biophys. J.*, vol. 95, no. 7, pp. 3306–3321, 2008, doi: 10.1529/biophysj.108.137471.
- [18] Z. Oren, J. C. Lerman, G. H. Gudmundsson, B. Agerberth, and Y. Shai, “Structure and organization of the human antimicrobial peptide LL-37 in phospholipid membranes : relevance to the molecular basis for its non-cell-selective activity,” *Biochem. J.*, vol. 341, pp. 501–513, 1999.
- [19] Y. Pouny, D. Rapaport, A. Mor, P. Nicolas, and Y. Shai, “Interaction of Antimicrobial Dermaseptin and Its Fluorescently Labeled Analogues with Phospholipid Membranes1,” vol. 31, pp. 12416–12423, 1241, doi: 10.1021/bi00164a017.
- [20] E. J. Prenner, R. N. A. H. Lewis, M. Jelokhani-Niaraki, R. S. Hodges, and R. N. McElhaney, “Cholesterol attenuates the interaction of the antimicrobial peptide gramicidin S with phospholipid bilayer membranes,” *Biochim. Biophys. Acta - Biomembr.*, vol. 1510, no. 1–2, pp. 83–92, Feb. 2001, doi: 10.1016/S0005-2736(00)00337-0.
- [21] Z. Su, J. J. Leitch, R. J. Faragher, A. L. Schwan, and J. Lipkowski, “Electrochimica Acta Gramicidin A ion channel formation in model phospholipid bilayers tethered to gold ( 111 ) electrode surfaces,” *Electrochim. Acta*, vol. 243, pp. 364–373, 2017, doi: 10.1016/j.electacta.2017.05.059.
- [22] D. J. Hirsh, J. Hammer, W. L. Maloy, J. Blazyk, and J. Schaefer, “Secondary Structure and Location of a Magainin Analogue in Synthetic Phospholipid Bilayers.”
- [23] E. Gazit, I. R. Miller, P. C. Biggin, M. S. P. Sansom, and Y. Shai, “Structure and Orientation of the Mammalian Antibacterial Peptide Cecropin P1 within Phospholipid Membranes,” pp. 860–870, 1996.
- [24] Z. Su, J. J. Leitch, R. J. Faragher, A. L. Schwan, and J. Lipkowski, “Gramicidin A ion channel formation in model phospholipid bilayers tethered to gold (111) electrode surfaces,” *Electrochim. Acta*, 2017, doi: 10.1016/j.electacta.2017.05.059.
- [25] P. Petkov, E. Lilkova, N. Ilieva, and L. Litov, “Self-association of antimicrobial peptides: A molecular dynamics simulation study on bombinin,” *Int. J. Mol. Sci.*, vol. 20, no. 21, pp. 15–23, 2019, doi: 10.3390/ijms20215450.
- [26] M. J. Bodkin and J. M. Goodfellow, “Hydrophobic solvation in aqueous trifluoroethanol solution,” *Biopolymers*, vol. 39, no. 1, pp. 43–50, 1996, doi: 10.1002/(sici)1097-

0282(199607)39:1<43::aid-bip5>3.3.co;2-5.

- [27] M. Buck, "Trifluoroethanol and colleagues: Cosolvents come of age. Recent studies with peptides and proteins," *Artic. Q. Rev. Biophys.*, 1998, doi: 10.1017/S003358359800345X.
- [28] M. Jelokhani-Niaraki, L. H. Kondejewski, S. W. Farmer, R. E. W. Hancock, C. M. Kay, and R. S. Hodges, "Diastereoisomeric analogues of gramicidin S: Structure, biological activity and interaction with lipid bilayers," *Biochem. J.*, vol. 349, no. 3, pp. 747–755, 2000, doi: 10.1042/bj3490747.
- [29] D. Balasubramanian, "The Conformation of Gramicidin S in Solution," *J. Am. Chem. Soc.*, vol. 89, no. 21, pp. 5445–5449, Oct. 1967, doi: 10.1021/ja00997a027.
- [30] M. Jelokhani-Niaraki, E. J. Prenner, C. M. Kay, R. N. McElhaney, R. S. Hodges, and L. H. Kondejewski, "Conformation and other biophysical properties of cyclic antimicrobial peptides in aqueous solutions," *J. Pept. Res.*, vol. 58, no. 4, pp. 293–306, 2001, doi: 10.1034/j.1399-3011.2001.00893.x.
- [31] S. Laiken, M. Printz, and L. C. Craig, "Circular dichroism of the tyrocidines and gramicidin S-A.," *J. Biol. Chem.*, vol. 244, no. 16, pp. 4454–4457, 1969.
- [32] F. O'Boyle and B. A. Wallace, "The temperature dependence of gramicidin conformational States in octanol.," *Protein Pept. Lett.*, vol. 10, no. 1, pp. 9–17, 2003, doi: 10.2174/0929866033408246.
- [33] R. N. A. H. Lewis *et al.*, "Fourier transform infrared spectroscopic studies of the interaction of the antimicrobial peptide gramicidin S with lipid micelles and with lipid monolayer and bilayer membranes," *Biochemistry*, vol. 38, no. 46, pp. 15193–15203, 1999, doi: 10.1021/bi9912342.
- [34] A. Barth, "The infrared absorption of amino acid side chains," *Progress in Biophysics and Molecular Biology*, vol. 74, no. 3–5, pp. 141–173, 2000, doi: 10.1016/S0079-6107(00)00021-3.
- [35] A. Barth and C. Zscherp, "What vibrations tell about proteins," *Q. Rev. Biophys.*, vol. 35, no. 4, pp. 369–430, 2002, doi: 10.1017/S0033583502003815.
- [36] A. Barth, "Infrared spectroscopy of proteins," *Biochim. Biophys. Acta - Bioenerg.*, vol. 1767, no. 9, pp. 1073–1101, 2007, doi: 10.1016/j.bbabi.2007.06.004.
- [37] F. D. Sonnichsen, J. E. Van Eyk, R. S. Hodges, and B. D. Sykes, "Effect of Trifluoroethanol on Protein Secondary Structure: An NMR and CD Study Using a Synthetic Actin Peptide," *Biochemistry*, vol. 31, no. 37, pp. 8790–8798, 1992, doi: 10.1021/bi00152a015.
- [38] M. Buck, "Trifluoroethanol and colleagues: Cosolvents come of age. Recent studies with peptides and proteins," *Quarterly Reviews of Biophysics*, vol. 31, no. 3, pp. 297–355, 1998, doi: 10.1017/S003358359800345X.
- [39] M. Candelaresi *et al.*, "A structural and dynamic investigation of the inhibition of catalase by

- nitric oxide,” *Org. Biomol. Chem.*, vol. 11, no. 44, pp. 7778–7788, 2013, doi: 10.1039/c3ob41977k.
- [40] H. H. Paradies, “Aggregation of Tyrocidine in Aqueous Solutions,” *Biochem. Biophys. Res. Commun.*, vol. 88, no. 3, pp. 810–817, 1979.
- [41] V. M. Naik and S. Krimm, “Vibrational analysis of peptides, polypeptides, and proteins. XVII. Normal modes of crystalline Pro-Leu-Gly-NH<sub>2</sub>, a type II  $\beta$ -turn,” *Int. J. Pept. Protein Res.*, vol. 23, no. 1, pp. 1–24, 1984, doi: 10.1111/j.1399-3011.1984.tb02686.x.
- [42] S. S. Helle and P. W. Zandstra, “Unusual Surface Tension Behavior of an Aqueous Solution of Gramicidin S,” *J. Colloid Interface Sci.*, vol. 151, no. 1, pp. 130–135, Jun. 1992, doi: 10.1016/0021-9797(92)90243-F.
- [43] R. M. Culik, R. M. Abaskharon, I. M. Pazos, and F. Gai, “Experimental validation of the role of trifluoroethanol as a nanocrowder,” *J. Phys. Chem. B*, vol. 118, no. 39, pp. 11455–11461, 2014, doi: 10.1021/jp508056w.
- [44] Y. Luo and R. L. Baldwin, “Trifluoroethanol stabilizes the pH 4 folding intermediate of sperm whale apomyoglobin,” *J. Mol. Biol.*, vol. 279, no. 1, pp. 49–57, 1998, doi: 10.1006/jmbi.1998.1774.
- [45] M. D. Díaz, M. Fioroni, K. Burger, and S. Berger, “Evidence of complete hydrophobic coating of bombesin by trifluoroethanol in aqueous solution: An NMR spectroscopic and molecular dynamics study,” *Chem. - A Eur. J.*, vol. 8, no. 7, pp. 1663–1669, 2002, doi: 10.1002/1521-3765(20020402)8:7<1663::AID-CHEM1663>3.0.CO;2-P.
- [46] D. Roccatano, G. Colombo, M. Fioroni, and A. E. Mark, “Mechanism by which 2,2,2-trifluoroethanol/water mixtures stabilize secondary-structure formation in peptides: A molecular dynamics study,” *Proc. Natl. Acad. Sci. U. S. A.*, vol. 99, no. 19, pp. 12179–12184, 2002, doi: 10.1073/pnas.182199699.
- [47] R. Rajan and P. Balaram, “A model for the interaction of trifluoroethanol with peptides and proteins,” *Int. J. Pept. Protein Res.*, vol. 48, no. 4, pp. 328–336, 1996, doi: 10.1111/j.1399-3011.1996.tb00849.x.
- [48] R. M. Culik, R. M. Abaskharon, I. M. Pazos, and F. Gai, “Experimental validation of the role of trifluoroethanol as a nanocrowder,” *J. Phys. Chem. B*, vol. 118, no. 39, pp. 11455–11461, 2014, doi: 10.1021/jp508056w.
- [49] L. H. Kondejewski, D. L. Lee, M. Jelokhani-Niaraki, S. W. Farmer, R. E. W. Hancock, and R. S. Hodges, “Optimization of microbial specificity in cyclic peptides by modulation of hydrophobicity within a defined structural framework,” *J. Biol. Chem.*, vol. 277, no. 1, pp. 67–74, 2002, doi: 10.1074/jbc.M107825200.
- [50] M. Buck, H. Schwalbe, and C. M. Dobson, “Characterization of Conformational Preferences

- in a Partly Folded Protein by Heteronuclear NMR Spectroscopy: Assignment and Secondary Structure Analysis of Hen Egg-White Lysozyme in Trifluoroethanol,” *Biochemistry*, vol. 34, no. 40, pp. 13219–13232, 1995, doi: 10.1021/bi00040a038.
- [51] M. Fioroni, M. D. Diaz, K. Burger, and S. Berger, “Solvation phenomena of a tetrapeptide in water/trifluoroethanol and water/ethanol mixtures: A diffusion NMR, intermolecular NOE, and molecular dynamics study,” *J. Am. Chem. Soc.*, vol. 124, no. 26, pp. 7737–7744, 2002, doi: 10.1021/ja0259335.
- [52] J. Kubelka, J. Kim, P. Bour, and T. A. Keiderling, “Contribution of transition dipole coupling to amide coupling in IR spectra of peptide secondary structures,” *Vib. Spectrosc.*, vol. 42, no. 1, pp. 63–73, 2006, doi: 10.1016/j.vibspec.2006.04.003.
- [53] E. B. Dunkelberger, M. Grechko, and M. T. Zanni, “Transition Dipoles from 1D and 2D Infrared Spectroscopy Help Reveal the Secondary Structures of Proteins: Application to Amyloids,” *J. Phys. Chem. B*, vol. 119, no. 44, pp. 14065–14075, 2015, doi: 10.1021/acs.jpcc.5b07706.
- [54] L. Minnes *et al.*, “Quantifying Secondary Structure Changes in Calmodulin Using 2D-IR Spectroscopy,” *Anal. Chem.*, vol. 89, no. 20, pp. 10898–10906, 2017, doi: 10.1021/acs.analchem.7b02610.
- [55] M. Grechko and M. T. Zanni, “Quantification of transition dipole strengths using 1D and 2D spectroscopy for the identification of molecular structures via exciton delocalization: Application to  $\alpha$ -helices,” *J. Chem. Phys.*, vol. 137, no. 18, p. 184202, 2012, doi: 10.1063/1.4764861.
- [56] D. E. Moilanen, D. Wong, D. E. Rosenfeld, E. E. Fenn, and M. D. Fayer, “Ion-water hydrogen-bond switching observed with 2D IR vibrational echo chemical exchange spectroscopy,” *Proc. Natl. Acad. Sci. U. S. A.*, vol. 106, no. 2, pp. 375–380, 2009, doi: 10.1073/pnas.0811489106.
- [57] J. Moger, P. Gribbon, a Sewing, and C. P. Winlove, “Feasibility study using surface-enhanced Raman spectroscopy for the quantitative detection of tyrosine and serine phosphorylation,” *Biochim. Biophys. Acta*, vol. 1770, no. 6, pp. 912–918, 2007, doi: 10.1016/j.bbagen.2007.01.018.
- [58] A. Barth and C. Zscherp, “What vibrations tell us about proteins,” *Q. Rev. Biophys.*, vol. 35, no. 4, pp. 369–430, 2002, doi: 10.1017/S0033583502003815.
- [59] E. J. Prenner, R. N. A. Lewis, and R. N. McElhaney, “The interaction of the antimicrobial peptide gramicidin S with lipid bilayer model and biological membranes,” *Biochim. Biophys. Acta - Biomembr.*, vol. 1462, no. 1–2, pp. 201–221, 1999, doi: 10.1016/S0005-2736(99)00207-2.
- [60] I. V. Tetko and D. J. Livingstone, “Rule-based systems to predict lipophilicity,” in

*Comprehensive Medicinal Chemistry II*, vol. 5, Elsevier Ltd., 2006, pp. 649–668.

- [61] H. Wang, J. Varady, L. Ng, and S. Sung, “Molecular Dynamics Simulations of beta-Hairpin Folding,” *Proteins Struct. Funct. Genet.*, vol. 333, no. June, pp. 325–333, 1999.
- [62] A. W. Lee *et al.*, “Biochemistry (in press). Comparing the Polarities of the Amino Acids: Side-Chain Distribution Coefficients between the Vapor Phase, Cyclohexane, 1-Octanol, and Neutral Aqueous Solution\*,” *Proc. Natl. Acad. Sci. U.S.A.*, vol. 27, pp. 3693–3677, 1964, Accessed: Jan. 28, 2021. [Online]. Available: <https://pubs.acs.org/sharingguidelines>.
- [63] C. Solanas *et al.*, “Therapeutic index of gramicidin S is strongly modulated by D-phenylalanine analogues at the  $\beta$ -turn,” *J. Med. Chem.*, vol. 52, no. 3, pp. 664–674, 2009, doi: 10.1021/jm800886n.
- [64] V. M. Naik, S. Krimm, J. B. Denton, G. Nemethy, and H. A. Scheragai, “Vibrational analysis of peptides, polypeptides and proteins,” *Int. J. Pept. Protein Res.*, vol. 24, no. 6, pp. 613–626, 1984, doi: 10.1111/j.1399-3011.1984.tb03168.x.
- [65] C. B. Silva, J. G. da Silva Filho, G. S. Pinheiro, A. M. R. Teixeira, and P. T. C. Freire, “Vibrational and structural properties of L-Alanyl-L-Phenylalanine dipeptide by Raman spectroscopy, infrared and DFT calculations,” *Vib. Spectrosc.*, vol. 98, no. July, pp. 128–133, 2018, doi: 10.1016/j.vibspec.2018.08.001.
- [66] Y. Ji *et al.*, “DFT-Calculated IR Spectrum Amide I, II, and III Band Contributions of N-Methylacetamide Fine Components,” *ACS Omega*, vol. 5, no. 15, pp. 8572–8578, 2020, doi: 10.1021/acsomega.9b04421.
- [67] C. W. Bauschlicher and S. R. Langhoff, “The calculation of accurate harmonic frequencies of large molecules: The polycyclic aromatic hydrocarbons, a case study,” *Spectrochim. Acta - Part A Mol. Biomol. Spectrosc.*, vol. 53, no. 8, pp. 1225–1240, 1997, doi: 10.1016/S1386-1425(97)00022-X.

## Chapter 4 Temperature effects on the structure of Gramicidin S (GS)

### 4.1 Introduction

This chapter describes the thermally induced conformational changes in GS aggregates. IR spectroscopy has been employed in monitoring protein interactions, changes in aggregation, and folding / unfolding behaviour of peptides [1]–[4]. Peak shifts in the amide I band are small compared to the linewidth of the band, therefore secondary structures do not form fully resolved peaks and they fall under one broad band with several shoulders [5], [6]. However, different protein and peptide secondary structures have different temperature stabilities and the amide I band shows temperature dependent frequency shifts. These shifts, together with mathematical models, can be used to elucidate structural changes in proteins and peptides [2], [6]. One of the main reasons why temperature dependent studies are done on proteins is for determining critical conditions for storage of therapeutic proteins [7]. These temperature conformational studies are sometimes done in organic solvents in order to mimic a particular environment that could promote a particular conformation [8], [9].

In Chapter 3 our results showed that aggregation of GS possibly takes place in the amphipathic alcohol, 1-octanol, with increasing peptide concentration. The focus of the work is driven to investigate the higher order structure and conformation of GS, as a model cyclodecapeptide. It is fundamental and significant as it serves as a basis for understanding peptide structure and behaviour of the broader cyclodecapeptide class. The structure of GS as a cationic cyclic antimicrobial peptide has already been described in the previous chapters. This study aims to understand the solution phase behaviour of GS as a function of temperature. 1-octanol is chosen as a solvent as it complements the amphipathic structure of GS, in addition to its properties such as high temperature stability, lack of significant interference with the GS amide I mode and the solubility of GS.

The goal of this chapter is to test the hypothesis that temperature induced changes in the GS 2D-IR spectra can be correlated to the gradual disruption of higher order structures/aggregates in concentrated solution of GS. The study demonstrates the application of advanced spectroscopic techniques in the study of GS conformational behaviour and identification of structural changes of GS and GS oligomers/aggregates in solution phase. The information obtained on the GS model cyclodecapeptide system, will assist in the development of *ab initio* predictions of peptide structure and so facilitate 2D-IR simulations on more complex members of the cyclodecapeptide group, in particular promoting developments of advanced antimicrobial agents.

## 4.2 Sample preparation and measurements

A solution of 5.00 mg/mL (4.38 mM) was prepared and housed in a temperature-controlled transmission (Harrick) cell. 2D-IR spectra were collected at waiting times of 0.1 ps between 0.4 – 3 ps. For both FTIR and 2D-IR measurements the temperature was controlled using an oil bath and at each set temperature, a measurement was taken after the sample equilibrated at that temperature ( $\pm 1$  °C) for 15 mins. Temperature range between 20 °C - 80 °C was considered. At each set temperature, the solvent spectrum was subtracted from solution spectrum to remove any solvent contributions from the spectra, ensuring that only temperature changes to the peptide are measured. Temperature of the cell was measured using a thermocouple.

## 4.3 Results

### 4.3.1 FTIR Absorption Spectroscopy

To monitor structural changes the spectral range of 1600 – 1700  $\text{cm}^{-1}$  was chosen, i.e. focusing on the amide I mode, for the temperature measurements. IR spectra from Chapter 3 for GS in 1-octanol at a high concentration of 5.00 mg/mL showed that dominant  $\beta$ -sheet structures existed in 1635-1645  $\text{cm}^{-1}$  while there was loss in  $\beta$ -turns at 1645 – 1700  $\text{cm}^{-1}$ . Increasing temperature is expected to disrupt the aggregates.

From *Figure 4.1*, in its native state at 20 °C, GS shows a broad peak is centred at 1645  $\text{cm}^{-1}$ . Upon increase in temperature to 80 °C, the peak broadens and blue shifts to 1647  $\text{cm}^{-1}$ . An isosbestic point is present at 1650  $\text{cm}^{-1}$  (*Figure 4.1a*). The temperature induced changes of the IR spectra in *Figure 4.1a* are highlighted in the difference spectra in *Figure 4.1b* where loss of structure is identified at 1645-1647 and 1665-1666  $\text{cm}^{-1}$  from C=O stretching of  $\beta$ -sheets and  $\beta$ -turns, respectively. A gain in structure is present around 1620  $\text{cm}^{-1}$  where there are Phe C-C stretch vibrations and at 1680-1699  $\text{cm}^{-1}$  where there are C=O stretch vibrations from  $\beta$ -sheets (refer to Chapter 3, *Table 3.5*).

Gaussian fittings to the IR data were considered for GS in 1-octanol at 20 and at 80 °C. At 20 °C the IR difference spectra for GS in 1-octanol highlighted two major changes which were an increase in absorption in the range 1635 – 1645  $\text{cm}^{-1}$  resulting from a gain in  $\beta$ -sheet content and a loss in absorption in the range 1645 – 1700  $\text{cm}^{-1}$  (Chapter 3 section 3.3.1 on IR global analysis). Therefore, two peaks were fitted at 20 °C to represent those structures (*Figure 4.2a*). At high temperature 80 °C, major spectral changes were identified from the difference spectra by a gain in intensity in the range 1615-1630 and 1670-1699  $\text{cm}^{-1}$  and a loss in main band at 1645 - 1647  $\text{cm}^{-1}$ . Accordingly, three bands were fitted at 80 °C. Also, the idea of fitting 3 bands at 80 °C is supported again by similar changes occurring in the same ranges which are reported below for the PC 2 component of FTIR data (section

4.3.3). In fitting the peaks, the width and peak positions were not fixed so as to observe thermal effects on spectral changes in peak shift and decrease/increase in intensity.

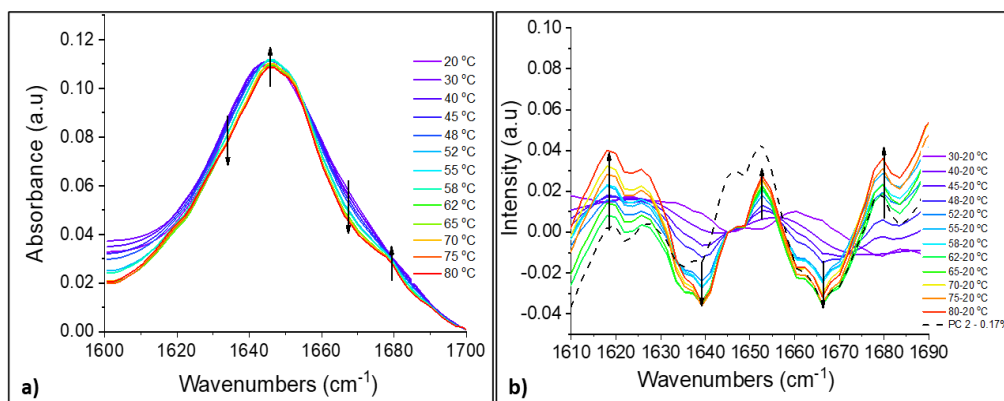


Figure 4.1 (a) FTIR absorption spectra of the amide I region measured over the temperature range 20 – 80 °C for GS in solvent 1-octanol. The spectra have been solvent subtracted and for presentation the range 1600 – 1700  $\text{cm}^{-1}$  is presented here. In (b) difference spectra obtained by subtracting the normalised spectrum at 20 °C from the normalised spectra at elevated temperatures. In (b) the black dashed line is for the PC2 contribution.

Gaussian peak fitting to the absorption plots confirmed the subtle shift to higher wavenumbers for the main band from 1645  $\text{cm}^{-1}$  to 1647  $\text{cm}^{-1}$  as well as decrease of the main band in full width half maximum (FWHM) by 6  $\text{cm}^{-1}$ . As the band broadens some features emerge at higher frequency and high temperature, as depicted from the fits. An identified band near 1620  $\text{cm}^{-1}$  is contributed to by the C-C stretch of the Phe ring and one near 1670  $\text{cm}^{-1}$  from C=O stretch of the  $\beta$ -turns. For the fits at 20 °C and 80 °C, the low residual values were in range  $\pm 0.05\%$  and  $\pm 0.15\%$ , respectively, suggesting a good fit (Figure 4.2a and b). The narrowing of the main absorption band at 1645  $\text{cm}^{-1}$  was confirmed by the decrease in FWHM (Figure 4.2c) and integral area under the graph (Figure 4.2d). Using first derivatives to locate peak maxima positions, the temperature curves are shown in Figure 4.3.

In GS amide I the  $\beta$ -sheet and ornithine structures are located at 1642 and 1645  $\text{cm}^{-1}$  respectively (refer to Table 3.5). With increasing temperature, the shifting of the  $\beta$ -sheet structures towards 1645  $\text{cm}^{-1}$  and the ornithine shift towards 1647  $\text{cm}^{-1}$  indicate conformational change in which the Orn vibrational coupling is disrupted and more independent vibrations are observed. The emergence of the 1620  $\text{cm}^{-1}$  signal at 80 °C (Figure 4.2b) may indicate a conformational and/or environmental change of the Phe side chain, while the signal at 1647  $\text{cm}^{-1}$  relates to the Orn side chain and the signal at 1673  $\text{cm}^{-1}$  could be because of “unmasking”, i.e. the release of the C=O groups to form H-bond in the  $\beta$ -turns or vibrational uncoupling in the emerging conformations. From the melting curves two transition points are identified with melting temperatures at  $T_{m1} = 43\text{ °C}$  and  $T_{m2} = 57\text{ °C}$  (Figure 4.3). In Figure 4.3 two melting curves are fitted to show clearly the two melting temperatures. With

increasing temperature, the structures from Phe contribution at  $1620\text{ cm}^{-1}$ , Orn at  $1647\text{ cm}^{-1}$  and C=O  $\beta$ -turns at  $1673\text{ cm}^{-1}$  become apparent and are present in solution above  $T_{m2}$  of  $57\text{ }^{\circ}\text{C}$  (Figure 4.2c and d and Figure 4.3).

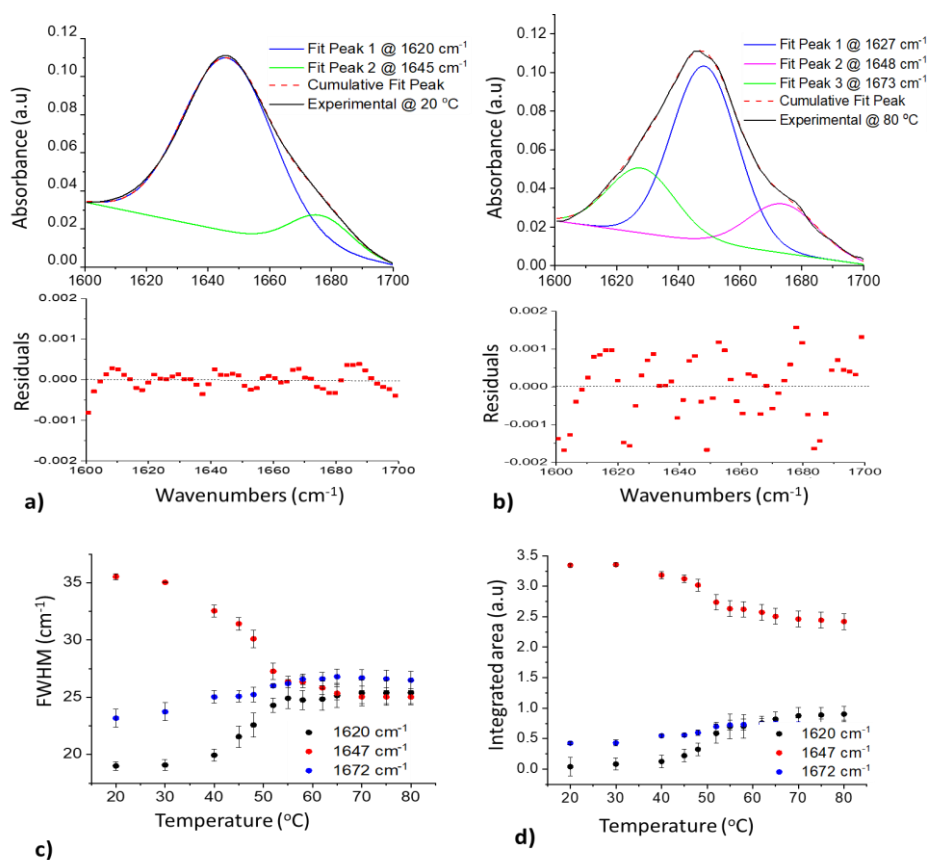


Figure 4.2 Graph a). shows the experimental IR spectra with fitted peaks at native temperature  $20\text{ }^{\circ}\text{C}$  for GS in the native state, the fits are according to the major structures present which are contributions from  $\beta$ -sheet  $1635\text{-}1645\text{ cm}^{-1}$  and  $\beta$ -turns  $1645\text{-}1700\text{ cm}^{-1}$ . Graph b) shows the experimental IR spectra at high temperature  $80\text{ }^{\circ}\text{C}$  with fitted peaks located at in range  $1615\text{-}1630$ ,  $1645\text{-}1647$  and  $1670\text{-}1699\text{ cm}^{-1}$ . The plotted residual data shows the goodness of the fits. Graph c). and d). show how the FWHM and the Integrated area, respectively, change with increasing temperature as the GS aggregate disintegrates.

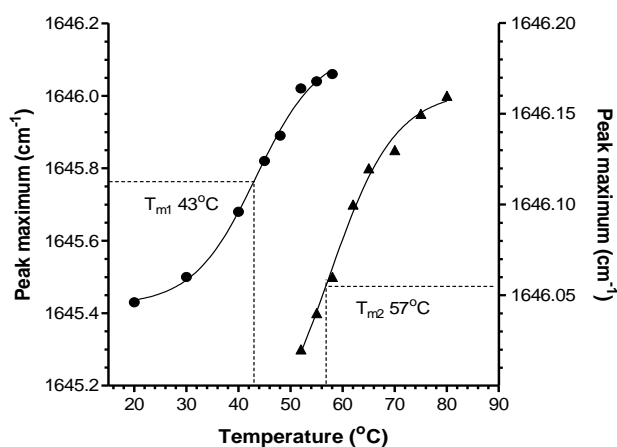


Figure 4.3 Melting curves (Boltzmann sigmoidal profiles) of the peak maxima shift of the main absorption band at  $1645\text{ cm}^{-1}$  fitted for the first transition from  $20\text{ - }58\text{ }^{\circ}\text{C}$  with first melting temperature  $T_{m1} = 43\text{ }^{\circ}\text{C}$  and the second transition with melting temperature  $T_{m2} = 57\text{ }^{\circ}\text{C}$  fitted from  $52\text{ - }80\text{ }^{\circ}\text{C}$ .

To confirm that the observed structural changes over the considered temperature range were emerging and that GS did not undergo irreversible denaturation, the heated sample was allowed to cool and FTIR were measured again. Comparison of the unheated sample spectrum with the cooled spectrum indicated that the original structures/conformations were regained.

### 4.3.2 2D-IR Spectroscopy of GS in 1-octanol

To follow up on the temperature dependent changes observed for GS in 1-octanol using FTIR, the 2D-IR analysis of GS at different temperatures aimed to resolve and identify the emergence of minor bands at high temperature and behaviour of the main bands. The temperature range of the 2D-IR measurements was kept the same as for the FTIR measurements. The identified peak positions in the 2D spectra are given as the probe index.

Spectra acquired in temperature range 20 – 80 °C are presented in *Figure 4.4*. The 2D-IR spectra taken at 20 °C shows a positive diagonal peak at 1650 cm<sup>-1</sup> for the  $\nu = 0 - 1$  transition. A negative off-diagonal peak for the  $\nu = 1 - 2$  transition is at 1630 cm<sup>-1</sup>, shifted by the anharmonicity of the amide I mode. Pump slices taken at 1640, 1650 and 1660 cm<sup>-1</sup> showed that the anharmonic shifts were not constant giving 15, 15 and 13 cm<sup>-1</sup> shifts, respectively at each wavenumber. At 80 °C, the diagonal peak was present at 1651 cm<sup>-1</sup> while the off-diagonal peak was at 1636 cm<sup>-1</sup> for the  $\nu = 0 - 1$  and  $\nu = 1 - 2$  transitions, respectively. Again, pump slices taken at 1640, 1650 and 1665 cm<sup>-1</sup> showed non-constant shifts of 21, 19 and 16 cm<sup>-1</sup>, respectively. The small anharmonicities are indicative of greater coupling at low temperature and these levels of coupling are reduced at higher temperature with larger shifts [10]. This will be elaborated further when discussing the transition dipole in section 4.3.5.2.

The difference spectra for the 20 to 80 °C range are presented in *Figure 4.5*. The spectrum for 80 - 20 °C shows an intense positive peak at 1646 cm<sup>-1</sup> showing a gain in intensity and two negative peaks at 1613 cm<sup>-1</sup> and 1666 cm<sup>-1</sup> representing a loss in intensity (*Figure 4.5*). An off-diagonal shoulder below the diagonal is gradually lost with increasing temperature. The positive peak at 1646 cm<sup>-1</sup> starts to elongate at temperatures 43 / 47 °C (first T<sub>m1</sub>) indicating interference of inter-peptide hydrogen bonds as they gradually break. While after the second transition T<sub>m2</sub> which is in-between 55-58 °C the intra-peptide hydrogen bonds protecting the oligomers are exposed at high temperature [11], [12].

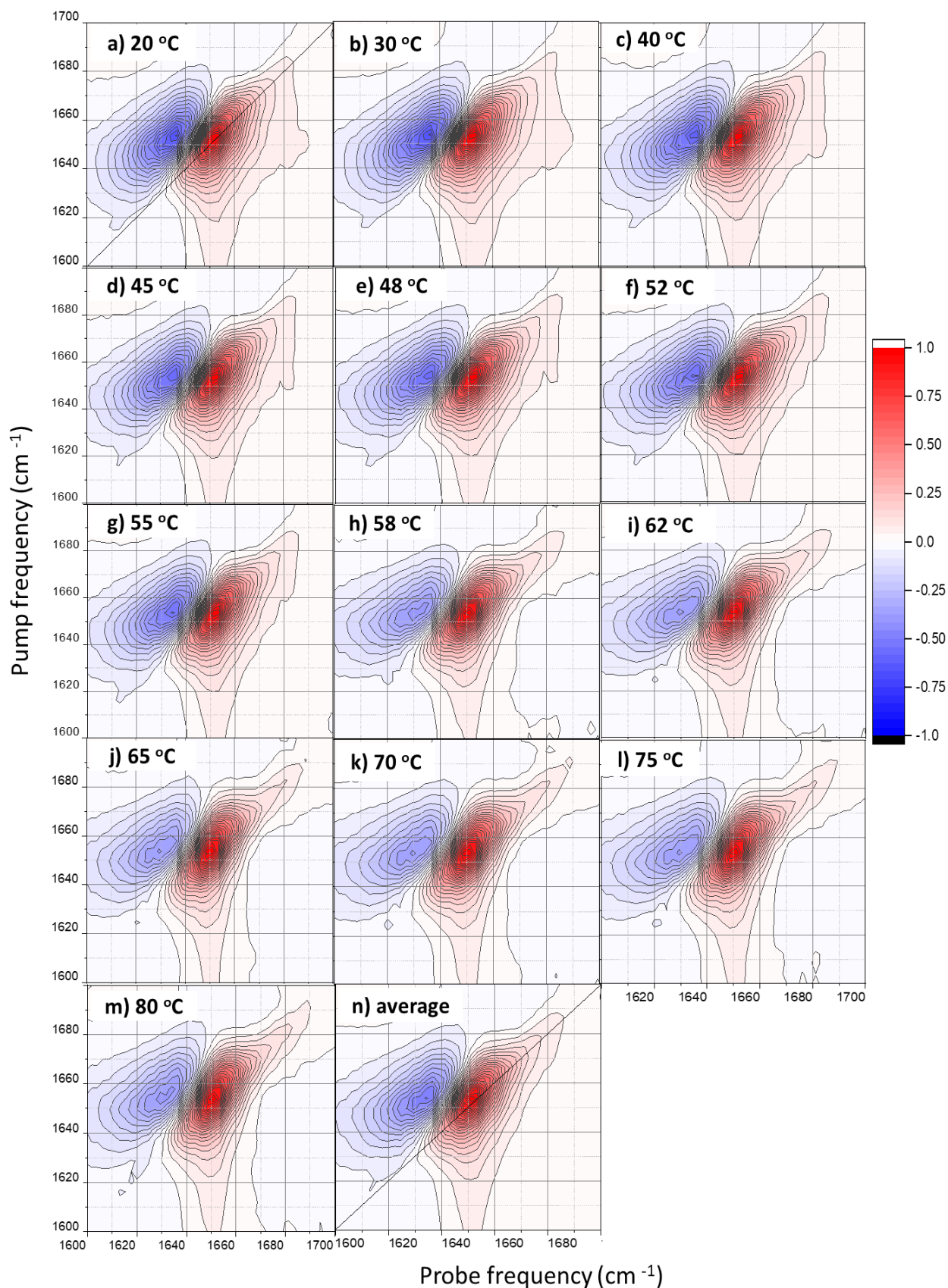


Figure 4.4 2D-IR spectra measured for the temperature range 20 oC - 80 oC as indicated. The average spectrum is for all temperatures and is presented for reference.

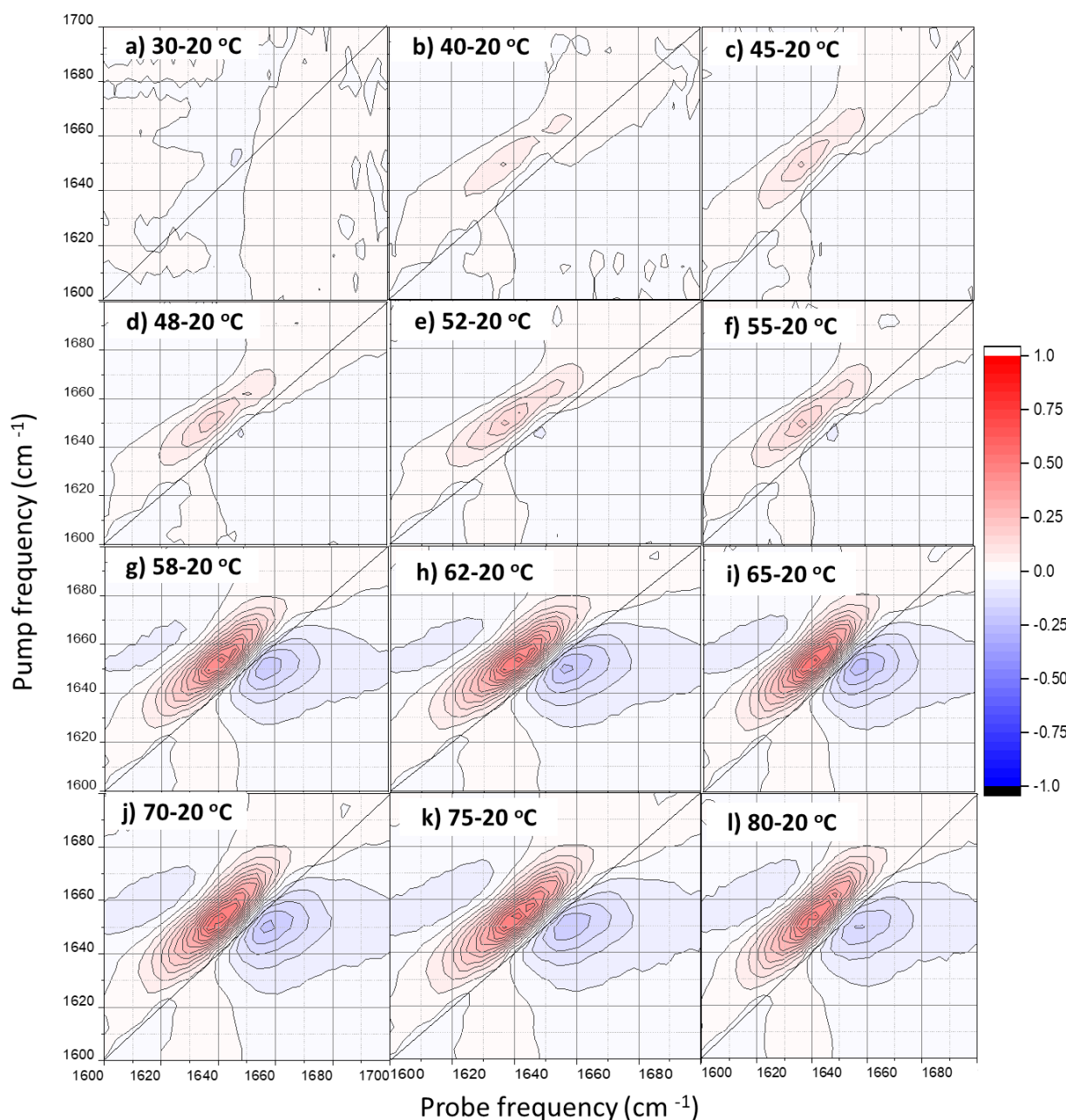


Figure 4.5 Difference spectra for 30 to 80 °C. Each spectrum was obtained by subtracting the spectrum at 20 °C from spectrum at elevated temperatures.

### 4.3.3 PCA of temperature dependent changes in the FTIR and 2D-IR spectra

PCA was applied to both the FTIR and the 2D-IR data at all the temperatures. This was done to highlight the main temperature dependent variation in both the FTIR and 2D-IR data. For both FTIR and 2D-IR, the data was well represented by only the first two principal components with PC 1 (96.19 %) being temperature independent and containing a larger part of the variance and PC 2 (3.72 %) showing a strong temperature dependence. 2D-IR spectra measured in the range 20 – 80 °C were represented in PC 1 (Figure 4.6a) which in-turn resembled the average spectra (Figure 4.6c) across the

temperatures measured and the difference spectra was represented by PC 2 (Figure 4.6b), showing the temperature dependant variations as obtained from the difference spectra. PC 1 shows a gain in intensity at  $1650\text{ cm}^{-1}$  and loss at  $1634\text{ cm}^{-1}$ . PC 2 showed a positive broad peak centred at  $1646\text{ cm}^{-1}$  and loss of intensity at  $1630$  and  $1666\text{ cm}^{-1}$ , respectively. There is also gain near  $1620\text{ cm}^{-1}$  and at higher frequency from  $1685$  to  $1700\text{ cm}^{-1}$ . From the assignment in Chapter 3 and based on computations and mode observations in GaussView 5, this confirms structures from Phe and  $\beta$ -turns and sheets located in that region which are present at high temperature as observed from FTIR and 2D-IR results above (refer to section 3.4.3).

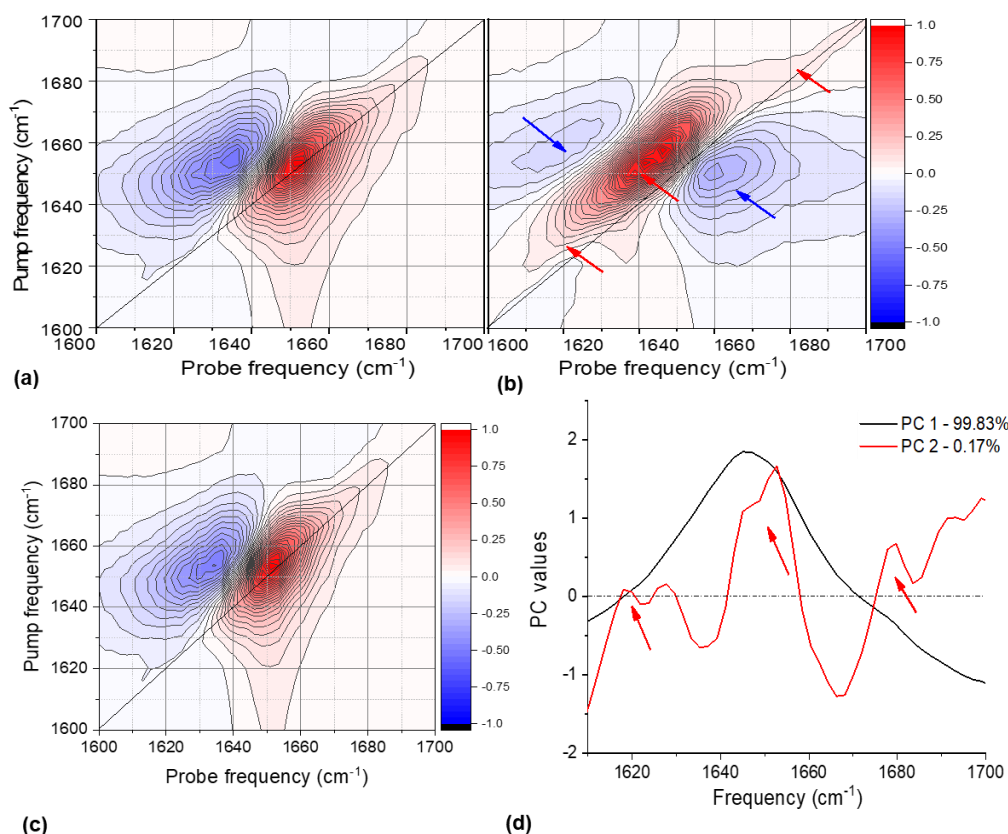


Figure 4.6 (a) and (b) are PC1 and PC2 spectral contributions from 2D-IR. Spectrum (c) is the average spectra which resembles the PC1 contribution in (a). The PC contributions from 1D FTIR data are shown in (d).

For FTIR the variance was largely represented by PC 1 (99.83 %) and less in PC 2 (0.17 %) (Figure 4.6d). The spectra could be reconstructed from the two PC contributions. The FTIR spectrum reconstructed from PC 1 showed a positive broad band centred at  $1648\text{ cm}^{-1}$  and the PC 2 reconstruction had a gain in features near  $1620$ ,  $1650$  and  $1680$  and losses at  $1635$  and  $1663\text{ cm}^{-1}$ . These features correspond to those obtained in 2D. PCA results revealed the major variations of the data to support further interpretation, together with assignments made on the GS in 1-octanol spectra from Chapter 3.

The PCA results from both 1D IR and 2D-IR data both show that at low temperature, the H-bonding inside the peptide (intra-peptide H-bond in the two  $\beta$ -turns and antiparallel  $\beta$ -sheet) is strong and that the multiple interpeptide H-bond and other non-covalent interactions such as aromatic stacking of the Phe residues and hydrophobic clustering of the hydrophobic side chains (Leu, Val, Phe and to a lesser extent Pro) keep GS at high concentrations as oligomers or aggregated structures. With increasing temperature, a temperature,  $T_{m2}$ , is reached where there is significant loss in off-diagonal peaks at lower and higher frequency. This is discussed further with reference to melting curve profiles in sections below. Spectral density is lost at near  $1640\text{ cm}^{-1}$  and  $1650\text{ cm}^{-1}$ . This loss is from C=O stretch of amide I assigned to  $\beta$ -sheets of GS, correlating with our FTIR results (refer *Table 4.1* under the spectral assignment section), as according to our spectral assignment in Chapter 3. The gain in structure at  $1618\text{ cm}^{-1}$  is from the stretching of the C-C ring, while the gain at  $1645\text{--}1647\text{ cm}^{-1}$  is from bending of the  $\text{NH}_3^+$  of Orn and the gain at  $1685\text{--}1699\text{ cm}^{-1}$  is from the  $\beta$ -turn and  $\beta$ -sheet C=O stretch in the amide I region. This loss is an indication of disruption of stacks as the oligomers melt with increasing temperature, in addition to a loss in the inter H-bond which were keeping the oligomers in place.

#### 4.3.4 Thermodynamic analysis of GS thermal profile

The thermal profiling for a protein can be characterised by different approaches. For GS we assumed that the changes were related to loss of oligomers/aggregates and loss of intrapeptide secondary structures. Thermodynamic studies ultimately provide the melting temperature profiles and calculation of Gibbs free energy can be used to determine the transformational changes and direction of equilibrium. In addition, ratio plots of intensity and bandwidth changes can be used to characterise the thermal profile. These methods are discussed below.

In general, the disappearance of the cross peaks in the 2D-IR spectra was gradual from  $20\text{ }^\circ\text{C}$  to  $55\text{ }^\circ\text{C}$  and we observed a significant loss above  $55\text{ }^\circ\text{C}$ . From the PCA results, the thermal profile for temperature range  $20\text{--}80\text{ }^\circ\text{C}$  shows two transition temperatures at  $41$  and  $57\text{ }^\circ\text{C}$  for 2D-IR and  $45$  and  $60\text{ }^\circ\text{C}$  for FTIR (*Figure 4.7*). The melting temperature values correlate with those obtained in the global analysis on thermal induced changes observed in FTIR (*Figure 4.3*).

The melting process of GS gave a bimodal profile as shown from the PC coefficients in (*Figure 4.7*). To confirm the integrity of the results once the maximum temperature measurement had been made the sample was allowed to cool back to  $20\text{ }^\circ\text{C}$  and the measurement was repeated. The spectrum collected after the sample had cooled back to  $20\text{ }^\circ\text{C}$  was similar to that collected at the beginning of the temperature ramp again at  $20\text{ }^\circ\text{C}$ . Within experimental error spectra differed by a minimal  $3.7\%$ , demonstrating that the melting process was reversible (*Figure 4.8*).

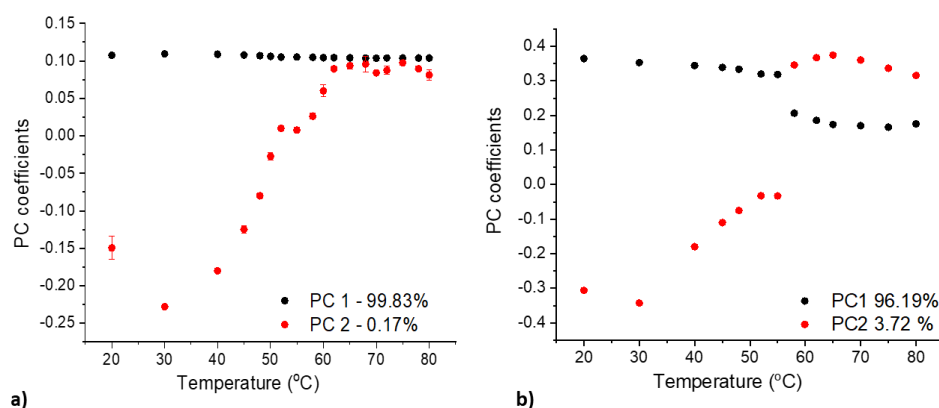


Figure 4.7 PC1 and PC2 coefficients vs temperature for a) FTIR and b) 2D-IR. Both the PC2 profiles show thermal induced changes from PCA analysis on the IR and 2D-IR data.

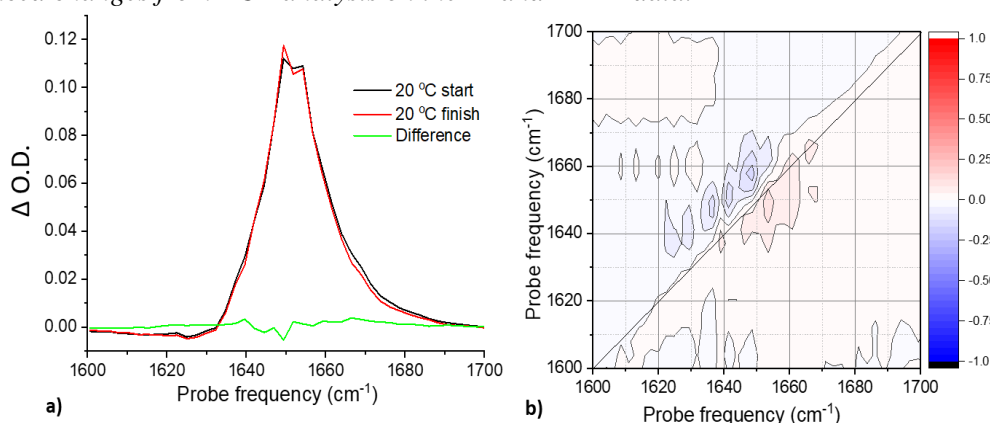


Figure 4.8 Plot a) shows the diagonal spectra taken from 2D spectra at 20 °C before heating (black curve) and after the sample had cooled back to room temperature of 20 °C (red curve) together with the difference spectrum (green curve). In spectrum (b) is the 2D-IR difference spectrum. The difference spectrum accounts for only ~ 3.7 % content and is to show that no peptide structure content was lost due to denaturation.

For the solution phase structures of GS in 1-octanol we assume that the bulk of the non-covalent structural elements that we are observing in the amide I region is the C=O vibrations of  $\beta$ -sheets (inter- and intrapeptide H-bond) and the intrapeptide  $\beta$ -turns. Thus, the transitions we observed are therefore assumed to be from aggregates with interpeptide H-bond which dissociate to smaller oligomers which also further dissociate to monomeric structures with intrapeptide  $\beta$ -sheets and  $\beta$ -turns. Since GS is known to maintain its robust structure under varying temperature or solvent conditions and is robust [13], to obtain a fully denatured GS without any intra-peptide H-bond a  $T_m$  higher than 80 °C could be expected. We can therefore apply the following (Equation 4.1);



We apply legitimate thermodynamic functions to see how the stability of the  $\beta$ -sheet structure for GS changes with temperature and characterise the two-state unfolding/dissociation process, identified in

Figure 4.3 and Figure 4.7, to calculate the energy needed in melting away the inter-peptide hydrogen-bonds. In the discussion below, unfolded peptide refers to dissociated or unaggregated peptide.

The 2D-IR diagonal curves was used to investigate the thermodynamic behaviour of the unfolding process. This is because the integrated area underneath the 2D-IR diagonal curve varies with temperature and is not conserved [1], and thermodynamic parameters which describe the reversible process of dissociation of the oligomers can be deduced. The thermodynamic parameters include the Van't Hoff enthalpy, ( $\Delta H$ ), the entropy ( $\Delta S$ ) of unfolding/dissociation, the melting temperatures, ( $T_m$ ), and the free energy of unfolding ( $\Delta G$ ) could be determined. At the melting temperature,  $T_{m1}$ , the larger aggregates and smaller oligomeric populations are equal in concentration and energies [14]–[16]. At the melting temperature,  $T_{m2}$ , the smaller oligomeric GS and monomeric GS populations are equal in concentration and energy. Above  $T_{m2}$ , ( $T > T_{m2}$ ) the native state (oligomers) is less stable and below  $T_{m2}$ , ( $T < T_{m2}$ ) the native state is more stable. The  $T_{m2}$  value is obtained from the midpoint of the protein melting transition curve, where the fraction of the dissociated/unfolded population is half the total population.

Firstly, the fraction,  $f$ , of dissociated/unfolded peptide aggregates (referred to as  $f_{unfolding}$ ) can be obtained from the observed/measured 2D-IR spectral signal ( $S$ ) values according to Equation 4.2. This signal,  $S$ , being the absolute signal of the 2D-IR diagonal spectra at each temperature. A spectral representation of how the unfolded fraction varies with temperature gives the plot in Figure 4.9. The data points plotted in Figure 4.9 were obtained from the PCA results, and agrees with the melting curve.

$$f_{unfolding} = \frac{S_{observed} - S_{folded}}{S_{unfolding} - S_{folded}} \quad 4.2$$

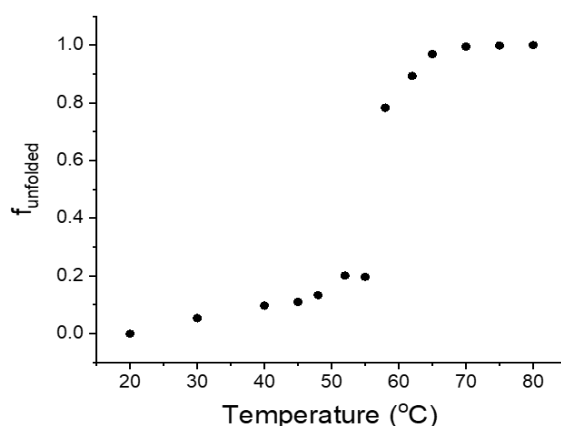


Figure 4.9 Spectral representation of the fraction of dissociated/unaggregated/unfolded peptide with the plotted values calculated from the observed signal.

Where the fraction of unaggregated/dissociated/unfolded peptide is  $0 < f_{unfolded} > 1$ . In the simplest case of unfolding between two transitions of association/folding and dissociation/unfolding, at any temperature the constant of folding or the equilibrium constant,  $K_{eq}$ , is given by the ratio of the fraction of the unfolded,  $f_{dissociated/unfolded}$ , and the folded peptide,  $f_{associated/folded}$  ;

$$K_{eq} = \frac{f_{dissociated/unfolded}}{f_{associated/folded}} \quad 4.3$$

The changes in entropy,  $S$ , enthalpy,  $H$ , and Gibbs free energy,  $G$ , are given by the classical equation [16]–[18];

$$\Delta G = \Delta H - T\Delta S \quad 4.4$$

The reaction equation for association/folding and dissociation/unfolding;

$$\Delta G = -RT \ln K_{eq} \quad 4.5$$

Where  $R$  is the Gas constant =  $1.98 \text{ cal mol}^{-1} \text{ K}^{-1}$ , and  $T$  is the absolute temperature in (Kelvins) and  $K_{eq}$  is the equilibrium constant.

Combining *Equation (4.4)* and *(4.5)* gives;

$$\ln K_{eq} = -\frac{\Delta H}{R} \frac{1}{T} + \frac{\Delta S}{R} \quad 4.6$$

Where *Equation (4.6)* is straight line equation in the form  $y = mx + c$ , whose gradient and intercept can be used to extract the enthalpy and entropy, respectively;

$$\text{Gradient, } m = -\frac{\Delta H}{R} \quad 4.7$$

$$\text{Intercept, } c = \frac{\Delta S}{R} \quad 4.8$$

Thus;  $\Delta H = -(m * R)$  and  $\Delta S = (c * R)$ .

From the profiled dissociation / unfolding / melting process of solution phase GS (*Figure 4.7*), transitions can be identified within two temperature ranges; at 40-55 and 48-80 °C.  $T_{ml}$  was identified as 43 °C (316 K) from *Figure 4.3*; 45 °C (318 K) from *Figure 4.7a* and 41 °C (314 K) from *Figure*

4.7b. This gave a broad range of values from 41-47 °C (314 - 320 K) as  $T_{m1}$  from data obtained from different methods. This discrepancy could be due to multiple aggregated structures converting to a relatively homogenous oligomer population and will be discussed under the spectral assignments below.  $T_{m2}$  was calculated as 57 °C (330 K) from *Figure 4.3*, *Figure 4.7b* and *Figure 4.11a*. *Figure 4.11* shows the separation the pre- and post-transition states with reference to  $T_{m2}$ .  $T_{m3}$  could not be determined from the current datasets. Two temperature regions 40-55 and 48-80 °C were selected from *Figure 4.9* and Boltzmann sigmoidal profiles were fitted so as to identify  $T_{m1}$  and  $T_{m2}$  as shown in *Figure 4.10*. In the appendix section *Table 7.1* is for the calculated values on free energy.

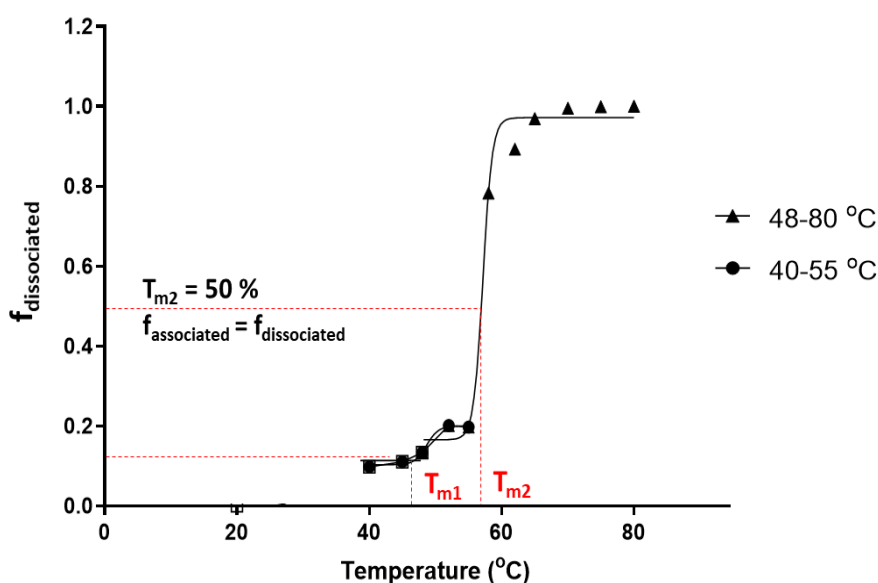


*Figure 4.10* Boltzmann sigmoidal combination of profiles from the fraction of dissociated peptide. The two profiles are fitted in the temperature ranges 40 – 55, 48 – 80 °C. Identified transition temperatures  $T_{m1}$  and  $T_{m2}$  are shown.

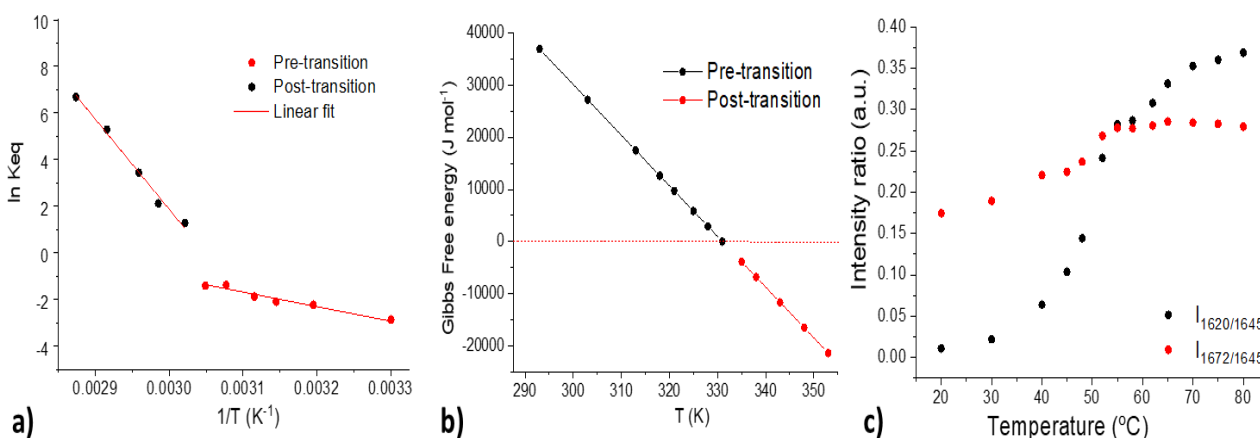


*Figure 4.11* a) The Van't Hoff plot; (b) Gibbs free energy plot; and (c) is the intensity ratio between the main absorption band at  $1645\text{ cm}^{-1}$  and the emerging bands around  $1620$  and  $1670\text{ cm}^{-1}$  identified from the Gaussian fits in *Figure 4.2*. These plots are with reference to the transition temperature  $T_{m2} = 57\text{ °C}$ .

A consistent  $T_{m2}$  value of 57°C (330 K) was obtained using analysis methods which include PCA and fitting of the Boltzmann sigmoidal profile. Thus, for calculation of thermodynamic parameters  $T_{m2}$  was used as the reference temperature for pre- and post-transitions where GS oligomers form GS monomers. Using this  $T_{m2}$  value and the derived equation above, the enthalpy was calculated as  $\Delta H = -321.5 \pm 0.03$  kJ/mol, and entropy as  $\Delta S = 0.98 \pm 0.02$  kJ/mol-K for the pre-transition reaction from 20 – 57 °C and the  $\Delta H = -52.0143 \pm 0.0004$  kJ/mol and  $\Delta S = 0.15 \pm 0.01$  kJ/mol for the post-transition reaction from 57 – 80 °C. The free energy  $\Delta G$  at  $T_{m2}$  is  $-3.5 \pm 0.1$  kJ/mol. Overall, we have negative enthalpy and positive entropy at both pre- and post-transitions. The increasing enthalpy implies that as heat is being added to the system of GS oligomers, the oligomers are dissociating, and the system energy is increasing, and the process of melting oligomers is being favoured and the decreasing free energy indicates an endothermic process. Our values relate well to enthalpy and entropy changes for unfolding endotherm reaction which been reported for proteins such as BSA and lysozyme [19] and free energy values obtained for experiments in pressure and temperature induced unfolding processes [20], [21]. The thermal profile and the melting temperature are further supported using FTIR spectra after band fitting from (*Figure 4.2*), where the ratio was between the fitted bands of (absorbance of the most intense band) / (absorbance of the emerging bands) (*Figure 4.11c*).

Additionally, from the band fitting done on FTIR spectra in *Figure 4.2*, the temperature dependence for the centre frequency shift showed that the emerging band at low frequency shifted the most with increasing temperature (*Figure 4.12*). This could be due to formation of hydrogen bonds by the amine groups (donors) with the oxygen of the carboxyl groups (acceptors) forming a H-bond network other than  $\beta$ -sheet or  $\beta$ -turns and/or the interaction of both N-H and C=O groups with the -OH of 1-octanol (donor and acceptor) leading to a significant red-shift within the spectrum [22]. Alternatively, the emergence of the peak at 1620  $\text{cm}^{-1}$  could be due to the release of the Phe side chain from GS aggregate structures dependent on aromatic stacking and other non-covalent interactions.

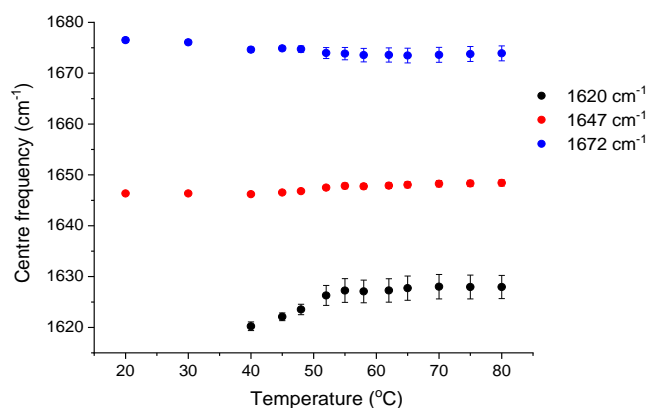


*Figure 4.12* Change in the centre frequency with temperature for the fitted bands from *Figure 4.2*.

### 4.3.5 Assignment of spectra from FTIR and 2D-IR

#### 4.3.5.1 Assignment of spectra from FTIR second derivatives

To support the features reported in the transition dipole spectra and to further delineate the finer spectral details to deduce the peptide structures contributing to the amide I absorption spectra over the temperature range, 2<sup>nd</sup> derivative spectra of the normalised FTIR spectra were calculated, using the same method as described in Chapter 2 and used in Chapter 3. Trends which occur due to the thermal changes in the fine details of the peptide structure identified in Chapter 3 were highlighted, in corroboration with results from PCA and transition dipole spectra. As an example of how temperature influences the details of the peptide structure, the S/N graphs and the 2<sup>nd</sup> derivative spectra are presented at the two extreme temperatures 20 and 80 °C in *Figure 4.13*.

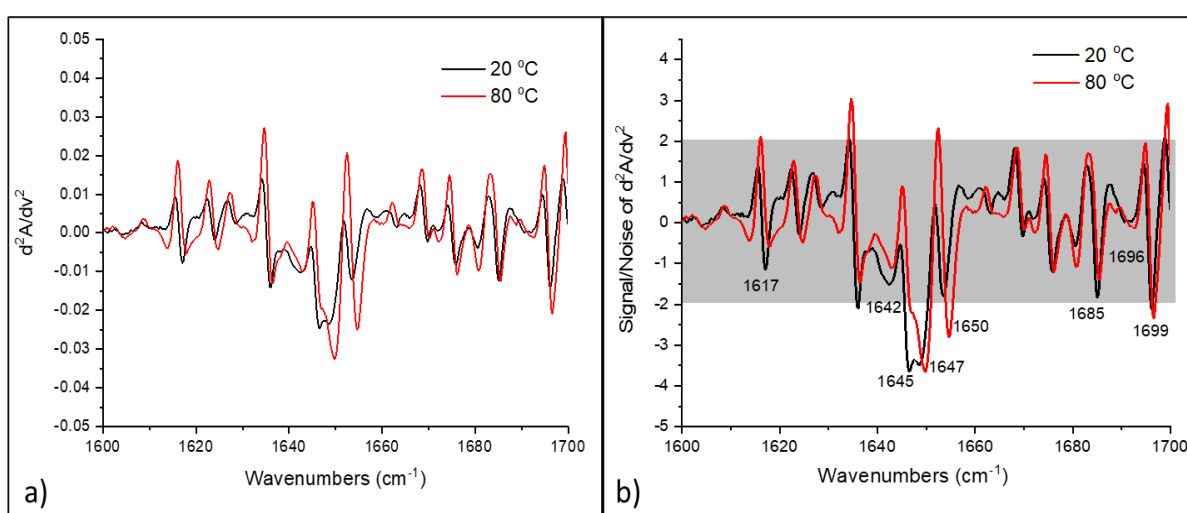


*Figure 4.13* The second derivative spectra in (a) and derived S/N spectra (b), only shown for the two extreme temperatures 20 °C and 80 °C, showing wavenumbers ( $\text{cm}^{-1}$ ) of the prominent peaks indicating the prominent peptide structures, the grey boxes show the spectral features with  $S/N < 2$ .

The first transitions at  $T_m$  41-47 °C is proposed to be from the dissociation of aggregates, unmasking or uncoupling the C=O groups of the  $\beta$ -sheets and turns in the smaller oligomeric structures (refer to *Table 4.1*). The trends in our second derivative analysis indicate a significant decrease in C=O stretch vibrations of  $\beta$ -sheets at 1642 and 1650  $\text{cm}^{-1}$  around 45 °C (refer to *Figure 4.5* and *Table 4.1*). From the structure analysis using the fine spectral details (*Figure 4.14*), there is loss of carbonyl stretching of the  $\beta$ -sheet at 1642  $\text{cm}^{-1}$  at an approximate  $T_m$  of 40 °C. This first transition could be related to disassembly of larger oligomers melting at “living” temperatures. Along with this we observed the loss of carbonyl stretch vibration of  $\beta$ -sheets near 1650  $\text{cm}^{-1}$  at a higher  $T_m$  of 45 °C, which also exhibited as an off-diagonal peak in 2D-IR (refer to discussion below). This may be again related to the loss of interpeptide H-bonding, yielding of smaller more stable oligomers. Conversely, there is

an increase in C=O stretch vibrations of  $\beta$ -sheets at 1696 and 1699  $\text{cm}^{-1}$  around 45 $^{\circ}\text{C}$ , as well as those of the  $\beta$ -turns at 1685  $\text{cm}^{-1}$ . From results reported in Chapter 3 we observed that when concentration was increasing, the vibrations of these structures were increasing. With increase in temperature, the decrease showed disruption of some of the  $\beta$ -sheet structures vibrating at the lower wavenumbers, which indicate that these carbonyl groups are possibly involved in intrapeptide oligomers/aggregates.

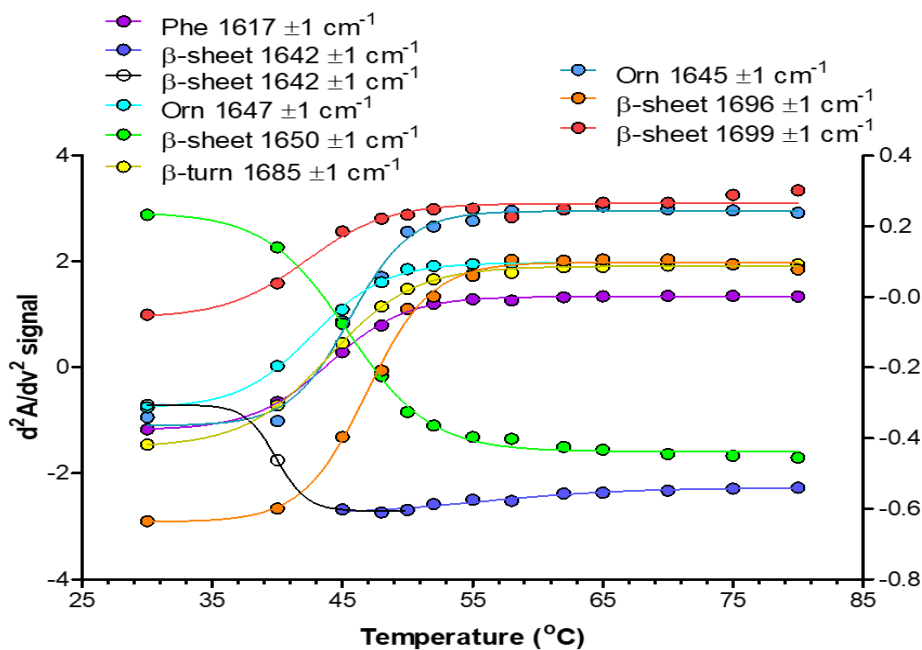


Figure 4.14 Melting curves of fine spectral structure components present in GS at 5.00 mg/mL solution, identified in Chapter 3 and shown in Figure 4.13b. the melting temperature was determined for each curve.

The Phe C-C ring stretch vibrations at 1617  $\text{cm}^{-1}$  which were lost with increasing concentration (refer to Table 3.5) are now increasing with increasing temperature at around 45  $^{\circ}\text{C}$ . The ornithine  $\text{NH}_3^+$  bending vibrations at 1645/7  $\text{cm}^{-1}$  were increasing with increasing concentration (Table 3.5) and with increasing temperature the structures also increase at around 45  $^{\circ}\text{C}$ . From our spectral assignments on vibrational modes using GaussView 5 software on the trimer model, the FTIR spectrum for the trimer showed that the ornithine coupled to the  $\beta$ -sheet carbonyls existed in the oligomer. With changes in temperature for  $T < 45$   $^{\circ}\text{C}$  the  $\beta$ -sheet carbonyl structures decrease as the intrapeptide oligomers disintegrate while the ornithine bends increase and for  $T > 45$   $^{\circ}\text{C}$  both the  $\beta$ -sheet carbonyls and ornithine increase (Figure 4.14). For the second transition  $T_{m2}$  at 57  $^{\circ}\text{C}$  we could only identify a minor increase in C=O stretching at 1642  $\text{cm}^{-2}$  at  $T > 40$   $^{\circ}\text{C}$  utilising FTIR (Table 4.1). For an in-depth analysis of this transition the 2D-IR analysis of GS over the same temperature range was considered (Figure 4.15).

Table 4.1 The fine spectral structure components present in GS at 5.00 mg/mL solution, identified in Ch. 3 and shown in Figure 4.13 above. The identified structures are labelled according to the contributing groups and their response (increase or decrease) to increasing temperature. Values for melting temperature  $\pm$  standard deviation are given.

Wavenumber $\pm 1 \text{ cm}^{-1}$	Signal		$T_m$ ( $^{\circ}\text{C}$ )	SD
	Group	Response		
1617	Phe ring	Increase	44	0.2
	$\beta$ -sheet	Increase		
1642	C=O	$>40^{\circ}\text{C}$	56	2.8
	$\beta$ -sheet	Decrease		
1642	C=O	$<40^{\circ}\text{C}$	40	0.1
1645	Orn $\text{NH}_3^+$	Increase	46	0.4
1647	Orn $\text{NH}_3^+$	Increase	43	0.2
	$\beta$ -sheet	Decrease		
1650	C=O		45	0.2
1685	$\beta$ -turn C=O	Increase	44	0.2
	$\beta$ -sheet	Increase		
1696	C=O		47	0.2
	$\beta$ -sheet	Increase		
1699	C=O		42	0.9

#### 4.3.5.2 Assignment of spectra from 2D-IR

Our calculations for assignment of the secondary structure using both FTIR and 2D-IR with response to temperature changes are from the transition dipole method by Minnes *et al.* [1] in accordance to Grechko and Zanni [10], [23]. This method has been described in Chapter 2, however, here we apply the method to temperature dependent measurements. To highlight, changes in coupling, the integrated area under the 1D spectrum is conserved while that of 2D is not conserved, which was observed in these results as seen in (Figure 4.7) and this shall be envisaged from the ratio of the signal of 2D diagonal and the FTIR absorption where, the 2D diagonal signal increases relative to that of the FTIR when there is coupling [1]. The relative changes in transition dipole, denoted as  $d(\omega)^{rel}$ , with reference to the initial temperature at 20  $^{\circ}\text{C}$  were obtained using the following Equation 4.9;

$$d(\omega)^{rel} = \frac{2D - IR_T(\omega)}{FTIR_T(\omega)} \frac{OD_{20}}{\Delta OD_{20}} \quad 4.9$$

$d(\omega)^{rel}$  represents the ‘spectrum’ of the relative transition dipole strength and is a function of frequency,  $\omega$ .  $2D-IR_T(\omega)$  and  $FTIR_T(\omega)$  are functions of frequency ( $\omega$ ) for the absolute values of the 2D diagonal and the 1D spectral signals, respectively, at different temperatures (T).  $OD_{20}$  and  $\Delta OD_{20}$  are the maxima of the 1D spectrum and the 2D diagonal signal, respectively at  $T = 20\text{ }^\circ\text{C}$  which in this case is the reference temperature.

The calculated integral area for the 1D absorption spectra does not change but that of 2D decreases with increasing temperature as shown in *Figure 4.15d*. The calculated transition dipole strength spectra show significant changes in the system (*Figure 4.15c*). A slight gain near  $1625\text{ cm}^{-1}$  confirms the increasing structure contributed by C-C stretch of Phe. The decrease in intensity at  $1630$  and  $1660\text{ cm}^{-1}$  indicates loss of C=O stretch of  $\beta$ -sheets and N-H bending in Orn side chain, respectively and this corroborated the results from PCA. From *Figure 4.15c*, the decrease in intensity of the transition dipole spectra is significant. This is a strong indication that with increasing temperature, coupling decreases [24], [25] and, in this case, coupling of long aggregated  $\beta$ -sheet strands, leading to formation of fine structure and low and high wavenumbers. This further confirms why the FTIR absorption band broadens at high temperature as new structures emerge while we lose  $\beta$ -sheets.

Comparing the concentration and temperature induced changes, the results are different. With increase in concentration there is loss of diagonal and off-diagonal structures. The fine structure is lost as aggregates form as indicated by loss of amide I bands related to  $\beta$ -sheets and turns at high frequency (*Figure 4.16a*). From the results in Chapter 3 there was shifting of the main band with increasing concentration, this shift could be an indication of the interactions of a H-bonded network, strengthening the aggregated structures centred near  $1640\text{ cm}^{-1}$ . However, when the aggregated structures at  $5.00\text{ mg/mL}$  are heated, the aggregates are disrupted, and they disassemble to reveal/unmask the fine structural details of smaller oligomers and GS monomers (*Figure 4.16b*). These fine structural details are also observed in octanol at low GS concentration. Thus, with increasing concentration, the amide I signal is lost as the loose fine structure of GS is masked within a network of GS aggregates. While with increasing temperature, the interpeptide hydrogen bonds (inter peptide H-bond in the two  $\beta$ -turns and antiparallel  $\beta$ -sheet) and other weak non-covalent interactions, (such as aromatic stacking of the Phe residues and hydrophobic clustering of the hydrophobic side chains (Leu, Val, Phe and to a lesser extent Pro) which were holding the aggregates in place) are lost revealing the fine structure of small GS oligomers and GS monomers.

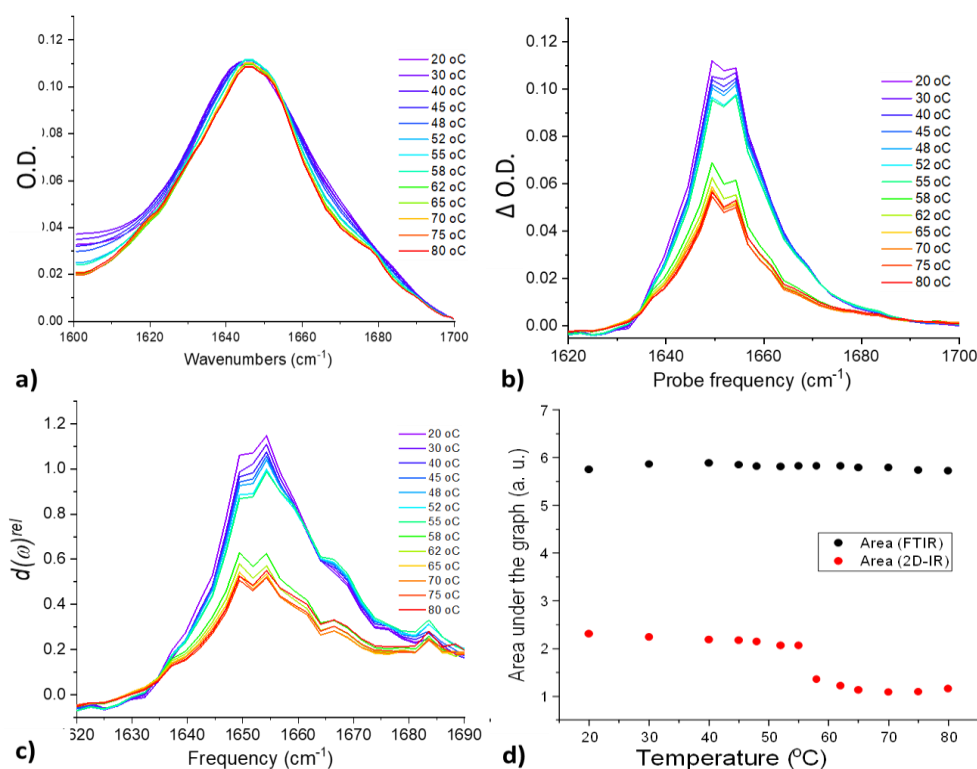


Figure 4.15 Global comparison of FTIR and 2D-IR spectra that were generated for GS from 20-80°C. (a) is the FTIR absorption spectra (b) are the 2D diagonal signals and (c) shows the calculated  $d(\omega)_{rel}$  spectra, (d) shows the integral area under the graphs for 1D and 2D.

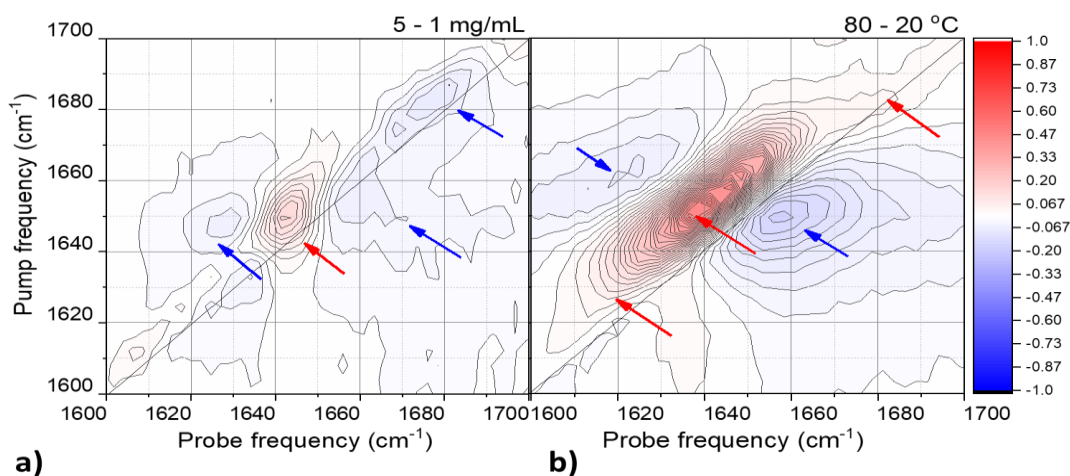


Figure 4.16 Comparison features of (a) GS difference spectra for concentrations 5.00-1.00 mg/mL and (b) difference spectrum for temperatures 80-20 °C at 5.00 mg/mL

From the 2D-IR analysis it was deduced that the  $T_{m2}$  transition at 57 °C is from increasing vibrations from Phe and Orn side chains, as well as the carbonyl groups in  $\beta$ -turns and  $\beta$ -sheets. This is indicated by the intense elongated feature which forms with increasing temperature, observed in 2D-IR (Figure 4.16b) which is due to the gain in fine structure contributed by C-C vibrations of the Phe ring (1617 cm<sup>-1</sup>), N-H bending of the Orn side chain (1645 cm<sup>-1</sup>), and C=O stretch of the  $\beta$ -turns (1685 cm<sup>-1</sup>)

and  $\beta$ -sheets ( $1699\text{ cm}^{-1}$ ) (also refer to discussion on *Figure 4.14*). The off-diagonal peak between  $1660\text{--}1680\text{ cm}^{-1}$ , contributed to by C=O stretch of the  $\beta$ -turns which was lost at high concentration (refer to Chapter 3), is gained at high temperature. Thus, the structures, which were buried/obscured in aggregates/oligomers, start to emerge.

Despite the general loss of  $\beta$ -sheet vibrations at  $1642\text{ cm}^{-1}$ , the gain in fine structural detail at elevated temperature is akin to the gain in structural detail observed of GS dissolved in TFE (refer to Chapter 3). This suggests that while fine structure exists in TFE due to its nature as strong H-bonding solvent; such structures can also exist in 1-octanol at elevated temperatures.

#### 4.4 Discussion

From chapter 3 solvent effects on the GS amide I IR absorption showed that ordered structures such as the  $\beta$ -sheets carbonyls at low frequency behaved in the same manner, i.e. emerging in solution and increasing with increasing peptide concentration, regardless of the solvent environment. Results indicated that there was a limited effect on the carbonyl stretching and N-H bending when the solvent system changes as this  $\beta$ -sheet hydrogen bonds are buried inside the cyclic peptide structure. However, results in this chapter showed that these  $\beta$ -sheets are affected by thermal changes. At high temperature, the decrease in intensity of the main band centred near  $1650\text{ cm}^{-1}$  where  $\beta$  sheet structures are present is an indication of aggregates dissociating, unmasking or uncoupling the C=O groups of the  $\beta$ -sheets and turns (located at high frequency) in the smaller oligomeric structures. Our results indicate that in the temperature range considered, no significant conformation change of the GS monomer was exhibited. Jelokhani-Niaraki *et al.* [26] considered the temperature induced changes in the range  $5\text{--}85\text{ }^{\circ}\text{C}$ , of GS and GS10 and reported no conformational changes. These spectral and structural changes were confirmed from the transition dipole analysis.

This process of dissociating aggregates was profiled using thermodynamic parameters. A bimodal profile was deduced with two identified melting/transition temperatures at  $T_{m1} = 45\text{ }^{\circ}\text{C}$  and  $T_{m2} = 57\text{ }^{\circ}\text{C}$ . The melting of the oligomers was an endothermic process. The thermal event centred at  $T_{m2}=57\text{ }^{\circ}\text{C}$  for increase  $\beta$ -sheet carbonyls is akin to the transition temperatures observed in a number of structure melting and thermal denaturation studies of proteins [27]–[34]. It has been observed that the  $T_m$  of  $\beta$ -sheet structures in protein varies from  $60\text{--}70^{\circ}\text{C}$ , depending on solvent system [35]–[37]. In an FTIR temperature dependent study by Lewis *et al.* [38], the GS amide I band of the phospholipid membrane-bound GS was invariant for low temperature range of  $20\text{--}48\text{ }^{\circ}\text{C}$ , however, upon thermal increase and for temperatures above  $52\text{ }^{\circ}\text{C}$  there was identified a shift in the amide I band of GS which corresponded to shifts in carbonyl and methylene stretches of the lipid matrix [38]. The conformation of the GS molecule (monomer) has been proposed to remain unchanged under varying conditions,

such as high temperatures, solvent variations with different polarity, in micelles, phospholipid bilayers or detergents and even when agents which alter conformation are present [33], [39], [40]. At high temperature the multiple interpeptide H-bonds and the non-covalent interactions such as aromatic stacking of the Phe residues and hydrophobic clustering are disrupted as the oligomers melt. A thermally induced solvent study on GS and its derivatives reported that the peptide molecules gain kinetic energy and overcome hydrophobic interactions within their aggregates [26]. There is absence of spectral features due to  $\alpha$  - or  $3_{10}$  helices in the region  $1650\text{-}1660\text{ cm}^{-1}$  for GS at native and at high temperature, and as expected for cyclic GS the presence of  $\beta$ -sheet structures at  $1620\text{-}1640\text{ cm}^{-1}$  were clearly defined by both FTIR and 2D-IR [9], [41].

From the thermodynamic parameters generated for aggregated GS, the entropic effects can be used to determine the peptide's thermostability. Amino acid residues with a  $\beta$ -carbon, such as valine, have more backbone conformational stability than amino acids without a  $\beta$ -carbon which are more flexible. Matthews *et al.* [42] investigated amino acid substitutions which decreased the configurational entropy of unfolding of bacteriophage T4 lysozyme and enhanced protein's stability, by substituting amino acid glycine, which lacks a  $\beta$ -carbon, with alanine which has a  $\beta$ -carbon. Further stating that amino acids with the pyrrolidone ring such as proline has also few backbone conformational degrees of freedom [42]. Thus, from our results the low entropic value of  $\Delta S = 0.98 \pm 0.02\text{ kJ/mol-K}$  for the pre-transition reaction ( $20 - 57\text{ }^\circ\text{C}$ ) and the  $\Delta S = 0.15 \pm 0.01\text{ kJ/mol}$  for the post-transition reaction ( $57 - 80\text{ }^\circ\text{C}$ ) suggest a decrease in entropy of unfolding for GS aggregates. Implying that since GS is already stable not much energy is required to restrict its conformation even as it folds in a reversible process. In GS amino acid sequence, the presence of amino acid residues such as valine and proline contribute to its thermal stability, thus less energy is required to restrict the conformation of GS.

## 4.5 Conclusion

Our hypothesis from Chapter 3 has been confirmed, that increasing temperature disrupts aggregation. Apart from applying different types of analysis methods which were done with FTIR data, 2D-IR greatly enabled the analysis of complex aggregated structures of GS in solution due to the better structural resolution it provides. Octanol served as a good mimic for the hydrophobic core of membranes and protein interiors with its long hydrocarbon chain and the polar headgroup. More structures of GS which contribute to its amphipathicity were better resolved and emerged at elevated temperatures. In combating microbes such as bacterial membranes with PE bilayers, it has been reported that they form inverted cubic phases in the presence of GS at elevated temperatures [13]. Higher temperatures can also provide deeper peptide penetration into bacterial membranes [43]. Entropic values indicated that GS consists of amino acid residues which support its stability. The

stability of the peptide can be increased by substitution with amino acid residues which generate derivatives which are thermally stable.

## 4.6 References

- [1] L. Minnes *et al.*, “Quantifying Secondary Structure Changes in Calmodulin Using 2D-IR Spectroscopy,” *Anal. Chem.*, vol. 89, no. 20, pp. 10898–10906, 2017, doi: 10.1021/acs.analchem.7b02610.
- [2] J. Kubelka, “Multivariate Analysis of Spectral Data with Frequency Shifts: Application to Temperature Dependent Infrared Spectra of Peptides and Proteins,” 2013, doi: 10.1021/ac402083p.
- [3] B. A. Anderson, A. Literati, B. Ball, and J. Kubelka, “Temperature dependence of amino acid side chain IR absorptions in the amide I’ region,” *Biopolymers*, vol. 101, no. 5, pp. 536–548, 2014, doi: 10.1002/bip.22416.
- [4] B. A. Anderson, G. S. Kubelka, and J. Kubelka, “Temperature dependence of peptide carboxylic group IR spectra in the amide I’ region at neutral and acidic pH,” *Vib. Spectrosc.*, vol. 77, pp. 40–50, 2015, doi: 10.1016/j.vibspec.2015.02.005.
- [5] A. Barth and C. Zscherp, “What vibrations tell about proteins,” *Q. Rev. Biophys.*, vol. 35, no. 4, pp. 369–430, 2002, doi: 10.1017/S0033583502003815.
- [6] S. Sukumaran, “Protein secondary structure elucidation using FTIR spectroscopy,” 2018.
- [7] M. Jackson and H. H. Mantsch, “The Use and Misuse of FTIR Spectroscopy in the Determination of Protein Structure,” *Crit. Rev. Biochem. Mol. Biol.*, vol. 30, no. 2, pp. 95–120, 1995, doi: 10.3109/10409239509085140.
- [8] B. A. Wallace and F. O’ Boyle, “The temperature dependence of Gramicidin conformational states in octanol,” *Protein Pept. Lett.*, vol. 10, no. 1, pp. 9–17, 2003, [Online]. Available: [http://people.cryst.bbk.ac.uk/~ubcg25a/farah\\_ppl\\_reprint.pdf](http://people.cryst.bbk.ac.uk/~ubcg25a/farah_ppl_reprint.pdf).
- [9] P. Stevenson and A. Tokmakoff, “Distinguishing gramicidin D conformers through two-dimensional infrared spectroscopy of vibrational excitons,” *J. Chem. Phys.*, vol. 142, no. 21, 2015, doi: 10.1063/1.4917321.
- [10] M. Grechko and M. T. Zanni, “Quantification of transition dipole strengths using 1D and 2D spectroscopy for the identification of molecular structures via exciton delocalization: Application to  $\alpha$ -helices,” *J. Chem. Phys.*, vol. 137, no. 18, p. 184202, 2012, doi: 10.1063/1.4764861.
- [11] S. K. Kim, T. Ha, and J. P. Schermann, “Editorial: Biomolecular structures: From isolated molecules to the cell crowded medium,” *Phys. Chem. Chem. Phys.*, vol. 12, no. 14, pp. 3334–3335, 2010, doi: 10.1039/c004156b.

- [12] F. Meersman, L. Smeller, and K. Heremans, “Comparative Fourier transform infrared spectroscopy study of cold-, pressure-, and heat-induced unfolding and aggregation of myoglobin,” *Biophys. J.*, vol. 82, no. 5, pp. 2635–2644, May 2002, doi: 10.1016/S0006-3495(02)75605-1.
- [13] R. N. A. H. Lewis *et al.*, “Fourier transform infrared spectroscopic studies of the interaction of the antimicrobial peptide gramicidin S with lipid micelles and with lipid monolayer and bilayer membranes,” *Biochemistry*, vol. 38, no. 46, pp. 15193–15203, 1999, doi: 10.1021/bi9912342.
- [14] J. Berg, J. Tymoczko, and L. Stryer, *Biochemistry*, 7th ed. 2002.
- [15] N. J. Greenfield, “Using circular dichroism collected as a function of temperature to determine the thermodynamics of protein unfolding and binding interactions,” *Nat. Protoc.*, vol. 1, no. 6, pp. 2527–2535, 2007, doi: 10.1038/nprot.2006.204.
- [16] N. J. Greenfield, “Using circular dichroism collected as a function of temperature to determine the thermodynamics of protein unfolding and binding interactions,” *Nat. Protoc.*, vol. 1, no. 6, pp. 2527–2535, 2007, doi: 10.1038/nprot.2006.204.
- [17] N. J. Greenfield, “Determination of the folding of proteins as a function of denaturants, osmolytes or ligands using circular dichroism,” *Nat. Protoc.*, vol. 1, no. 6, pp. 2733–2741, 2007, doi: 10.1038/nprot.2006.229.
- [18] N. J. Greenfield, “Analysis of the kinetics of folding of proteins and peptides using circular dichroism,” *Nat. Protoc.*, vol. 1, no. 6, pp. 2891–2899, 2009, doi: 10.1038/nprot.2006.244.Analysis.
- [19] G. Panick and R. Winter, “Pressure-induced unfolding/refolding of ribonuclease A: Static and kinetic fourier transform infrared spectroscopy study,” *Biochemistry*, vol. 39, no. 7, pp. 1862–1869, 2000, doi: 10.1021/bi992176n.
- [20] H. Herberhold, C. A. Royer, and R. Winter, “Effects of Chaotropic and Kosmotropic Cosolvents on the Pressure-Induced Unfolding and Denaturation of Proteins: An FT-IR Study on Staphylococcal Nuclease,” *Biochemistry*, vol. 43, no. 12, pp. 3336–3345, 2004, doi: 10.1021/bi036106z.
- [21] S. Matheus, W. Friess, and H. C. Mahler, “FTIR and nDSC as analytical tools for high-concentration protein formulations,” *Pharm. Res.*, vol. 23, no. 6, pp. 1350–1363, 2006, doi: 10.1007/s11095-006-0142-8.
- [22] I. S. Ryu, X. Liu, Y. Jin, J. Sun, and Y. J. Lee, “Stoichiometric analysis of competing intermolecular hydrogen bonds using infrared spectroscopy,” *RSC Adv.*, vol. 8, no. 42, pp. 23481–23488, Jun. 2018, doi: 10.1039/c8ra02919a.
- [23] E. B. Dunkelberger, M. Grechko, and M. T. Zanni, “Transition Dipoles from 1D and 2D Infrared Spectroscopy Help Reveal the Secondary Structures of Proteins: Application to

- Amyloids,” *J. Phys. Chem. B*, vol. 119, no. 44, pp. 14065–14075, 2015, doi: 10.1021/acs.jpcc.5b07706.
- [24] J. Kubelka and T. A. Keiderling, “Differentiation of-Sheet-Forming Structures: Ab Initio-Based Simulations of IR Absorption and Vibrational CD for Model Peptide and Protein-Sheets,” 2001, doi: 10.1021/ja0116627.
- [25] C. M. Davis, L. Zanetti-Polzi, M. Gruebele, A. Amadei, R. B. Dyer, and I. Daidone, “A quantitative connection of experimental and simulated folding landscapes by vibrational spectroscopy †,” 2018, doi: 10.1039/c8sc03786h.
- [26] M. Jelokhani-Niaraki, E. J. Prenner, C. M. Kay, R. N. McElhaney, R. S. Hodges, and L. H. Kondejewski, “Conformation and other biophysical properties of cyclic antimicrobial peptides in aqueous solutions,” *J. Pept. Res.*, vol. 58, no. 4, pp. 293–306, 2001, doi: 10.1034/j.1399-3011.2001.00893.x.
- [27] F. O’Boyle and B. A. Wallace, “The temperature dependence of gramicidin conformational States in octanol,” *Protein Pept. Lett.*, vol. 10, no. 1, pp. 9–17, 2003, doi: 10.2174/0929866033408246.
- [28] J. L. R. Arrondo, F. M. Goñi, J. Castresana, and J. M. Valpuesta, “Structure and Thermal Denaturation of Crystalline and Noncrystalline Cytochrome Oxidase as Studied by Infrared Spectroscopy,” *Biochemistry*, vol. 33, no. 38, pp. 11650–11655, 1994, doi: 10.1021/bi00204a029.
- [29] W. K. Surewicz, J. J. Leddy, and H. H. Mantsch, “Structure, Stability, and Receptor Interaction of Cholera Toxin As Studied by Fourier-Transform Infrared Spectroscopy,” *Biochemistry*, vol. 29, no. 35, pp. 8106–8111, 1990, doi: 10.1021/bi00487a017.
- [30] A. Martínez, J. Haavik, T. Flatmark, J. L. R. Arrondo, and A. Muga, “Conformational Properties and Stability of Tyrosine Hydroxylase Studied by Infrared Spectroscopy,” *J. Biol. Chem.*, vol. 271, no. 33, pp. 19737–19742, 1996, doi: 10.1074/jbc.271.33.19737.
- [31] R. Chehín, I. Iloro, M. J. Marcos, E. Villar, V. L. Shnyrov, and J. L. R. Arrondo, “Thermal and pH-induced conformational changes of a  $\beta$ -sheet protein monitored by infrared spectroscopy,” *Biochemistry*, vol. 38, no. 5, pp. 1525–1530, 1999, doi: 10.1021/bi981567j.
- [32] J. L. R. Arrondo, F. J. Blanco, L. Serrano, and F. M. Goñi, “Infrared evidence of a  $\beta$ -hairpin peptide structure in solution,” *FEBS Lett.*, vol. 384, no. 1, pp. 35–37, 1996, doi: 10.1016/0014-5793(96)00261-X.
- [33] R. N. A. H. Lewis *et al.*, “Fourier transform infrared spectroscopic studies of the interaction of the antimicrobial peptide gramicidin S with lipid micelles and with lipid monolayer and bilayer membranes,” *Biochemistry*, vol. 38, no. 46, pp. 15193–15203, 1999, doi: 10.1021/bi9912342.
- [34] S. J. Maness, S. Franzen, A. C. Gibbs, T. P. Causgrove, and R. B. Dyer, “Nanosecond

- temperature jump relaxation dynamics of cyclic  $\beta$ -hairpin peptides,” *Biophys. J.*, vol. 84, no. 6, pp. 3874–3882, Jun. 2003, doi: 10.1016/S0006-3495(03)75115-7.
- [35] L. J. Brown *et al.*, “Functional and spectroscopic studies of a familial hypertrophic cardiomyopathy mutation in Motif X of cardiac myosin binding protein-C,” *Eur. Biophys. J.*, vol. 31, no. 5, pp. 400–408, 2002, doi: 10.1007/s00249-002-0236-0.
- [36] J. Wu, J. T. Yang, and C. S. C. Wu, “ $\beta$ -II conformation of all- $\beta$  proteins can be distinguished from unordered form by circular dichroism,” *Anal. Biochem.*, vol. 200, no. 2, pp. 359–364, 1992, doi: 10.1016/0003-2697(92)90479-Q.
- [37] Z. Markovic-Housley and R. M. Garavito, “Effect of temperature and low pH on structure and stability of matrix porin in micellar detergent solutions,” *Biochim. Biophys. Acta (BBA)/Protein Struct. Mol.*, vol. 869, no. 2, pp. 158–170, Jan. 1986, doi: 10.1016/0167-4838(86)90290-6.
- [38] R. N. A. H. Lewis *et al.*, “Fourier transform infrared spectroscopic studies of the interaction of the antimicrobial peptide gramicidin S with lipid micelles and with lipid monolayer and bilayer membranes,” *Biochemistry*, vol. 38, no. 46, pp. 15193–15203, 1999, doi: 10.1021/bi9912342.
- [39] E. J. Prenner, R. N. A. . Lewis, and R. N. McElhaney, “The interaction of the antimicrobial peptide gramicidin S with lipid bilayer model and biological membranes,” *Biochim. Biophys. Acta - Biomembr.*, vol. 1462, no. 1–2, pp. 201–221, 1999, doi: 10.1016/S0005-2736(99)00207-2.
- [40] M. Jelokhani-Niaraki, L. H. Kondejewski, S. W. Farmer, R. E. W. Hancock, C. M. Kay, and R. S. Hodges, “Diastereoisomeric analogues of gramicidin S: Structure, biological activity and interaction with lipid bilayers,” *Biochem. J.*, vol. 349, no. 3, pp. 747–755, 2000, doi: 10.1042/bj3490747.
- [41] N. Demirdöven, C. M. Cheatum, H. S. Chung, M. Khalil, J. Knoester, and A. Tokmakoff, “Two-dimensional infrared spectroscopy of antiparallel  $\beta$ -sheet secondary structure,” *J. Am. Chem. Soc.*, vol. 126, no. 25, pp. 7981–7990, 2004, doi: 10.1021/ja049811j.
- [42] B. W. Matthews, H. Nicholson, and W. J. Becktel, “Enhanced protein thermostability from site-directed mutations that decrease the entropy of unfolding,” *Proc. Natl. Acad. Sci. U. S. A.*, vol. 84, no. 19, pp. 6663–6667, 1987, doi: 10.1073/pnas.84.19.6663.
- [43] A. T. Bockus, C. M. Mcewen, and R. S. Lokey, “Form and Function in Cyclic Peptide Natural Products: A Pharmacokinetic Perspective,” *Curr. Top. Med. Chem.*, vol. 13, pp. 821–836, 2013, doi: 10.2174/1568026611313070005.

## **Chapter 5 Fundamental characterisation of Gramicidin S (GS) with Raman and Surface Enhanced Raman Spectroscopy**

### **5.1 Introduction**

A fundamental characterisation of Gramicidin S (GS) using conventional Raman spectroscopy (RS) shall be done in corroboration with spectral simulation. From the IR solvent studies in Chapter 1 using solvents TFE, D<sub>2</sub>O and 1-octanol, results showed that changing the solvation strength resulted in induced loss of structures in D<sub>2</sub>O and 1-octanol, mainly  $\beta$ -sheets and  $\beta$ -turns at higher frequency which was an indication of a loss in ordered structure, while intra-peptide hydrogen bonds in the short  $\beta$ -sheets at lower frequency persisted as there were solvent protected hydrogen bonds. With increasing peptide concentration, hydrophobic residues (Leu and Val) are forced to self-associate forming oligomers and the  $\beta$ -sheet structures which they contribute to persists. The existence and absence of the afore-mentioned structures for aggregated GS shall be investigated using Raman spectroscopy.

RS provides structural and conformational details of proteins and peptides. With RS aqueous samples can be analysed. Chapter 5 will report for the first time results from a fundamental characterisation on an aqueous solution of GS in water, as well as characterisation of a Raman spectrum of GS powder. Results shall be correlated to DFT and QM/MM spectral simulations to aid interpretation. In addition, we take the opportunity to perform an intercomparison of RS and IR experimental and calculated results.

For biomolecules, the Raman scattering is weak due to the small Raman cross section, therefore SERS substrates shall be considered in a concentration study to detect low GS solution concentrations. We report the SERS spectrum of GS at low concentrations and identify that GS itself induces aggregation on metallic nanoparticles.

### **5.2 Results and Discussion**

#### **5.2.1 Characterisation of Gramicidin S using Raman spectroscopy and spectral modelling**

##### **5.2.1.1 Raman Spectroscopy: Solvent effects**

Raman spectra of solids are always more complex and sharper compared to the spectra in solution [1]. We analysed the Raman spectrum of GS in solid form (*Figure 5.1a*) and one of GS in solution with water at a high concentration of 10.00 mM (11.4 mg/mL) (*Figure 5.1b*). Water displays weak

Raman scattering and adds little interference on the spectra of the solute. When a compound such as a peptide interacts with a solvent, the induced system changes are observed in Raman bands such as broadening of bands, shifting of band maxima and in some cases bands merge while others become hidden. The Raman bands for GS powder are strong sharp peaks, compared to those of GS aqueous solution at 10.0 mM, as shown in (*Figure 5.1*). Significant peaks are summarised in *Table 5.1* and discussed according to the class of amino acid they belong to. The spectral region 400-1800  $\text{cm}^{-1}$  is presented for GS containing the amino acids L-valine, L-leucine, D-phenylalanine, L-proline and L-ornithine. In further discussions, we shall refer to the spectrum for GS solution at 0.01 M (10.0 mM) as the normal Raman spectrum.

### ***Aliphatic amino acid residues***

Aliphatic amino acids present in GS are proline (Pro), leucine (Leu) and valine (Val). Pro markers were observed at 916 and 918  $\text{cm}^{-1}$  in the powder and solution spectra, respectively (*Figure 5.1*). This marker represents the ring breathing vibration in Pro side chain [1], [2]. Additional Pro contributions are present through the weak and narrow band at 1204  $\text{cm}^{-1}$  and a weak band near 850  $\text{cm}^{-1}$ . The strong broad band between 1400 and 1500  $\text{cm}^{-1}$  is also from C-H vibrations of aliphatic amino acids, though Leu is non-aromatic and its bands are weak and difficult to identify. This is consistent to bands positions from peptides and proteins [3], [4]. Contributions from Val, expected at 924 - 943  $\text{cm}^{-1}$ , are not significant, the intensity probably hidden because of the strong Pro band at 916  $\text{cm}^{-1}$ .

### ***Aromatic amino acid residues***

The aromatic amino acid present is phenylalanine (Phe). The strongest markers are from Phe located in the middle fingerprint region of the spectrum at 1002 and 1030  $\text{cm}^{-1}$  in the solid spectrum and they are well separated and resolved. In the solution spectrum the two bands are not as well separated as in the solid spectrum with the weaker 1030  $\text{cm}^{-1}$  band down-shifting to 1017  $\text{cm}^{-1}$  to merge with the stronger band while also broadening the two bands. Several Phe bands are identifiable at 1203, and 1584  $\text{cm}^{-1}$  in the solid spectrum (*Figure 5.1*).

### ***Amide I, II, III vibrations***

The secondary structure is characterised by the amide I Raman band. The Amide I band arise due to the contribution by the C=O stretch and minor contributions from the out-of-phase C-N stretch vibration [5], [6]. The Raman amide I mode is expected from 1640-1680  $\text{cm}^{-1}$ ; in the solid GS spectrum it appears at 1665  $\text{cm}^{-1}$  while in the solution spectra it is shifted to 1668  $\text{cm}^{-1}$  (*Figure 5.2*). From the amide I band in the IR studies the major absorption band is located 1640-1650  $\text{cm}^{-1}$  and a weak minor absorption band located in the range 1660-1680  $\text{cm}^{-1}$ . Therefore, after excluding the IR

absorption band, the position of the GS amide I Raman band is as expected; indicative of the anti-parallel  $\beta$ -sheet conformation [7]. Additionally the position of the amide I band in our studies on GS supports the fact the anti-parallel  $\beta$ -sheets have a more red-shifted amide I band [6].

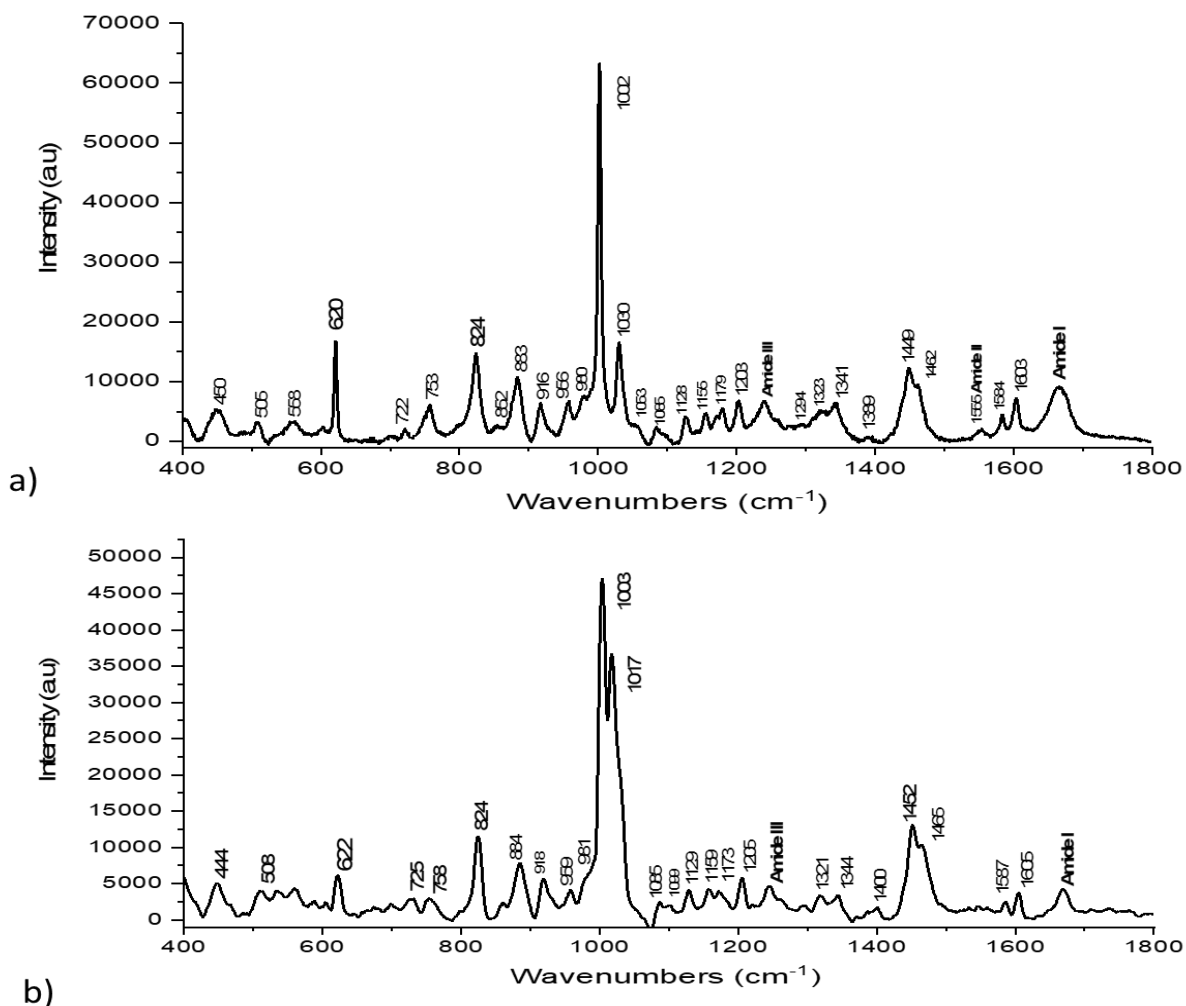


Figure 5.1 Raman spectrum of a) GS powder acquired for 30s and b) 10 mM GS in aqueous solution acquired for 5 mins, with assigned spectra, region 400 – 1800  $\text{cm}^{-1}$ . The spectra were acquired with 830 nm excitation source.

The amide II vibration is expected near  $1550 \text{ cm}^{-1}$ , the solid and solution GS spectra show this broadened weak band at  $1554/5 \text{ cm}^{-1}$ , respectively. The band is contributed to by out-of-phase vibrations of C-N stretch and N-H bending motion [5], [6]. The amide III expected in range  $1200\text{--}1350 \text{ cm}^{-1}$  is positioned at  $1240$  and  $1242 \text{ cm}^{-1}$  in the solid and solution spectra, respectively. These bands are also as expected for antiparallel  $\beta$ -sheet [7]. The amide III is contributed to by N-H in-plane bending and C-N stretching vibration [5], [7].

The discussed band assignments for GS in solution and powder are summarised in *Table 5.1* and compared with literature.

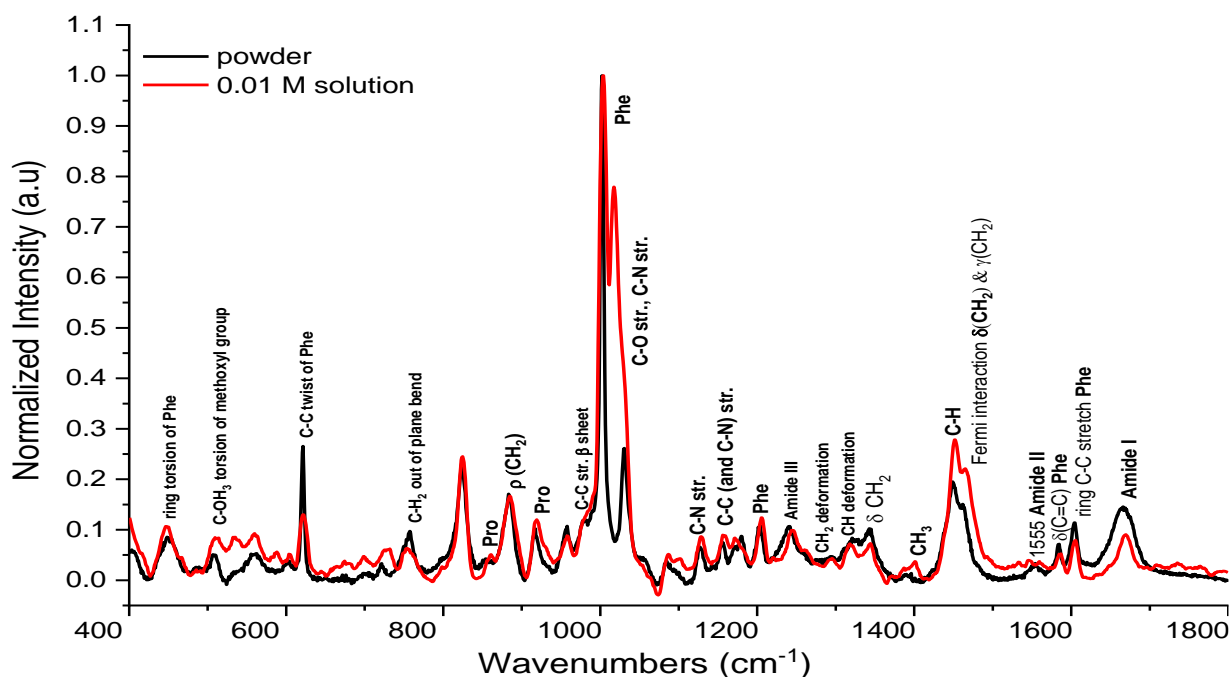


Figure 5.2 Normalised Raman spectrum of GS powder and GS in aqueous solution with assigned spectra, region 400 – 1800  $\text{cm}^{-1}$ . Comparison of the two spectra show the differences of the powdered GS and aqueous phase GS. Band assignments were done with reference to [1], [6]–[13].

Table 5.1 Table of selected Raman bands obtained experimentally from the spectrum of GS powder and solution.

Band Assignment	Literature	Measured	
		GS solid	GS solution ( $1 \times 10^{-2}$ M)
		<b>RS</b>	
Pro	918	916	918
C-C stretch $\beta$ -sheet	980	980	981
C-C aromatic ring stretch Phe	1000, 1030	1002, 1030	1003, 1017
Amide III and $\text{CH}_2$ wag. from proline side chains Phe	1204	1204	1205
Amide III ( $\beta$ -sheet and random coil)	1242	1241	1244
Amide II N-H bending	1554	1555	1555
$\delta(\text{C}=\text{C})$ , Phe	1582/4	1584	1587
Ring C-C stretch of phenyl	1605	1603	1605
Amide I C=O stretch	1600-1700	1665	1666

### 5.2.1.2 Comparison of experimental IR and Raman amide I band in different solvents

Comparing the experimental results for Raman and IR (Figure 5.3), the amide I region was considered for elucidating the changes in secondary structure in different solvents. In Chapter 1, we reported on significant changes which occur to amide I with solvents with different dielectric constants and thus different polarity. IR spectra are for samples at 10.0 mg/mL (8.7 mM) which is slightly lower than the 10.0 mM solution concentration used for the Raman studies. For comparison spectra were normalised to the amide I band to account differences in intensity. For various polypeptides conformations, the most intense amide I bands in Raman spectra are located in the range 1665 – 1680  $\text{cm}^{-1}$  [14], [15] while those in IR spectra the bands are located in range 1620 – 1640  $\text{cm}^{-1}$  in  $\text{H}_2\text{O}$  and shifted to 1615 – 1635  $\text{cm}^{-1}$  in  $\text{D}_2\text{O}$  for secondary structure of  $\beta$  – sheets [5], [16], [17]. Our IR results have showed that with decrease in dielectric constant, which is also decrease in polarity, the amide I band shifts to higher frequency, while RS results show an amide I band shift to lower frequency (Table 5.2).

This peak shift is an indication of the different H-bonding potential of the solvent [18], [19]. In a Raman study of a peptide penetratin in varying composition of water/TFE, an amide I band shift was observed from 1675 to 1655  $\text{cm}^{-1}$  for 100 % water and 100 % TFE, respectively, which indicated transition of peptide structure [20]. Our results for GS in TFE a band shift of the major band at 1661  $\text{cm}^{-1}$  attributed to from C=O stretch of  $\beta$  – turn is also observed.

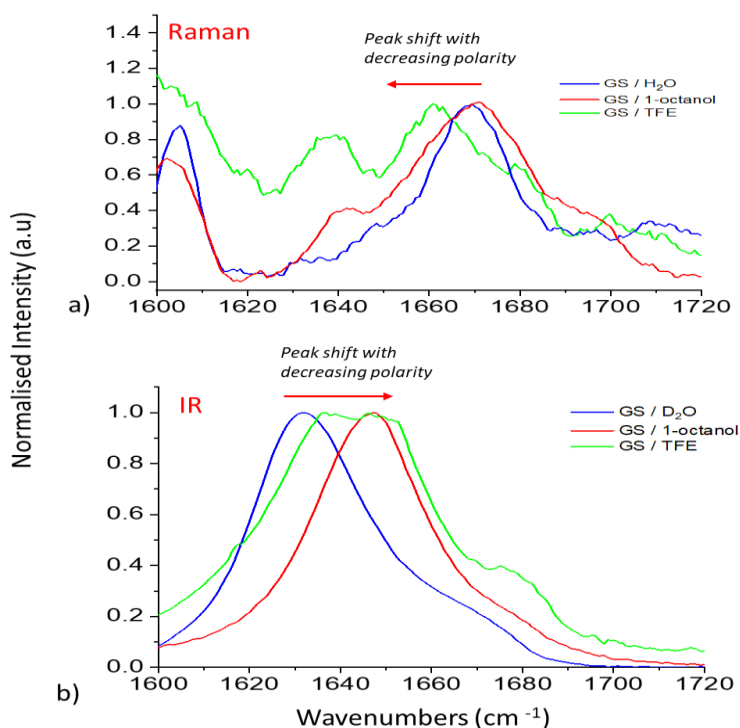


Figure 5.3 Experimental Raman and IR spectra for GS in different solvents. The spectra are all normalised to the amide I band.

Table 5.2 Global analysis of the peak maxima of the amide I FTIR and Raman spectra of GS in three solvents of different polarity

Solvent	Dielectric constant	Peak Maximum (cm <sup>-1</sup> )	
		IR	Raman
H <sub>2</sub> O	80.10		1669
D <sub>2</sub> O	78.28	1633	
1-Octanol	10.30	1647	1670
TFE	8.55	1643	1661

A shoulder observed in the Raman spectra for GS in water and octanol near 1640 cm<sup>-1</sup> (Figure 5.3) becomes more pronounced in TFE and it is contributed by C=O stretch of  $\beta$ -sheet. This indicates several structures being promoted in TFE. These contributions in TFE were also present in our IR and 2D-IR measurements (from Chapter 1), thus confirming the destabilisation of aggregates and quaternary structures by disrupting H-bonding induced by TFE [21].

### 5.2.1.3 Simulation of GS spectra using DFT and QM/MM calculations

Simulations have been performed in-order to support spectral assignments and investigate structure to spectroscopy relationships. The models employed in the simulations are the monomer and trimer models described in the section 2.3 and spectral simulation using the Gaussian 09 package.

From the monomer model, two GS monomer atom selections were further considered to identify and highlight contributions from the backbone and those from the substituents (Figure 5.4). The atom selections were considered in-order to observe structural contributions to the spectra caused by substituent features apart from the backbone feature and to observe how different parts of the selection influence the spectrum.

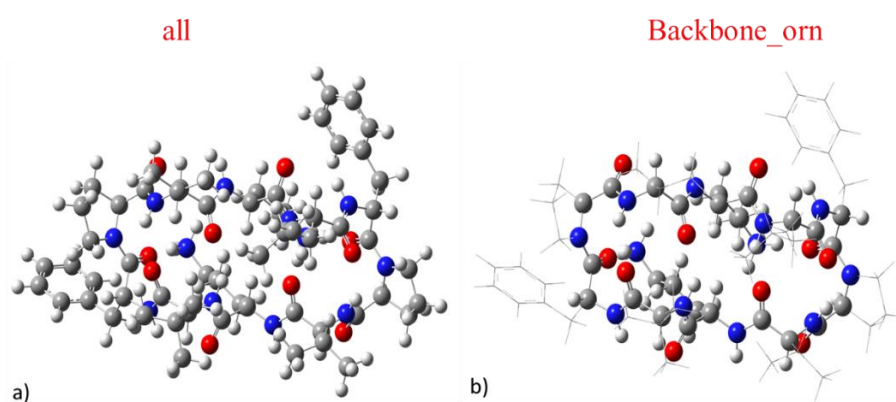
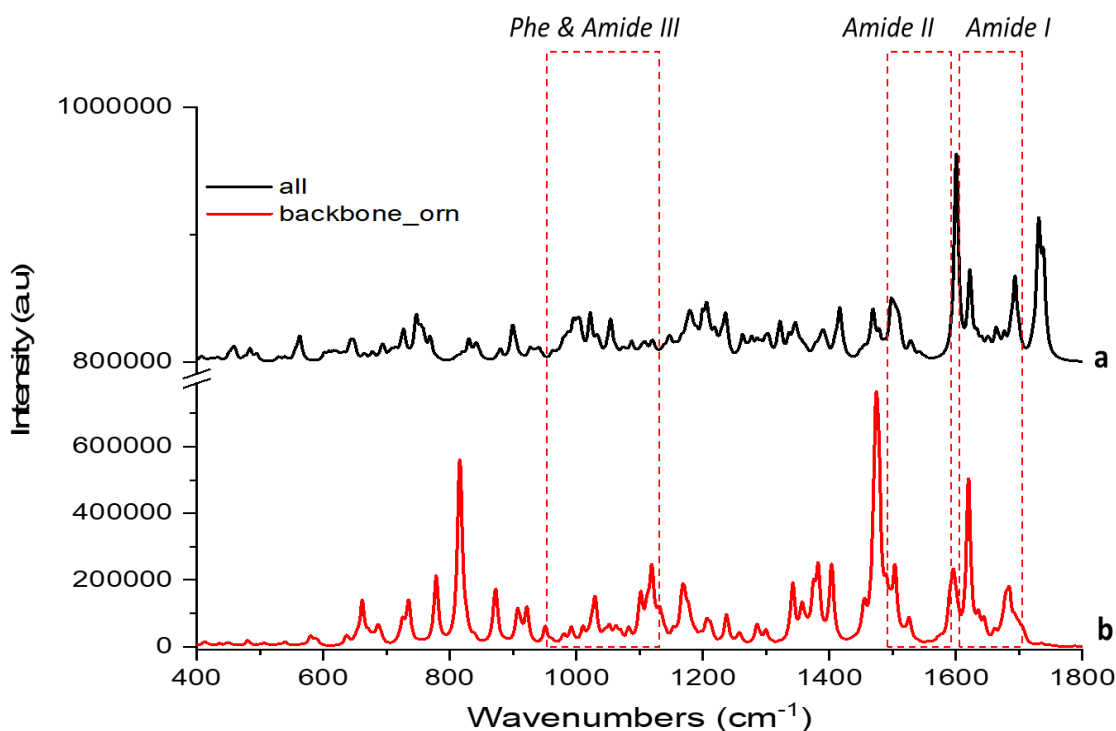


Figure 5.4 The two different atom selections used for the monomer in simulating the spectra. These are: a). All as high layer; b). Orn plus backbone as high layer, the rest as low layer. The highlighted ball features represent portions used as higher layer and the non-selected balls represent portions treated a low layer.

In DFT calculation, all atoms are treated as a single layer. In QM / MM the structures are treated as two layers: the high layer with quantum mechanics (QM) framework and low layer with molecular mechanics (MM). The atom selections considered were: (1) all atoms with amino acid and backbone features as high layer (all) and (2) Orn side chain plus backbone as high layer, the rest as low layer and (Backbone\_orn). *Figure 5.5* and *Figure 5.6* below show the QM/MM and the DFT calculated spectra, respectively. The regions highlighted are the expected features of amide I and II, as well as the Phe contributions.

#### 5.2.1.4 Comparison of Raman experimental and calculated spectra

From our experimental results on GS solution spectra, key modes have been summarised in *Table 5.3* below. These modes are amide I, II, III which contribute to the secondary structure of GS and the Phe mode which gives significant intensity in mid fingerprint region (see *Figure 5.5*). The bands for the selected modes shall be compared to spectral features observed from the chosen monomer spectrum in (*Figure 5.7*) with focus on band positions.



*Figure 5.5* QM/MM calculated Raman spectra for the two GS model atom selections in *Figure 5.4*. Spectrum (black) is for All as high layer; (red) is for Orn + backbone as high layer, the rest as low layer. The spectra have been offset for clarity.

We now discuss the calculated QM/MM spectra (*Figure 5.5a* and *b*) and the DFT spectra (*Figure 5.6*). The C-C Phe stretch vibrations at 1000 and 1017  $\text{cm}^{-1}$  (refer to *Table 5.3*) are present in all (QM/MM and DFT) spectra. Contribution of the amide II expected at 1555  $\text{cm}^{-1}$  is present in the

QM/MM spectrum (a) as well as the DFT spectra, however, the bands are weak. The amide I band is expected to be located in range  $1640 - 1670 \text{ cm}^{-1}$  [15], which is present in both QM/MM calculated spectra (a) and (b). The all QM/MM spectrum shows intense Phe band near  $1600 \text{ cm}^{-1}$  however, while the presence of the Phe close to the amide I region gives strong bands which overshadow the contribution of the amide I. A representation of features contributing to amide I, II, III and Phe are present in the QM/MM spectrum (a) for all amino acids in regions  $1640-1700$ ,  $1505-1586$ ,  $1200-1400$  and  $1600 \text{ cm}^{-1}$  and these bands correlate well with the experimental Raman spectrum of GS in water (Table 5.3). In DFT, all the atom selections gave similar spectra because one layer is considered with DFT calculations (Figure 5.6).

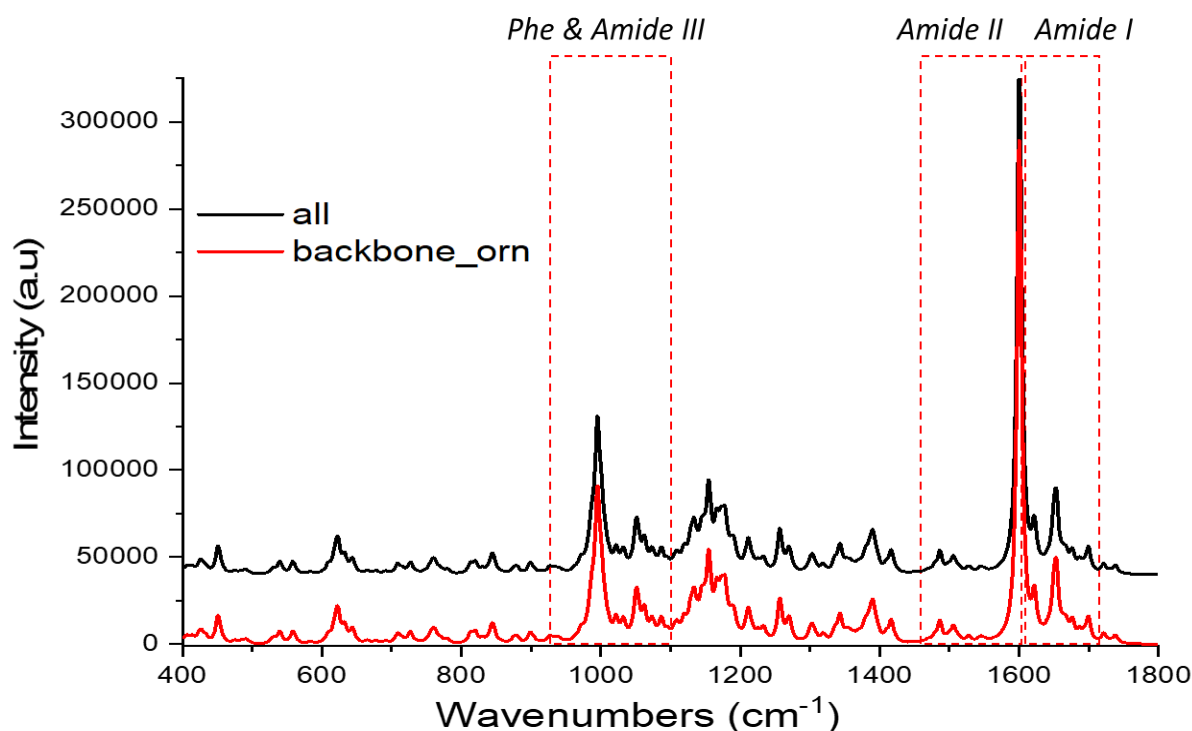


Figure 5.6 DFT calculated spectra for the two atom selections for all (black spectrum) and Orn + backbone (red spectrum) in Figure 5.4. The spectra are identical since the models are treated the same in DFT calculation.

The GS monomer model for backbone plus ornithine (Figure 5.4b) features was utilised because results from our solvent studies showed that of the factors contributing to GS activity, residues contributing to amphipathicity responded more to the solvent environment. Orn residues provide the cationicity and hydrophilicity in GS and its response to a strongly H-bonded solvent (TFE) was evident. The QM/MM spectrum (Figure 5.5b) shows the contribution of Orn and the backbone which is mainly the  $\beta$ -sheet and turns. In spectrum a) bands for the ‘all’ selection show that the presence of aromatics from Phe and Pro suppresses some vibrational modes such as the carbon stretches near  $800 \text{ cm}^{-1}$  while at the same time contributions from Val and Pro near  $1712$  and  $1730 \text{ cm}^{-1}$  are present. Thus, the all spectrum is represented by vibrational modes of residues which contribute to the

characteristics which render GS active. Therefore, spectra from QM/MM simulations were considered for further comparison of the monomer model (section 5.2.1.5) and trimer model (section 5.2.1.6) in comparison with the experimental spectra contributions of 10.00 mM GS in water (Table 5.3).

### 5.2.1.5 Spectral assignment for calculated Raman and IR spectra of monomer model

From the QM/MM simulations, the monomer spectrum for all amino acid and backbone features (all) (Figure 5.5a) showed several features which correlated well with those from the experimental spectrum of GS solution. Though there were slight band shifts, these band shifts could be explained. The variations in band positions between the calculated monomer (all spectra) and experimental for GS solution are from the high concentration of GS solution at 10.00 mM which is 11.4 mg/mL, a concentration at which GS in water is expected to aggregate, as reported in Chapter 1. Therefore, it is expected that the experimental spectrum would differ from that of the QM/MM simulated spectrum of GS monomer, given in Figure 5.7.

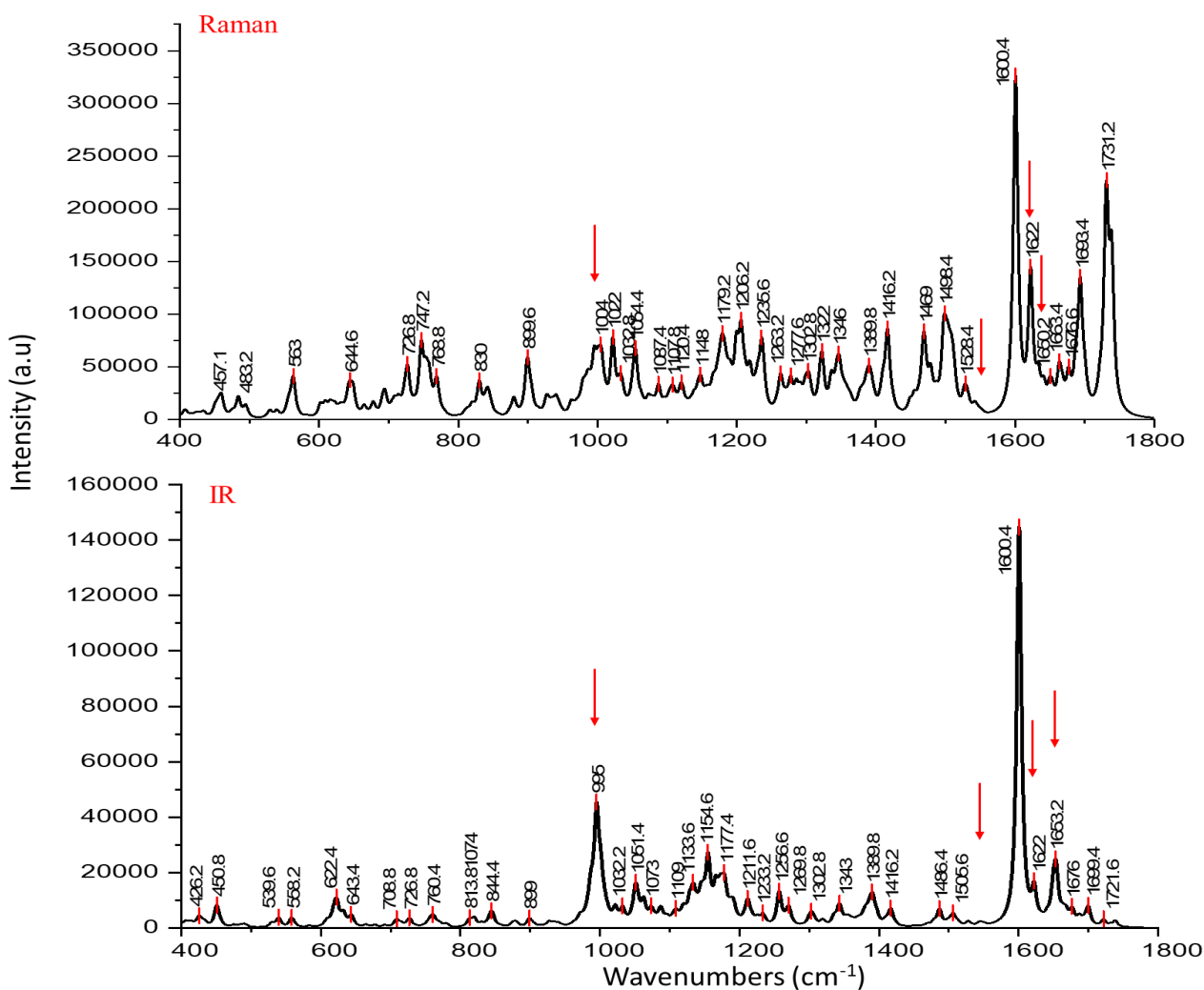


Figure 5.7 QM / MM Raman and IR calculated spectra for the GS monomer model for all amino acid and backbone features. The red arrows indicate some of the correlating bands.

With this knowledge, both the QM/MM Raman and IR simulated spectra for the monomer unit of all amino acids and backbone were analysed to find spectral correlations between the two techniques as they are complementary. Also, the monomer spectrum could be a prediction model and a representative of spectrum for extremely low GS concentration which cannot be experimentally obtained due to instrumental sensitivity for normal RS. Significant bands are discussed below, and correlations are identified between the simulated Raman and IR spectra (refer to *Table 5.3*). Reference shall also be made to the results obtained in Chapter 1.

The band assignment of vibrational modes in the monomer and trimer models below was done by visually observing the structural groups and modes of vibration using GaussView 5 software and assigning to the spectral feature which the vibrating mode contributes to. Viewing the vibrating modes in GaussView 5 software enabled the assignment of the calculated peak with the contributing amino acid. The FTIR and Raman selected modes are discussed below for monomer and trimer, with reference to *Table 5.3*.

*IR: Amide I and II regions 1740 – 1450 cm<sup>-1</sup>*

With reference to the chosen monomer spectrum for ‘all’ magnified in *Figure 5.7* and with reference to *Table 5.3*, the IR bands at 1700 cm<sup>-1</sup> and 1676 cm<sup>-1</sup> are the carbonyl stretch vibrations from the monomer model. At 1653 cm<sup>-1</sup> is the Orn wagging/bending vibration coupled with carbonyl stretch. This band is not observed in the experimental spectra, most likely because Orn is shielded or coupled to another vibrational mode. The Phe stretch in the calculated Raman and IR spectra is present at 1622 cm<sup>-1</sup>. At 1600 cm<sup>-1</sup> is the NH bending coupled to Phe carbon stretch. Phe is aromatic so has a major contribution to IR, and Orn has an amino group which largely contributes also to the amide I. From 1542 – 1550 cm<sup>-1</sup> are the Phe C-C stretch and C-H bend. A Phe band is present at 1550 cm<sup>-1</sup> which is not present in the IR spectra, possibly because it is in another environment (refer to Chapter 3). At 1527 cm<sup>-1</sup> there is another Phe vibration mode, and at 1505 and 1486 cm<sup>-1</sup> are the CH bending vibrations of the aliphatic side chains.

*Raman: Amide I and II region 1740 – 1450 cm<sup>-1</sup>*

In the Raman spectrum (*Figure 5.7*) the Val stretching vibration is observed at 1730 and 1738 cm<sup>-1</sup>. The carbonyl stretch at 1693 cm<sup>-1</sup> is correlated to a similar band obtained for GS in 1-octanol and TFE and there is no shift (refer to Chapter 3). The IR simulated spectrum gave a carbonyl stretch at 1700 cm<sup>-1</sup>, and from IR experimental results we obtained 1695 cm<sup>-1</sup> for GS in TFE and 1696 cm<sup>-1</sup> for GS in 1-octanol (refer to Chapter 3). At 1676 cm<sup>-1</sup> is another carbonyl stretch. More carbonyl vibrations are identified in the monomer model, relating the carbonyl vibration assigned in experimental spectra for GS in 1-octanol and TFE (Chapter 1, *Table 3.5*). This indicates that at certain

concentrations, lower than 1.00 mg/mL, for 1-octanol and TFE, GS monomers in solution are prevalent.

Table 5.3 Table of assignments for simulated monomer and trimer models for IR and Raman QM / MM calculations. Assignments for the experimental GS solution at  $1 \times 10^{-2}$  M are included for correlations.

Secondary Structure	Absorbing Group	Literature Models <sup>a-e</sup>	GS <sup>f</sup>	QM/MM Simulation of GS IR		QM/MM Simulation of GS Raman		Raman exp.
				Trimer model	Monomer model	Trimer model	Monomer model	GS at 10 mM
β-sheet Amide I	Val C=O str					1732		
	C=O stretching	1700 1695-7 1691-3 1641-3 1630-9 1624-9	1700  1643	1693  1643 1631-3 1640	1700	1643	1693	1702   1630-3, 1639 1629
β-sheet Amide II	N-H Bending	1534  1523	1532	1533 1546 1523 1577		1601 1598 1533  1586	1527	1539 1542 1521
β-turn Amide I	Pro C=O str					1712		
	C=O stretching	1683-91 1678-82 1670-75 1666-74 1659-65 1654-8		1685 1682  1666 1652/3	1676  1653	1666  1608	1676	1666
β-sheet Amide II	N-H Bending	1559 1546-7 1575	1563  1546	1568  1557 1545		1545		1569 1560 1553 1546 1577

<sup>a</sup>Krimm *et al.* (1983); <sup>b</sup>Venyaminov & Kalin (1990); <sup>c</sup>Barth (2007); <sup>d</sup>Barth (2000); <sup>e</sup>Kong *et al.* (2007); <sup>f</sup>Naik *et al.* (1984)

Table 5.3 Continued

Amino acid	Absorbing Group	Literature Models <sup>a-e</sup>	GS <sup>f</sup>	QM/MM Simulation of GS IR		QM/MM Simulation of GS Raman		Raman exp.	
				Trimer model	Monomer model	Trimer model	Monomer model	GS at 10 mM	
Orn Amide I	N-H Bending	1672-3 1667 1660 1659 1647		1666  1656 1643 1641 1637	1653	1643 1640	1663	1666	
Orn Amide II	N-H Bending						1497		
Phe Amide I	N-H Bending			1624	1622		1622	1618	
Phe Amide II	C-C, C=C in ring Stretching	1602	1601	1601 1608	1600		1600	1605	
		1585	1586		1542-1550 1527	1586 1567 1545 1525 1521	1542-1550 1527	1517 1512 1508 1465	
			1525		1505	1505	1505	1468	
			1507	1507	1505	1505	1505	1468	
	C <sub>β</sub> C-H str					1484			
	C=O str					1450		1452	
Phe Amide III	C-C, C=C in ring Stretching					1074		1017	
						1003	1055	1003	
							1022		
Leu amide III	C-C Stretching					1003		1003	
Leu Amide II	C-H Bending				1486	1505 1567  1468	1502 1486 1468 1400		
						1492	1497		
Val Amide I	C=O Stretching					1732			
Val Amide II	C-H Bending					1492	1478 1470		
Pro Amide I	C=O Stretching					1712			
Pro Amide III	C-C Stretching						1032		

The calculated Raman band at  $1663\text{ cm}^{-1}$  is from the Orn vibrational coupling with the backbone carbonyls and in the IR model spectrum the same band is observed at  $1653\text{ cm}^{-1}$ . At  $1622\text{ cm}^{-1}$  is the Phe C-C stretch, the same band is observed in FTIR spectrum, as expected. At  $1600\text{ cm}^{-1}$  is the Phe carbonyl stretch and the  $1527\text{ cm}^{-1}$  band is from the Phe amino group coupling with Phe stretch mode. In the range  $1542\text{-}1550\text{ cm}^{-1}$  is the Phe C-C stretching and C-H bending, similar to the FTIR bands. The band at  $1497\text{ cm}^{-1}$  is from the Orn side chain N-H and CH wag. At  $1502$  and  $1486\text{ cm}^{-1}$  are bands from the CH bending of Phe. Val side chain C-C and C=O contributions are observed at  $1470$  and  $1678\text{ cm}^{-1}$ , respectively. At  $1468\text{ cm}^{-1}$  is the CH coupling with the Phe C-C and C=C stretch. Bands around  $1400\text{ cm}^{-1}$  are C-H modes. In the mid fingerprint region at  $1022$  and  $1055\text{ cm}^{-1}$  both bands are from Phe C-C and C=C stretch. At  $1032\text{ cm}^{-1}$  is the Pro band. At  $1000\text{ cm}^{-1}$  the whole structure is vibrating. Assignments of the spectra in *Figure 5.7* are summarised in *Table 5.3*.

### 5.2.1.6 Spectral assignment for calculated Raman and IR spectrum of trimer model

Since the monomer model represented GS spectra at low concentrations which could not be experimentally obtained, the trimer model is better representative of the spectral features of GS at the higher experimental concentrations. That is  $10.0\text{ mM}$  ( $11.4\text{ mg/mL}$ ) solution GS occurs as aggregates so the trimer model represents part of a GS aggregate / oligomer (*Figure 5.8*). For the trimer model, since the system is so large and assignments are problematic, efforts to simplify the calculated spectra were made by selecting only certain atoms QM calculation. However, modes involving the whole trimer model are considered in the spectra. The Raman and IR spectra of the trimer model (*Figure 5.9*) are mainly due to QM, being modulated or demodulated by fringe contributions from MM.

#### *IR: Amide I region $1735 - 1600\text{ cm}^{-1}$*

For the trimer the amide I and II modes shall be assigned as well as notable bands from amino acid residues. The band at  $1712\text{ cm}^{-1}$  is contributed to by proline and carbonyl stretching of the  $\beta$ -sheet. At  $1712\text{ cm}^{-1}$  there is additional carbonyl stretch from  $\beta$ -sheet and  $\beta$ -turns, from observation in GaussView software all the  $\beta$ -sheet carbonyls vibrate with the carbonyls in  $\beta$ -turns vibrating more than those in the  $\beta$ -sheet. This is because in this case the  $\beta$ -turns are not as restricted in motion as they are on the open ends. The carbonyl movement in  $\beta$ -sheets is not as intense as in  $\beta$ -turns because it is limited in the trimer “sandwich”. Very little vibration is observed in the trimer model at  $1686\text{ cm}^{-1}$ . The carbonyl stretch of  $\beta$ -turns at  $1666\text{ cm}^{-1}$  is also vibrationally coupled to the Orn side. At  $1643\text{ cm}^{-1}$  there is also Orn NH-side chain bending, which is important to identify, as it is not a  $\beta$ -sheet and there is also vibronic coupling between Orn N-H and  $\beta$ -sheet carbonyls. The bands at  $1637$  and  $1641\text{ cm}^{-1}$  are also from Orn and may most probably be coupled to the one at  $1643\text{ cm}^{-1}$  leading to a broad band in experimental spectra. The contributions from Orn N-H and  $\beta$ -sheet carbonyls are also

observed in FTIR second derivative analysis where the  $\beta$ -sheet and Orn bands are present and increase with increasing concentration. This is also observed in PC1 for GS in TFE where Orn N-H and  $\beta$ -sheet carbonyls are present in the positive elongated feature from  $1630 - 1650 \text{ cm}^{-1}$  (refer to 3.3.3).

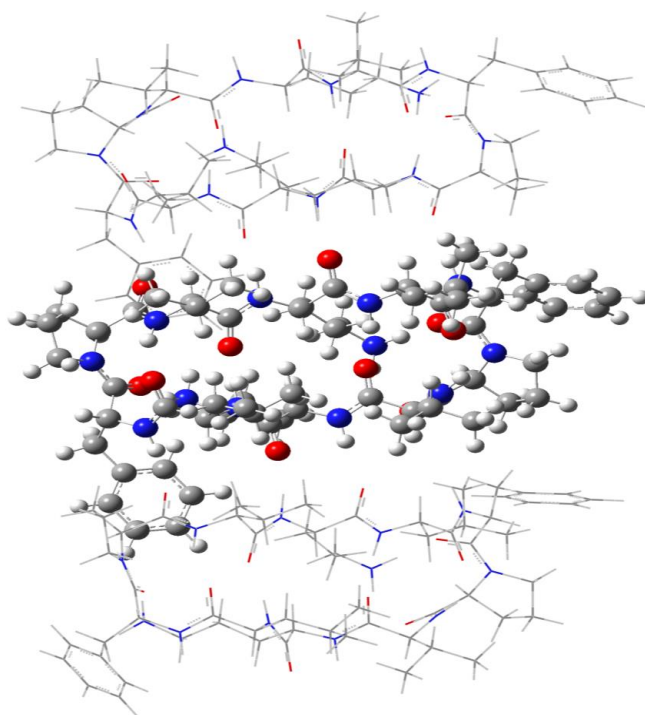


*Figure 5.8 GS trimer model utilised in the QM / MM simulation to generate FTIR and Raman spectra showing three monomer units(GS sandwich). The highlighted atoms are shown as ball-and-stick model and represent portions used as higher layer and the non-selected atoms, shown as stick models, represent portions treated a low layer. The middle selected GS molecule in the trimer was assigned to QM calculation and the other two molecules were assigned to MM calculations. This trimer model allowed for nearest neighbour interactions.*

#### *IR: Amide II region $1600 - 1450 \text{ cm}^{-1}$*

The region  $1450-1600 \text{ cm}^{-1}$  for the amide II leads to vibrational modes of the ring structure backbone, as well as the side chains. Band at  $1533 \text{ cm}^{-1}$  is from bending of the Orn side chain N-H group and there are also contributions from Leu C-H and C-C groups. At  $1546 \text{ cm}^{-1}$  are the Phe C-C and C=C stretch bands. At  $1568 \text{ cm}^{-1}$  the wagging of amides in the two  $\beta$ -turns were observed, and as these are the amides sitting at the ends of the trimer sandwich which may have more freedom to move. At  $1557 \text{ cm}^{-1}$  there is more movement in the two top and bottom layers of the trimer sandwich. For the middle layer there is a possible vibronic coupling at  $1545 \text{ cm}^{-1}$  between Phe and amide in the  $\beta$ -turns, as viewed from GaussView 5 software. The vibrational mode at  $1533 \text{ cm}^{-1}$  is linked to amide I and the N-H bending was observed in the  $\beta$ -sheet. Additionally, at  $1577 \text{ cm}^{-1}$  is the  $\beta$ -sheet mode. The vibration mode at  $1624 \text{ cm}^{-1}$  was observed to be unrelated to that at  $1601 \text{ cm}^{-1}$ . At  $1601 \text{ cm}^{-1}$  and  $1608 \text{ cm}^{-1}$  are N-H bending of the amide in the  $\beta$ -sheets and NH bending, respectively. At  $1507 \text{ cm}^{-1}$  there is contribution from the side chain phenyl group of the Phe residue. The vibrational modes at  $1533,$

1577  $\text{cm}^{-1}$  are also observed in second derivative analysis and increase with increasing peptide concentration regardless of the solvent environment.

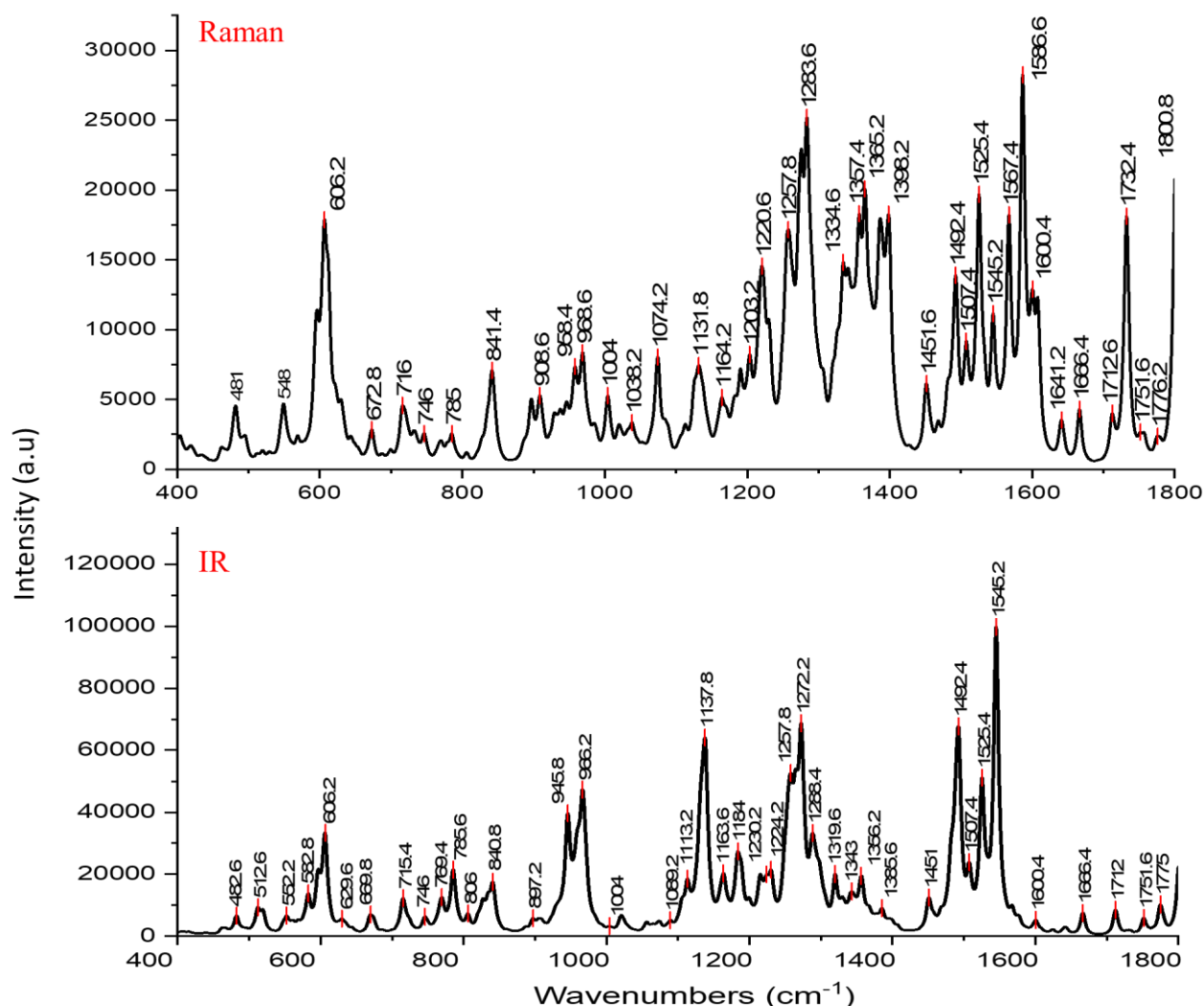


Figure 5.9 QM / MM Raman and FTIR calculated spectra for the GS trimer model.

#### Raman: Amide I region 1735 – 1600 $\text{cm}^{-1}$

At 1732  $\text{cm}^{-1}$  is the Val carbonyl which is part of the  $\beta$ -sheet. In the monomer model this mode is at 1730 and 1738  $\text{cm}^{-1}$ , slightly higher energies as the mode was more free in the monomer than in the trimer. The band at 1712  $\text{cm}^{-1}$  is from the Pro carbonyl which is part of the  $\beta$ -turn which is stretching and some carbons (C-C bonds) bending. The calculated Raman and FTIR vibrational bands which are in correlation from the spectrum in Figure 5.9 are at 1666  $\text{cm}^{-1}$  from carbonyl stretching of the  $\beta$ -turn, at 1640  $\text{cm}^{-1}$  from bending of the Orn amino group, at 1643  $\text{cm}^{-1}$  from Orn bending coupled to  $\beta$ -sheet and at 1608  $\text{cm}^{-1}$  from bending on the amides in the  $\beta$ -turn. At 1601  $\text{cm}^{-1}$  vibrations are all  $\beta$ -sheet. Here, this  $\beta$ -sheet refers to Leu carbonyl, Orn amino group, and Val carbonyl. Orn and Val on one side and the Orn & valine on the other side. Band at 1598  $\text{cm}^{-1}$  is from  $\beta$ -sheet, this is part of the

1601 & 1608  $\text{cm}^{-1}$  groups. These identified vibrational modes from the Raman calculated spectra in range 1643-1598  $\text{cm}^{-1}$ , are represented by the shoulder from 1620-1650  $\text{cm}^{-1}$  in experimental Raman spectra (refer to results on *Figure 5.3*).

*Raman: Amide II region 1600 – 1450  $\text{cm}^{-1}$*

At 1586  $\text{cm}^{-1}$  the  $\beta$ -sheet amide N-H group stretching is vibrationally coupled to Phe side chain stretch. For the band at 1567  $\text{cm}^{-1}$ , both Phe and Leu C-C, N-H, C-H modes are vibrationally coupling. The peak broadening in this range is because many groups are contributing to the vibration and not just a single group. All these groups will have slightly different energies and will couple, therefore it is expected that this will result experimentally in peak broadening and not sharp well resolved peaks. At 1545  $\text{cm}^{-1}$  the  $\beta$ -turn N-H groups coupled to the Phe stretch, and this mode also correlates to the one observed in FTIR (see *Figure 5.9*). At 1533  $\text{cm}^{-1}$  is the  $\beta$ -sheet, and the Phe contribution is at 1525  $\text{cm}^{-1}$ . At 1507  $\text{cm}^{-1}$  there is coupling between Phe and Leu. These calculated modes contributing to amide II are represented in weak broadened amide II band in the experimental Raman spectra discussed in section 5.2.1.1.

*Raman: Amide III region 1500 – 1450  $\text{cm}^{-1}$  and signature for Phe*

All the C-H, carbon hydrogen bonds are at 1492  $\text{cm}^{-1}$  which are the aliphatic carbons, C-C stretch & C-H wags, mostly bends and no Phe. The band at 1484  $\text{cm}^{-1}$  is from  $\beta$ -carbon of the Phe mode. At 1468  $\text{cm}^{-1}$  is the C-H wagging and at 1450  $\text{cm}^{-1}$  we have Phe C=O stretch & side chain. The vibrational mode at 1003  $\text{cm}^{-1}$  is coupling between Phe and Leu. At 1074  $\text{cm}^{-1}$  we have Phe coupling with the whole molecule. At 969 and 958  $\text{cm}^{-1}$  is vibration of the whole molecule. Lastly, mode at 1521  $\text{cm}^{-1}$  is from Phe and not amines and at 1565  $\text{cm}^{-1}$  we also have amines. The Phe contributions located in the mid fingerprint region are strong both in calculated (*Figure 5.9*) and in experimental spectra (*Figure 5.1*).

### 5.2.1.7 Comparing secondary structure for calculated Raman trimer model and experimental GS Raman spectrum

The notable bands in the secondary structure and mid fingerprint region of the calculated Raman spectrum for trimer model and the experimental GS spectrum at 10.00 mM (*Figure 5.10*, refer to *Table 5.3*) are compared and discussed below. From amide I, the band at 1666  $\text{cm}^{-1}$  in the calculated spectra corresponds to the amide I band centred at 1666  $\text{cm}^{-1}$ . This confirms our assignment that the RS band is shifted to higher frequency in the amide I region (*Figure 5.10*). The shoulder near 1640 in GS experimental spectrum, is represented by the strong peak at 1641  $\text{cm}^{-1}$  in the calculated

spectrum, attributed to ornithine. The ornithine band is not evident in the experimental spectrum, most likely because of the solvent environment it is in which inhibits the H-bonding from taking part in the bending and it is thus restricted. The  $\beta$ -sheet NH coupled to Phe at  $1586\text{ cm}^{-1}$  in trimer model correlates with the Phe contribution at  $1605\text{ cm}^{-1}$  in experimental spectrum. The prominent band at  $1003$  and  $1017\text{ cm}^{-1}$  attributed to Phe in experimental spectrum at  $1003$  and  $1074\text{ cm}^{-1}$  from the coupling between Phe and Leu and coupling between Phe and whole molecule, respectively. Considering the similarities in band positions highlighted above, the calculated and experimental spectra correlate well (*Figure 5.10*).

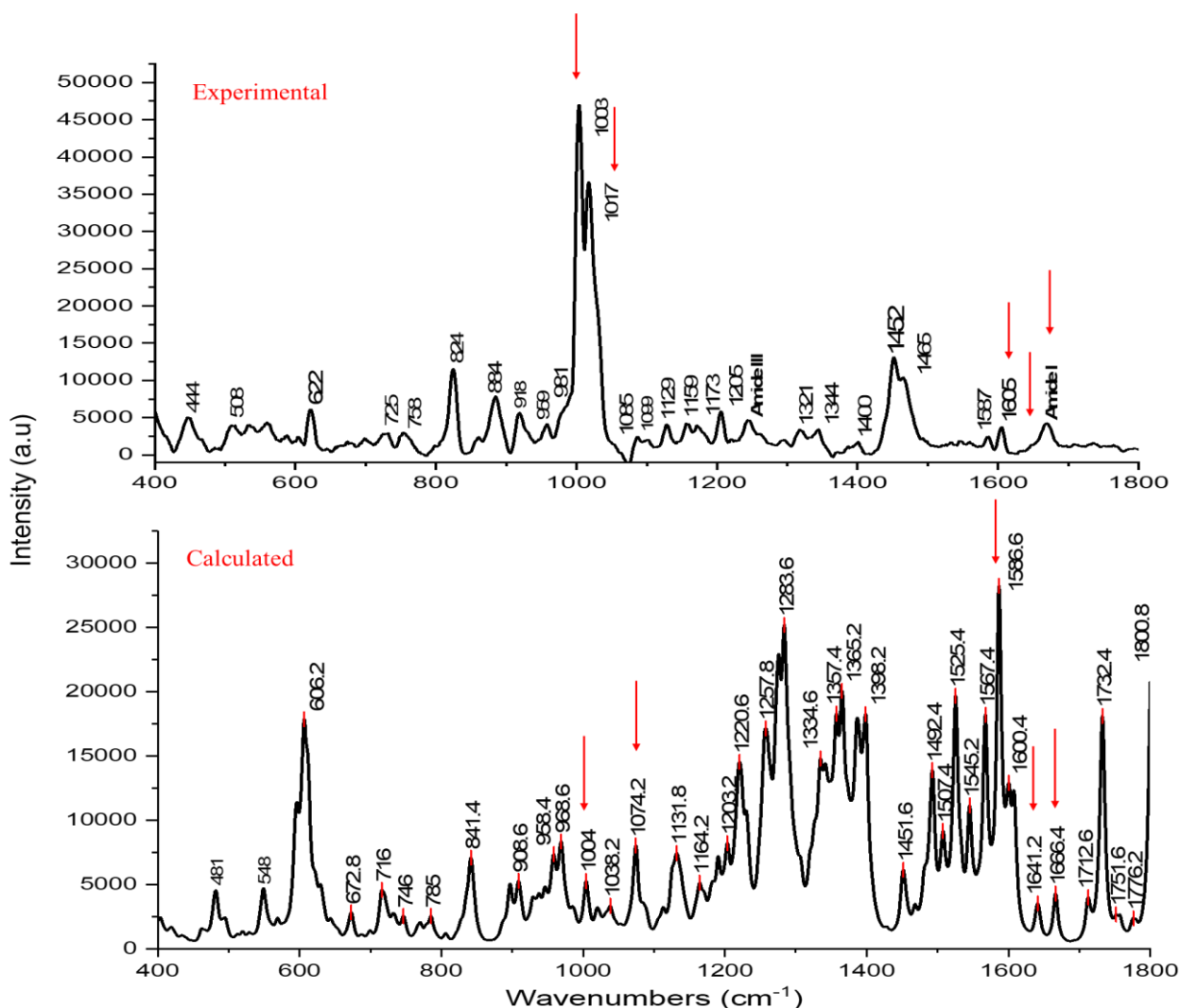


*Figure 5.10 Spectrum a) is experimental Raman spectrum for GS in water at 10mM, b) is the calculated Raman spectrum for trimer model.*

### 5.2.1.8 Comparison of band intensities for experimental and calculated spectra

Apart from band positions discussed above, band intensities are considered for amide I and II modes which contribute to the secondary structure. In a Raman spectrum, bands are observed when they are

Raman active, thus if a vibrational mode is not Raman active it will be absent from the spectrum. Since IR and Raman are complementary techniques, similar bands were observed, thus the band intensities for the calculated and measured RS bands are considered as well as the differences in band intensity between the GS monomer and trimer model spectra.

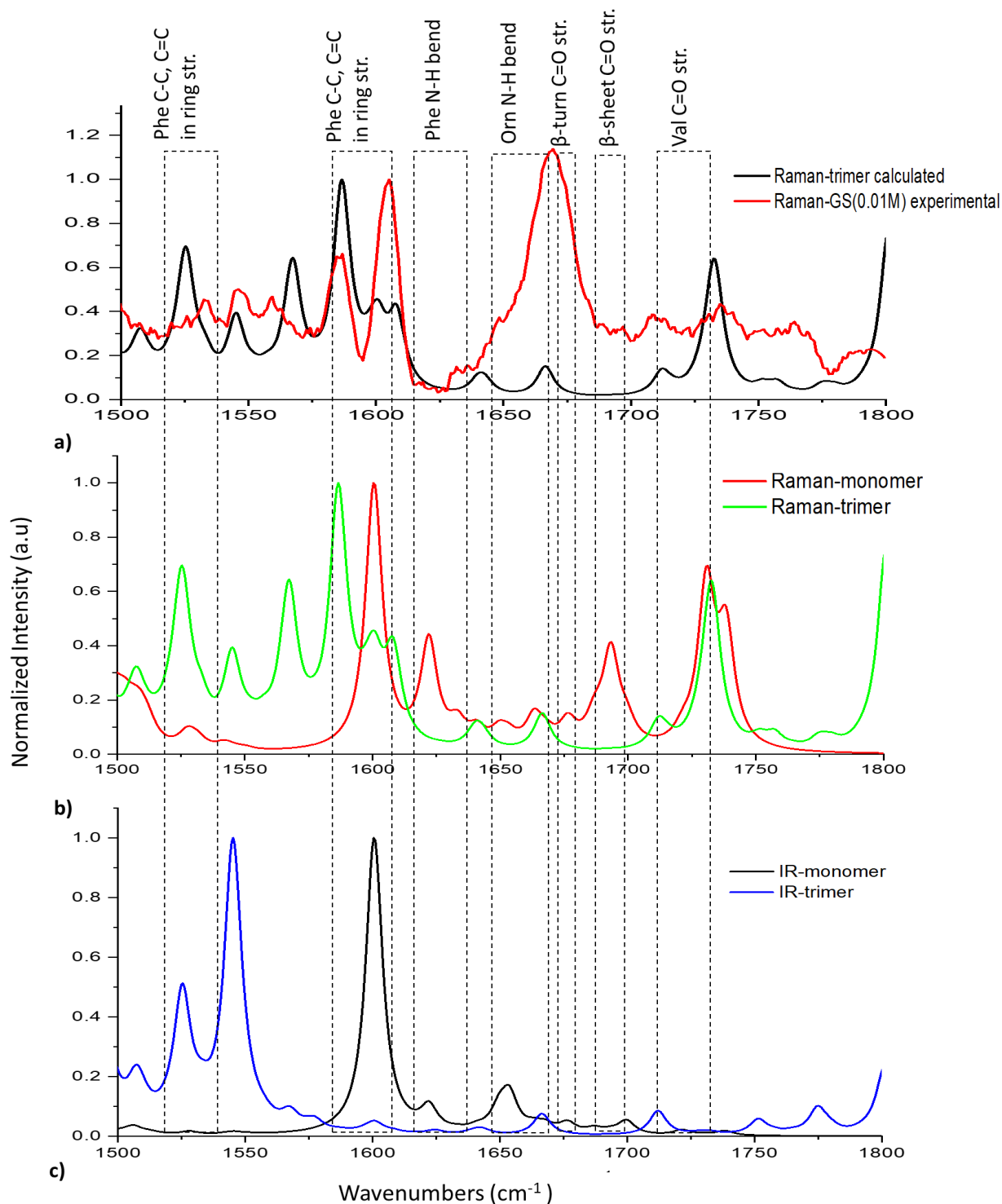


Figure 5.11 Normalized spectra for amide I and II modes for calculated Raman monomer and trimer models and the experimental Raman spectrum for GS at 0.01 M.

In *Figure 5.11* bands contributing to the amide I and II have been identified and discussed in the sections above. Here, significant differences in intensities are discussed. From *Figure 5.11a*, the amide I centred at  $1666\text{ cm}^{-1}$  in the experimental spectrum is a strong broad band from the  $\beta$ -turn C=O stretch, with possible contributions of  $\beta$ -sheet structures. The high intensity of the band at  $1666\text{ cm}^{-1}$  in the solution spectrum is attributed to the sensitivity of the mode to the solvent environment and peptide-solvent and peptide-peptide hydrogen bonds contributing to several C=O modes in the GS preparation at high concentration. The absence of the Orn band in the experimental spectrum shows that the Orn is in a different environment in solution, whereas in the calculated spectra it is present. In the calculated trimer spectrum, the  $\beta$ -turn C=O stretch band is weak as it is restricted. The contribution from Phe C-C stretch near  $1600\text{ cm}^{-1}$  is present in both the calculated and measured spectra presenting strong bands (*Figure 5.11a*).

The Raman monomer and trimer bands of the modelled GS spectra are shown in (*Figure 5.11b*). Comparison of the experimental spectrum in *Figure 5.11a* with the model spectra in *Figure 5.11b* highlights the complexity of the GS conformations in solution. The experimental Raman spectrum have correlating bands with that of the model spectra, both with bands from trimers indicating oligomers and bands from monomers. The monomer bands at  $1730$  and  $1738\text{ cm}^{-1}$  in the model spectrum are more intense than the trimer band at  $1732\text{ cm}^{-1}$  from the Val carbonyl which is part of the  $\beta$ -sheet. In the monomer the band is free to move, thus it vibrates more and has a higher intensity. Both these bands are found in the experimental spectrum, but is much less intense, in comparison with the band at  $1666\text{ cm}^{-1}$ . In the model spectra, in particular the monomer spectrum the band near  $1600\text{ cm}^{-1}$  is from mainly the Phe ring stretch band, and several contributions from Leu carbonyl, Orn amino group and Val carbonyl, thus the high intensity. This intense band is also observed in the experimental spectrum indicating the existence of monomeric GS in solution. This Phe ring stretch band is shifted to  $1586\text{ cm}^{-1}$  and is prominent in both the trimer spectrum and the experimental spectrum indicating presence of oligomers in which the Phe is in a different environment in solution. The amide II mode exhibits intense and broad peaks compared to those in the amide I, because not just a single but several groups from  $\beta$ -sheet amide stretch coupled to Phe and the Phe and Leu C-C, N-H, C-H modes are coupling, vibrating and contributing to several broad intense peaks.

Similar modes are present in both Raman and IR as expected. The IR monomer and trimer model spectra are shown in *Figure 5.11c*. In the IR monomer spectrum, the most intense is the band at  $1600\text{ cm}^{-1}$  from N-H bending coupled to Phe carbon stretch. The aromatic Phe band near  $1600\text{ cm}^{-1}$  and the N-H bend from the Orn group at  $1653\text{ cm}^{-1}$  are major contributors to IR spectra. The Phe contribution near  $1600\text{ cm}^{-1}$  is strong in both Raman and IR spectra and in both calculated and measured spectra. This suggest that the aromatic Phe is a residue not greatly affected by solvent environment, as

compared to the Orn residue which was not present in the measured spectra due to solvent effects. The amide I contributions are intense and more significant in the monomer than in the trimer Raman and IR spectra, while the amide II contributions are stronger in the trimer Raman and IR spectra than in the monomer spectra. Major contributors of the trimer are the unrestricted  $\beta$ -turns which at the ends of the trimer ‘sandwich’ which vibrate more freely and give intense bands. The  $\beta$ -sheet are restricted in movement, however intense bands appear when the  $\beta$ -sheets are coupled to the aromatic Phe or the amino group in Orn. The discussed bands are summarised in *Table 5.4*.

*Table 5.4 Raman and IR bands for GS monomer and trimer vibrational modes in the amide I and II region.*

		Calculated				Experimental
		Raman monomer	IR monomer	Raman trimer	IR trimer	GS @10 mM
Amide I	Phe C-C, C=C in ring str.	1527 (w)	1527 (vw)	1525 (w)		
	Phe C-C, C=C in ring str.	1600 (vs)	1600 (vs)	1586 (vs)	1601 (vw)	1605 (vs) 1586 (vs)
Amide II	Phe N-H bend	1622 (vs)	1622 (w)		1624 (vw)	1618 (vw)
	Orn N-H bend	1663 (w)	1663 (s)	1643 (w)	1666 (vw)	1666 (vs)
	$\beta$ - turn C=O str.	1676 (w)	1676 (vw)	1666 (w)	1666 (w)	1666 (vs)
	$\beta$ - sheet C=O str.	1693 (vs)	1693 (w)		1693 (vw)	1702 (w)
	Val C=O str.			1732 (vs)		

vs= very strong; s = strong; w = weak; vw = very weak

## 5.2.2 Characterisation of Gramicidin S mixed with metal nanoparticles using RS and SERS

To further elucidate the structure of GS at lower concentration, SERS was considered. With SERS molecules adsorbed on or close to a metallic surface can be detected as a result of increased Raman signals. SERS has been considered as a useful technique for structural characterisation and

quantification of proteins as well as other biomolecules [22]. By applying SERS on GS details on structure of GS on a metallic substrate shall be compared to the structural details of GS in crystalline form and in aqueous solution.

### 5.2.2.1 Characterisation of Nanoparticles

#### *UV - Vis*

UV-Vis absorption spectra (*Figure 5.12*) of the Ag and Au NPs were collected at ambient temperature using a UV-NIR spectrophotometer; Lambda 950 UV / VIS spectrometer (Perkin Elmer). Scans were taken in the range 200 – 1000 nm. A quartz cuvette of path length 1 cm was used. A volume of 2.00 mL of each of the undiluted Ag and Au colloids was used to obtain their respective absorption spectra. Since these are relatively large size NPs, (100 nm) Ag has a major peak centred at 483 nm which is the dipole plasmon resonance peak and a minor peak at 403 nm which is the quadrupole plasmon resonance peak. Au only has a major dipole plasmon resonance peak centred at 570 nm. The full width at half maximum (FWHM) for Ag and Au was 214 nm and 135 nm, respectively. A FWHM of more than 100 nm confirms the presence of poly-dispersed NPs [23].

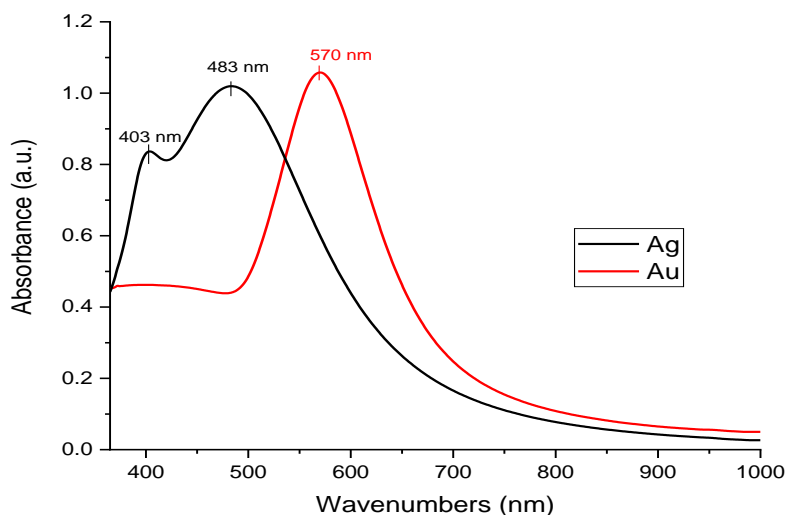


*Figure 5.12 Absorption Spectra of 100 nm sized silver and gold colloids.*

#### **TEM**

To further characterise the morphology of NPs transmission electron micrographs of the NPs were collected using a JEOL JEM-2100 with an accelerating voltage of 200 kV (*Figure 5.13*). For sample preparation, a drop of the NPs colloidal solution was deposited on carbon coated copper grid (G400-Cu) and allowed to dry under ambient conditions before scanning.

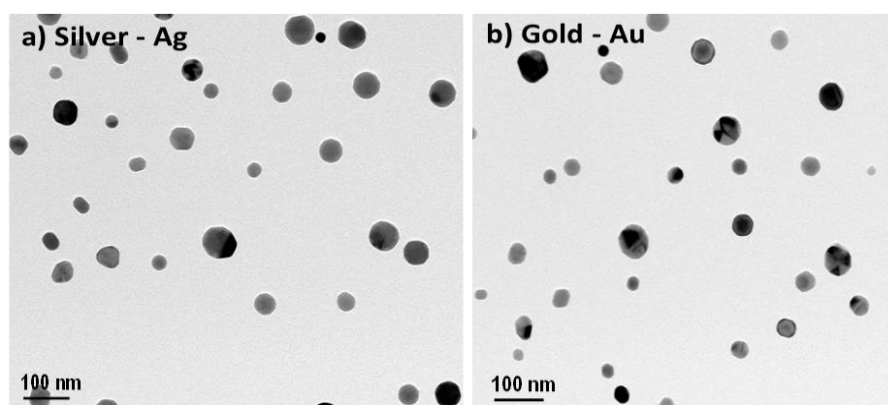


Figure 5.13 TEM images for Ag and Au nanoparticles

### ***Evidence of Aggregation of Ag and Au nanoparticles by GS***

A unique property of the cationic peptides is their ability to induce aggregation of the colloidal nanoparticles (NPs) [24]. It is known from literature that negatively charged Au and Ag NPs of size  $\sim 95$  nm can become aggregated in the presence of adsorbed cationic peptides at very low concentrations, consequently enabling the detection of the adsorbed peptide at those concentrations with SERS [25], [26]. Furthermore, López-Tobar *et al.* [26] reported that the use of large size NPs reduces electrostatic repulsion present in small size NPs, therefore, with larger size colloids ( $\sim 90$  nm diameter) there is less need to use an aggregating agent. Our study employed commercially available  $100 \pm 10$  nm sized silver and gold NPs. When aggregation occurs “hot-spots” are formed in which electromagnetic radiation can be strongly enhanced [27], [28]. An absorption spectrum of the NPs alone was collected and compared with the spectra of NPs in the presence of increasing concentrations of GS (Figure 5.12 and Figure 5.14). Comparing the spectrum of NPs only and that of NPs with GS (NP/GS) at different concentrations, there was decrease in absorption by the NP/GS compared to the NPs alone. Emergence of an additional band at higher wavelengths indicate a plasmonic red-shift, which confirms aggregation due to surface adsorption of the peptides to the NP surface. From the GS concentrations ranging from  $10^{-8}$  -  $10^{-4}$  M (blue to red spectrum in Figure 5.14), the lowest concentration, referred to as the *optimum* peptide concentration, which gave a large plasmonic redshift was GS at  $1 \times 10^{-5}$  M (Figure 5.14a, orange spectrum) for AgNPs. A higher concentration of GS at  $1 \times 10^{-4}$  M (Figure 5.14a, red spectrum) also caused a plasmonic redshift with AgNPs. For AuNPs no plasmonic red-shift was present with lower GS concentrations across the range 650 – 1000 nm, and a small decrease in intensity was identified with a GS concentration of  $1 \times 10^{-4}$  M (Figure 5.14b, red spectrum). The results were reproducible in that three different batches of 100 nm sized silver nanoparticles that were used in the UV-Vis measurements to assess if the GS concentration of  $1 \times 10^{-5}$  M would still give a large plasmonic red-shift. In all three measurements,

taken at different days,  $1 \times 10^{-5}$  M remained the optimum concentration. Furthermore, SER spectra of the three sample solutions were collected. Using the Phe prominent band, the enhancement factor (EF) was calculated and it was constant over the different samples. This confirmed the reproducibility of the SERS results (reported in section 5.2.2.2). As previously mentioned, the redshifts are the first strong indications of NP aggregation, showing that with GS (since it does induce aggregation) we can probe molecular interactions at very low concentrations.

Further evidence for NP aggregation was revealed from the TEM images of Ag with GS at a concentration of  $10^{-5}$  M (Figure 5.15a) and Au with GS at a concentration of  $10^{-4}$  M (Figure 5.15b). For reference unaggregated NPs are first reported in (Figure 5.13). Nanoparticle aggregation by GS did not occur for lower concentrations of GS at  $10^{-6}$  (green spectrum),  $10^{-7}$  (red spectrum) and  $10^{-8}$  M (blue spectrum), regardless of the time of incubation (Figure 5.16).

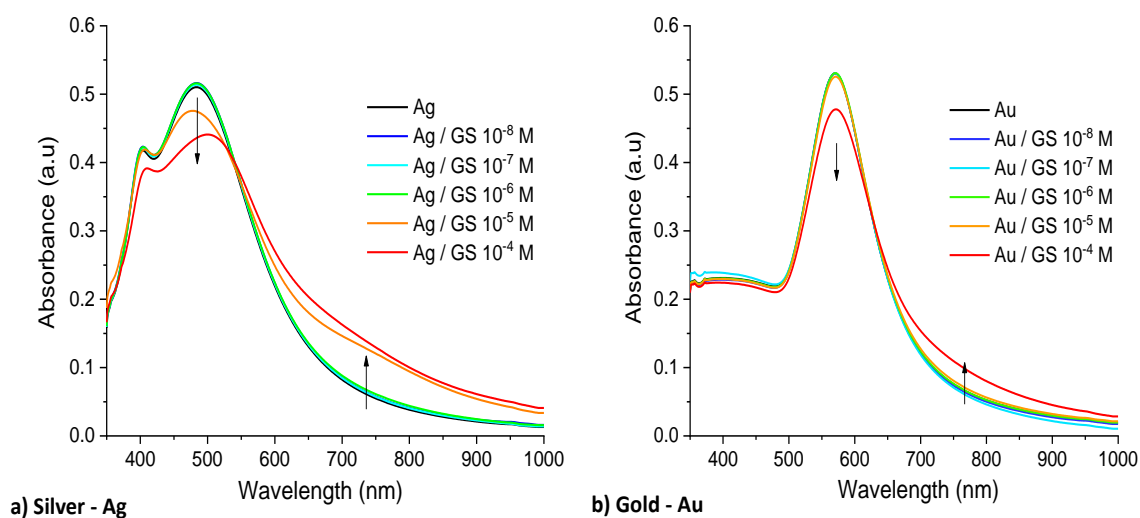


Figure 5.14 Absorption spectra of Ag and Au NPs with GS in solution. The black spectrum is for the NPs in the absence of the peptide. Coloured spectra of NPs in the presence of the peptide at various concentrations ranging from GS  $10^{-8}$  –  $10^{-4}$  M. The decreased peak intensity and increased absorption at longer wavenumbers are due to aggregation and used to identify the optimum peptide concentration, see text.

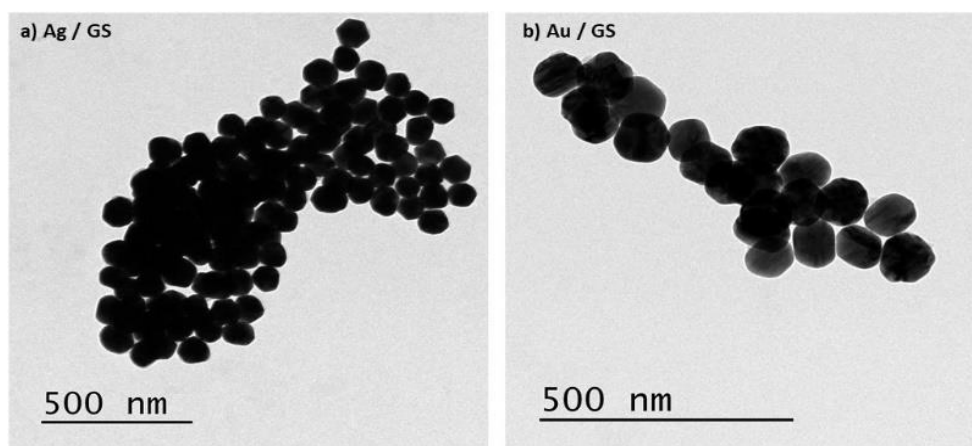


Figure 5.15 TEM micrographs showing the aggregated NPs for Ag/GS  $1 \times 10^{-5}$  M (a) and Au/GS  $1 \times 10^{-4}$  M (b).

The NP aggregation observed is a positive effect which we anticipated for the cationic cyclic peptide GS. It further showed that of the concentrations considered, only the GS concentrations of  $10^{-5}$  with Ag showed a significant redshift. Much lower peptide concentrations have been reported to cause NP aggregation in studies done on somatostatin-14, a therapeutic peptide, where concentrations down to  $10^{-7}$  M aggregated Au NPs [25]. This enhancement may be due to the presence of more cationic residues, as well as aromatic residues in the peptide structure, such as tryptophan in addition to phenylalanine, facilitating the aggregation of the peptides at much lower concentration [24].

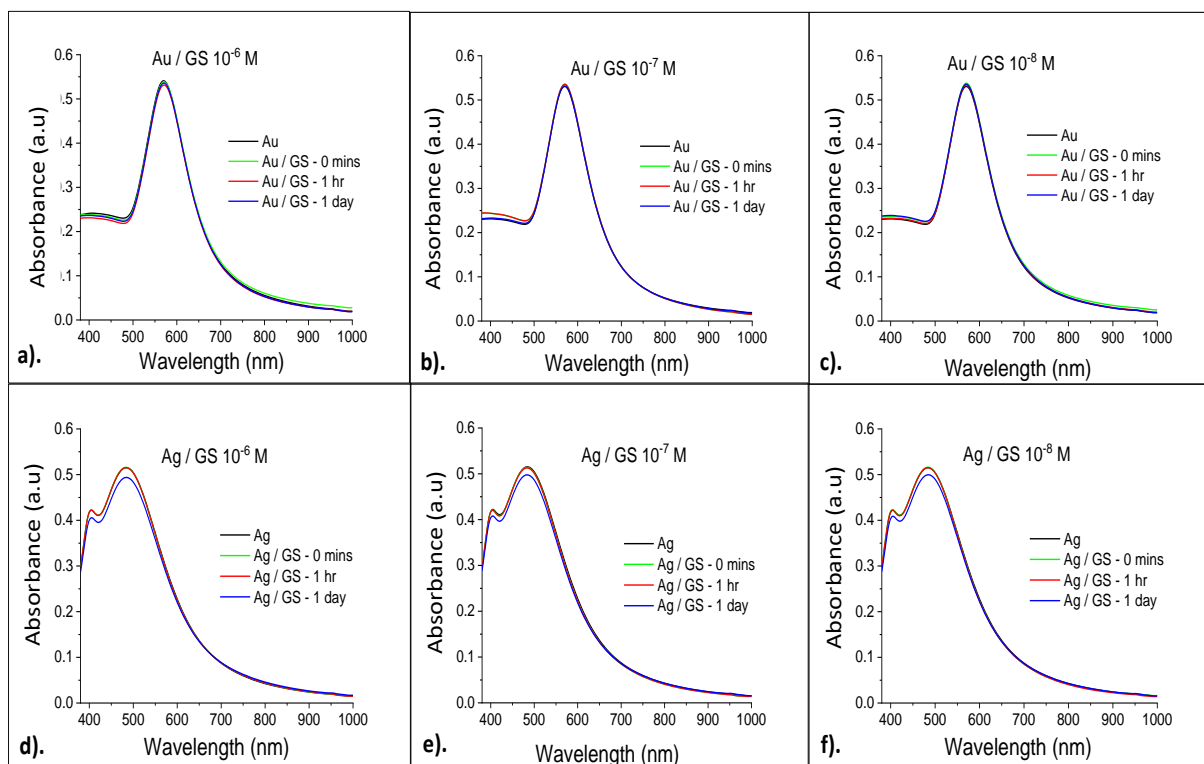


Figure 5.16 Absorption spectra for Au / GS with GS at  $10^{-6}$ ,  $10^{-7}$  and  $10^{-8}$  M (a, b and c, respectively) and Ag / GS with GS at  $10^{-6}$ ,  $10^{-7}$  and  $10^{-8}$  M (d, e and f, respectively). Time tracking for a day showed no plasmonic redshift in these spectra.

### 5.2.2.2 RS and SERS with Ag and Au nanoparticles

For SERS measurements, the excitation wavelength of 830 nm was utilised as it falls within the redshifted plasmon band in (Figure 5.14) and this, together with the large size NPs and optimum peptide concentration would give a strong SERS signal [26]. The Raman band intensity decreases with decrease in concentration, as expected. For comparison, spectra for GS at  $1 \times 10^{-2}$ ,  $1 \times 10^{-3}$  and  $1 \times 10^{-4}$  M are shown as well (Figure 5.17). Only GS concentrations greater than  $1 \times 10^{-4}$  M can be measured and the bands resolved without employing nanoparticles for SERS detection of the peptide. From the spectra in Figure 5.17, for low concentrations ( $1 \times 10^{-4}$  M) with vibrational bands undetectable with normal Raman spectroscopy, there is a particular concentration known as the

optimum concentration which aggregates nanoparticles. Thus, the SERS spectra at the optimum concentration for both Ag and Au NPs were recorded (*Figure 5.17*).

The Raman spectra of GS solution showed Raman band positions comparable to those from the GS powder (refer to *Figure 5.2*), but several of these features were lost in the presence of Ag and Au NPs which can be considered as solid surfaces. However, spectra were enhanced at lower GS concentrations and the SERS EF for silver nanoparticles is utilised to characterise the effect on the *optimum* concentration. The EF was calculated by considering the counts obtained at different concentrations with RS in relation to the counts obtained with nanoparticles in SERS. The prominent Phe band at  $1000\text{ cm}^{-1}$  was considered for this calculation due to its strong intensity (*Table 5.5*).

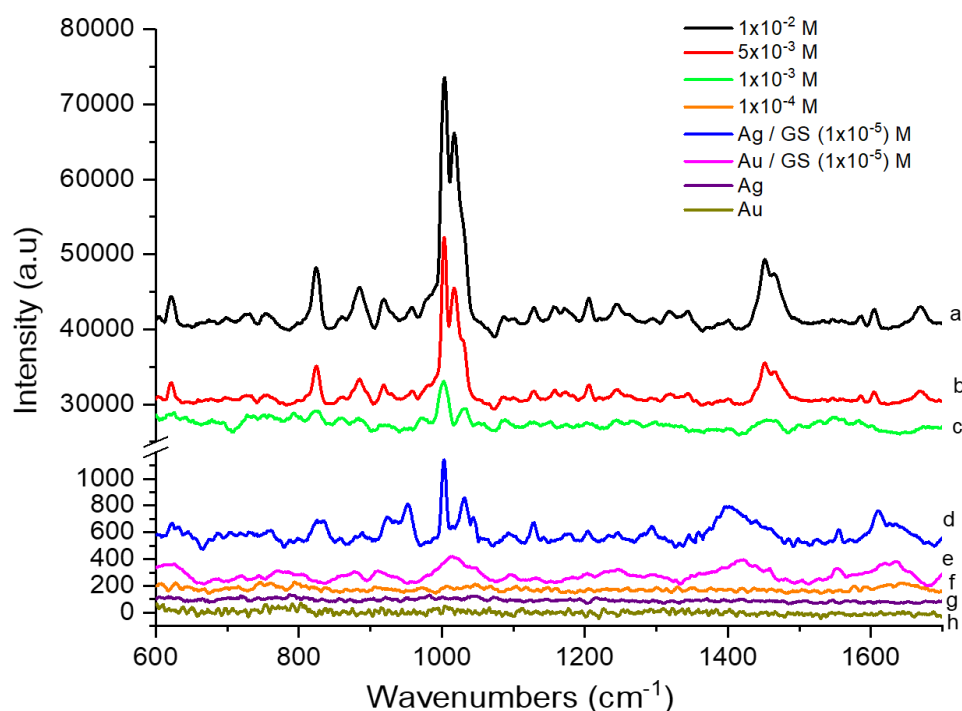


*Figure 5.17* Raman spectra for GS in aqueous solution at a)  $1 \times 10^{-2}$ , b)  $5 \times 10^{-3}$ , c)  $1 \times 10^{-3}$ , and f)  $1 \times 10^{-4}$  M. SERS spectra are presented for d) Ag with GS at  $1 \times 10^{-5}$  M and e) Au with GS at  $1 \times 10^{-4}$  M. Spectra g) and h) are for the Ag and Au NPs alone, respectively. Each spectrum was acquired for 10 and 12 mins for RS and SERS, respectively, with 830 nm laser excitation source. The spectra have been vertically offset by different values for clarity.

At  $1 \times 10^{-2}$  M,  $4801 \pm 253$  counts/min were obtained and by reducing peptide concentration the intensity decreased to  $699 \pm 56$  counts/min for  $1 \times 10^{-3}$  M. Using the gradient/slope of value  $4.7 \times 10^6 \pm 1.6 \times 10^5$  from the calibration curve in (*Figure 5.18*), we can deduce that further reduction in GS concentration to  $1 \times 10^{-5}$  M will give approximately  $48 \pm 5$  in 10 mins which is  $5 \pm 1$  counts/min with normal RS. SERS for Ag / GS at  $1 \times 10^{-5}$  M (*Figure 5.17*) gave  $658 \pm 4$  in 12 mins which is  $548 \pm 4$  counts in 10 mins which is  $55 \pm 1$  counts/min. Thus, from  $5 \pm 1$  counts/min with RS to  $54 \pm 5$  counts/min = an EF of  $10.9 \pm 2$  is obtained for GS at  $1 \times 10^{-5}$  M with reference to the Phe band.

Table 5.5 Average counts recorded from measurements with reference to the prominent band of Phe peak located near  $1000\text{ cm}^{-1}$ , to deduce the enhancement factor by Ag nanoparticles.

Concentration [M]	RS Counts [a.u]	
	Measured in 10 mins	Calculated / min
$1 \times 10^{-2}$	$48017 \pm 2536$	$4802 \pm 254$
$5 \times 10^{-3}$	$21399 \pm 1467$	$2140 \pm 147$
$1 \times 10^{-3}$	$6995 \pm 199$	$670 \pm 20$

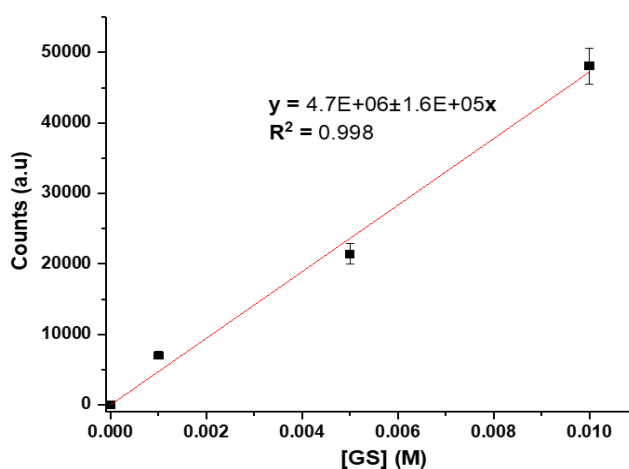


Figure 5.18 Calibrations for counts detected in RS used for calculating enhancement factor.

Similar calculations were performed for the Phe near  $1630\text{ cm}^{-1}$  and amide I band in  $1600\text{--}1700\text{ cm}^{-1}$  regions, yielding EF values of  $13.2 \pm 0.5$  and  $19.5 \pm 0.4$ , respectively. The differing EF values for the different modes are attributed to factors such as proximity and orientation of the GS vibrating groups on the nanoparticle surface. In a SERS study by Lopez-Tobar *et al.* [26], citrate Au NP with  $\sim 95\text{ nm}$  diameter were used in detecting cationic peptides and even though the EF values were not reported, concentrations as low as  $10^{-7}\text{ M}$  were detected. EFs of up to  $10^{15}$  have been reported under conditions of single molecule detection [29] and in cases where the actual number of molecules probed in a particular area can be accounted for [29], [30], which was not the case in our study.

The SERS spectrum for GS in AuNPs (Figure 5.17e) showed merged features which were not well resolved into individual peaks, such as the prominent bands of Phe located near  $1000\text{ cm}^{-1}$ . The enhancement with Au is not as big as that with Ag. However, presence of Au did lower the level of detection as a GS concentration of  $1 \times 10^{-4}\text{ M}$  was measured with Au and additionally displaying bands which are absent when there is no NPs as shown in spectrum f) in Figure 5.17. Since the SERS bands

with Au were not well resolved, this indicates the lack of a significant plasmonic red-shifted peak from the UV-Vis spectrum (*Figure 5.14b*) indicating that GS did not strongly adsorb to the Au metallic surface. The preference of GS to better adsorb to Ag than to Au is explained by the interactions between the peptide backbone and the Ag. According to a mass spectrometry study on cationic oligopeptides, Tang *et al.* suggested the  $\text{Ag}^+$  chelated with the N-terminus of the nitrogen and the carbonyl oxygen of the second residue, in the binding process of silver to the peptide backbone of glycylglycylphenylalanine (GGF) [31].

As previously stated, the SERS spectra for Ag/GS  $10^{-5}$  M has some features that are similar to those of the Raman spectra of solid GS and GS in aqueous solution, but there are noticeable differences (*Figure 5.17*). In *Table 5.6* below, the band assignments of GS in the three distinct environments are compared; 1) solid/crystalline GS; 2) GS aqueous solution of 10 mM (aggregates); and 3) GS adsorbed on a metallic silver surface. Band shifts are also indicated for bands which significantly shift due to SERS. Significant bands include the aromatic Phe markers which are significantly affected by the presence of NPs as they show a strong SERS signal in the fingerprint region near  $1000\text{ cm}^{-1}$ . There is red-shifting of Phe phenyl ring contribution from  $620$  to  $624\text{ cm}^{-1}$  which indicates a direct interaction of the ring  $\pi$  orbital with the metal [32]. The Pro band shifted from  $916$  to  $923\text{ cm}^{-1}$  from the C-C stretching of the C-COO<sup>-</sup> and is consistent with a surface effect of the CO bond vibrating perpendicular to the surface [33]. A C-C gauche stretch is shifted from  $1085$  to  $1096\text{ cm}^{-1}$  and the CH stretching of peptide bonds shift from  $1179$  to  $1176\text{ cm}^{-1}$  (*Table 5.6*).

The Amide I band was well represented in all three environments. Raman results for solid GS showed the main amide I band at  $1665\text{ cm}^{-1}$  and a band at  $1603\text{ cm}^{-1}$  contributed to by Phe. This agrees with Raman studies on crystalline GS by Naik *et al.* where the amide I band was located at  $1670\text{ cm}^{-1}$  [15]. The C-C stretch mode of Phe is shifted from  $1605$  to  $1610\text{ cm}^{-1}$  between Raman and SERS environments, another interaction of the phenyl ring with Ag. The SERS shift to longer wavenumbers was also observed for the Phe bands in the mid fingerprint region. This indicated a change in the Phe ring environment, thus a conformational change in GS in the presence of Ag.

The amide I, II and III modes are known to be strong indicators of secondary structural information [65]. However, amide II and III modes are less suited for conformational analyses due to interference from side chain vibrations [67]. For the Amide III mode there is a shift of the  $1241\text{ cm}^{-1}$  mode to  $1246\text{ cm}^{-1}$  in the presence of Ag. However, from solid GS there is a shift from  $1241\text{ cm}^{-1}$  to  $1246\text{ cm}^{-1}$  for  $\beta$ -sheet N-H bend and C-N stretch vibration. There was no peak shift for peptide bonds, Amide II or Orn side chain bands found at  $1555\text{ cm}^{-1}$  in SERS environment, indicating that the N-H bending was no significant interaction with Ag.

Table 5.6 RS and SERS band assignments for GS in the presence of AgNP in correlation with GS powder and GS in aqueous solution

Group/Structure	Vibrational mode	*Assignment from Literature	Experimental results			
			GS powder	GS in 10mM solution	GS + AgNP	**Band Shift cm <sup>-1</sup>
D-Phe phenyl ring	Ring torsion	447	449	444	nd	-
D-Phe phenyl ring	C-C twist	621	620	622	624	4, 2
Side chain CH <sub>2</sub> groups Pro	CH <sub>2</sub> out of plane bending	750	753	758	761	8, 3
Pro side chain	C-C stretching	823	823	824	825	2, 1
Peptide groups	C-H bending	883	883	885	nd	
Pro side chain	CH <sub>2</sub> out of plane twist, $\nu$ (C-C) stretch of the C-COO <sup>-</sup>	918	916	918	923	7, 5
Peptide bonds	C-H rocking	956	959	nd	nd	-
$\beta$ -sheet	C-C stretching	980	980	981	nd	-
D-Phe phenyl ring	C-C stretching	1000	1002	1003	1002	0, -1
D-Phe phenyl ring	C-C stretching	1030	1030	nd	nd	-
D-Phe phenyl ring	C-C stretching	1031	nd	nd	nd	-
D-Phe phenyl ring	C-C stretching	1011	1017	1017	nd	-
Peptide bonds, Orn side chain	C-O stretching, C-N stretching	1053	1053	nd	nd	-
Peptide groups	C-C gauche stretch	1086	1085	1085	1096	11, 11
Peptide bonds, Orn side chain	C-N stretching	1128	1128	1129	1127	-1, -2
Peptide groups	C-C and C-N stretch	1155	1155	1159	nd	-
Peptide bonds	C-H bending	na	1179	1181	1176	-3, -5
D-Phe	C $\beta$ -C ring stretch	1203	1203	1205	1203	0, -2
Pro side chain	CH <sub>2</sub> wagging	1204	1204	1205	1203	-1, -2
Phe Amide III	C-C stretch and ring deformation CH <sub>2</sub> wagging	1204	1204	1205	nd	-
Amide III $\beta$ -sheet	N-H bending and C-N stretch	1242	1241	1244	1246	5, 2
Aliphatic side chains	CH <sub>2</sub> deformation	1296	1294	nd	nd	-
Pro	NH & CH deformation	1323	1323	1321	nd	-
Leu/Pro side chain	$\delta$ (CH) residual vibrations	1344	1344	1344	1345	1, 1
Val, Leu side chain	CH <sub>3</sub> , CH <sub>2</sub> wagging CCH deformation	1386	1389	nd	nd	-
Leu side chain	C-H bending	1310/4	nd	nd	nd	-
Leu side chain	C-H bending	1342/5	nd	nd	nd	-
Leu side chain	C-H bending	1369/70	nd	nd	nd	-
Leu side chain	C-H bending	1390/5	nd	nd	nd	-
Pro side chain	C-H bending	1387	nd	nd	nd	-

\* [1], [4], [15]–[17], [33]–[41]\*\*Band shift from GS powder to GS + AgNP, band shift from GS in solution to GS + AgNP

Table 5.5 continued

Group/Structure	Vibrational mode	Assignment from Literature	Experimental results			
			GS as powder	GS in solution	GS +AgNP	*Band Shift $\text{cm}^{-1}$
Leu side chain	CH <sub>3</sub> asym. stretch	1445	nd	nd	nd	-
Leu side chain	CH <sub>3</sub> asym. stretch	1452	nd	1452	1450	0, -2
Pro side chain	CH <sub>2</sub> bend	1447-1472	1449	1452	1450	1, -2
Peptide bonds	C-N stretching	1435-1465	1449	1452	1450	1, -2
Leu/Pro side chain	Fermi interaction $\delta(\text{CH}_2)$ and $\gamma(\text{CH}_2)$	1463	1462	1465	nd	-
Peptide bonds, Amide II, Orn side chain	N-H bending C-N stretching	1554	1555	1555	1555	0, 0
D-Phe phenyl ring	$\delta$ (C=C) stretching	1582	1584	1587	nd	-
D-Phe phenyl ring	$\delta$ (C=C) stretching	1584	1584	nd	nd	-
D-Phe phenyl ring	C=C stretching	1605	1603	1605	1610	7, 5
Orn amino group	N-H bending	1647	nd	nd	nd	-
Orn amino group	N-H bending	1659	nd	nd	nd	-
Orn amino group	N-H bending	1660	nd	nd	nd	-
Peptide bonds	C=O stretching	1600 - 1700	1665	1666	1634	-31, -32

\* [1], [4], [38]–[41], [15]–[17], [33]–[37]

\*\*Band shift from GS powder to GS + AgNP, band shift from GS in solution to GS + AgNP  
v, stretching;  $\delta$ , deformation;  $\gamma$ , wagging;  $\beta$ , bending

Similarities in band position for bands in GS powder and solution spectra suggest that structure is retained to a large degree when GS goes into solution with water. In SERS, the Amide I band at  $1665 \text{ cm}^{-1}$  is broadened and downshifted to  $1634 \text{ cm}^{-1}$  when in the presence of Ag. This major shift in the amide I band suggests chelation by silver implying that the GS backbone conformation is altered in presence of Ag while the GS conformation is stable in the absence of Ag. This is in accordance with literature, because amide I bands for  $\beta$ -sheets are in the between  $1665$ – $1680 \text{ cm}^{-1}$  in Raman spectra, but in SERS the Amide I band tends to shift to lower frequencies due to weakening of the C=O bond from the interaction of the peptide bond (CO-NH) with the metallic substrate (chelation) [13], [42]. Raman studies done on a linear penta-decapeptide (15 residues) gramicidin A have reported the amide I to be at higher wavenumbers of  $1665 \text{ cm}^{-1}$ , in-line with our observation for GS [9], although GS is a cyclic peptide with a different secondary structure. Bands which experienced significant shift indicated interaction with silver, and they were considerably enhanced.

### 5.3 Discussion

For the amide I band the simulated IR and Raman spectral results highlight the features which are underneath the broad IR and Raman experimental spectra. For simulated spectra, correlating bands in both IR and Raman contributing to amide I mode include  $1666\text{ cm}^{-1}$  from carbonyl stretch of  $\beta$ -turn,  $1640\text{ cm}^{-1}$  and  $1643\text{ cm}^{-1}$  both from ornithine bending and  $1608\text{ cm}^{-1}$  from bending of amides in the  $\beta$ -turn (Table 5.3). Of these bands, the ornithine band at  $1666\text{ cm}^{-1}$  is identified in experimental results for GS in TFE and 1-octanol at  $1670$  and  $1673\text{ cm}^{-1}$  respectively (Table 3.5), but not in  $\text{D}_2\text{O}$  implying that in  $\text{D}_2\text{O}$ , the Orn is likely to be in an environment where it is restricted and is not free to vibrate. The amide II at  $1555\text{ cm}^{-1}$  and Phe band at  $1605\text{ cm}^{-1}$  in experimental Raman spectrum of GS solution are well presented in both monomer and trimer model in range  $1505\text{--}1586\text{ cm}^{-1}$  (Table 5.3). Most important to note is representation of  $\beta$ -turn structures and Orn from both IR and Raman simulated spectra and from experimental results. The presence of these structures results from measurements performed.  $\beta$ -turns are contributed to the D-Phe and Pro residues which contribute to the hydrophobicity of GS, while Orn contributes to the GS hydrophilicity. Results from SERS which correlated with those from IR are the identification of the C-C stretch of the Phe ring at  $1610\text{ cm}^{-1}$  in SERS, which was identified in both Raman experimental and simulated results, and in IR measurements the band is at  $1618$ ,  $1617$  and  $1616\text{ cm}^{-1}$  for GS in  $\text{D}_2\text{O}$ , TFE and 1-octanol, respectively. The amide I  $\text{NH}_3^+$  bend from Orn present in TFE and 1-octanol at  $1646$  and  $1645\text{--}1647\text{ cm}^{-1}$ , respectively, was not identified in the amide I of SERS, however it is possible that the band could be present but shifted in frequency due the presence of the metallic substrate. The amide II or side chains found at  $1555\text{ cm}^{-1}$  in SERS results were not shifted in frequency and were also identified at  $1505\text{--}1586\text{ cm}^{-1}$  in IR and Raman results. SERS results indicate that Phe is available for interaction with the metallic substrate, and is not masked inside the oligomeric structure. Additionally, the amide groups are also available for interaction with the metallic silver substrate which is why amide I is enhanced but not all amide I contributors are interacting in H-bond interaction.

Solvent studies also highlighted that the anti-parallel  $\beta$ -sheets buried inside the GS structure were not influenced by changes on solvent or concentration. These  $\beta$ -sheets are at  $1632$ ,  $1642$  and  $1636\text{ cm}^{-1}$  for GS in  $\text{D}_2\text{O}$ , 1-octanol and TFE, respectively (refer to Chapter 3). Simulated Raman results for the trimer model representing aggregated GS showed that the  $\beta$ -sheet at  $1631\text{--}3\text{ cm}^{-1}$  and the absence of this mode in the monomer model shows that at high peptide concentrations the  $\beta$ -sheet content increases due to continued self-association of the peptide structure. GS models have been simulated by Naik *et al.* [43] using normal mode calculations on low energy GS structures and identified bands from those studies correlated well with the bands highlighted from our simulated trimer model and the experimental result for GS solution, and results by Naik *et al.* [43] have been used as reference in the

summary *Table 5.3*. The simulations on GS trimer model considered aspects such as nearest neighbour interactions, solvent effect by using water as a solvent and intra-H-bonding. This was important as simulated results could be confidently correlated to those experimentally obtained.

The Raman spectrum for gramicidin S in solid and in aqueous solution with water has been reported in this thesis. By comparing the measured spectra with those of the known amino acids, known anti-parallel  $\beta$ -sheet forming proteins, linear gramicidin models, and GS we were able to assign the vibrational modes [1], [6]–[13]. More important is that spectral simulations performed in this study confidently confirmed vibrational modes present in aggregated aqueous GS. An intercomparison of vibrational modes present in GS identified with RS corroborated those from IR spectroscopy, as the techniques are complementary. Reproducible spectra were obtained from both RS and SERS measurements. GS being cationic was able to induce aggregation to the silver nanoparticles, a positive attribute of the ability of the peptide. The largest plasmonic red-shift being at a GS solution concentration of  $10^{-5}$  M which we report as the *optimum* concentration. The enhancement factor was different for different bands, the Phe band located in the mid fingerprint region and the amide I band had good signal to noise ratio and gave EFs of  $10.9 \pm 2.0$  and  $19.5 \pm 0.4$ . The low standard deviations for the EFs obtained for the different vibrational modes confirm the repeatability of the SERS spectra of GS with Ag metal. The ability of GS to positively aggregate the silver nanoparticles enabling detection of low GS concentrations is observed. The normal Raman spectra for GS shows the amide I band at longer frequency ( $1666 \text{ cm}^{-1}$ ), this band position relates to the band position for cationic peptides reported in Raman peptide studies where cationic peptides with type II'  $\beta$ -turn had an amide I band in the range  $1650\text{--}1680 \text{ cm}^{-1}$  [26], [44].

## 5.4 Conclusion

A fundamental characterisation on an aqueous solution of GS in water, as well as characterisation of a Raman spectrum of GS powder are reported for the first time. Results between complementary techniques, RS and IR, correlated very well for GS in solution. Theoretical results from QM/MM calculations on a GS monomer and GS trimer, as oligomer model, provided a means to assign the main spectral observations from experimental results. In both theoretical and experimental results residues contributing to the amphiphilic (hydrophobicity and hydrophilicity) character of GS are well represented as judged by the identified ornithine and  $\beta$ -turn amide bands which appear in both monomer and trimer IR and Raman spectra. This further suggests that these residues can be used as spectral markers in understanding monomeric and aggregated GS structures in selected environments. Comparison of the model spectra with the experimental spectrum of a high concentration GS in

solution indicated the presence of both monomeric and oligomeric GS in solution, with the Phe side in different environments in the oligomer (trimer in model) and in monomer.

The interactions of GS with metallic silver is also reported in this study, with aromatic amino acid residue, Phe, interacting more with the metallic substrate and having a significant enhancement factor. The high affinity of GS to bind more strongly to silver than to gold as well as the presence of aromatic Phe residues explains the intense and resolved bands identified at very low GS concentration of  $1 \times 10^{-5}$  M. This implies that RS, SERS and IR techniques are sensitive to the amphipathic nature of GS and can therefore be used to study the peptides solution behaviour in more detail.

## 5.5 References

- [1] G. Zhu, X. Zhu, Q. Fan, and X. Wan, "Raman spectra of amino acids and their aqueous solutions," *Spectrochim. Acta - Part A Mol. Biomol. Spectrosc.*, vol. 78, no. 3, pp. 1187–1195, 2011, doi: 10.1016/j.saa.2010.12.079.
- [2] W. B. Rippon, J. L. Koenig, and A. G. Walton, "Raman Spectroscopy of Proline Oligomers and Poly-L-proline," *Arch. Biochem. Biophys.*, vol. 92, no. 25, pp. 7455–7459, 1970, doi: 10.1016/0003-9861(59)90426-6.
- [3] A. Rygula, K. Majzner, K. M. Marzec, A. Kaczor, M. Pilarczyk, and M. Baranska, "Raman spectroscopy of proteins: A review," *J. Raman Spectrosc.*, vol. 44, no. 8, pp. 1061–1076, 2013, doi: 10.1002/jrs.4335.
- [4] A. C. S. Talari, Z. Movasaghi, S. Rehman, and I. U. Rehman, "Raman spectroscopy of biological tissues," *Appl. Spectrosc. Rev.*, vol. 50, no. 1, pp. 46–111, 2015, doi: 10.1080/05704928.2014.923902.
- [5] A. Barth and C. Zscherp, "What vibrations tell about proteins," *Q. Rev. Biophys.*, vol. 35, no. 4, pp. 369–430, 2002, doi: 10.1017/S0033583502003815.
- [6] D. Kourouski, R. P. Van Duyne, and I. K. Lednev, "Exploring the structure and formation mechanism of amyloid fibrils by Raman spectroscopy: A review," *Analyst*, vol. 140, no. 15, pp. 4967–4980, 2015, doi: 10.1039/c5an00342c.
- [7] J. Shao, J. Zheng, J. Liu, and C. M. Carr, "Fourier transform Raman and Fourier transform infrared spectroscopy studies of silk fibroin," *J. Appl. Polym. Sci.*, vol. 96, no. 6, pp. 1999–2004, 2005, doi: 10.1002/app.21346.
- [8] N. Derbel *et al.*, "Vibrational Analysis of Amino Acids and Short Peptides in Hydrated

- Media. I. L-glycine and L-leucine,” *J. Phys. Chem. B*, vol. 111, no. 43, pp. 1470–1477, 2007, doi: 10.1021/jp074264k.
- [9] K. J. Rothschild and H. E. Stanley, “Raman spectroscopic investigation of gramicidin A’ conformations,” *Science (80-. )*, vol. 185, no. 4151, pp. 616–618, 1974, [Online]. Available: <http://www.ncbi.nlm.nih.gov/pubmed/4135320>.
- [10] C. David, “Raman Spectroscopy for proteins,” *Raman Spectroscopy*, 2012. [http://www.horiba.com/fileadmin/uploads/Scientific/Documents/Raman/HORIBA\\_webinar\\_proteins.pdf](http://www.horiba.com/fileadmin/uploads/Scientific/Documents/Raman/HORIBA_webinar_proteins.pdf) (accessed Jul. 10, 2015).
- [11] E. M. Krauss and S. I. Chan, “Spectroscopic Studies of Intramolecular Hydrogen Bonding in Gramicidin S,” *J. Am. Chem. Soc.*, vol. 104, no. 7, pp. 1824–1830, 1982, doi: 10.1016/S0960-9822(99)80319-4.
- [12] E. M. Krauss and S. I. Chan, “Intramolecular Hydrogen Bonding in Gramicidin S. 2. Ornithine,” 1982. Accessed: Aug. 18, 2018. [Online]. Available: <https://pubs.acs.org/doi/pdf/10.1021/ja00389a012>.
- [13] S. Siddhanta and C. Narayana, “Surface Enhanced Raman Spectroscopy of Proteins: Implications for Drug Designing,” *Nanomater. Nanotechnol.*, vol. 2, no. 1, pp. 1–13, 2012.
- [14] M. C. Chen and R. C. Lord, “Laser-Excited Raman Spectroscopy of Biomolecules. VI. Polypeptides as Conformational Models,” *J. Am. Chem. Soc.*, vol. 96, no. 15, pp. 4750–4752, 1974, doi: 10.1021/ja00822a004.
- [15] V. M. Naik, S. Krimm, J. B. Denton, G. Nemethy, and H. A. Scheraga, “Vibrational analysis of peptides, polypeptides and proteins: XXVII. Structure of gramicidin S from normal mode analyses of low-energy conformations,” *Int. J. Pept. Protein Res.*, vol. 24, no. 6, pp. 613–626, 1984, doi: 10.1111/j.1399-3011.1984.tb03168.x.
- [16] A. Barth, “Infrared spectroscopy of proteins,” *Biochim. Biophys. Acta - Bioenerg.*, vol. 1767, no. 9, pp. 1073–1101, 2007, doi: 10.1016/j.bbabi.2007.06.004.
- [17] A. Barth, “The infrared absorption of amino acid side chains,” *Progress in Biophysics and Molecular Biology*, vol. 74, no. 3–5, pp. 141–173, 2000, doi: 10.1016/S0079-6107(00)00021-3.
- [18] E. J. Prenner, R. N. A. H. Lewis, M. Jelokhani-Niaraki, R. S. Hodges, and R. N. McElhaney, “Cholesterol attenuates the interaction of the antimicrobial peptide gramicidin S with

phospholipid bilayer membranes,” *Biochim. Biophys. Acta - Biomembr.*, vol. 1510, no. 1–2, pp. 83–92, Feb. 2001, doi: 10.1016/S0005-2736(00)00337-0.

- [19] R. N. A. H. Lewis *et al.*, “Fourier transform infrared spectroscopic studies of the interaction of the antimicrobial peptide gramicidin S with lipid micelles and with lipid monolayer and bilayer membranes,” *Biochemistry*, vol. 38, no. 46, pp. 15193–15203, 1999, doi: 10.1021/bi9912342.
- [20] J. M. Walker, “Peptide Modifications to Increase Metabolic Stability and Activity,” in *Methods in Molecular Biology*, Predrag Cudic Torrey, Ed. Humana Press, 2013, pp. 1–236.
- [21] M. Buck, “Trifluoroethanol and colleagues: Cosolvents come of age. Recent studies with peptides and proteins,” *Quarterly Reviews of Biophysics*, vol. 31, no. 3, pp. 297–355, 1998, doi: 10.1017/S003358359800345X.
- [22] N. Feliu, M. Hassan, E. Garcia Rico, D. Cui, W. Parak, and R. Alvarez-Puebla, “SERS Quantification and Characterization of Proteins and Other Biomolecules,” *Langmuir*, vol. 33, no. 38, pp. 9711–9730, 2017, doi: 10.1021/acs.langmuir.7b01567.
- [23] N. Leopold and B. Lendl, “A New Method for Fast Preparation of Highly Surface-Enhanced Raman Scattering (SERS) Active Silver Colloids at Room Temperature by Reduction of Silver Nitrate with Hydroxylamine Hydrochloride,” *J. Phys. Chem. B*, vol. 107, no. 24, pp. 5723–5727, 2003, doi: 10.1021/jp027460u.
- [24] B. Hernández *et al.*, “From bulk to plasmonic nanoparticle surfaces: The behavior of two potent therapeutic peptides, octreotide and pasireotide,” *Phys. Chem. Chem. Phys.*, vol. 18, no. 35, pp. 24437–24450, 2016, doi: 10.1039/c6cp04421b.
- [25] E. López-Tobar *et al.*, “Anchoring sites of fibrillogenic peptide hormone somatostatin-14 on plasmonic nanoparticles,” *J. Phys. Chem. C*, vol. 119, no. 15, pp. 8273–8279, 2015, doi: 10.1021/acs.jpcc.5b00485.
- [26] E. López-Tobar *et al.*, “Large size citrate-reduced gold colloids appear as optimal SERS substrates for cationic peptides,” *J. Raman Spectrosc.*, vol. 48, no. 1, pp. 30–37, 2017, doi: 10.1002/jrs.4976.
- [27] P. Alonso-González *et al.*, “Resolving the electromagnetic mechanism of surface-enhanced light scattering at single hot spots,” *Nat. Commun.*, vol. 3, no. 684, 2012.
- [28] R. W. Taylor *et al.*, “Precise Subnanometer Plasmonic Junctions for SERS within Gold

- Nanoparticle Assemblies Using Cucurbit [n] uril ‘ Glue ,’” *Am. Chem. Soc.*, vol. 5, no. 5, pp. 3878–3887, 2011.
- [29] K. Kneipp *et al.*, “Laparoscopic urologic surgery: Can our patients benefit while we learn?,” *Indian J. Urol.*, vol. 78, no. 9, pp. 1667–1670, 1997.
- [30] A. Virga *et al.*, “SERS active Ag nanoparticles in mesoporous silicon: Detection of organic molecules and peptide-antibody assays,” *J. Raman Spectrosc.*, vol. 43, no. 6, pp. 730–736, 2012, doi: 10.1002/jrs.3086.
- [31] X. Tang, W. Ens, K. G. Standing, and J. B. Westmore, “Daughter Ion Mass Spectra from Cationized Molecules of Small Oligopeptides in a Reflecting Time-of-Flight Mass Spectrometer,” *Anal. Chem.*, vol. 60, no. 17, pp. 1791–1799, 1988, doi: 10.1021/ac00168a029.
- [32] S. W. Joo and K. Kim, “Adsorption of phenylacetylene on gold nanoparticle surfaces investigated by surface-enhanced Raman scattering,” *J. Raman Spectrosc.*, vol. 35, no. 7, pp. 549–554, 2004, doi: 10.1002/jrs.1183.
- [33] J. J. Cárcamo, A. E. Aliaga, E. Clavijo, C. Garrido, J. S. Gómez-Jeria, and M. M. Campos-Vallette, “Proline and hydroxyproline deposited on silver nanoparticles. A Raman, SERS and theoretical study,” *J. Raman Spectrosc.*, vol. 43, no. 6, pp. 750–755, 2012, doi: 10.1002/jrs.3092.
- [34] P. K. Sengupta, S. Krimm, and S. L. Hsu, “Vibrational analysis of peptides, polypeptides, and proteins. XXI.  $\beta$ -Calcium-poly(L-glutamate),” *Biopolymers*, vol. 23, no. 8, pp. 1565–1594, 1984, doi: 10.1002/bip.360230811.
- [35] S. Y. Venyaminov and N. N. Kalnin, “Quantitative IR spectrophotometry of peptide compounds in water (H<sub>2</sub>O) solutions. II. Amide absorption bands of polypeptides and fibrous proteins in  $\alpha$ -,  $\beta$ -, and random coil conformations,” *Biopolymers*, vol. 30, no. 13–14, pp. 1259–1271, 1990, doi: 10.1002/bip.360301310.
- [36] J. Kong and S. Yu, “Fourier transform infrared spectroscopic analysis of protein secondary structures,” *Acta Biochim. Biophys. Sin. (Shanghai)*, vol. 39, no. 8, pp. 549–559, 2007, doi: 10.1111/j.1745-7270.2007.00320.x.
- [37] V. M. Naik and S. Krimm, “Vibrational analysis of the structure of crystalline Gramicidin A,” *Biophysics (Oxf)*, vol. 45, no. January, pp. 109–112, 1984.

- [38] B. Sjöberg, S. Foley, B. Cardey, and M. Enescu, “An experimental and theoretical study of the amino acid side chain Raman bands in proteins,” *Spectrochim. Acta - Part A Mol. Biomol. Spectrosc.*, vol. 128, no. February 2018, pp. 300–311, 2014, doi: 10.1016/j.saa.2014.02.080.
- [39] R. Murugan and S. Mohan, “IJP E Vibrational analysis of L-proline,” 1996.
- [40] W. F. Schmidt *et al.*, “Continuous gradient temperature Raman Spectroscopy identifies flexible sites in proline and alanine peptides,” *Vib. Spectrosc.*, vol. 80, pp. 59–65, 2015, doi: 10.1016/j.vibspec.2015.07.003.
- [41] D. Garfinkel and J. T. Edsall, “Raman Spectra of Amino Acids and Related Compounds. XI. The Ionization of Cysteine,” *J. Am. Chem. Soc.*, vol. 80, no. 15, pp. 3823–3826, 1958, doi: 10.1021/ja01548a004.
- [42] H. Li, K. W. M. Siu, R. Guevremont, and J. C. Y. Le Blanc, “Complexes of silver(I) with peptides and proteins as produced in electrospray mass spectrometry,” *J. Am. Soc. Mass Spectrom.*, vol. 8, no. 8, pp. 781–792, 1997, doi: 10.1016/S1044-0305(97)84130-X.
- [43] V. M. Naik, S. Krimm, J. B. Denton, G. Nemethy, and H. A. Scheragai, “Vibrational analysis of peptides, polypeptides and proteins,” *Int. J. Pept. Protein Res.*, vol. 24, no. 6, pp. 613–626, 1984, doi: 10.1111/j.1399-3011.1984.tb03168.x.
- [44] B. Hernández *et al.*, “From bulk to plasmonic nanoparticle surface: behavior of two potent therapeutic peptides, octreotide and pasireotide,” *Phys. Chem. Chem. Phys.*, no. 1, pp. 24437–24450, 2016, doi: 10.1039/C6CP04421B.

## Chapter 6 Conclusions and Further Work

In this study we report on the first use of 2D-IR as well as Surface Enhanced Raman Spectroscopy (SERS) to investigate the secondary structure of Gramicidin S (GS), a model anti-microbial peptide, as a function of its environment. These results were combined with traditional FTIR measurements in order to evaluate the structure. Results were further compared to those calculated using a quantum mechanics molecular mechanics (QM/MM) approach. Of significance is the fact that a broad range of vibrational spectroscopy methods, FTIR, RS, 2D-IR and SERS were implemented to provide complementary results that are sensitive to the structural changes occurring in GS, results being corroborated by theoretical models.

For analysis of the secondary structure of proteins and peptides located in the amide I and II fingerprint regions using 1D IR spectroscopy, information is usually hidden underneath the congested broad band. This makes it difficult to extract the information. However, with 2D-IR subtle details of protein structure which may otherwise be missed by using 1D IR spectroscopy can be obtained. 2D-IR spectroscopy is used extensively to probe biological secondary structure, whereby a correlation map is generated with spectral data spread over 2 frequency axes; an excitation (pump) and detection (probe) axes. Additionally, 2D-IR provides high time resolution on femtosecond and picosecond timescales for transient processes which is a limit with conventional techniques such as circular dichroism (CD), Mass spectrometry (MS), X-ray diffraction or Ultraviolet spectroscopy. However, both 1D and 2D-IR in combination with a multivariate data analysis method such as principal component analysis (PCA) can be effective in providing insight into secondary structural changes.

In studies on protein structure, organic solvents have been used to perturb the structure of proteins as they mimic the membrane environment. Solvents conditions can influence the structural and conformational changes of proteins and the conditions can be used to elucidate protein stability aggregation behaviour and folding pathways [1]. Cosolvents have been reported to interact with proteins by altering the secondary and tertiary structure of proteins through modulations of hydrophobic forces, leading to unfolding or aggregation [1]. Differing solvent environments such as, changes in polarity, hydrogen bonding, temperature and concentration can lead to different perturbations in protein structure which can be used to characterise how these conditions influence GS.

In **Chapter 3** we demonstrated how 2D-IR can be used to identify environmental solvent effects on the secondary structure of GS. Solvent environments are important because they can represent and mimic the target environments of GS, which will aid in understanding GS conformational behaviour when its molecularly solvated and when in aggregates. To achieve this, solvents were selected to 1)

emulate lipid environments (1-octanol); 2) to represent aqueous environments since water is ubiquitous in natural systems ( $D_2O$ ); and 3) to molecularly solvate the peptide as well to mimic membrane environment (TFE). In combination with PCA, 1D and 2D-IR spectra of GS in the selected solvents presented spectral differences which we were able to correlate with structural changes. By so doing resolution is enhanced and enabled identification of  $\beta$ -turns and  $\beta$ -sheets structures which can be correlated to solution conformation behaviour. In turn this can be correlated to when GS is in an aggregated form, by changing the solvation strength. Loss of  $\beta$ -turns indicated loss of secondary structure as the monomers relax/denature, while increasing  $\beta$ -sheet content indicated the self-association of hydrophobic residues to form aggregates which persisted and continued to self-assemble with increasing peptide concentration in  $D_2O$  and 1-octanol. TFE forms strong hydrogen bonds and the aggregates/oligomers are molecularly solvated to give fine spectral details. Further analysis of 1D and 2D-IR data allowed the interpretation of the influence of peptide concentration on the peptide's conformational behaviour. Increasing concentration resulted in aggregation/oligomerisation and broadening of spectral bands. When there is aggregation/oligomerisation, conformational changes occur, and it was identified by referring to the fingerprint region of the Amide I band. Here we observed anti-parallel  $\beta$ -sheets buried inside the cyclic GS structure of the monomers that are not affected by varying the solvent or concentration. Most importantly results indicated that of the three solvents, aggregates form from low concentrations (in our case 1.00 mg/mL) in water and 1-octanol, but in TFE there is molecular solvation even at low concentration. This conformational behaviour was influenced by the environment (solvent and concentration) and was observed due to the sensitivity afforded by 2D-IR. This know-how is important, because certain peptides are more active when aggregated/oligomerised because they adopt higher order conformations that enable them to form channels and pores in biological membranes.

**Chapter 4** details a study investigating the influence of temperature on the conformational behaviour of GS. From Chapter 3 it was showed that in 1-octanol (a lipid environment mimic), GS tends to aggregate/oligomerise. In Chapter 4, now we investigated the response of the aggregates/oligomers to temperature variations. By implementing variable temperature 1D and 2D-IR analysis on GS at 5.00 mg/mL which we know to be in aggregates, we could observe the formation and deformation of GS aggregates. By obtaining the whole profile of aggregated GS behaviour in response to temperature we could establish and resolve relevant thermodynamic parameters. The low entropic values of  $\Delta S = 0.15 \pm 0.01$  kJ/mol for unfolding of small GS oligomers/aggregates to monomeric structures indicate thermally stable GS. The process of deforming / freeing aggregates was endothermically favoured and the Gibbs free energy decreased and became more negative at elevated temperatures. With

increasing temperature enthalpy decreased implying less interaction of aggregates as hydrogen bonds are disrupted, thus increasing entropy and stability of the structures at elevated temperatures.

**Chapter 5** presents the further analysis of GS aggregates/oligomers with RS and SERS. SERS allowed the analysis of micromolar concentrations of GS by taking advantage of its interaction with metallic nanoparticles which enhances their response in RS. By further UV-Vis analysis of the peptide in solution with nanoparticles; a plasmonic red-shifted band could be attributed to the effect of peptide aggregating the nanoparticle. This was a positive attribute found more strongly for silver than for gold nanoparticles, at an optimum GS concentration of  $1 \times 10^{-5}$  M. TEM analysis confirmed the aggregated nanoparticles. To enhance our theoretical understanding, we simulated the spectroscopic response of GS by considering a single molecule (monomer) to mimic a solvated one and a trimer of GS molecules to mimic an aggregate. We found there are clear correlations between the simulated and the experimental spectra which strengthens our assignments.

2D-IR in combination with conventional IR and Raman spectroscopy proved to be an effective methodology in extracting subtle details from the secondary structure and conformational behaviour of GS. This work demonstrated that 2D based analytical methods can be applied in analysis of complex peptide aggregated systems using GS as a model. Novel results have been presented on the analysis of GS behaviour, in environments representative of membrane environments by employing the abilities of the advanced IR technique 2D-IR, supported by FTIR spectroscopy.

Antimicrobial resistance towards conventional drugs is a rising global challenge which presents the need to discover and develop novel antimicrobial agents. Clear advantages of antimicrobial peptides over conventional drugs include a low likelihood to develop bacterial resistance, a broad spectrum of activity and the simplicity in their chemical structure. The utilization of antimicrobial peptides clinically has been deterred by the need to fully understand structure and function of antimicrobial peptides, before they are rightfully used as therapeutic agents. To aid in this direction; this work employed a powerful and novel technique towards understanding the structure and behaviour of the antimicrobial peptide GS. Towards the generation of less toxic GS derivatives with high therapeutic index, this work has showed that 1). Both IR and Raman spectroscopic techniques can provide complementary results in analysing the behaviour of residues contributing to the amphipathic character of GS, as both techniques are sensitive to it. In particular, generation of GS analogues via substitution of aromatic and cationic residues. 2). Prior to peptide synthesis, this work has further proved that peptide models can be generated/simulated and utilised to predict peptide behaviour either as monomeric or oligomeric structures. Simulating peptides either as monomeric or oligomeric structures will depend on whether the peptide of interest is active as a monomer or in aggregated

form. By so doing, antibiotic peptide analogues can be modified before they are synthesised, thus being cost effective. 3). The Raman results presented have provided a standard and characterised GS Raman spectrum which serves as a reference which can be used for Raman mode assignments and characterisation of its derivatives. Since GS is non-specific, ideally selective bioactive GS derivatives with enhanced therapeutic index would be ideal such that targeted therapeutic treatment can be performed. And in cases where low antibiotic concentrations are required, metallic silver can be incorporated to enhance the signal via SERS.

Overall, the work in this thesis has elaborated IR and Raman methodologies in enhancing our understanding of GS conformation and structure. From several studies interaction of GS with membrane has explained reporting that GS binds to the membrane and causes disorganisation of lipoprotein systems and the permeability barrier of membranes [2], causing pores or channels in the membrane, resulting in the cell cytoplasmic contents leaking out, thus killing bacterial cells [3]–[6]. From the information in this study, further experiments can be conducted which can provide an element of reality. This study showed that spectral signatures can be used to monitor structural changes to GS in a selected aqueous environment and this knowhow helps in better understanding biological phenomena between GS and membranes. As GS works by binding and disorganising the permeability barrier of membranes, future work derived from this study can investigate the type of interaction lipid vesicles can have with GS. By collecting IR and Raman spectra, certain spectral signatures can be monitored in elucidating or drawing conclusions on the type of interaction which could be or could not be happening in the system.

Future work towards the 2D-IR laser system could be development of the system to limit the effects of atmospheric moisture which influences the spectral content of biological samples dissolved in organic solvents. The system can also be developed to reduce scattering effects which affect spectra quality at low concentrations. This can hopefully enable measurement of low sample concentrations in the micromolar range, enabling extraction of more from monomeric or slightly larger structures.

## 6.1 References

- [1] M. V. Khan, G. Rabbani, M. Ishtikhar, S. Khan, G. Saini, and R. H. Khan, “Non-fluorinated cosolvents: A potent amorphous aggregate inducer of metalloproteinase-conalbumin (ovotransferrin),” *Int. J. Biol. Macromol.*, vol. 78, pp. 417–428, Jul. 2015, doi: 10.1016/j.ijbiomac.2015.04.021.
- [2] G. Nagamurthi and S. Rambhav, “Gramicidin-S : Structure – activity relationship \*,” *J. Biosci.*, vol. 7, no. 3 & 4, pp. 323–329, 1985.

- [3] T. J. Franklin and G. A. Snow, *Biochemistry and Molecular Biology of Antimicrobial Drug Action*. New York (USA): Chapman and Hall, 1988.
- [4] E. J. Prenner, R. N. A. H. Lewis, M. Jelokhani-Niaraki, R. S. Hodges, and R. N. McElhaney, “Cholesterol attenuates the interaction of the antimicrobial peptide gramicidin S with phospholipid bilayer membranes,” *Biochim. Biophys. Acta - Biomembr.*, vol. 1510, no. 1–2, pp. 83–92, Feb. 2001, doi: 10.1016/S0005-2736(00)00337-0.
- [5] M. Rautenbach, H. A. Eyéghé-Bickong, N. M. Vlok, M. Stander, and A. de Beer, “Direct surfactin-gramicidin S antagonism supports detoxification in mixed producer cultures of *Bacillus subtilis* and *Aneurinibacillus migulanus*,” *Microbiol. (United Kingdom)*, vol. 158, no. 12, pp. 3072–3082, 2012, doi: 10.1099/mic.0.063131-0.
- [6] L. Béven and H. Wróblewski, “Effect of natural amphiphatic peptides on viability, membrane potential, cell shape and motility of mollicutes,” *Res. Microbiol.*, vol. 148, no. 2, pp. 163–175, 1997, doi: 10.1016/S0923-2508(97)87647-4.

## Chapter 7 Appendix

Table 7.1 Values calculated from experimental data, used to obtain the changes in Free energy with temperature. The are the values used in plotting the bimodal profile, Van Hoff plot and the Gibbs free energy plot Graphs in Figure 4.11. Values are to 4 s.f. (Refer to free energy calculations in section 4.3.4)

T [K]	1/T [K <sup>-1</sup> ]	Area under the IR graph	f <sub>unfolded</sub>	f <sub>folded</sub>	K <sub>eq</sub>	ln(K <sub>eq</sub> )	$\Delta G = -RT \ln K_{eq}$ [kJ mol <sup>-1</sup> ]
293.0	0.003413	2.304	0.000	1.000	0.000		
303.0	0.003300	2.239	0.05391	0.9460	0.05698	-2.864	7.217
313.0	0.003195	2.186	0.09735	0.9026	0.1078	-2.226	5.795
318.0	0.003145	2.171	0.1099	0.8900	0.1235	-2.090	5.528
321.0	0.003115	2.142	0.1334	0.8665	0.1540	-1.870	4.993
325.0	0.003077	2.060	0.2011	0.7988	0.2517	-1.379	3.727
328.0	0.003049	2.065	0.1970	0.8029	0.2453	-1.404	3.831
331.0	0.003021	1.351	0.7832	0.2167	3.612	1.284	-3.534
335.0	0.002985	1.217	0.8931	0.1068	8.358	2.123	-5.914
338.0	0.002959	1.125	0.9689	0.0310	31.16	3.439	-9.665
343.0	0.002915	1.093	0.9949	0.0050	198.8	5.292	-15.094
348.0	0.002874	1.089	0.9987	0.0012	805.1	6.691	-19.360
353.0	0.002833	1.087	1.000	0.000			